

Democratic and Popular Republic of Algeria
Ministry of High Education and Scientific Research
University of Ferhat Abbas Setif 1



THESIS

Presented at Faculty of Sciences

Department of Physics

To obtain the degree of

Doctor of Science

Option: Solid State Physics

By

Abdelghani Benahmed

Title

**Contribution to the study of some physical properties of
the ternary phosphides $LiAeP$ ($Ae=Sr, Ba$) and Zintl-phases
 Ae_3AlAs_3 ($Ae = Sr, Ba$)**

Discussed publicly at 06/ 10/ 2018 with the board of examiners:

Mr K. KASSALI,	Professor	Univ. F. Abbas Sétif 1, Chairman
Mr A. BOUHEMADOU	Professor	Univ.F. Abbas Sétif 1, Supervisor
Mr S. BOUCETTA	Professor	Univ.F. Abbas Sétif 1, Examiner
Mr F. SAHNOUNE	Professor	Univ. M. Boudiaf, M'sila, Examiner
Mr B. DAGHFEL	Professor	Univ. M. Boudiaf, M'sila, Examiner
Mr M. SALMI	M.C. A	Univ. M. Boudiaf, M'sila, Examiner
Mr N. GUECHI	M.C. A	Univ. Y. Farès de Médéa, Invited

Abstract

In the present work, we report the results of an ab initio study of some physical properties of two ternary phosphides: LiAeP (Ae = Sr, Ba), and two newly synthesized Zintl-phases: Ae_3AlAs_3 (Ae = Sr, Ba).

The structural, elastic electronic, optical and thermodynamic properties of the LiBaP and LiSrP compounds were performed using the pseudopotential plane-wave method within the framework of density functional theory with the GGA-PBEsol. Calculated equilibrium lattice constants are in good agreement with the available experimental data. Calculated cohesive energy confirms the thermodynamically stability of the considered materials. Single-crystal elastic constants C_{ij} and related properties were predicted using the static finite strain technique. Polycrystalline elastic moduli and related properties were estimated from the C_{ij} via the Voigt-Reuss-Hill approximations. Energy band dispersions along some high symmetry directions in the k -space and the density of states diagrams were computed and analysed. Obtained energy band structures show that both considered crystals are indirect band gap compounds. The band gap is approximately equal to 1.16 eV for LiSrP and 0.80 eV for LiBaP. The chemical bonding character was discussed through the electron density map plots. In order to understand the optical properties of LiSrP and LiBaP, the complex dielectric function, refractive index, extinction coefficient, reflectivity, absorption coefficient, electron energy-loss function and complex conductivity function were predicted for an incident radiation with an energy range up to 15 eV. The origin of the main peaks in the optical spectra was discussed in terms of the calculated electronic structure. We have predicted temperature and pressure dependence of the relative unit-cell volume, volume thermal expansion coefficient, heat capacities, Debye temperature and Grüneisen parameter via the quasi-harmonic Debye model.

The structural, elastic, electronic, optical and thermoelectric properties of the Zintl-phases Ae_3AlAs_3 (Ae = Sr, Ba) were investigated using two complementary approaches based on density functional theory. The pseudopotential plane-wave method was used to explore the structural and elastic properties whereas the full-potential linearized augmented plane wave approach was used to study the structural, electronic, optical and thermoelectric properties. Calculated structural parameters are in good consistency with the corresponding measured ones. Single-crystal and polycrystalline elastic constants and related properties were examined in details. Electronic properties, including energy band dispersions, density of states and charge-carrier effective masses, were computed using Tran-Blaha modified Becke-Johnson functional for the exchange-correlation potential. It is found that Sr_3AlAs_3 has a direct band gap semiconductor while Ba_3AlAs_3 has an indirect band gap semiconductor. Frequency-dependence of the linear optical functions were predicted for a wide photon energy range up to 15 eV. Charge carrier concentration and temperature dependences of the basic parameters of the thermoelectric properties were explored using the semi-classical Boltzmann transport model. Our calculations unveil that the studied compounds are characterised by a high thermopower for both carriers, especially the p -type conduction is more favourable.

ملخص

في هذا العمل، قمنا عن طريق مقارنة حسابية من المبادئ الأولى، بدراسة بعض الخصائص الفيزيائية لاثنتين من المركبات الفوسفورية الثلاثية:

$LiAeP$ (Ae = Sr, Ba) و لاثنتين من مركبات زنتل حديثا التركيب Ae_3AlAs_3 (Ae = Sr, Ba)

تمت دراسة الخصائص البنيوية، المرنة، الضوئية والثرموديناميكية لمركبات LiSrP و LiBaP باستخدام طريقة الامواج المستوية مع نظرية الكمونات الكاذبة، في إطار نظرية دالية الكثافة الإلكترونية DFT باستعمال تقريب التدرج المعمم GGA-PBEsol لطاقة التبادل-الارتباط (EXC). النتائج المتحصل عليها تمت مقارنتها مع النتائج التجريبية المتوفرة. وقد تبين ان ثوابت البنية البلورية المحسوبة عند التوازن متوافقة بشكل جيد مع البيانات التجريبية المتاحة وان طاقة التماسك المحسوبة تؤكد استقرار الديناميكيات الحرارية للمواد. بالنسبة للخواص المرنة تم التنبؤ بقيم معاملات المرونة C_{ij} لأحادي البلورة والخصائص ذات الصلة باستخدام تقنية التشوه المحدود. كما تم تقدير معاملات المرونة لمتعددة البلورات والخصائص ذات الصلة من معاملات المرونة C_{ij} عبر تقريب فويت، رويس وهيل. فيما يخص الخواص الإلكترونية تبين من خلال حساب وتحليل مستويات الطاقة على طول بعض اتجاهات عالية التناظر في الفضاء k وكثافة الحالات ان المركبات عبارة عن انصاف نواقل ذات فاصل طاقي اساسي غير مباشر. فاصل الطاقة يساوي تقريبا 1.16 إلكترون فولط لـ LiSrP و 0.80 إلكترون فولط لـ LiBaP. خواص الترابط الكيميائي لـ LiBaP و LiSrP كذلك تمت مناقشتها بواسطة مخططات التوزيع الإلكترونية. لدراسة الخواص الضوئية تم حساب دالة العزل الكهربائية، معامل الانكسار، معامل الاخمد، الانعكاسية، معامل الامتصاص، معامل فقدان الطاقة ومعامل الناقلية البصرية. وتم تعيين اصول الانتقالات الإلكترونية من خلال الخواص الضوئية. بالنسبة للخواص الترموديناميكية للمركبات المدروس تم التنبؤ بتأثير درجة الحرارة والضغط على حجم خلية الوحدة، عن طريق حساب معامل التمدد الحراري للحجم، السعة الحرارية، ودرجة حرارة ديبي، معامل قريبنزن باستخدام تقريب شبه التوافقي.

الخواص التركيبية، المرنة، الإلكترونية، البصرية والكهروحرارية لمركبي زنتل Ae_3AlAs_3 (Ae = Sr, Ba) تمت دراستها، باستخدام منهجين متكاملين يعتمدان على نظرية دالية الكثافة الإلكترونية DFT. طريقة الامواج مع نظرية الكمونات الكاذبة تم استخدامها في استكشاف الخصائص البنيوية و المرنة بينما طريقة الامواج المستوية المتزايدة خطيا مع نظرية الكمونات الكاملة تم استخدامها في دراسة الخواص الإلكترونية والبصرية والكهروحرارية. المعاملات البنيوية المحسوبة في اتفاق جيد مع البيانات التجريبية المتوفرة. ثوابت المرونة لأحادي البلورة ولمتعددة البلورات والخصائص ذات الصلة تم فحصها بالتفصيل. الخصائص الإلكترونية: مستويات الطاقة، كثافة الحالات، والكتل الفعالة تم حسابها باستعمال تقريب TB-mBJ لطاقة التبادل-الارتباط (EXC). وقد وجدنا أن كلا المركبين عبارة عن نصف ناقل Sr_3AlAs_3 ذو فاصل طاقي اساسي مباشر بنما Ba_3AlAs_3 ذو فاصل طاقي اساسي غير مباشر. الخواص البصرية تم التنبؤ بها بالاعتماد على تعلق المعاملات البصرية بالترددات الضوئية من أجل نطاق واسع من طاقة الفوتون يصل إلى 15 إلكترون فولط. تعلق المعاملات الأساسية للخواص الكهروحرارية بدرجة الحرارة وبتكريز حاملات الشحن تم دراسته باستخدام نموذج نقل بولتزمان شبه الكلاسيكي. وقد اظهرت النتائج ان كلا من المركبين يتميز بقدرة كهرو حرارية عالية لكل أنواع حاملات الشحن خاصة بالنسبة لنوع p فهو الأكثر تفضيلاً.

*This thesis is dedicated to the
memory of my late father*

Acknowledgement

First and foremost, I would like to express my deep gratitude to my supervisor professor Bouhemadou Abdelmadjid, for his professional guidance throughout the research period, for all of the encouragements and supports you gave me, on my research work, on my publication and thesis write-up.

I thank Dr. Guechi Nacir for supporting me and encouraging me in my work,

I thank the rapporteurs who have done me the honour to agree to read and judge this thesis.

I also extend my gratitude to those who have helped me in some way or another to carry out this work, particularly, Benhamza Abdelkader, Bedjaoui Abdelhak, Hamou Miloud, Benouis Mohamed, Meskine Nacer, Sbaa Souad, Bentaybe Abdelkader, Marboui Nourinne, Mastfay Mohamed, Rachache Mustafa, Alali Djamel.

Last but not least, I would like to thank my family: my parents who always encouraged me to pursue my scientific way to this distant point, and my brothers, sisters and my fiancé, for supporting me spiritually throughout this thesis as well as throughout my life so far in all its manifestations.

Nomenclature

Frequently used abbreviations:

DFT	Density Functional Theory
H	Hartree.
HF	Hartree-Fock.
xc	Exchange Correlation.
KS	Kohn-Sham.
LDA	Local Density Approximation.
LSDA	Local Spin Density Approximation.
GGA	Generalized Gradient Approximation.
PBEsol	Perdew-Burke-Ernzerhof functional for Solids.
TB-mBJ	Tran-Blaha modified Becke-Johnson potential.
PP-PW	Pseudopotential-Plane Wave.
ZB	Brillouin Zone.
AE	All Electrons.
NC	Norm-Conserving.
BHS	Bachelet, Hamann, Schlüter procedure for constructing norm-conserving PP.
KB	Kleinman and Bylander.
US-PP	Ultrasoft pseudopotential.
APW	Augmented Plane Wave.
LAPW	Linearized Augmented Plane Wave.
FP	Full Potential.
MT	Muffin-Tin region.
I	Interstitial region.
LO	Local Orbitals.
EOS	Equation Of State.
BM	Birch Murnaghan.
V-R-H	Voigt-Reuss-Hill.
E_g	Energy band gap.
VB	Valence Band.
CB	Conduction Band.
TDOS	Total Density Of States.
PDOS	Partial Density Of States.

Contents

I. General Introduction.....	1
I.1 Background	2
I.2 Statement of the problem and research objectives	4
I.2.1 The ternary phosphides LiAeP (Ae =Sr, Ba).....	4
I.2.2 The Zintl-phase Ae ₃ AlAs ₃ (Ae = Sr, Ba)	5
I.3 Organization of the thesis.....	6
References	7
II. Fundamentals of the Density Functional Theory.....	9
II.1 Introduction.....	10
II.2 Solving the Schrödinger equation.....	10
II.2.1 The Born-Oppenheimer approximation	11
II.2.2 The Hartree approximation	13
II.2.3 The Hartree-Fock approximation	15
II.3 The theory of the density functional	17
II.3.1 Hohenberg-Kohn's theorem.....	18
II.3.1.1 Hohenberg-Kohn's first theorem	18
II.3.1.2 Second theorem of Hohenberg-Kohn	18
II.3.2 Kohn and Sham's approach	19
II.3.3 The Kohn-Sham equations	21
II.3.4 The exchange–correlation potential	22
II.3.4.1 Local density approximation (LDA)	22
II.3.4.2 The generalized gradient approximation (GGA).....	24
II.3.4.3 The modified Becke–Johnson (MBJ) potential	25
References	27
III. Planes Waves and Pseudopotential Method.....	29
III.1 Introduction	30
III.1 Crystal symmetry and Bloch's theorem.....	30
III.1.1 Periodic systems.....	30
III.1.2 Bloch’s theorem	31
III.2 Expression of Kohn-Sham equations in the plane wave basis	32

III.3 The cut-off energy	32
III.4 Sampling the Brillouin Zone	33
III.5 Pseudopotential.....	33
III.5.1 The frozen core approximation.....	33
III.5.2 Concept of pseudopotentials	34
III.5.3 Ab initio Pseudopotentials	35
III.5.3.1 Method of Philips and Kleinman	36
III.5.3.2 Norm conserving pseudopotentials	38
III.5.3.2.1 Concept of Norm conserving pseudopotentials.....	38
III.5.3.2.2 The construction of the norm-conserving pseudopotential	38
III.5.3.3 Vanderbilt Pseudopotential (Ultrasoft)	41
III.5.3.3.1 Concept of Vanderbilt Pseudopotential (Ultrasoft).....	41
III.5.3.3.2 The construction of ultrasoft potentials	42
III.6 Resolution of Kohn-Sham equations.....	44
Reference.....	47
IV. Full-Potential Linearized Augmented Plane Wave Method	49
IV.1 Introduction	50
IV.2 The augmented plane wave (APW).....	50
IV.3 The linearized augmented plane wave method (LAPW)	52
IV.4 Local Orbitals	53
IV.5 The APW+ local orbitals.....	54
IV.6 The Full Potential (L)APW+lo Method	55
Reference	57
V. Theory of the Investigated Properties	58
V.1 Introduction.....	59
V.2 Ground State Energy.....	59
V.3 Elastic constants.....	59
V.4 Diagram of band structure and density of states.....	61
V.4.1 Electronic band structure	61
V.4.2 Density of electronic states	62
V.5 Optical properties.....	63
V.6 The Thermodynamic properties.....	65

V.7 Thermoelectric proprieties.....	67
V.7.1 The Seebeck effect.....	67
V.7.2 The Peltier effect.....	68
V.7.3 The Thomson effect.....	69
V.7.4 The Boltzmann transport Equation.....	70
V.7.5 The relaxation time.....	72
V.7.6 The transport coefficients.....	73
V.7.6.1 Electrical conductivity.....	74
V.7.6.2 Seebeck coefficient.....	75
V.7.6.3 The thermal conductivity.....	75
V.7.6.4 The Figure of merit.....	76
Reference:.....	78
VI. Computational Tools.....	81
VI.1 Introduction.....	82
VI.2 Cambridge serial total energy package (CASTEP).....	82
VI.3 The WIEN2k code.....	83
VI.4 Gibbs program.....	86
VI.5 The BoltzTrap.....	86
References.....	87
VII. Ab initio study of the Structural, Elastic, electronic, optical and thermodynamic properties of ternary phosphides LiAeP (Ae=Sr, Ba).....	88
VII.1 Computational details.....	89
VII.2 Results and discussion.....	90
VII.2.1 Structural parameters.....	90
VII.2.2 Elastic properties.....	97
VII.2.2.1 Elastic constants and related properties.....	97
VII.2.2.2 Elastic anisotropy.....	103
VII.2.3 Electronic structure and chemical bonding.....	107
VII.2.4 The effective mass.....	109
VII.2.5 Densities of states.....	110
VII.2.6 Optical properties.....	112
VII.2.6.1 The dielectric function.....	112

VII.2.6.2 The absorption coefficient	114
VII.2.6.3 The reflectivity.....	115
VII.2.6.4 The energy-loss function	115
VII.2.6.5 The refractive index.....	116
VII.2.7 Thermodynamic properties.....	117
VII.2.7.1 The lattice parameter under temperature	118
VII.2.7.2 The Bulk modulus.....	118
VII.2.7.3 The Debye temperature.....	119
VII.2.7.4 The Grüneisen parameter.....	120
VII.2.7.5 The heat capacity	121
VII.2.7.6 The coefficient of thermal expansion	122
Reference.....	124
VIII. Structural, elastic, electronic, optical and Thermoelectric properties of the Zintl-phase Ae_3AlAs_3 (Ae=Sr, Ba)	126
VIII.1 Computational details	127
VIII.2 Results and discussion	128
VIII.2.1 Structural parameters	128
VIII.2.2 Elastic constants and related properties	130
VIII.2.3 Electronic properties	136
VIII.2.3.1 Band structure.....	136
VIII.2.3.2 Density of states	137
VIII.2.3.3 Effective mass	139
VIII.2.4 Optical properties	140
VIII.2.4.1 The dielectric functions	140
VIII.2.4.2 The absorption coefficient.....	142
VIII.2.4.3 The reflectivity	143
VIII.2.4.4 The energy-loss function	143
VIII.2.4.5 The refractive index.....	143
VIII.2.5 Thermoelectric properties	145
References	149
IX. General Conclusions	151
IX.1 The ternary phosphides $LiAeP$ (Ae =Sr, Ba)	152

IX.2 The Zintl-phase Ae_3AlAs_3 ($Ae = Sr, Ba$) 153

III.1	Schematic diagram of the relationship between all-electron and pseudopotentials and wave functions.	35
III.2	A flow chart of a typical DFT calculation within the Kohn Sham method.....	46
IV.1	Division of the unit cell into two parts: The Muffin-Tin spheres, with radius R, around the nucleus and an interstitial region	50
V.1	An open circuit that displays the Seebeck effect; A and B are two dissimilar conductors. The terminals C and D are assumed to be at the same temperature, J_1 and J_2 are junctions held at two different temperatures, T_1 and T_2 , resulting in the formation of a voltage across points C and D. (Figure adopted from [35]).	68
V.2	Schematic representation of the Peltier effect; A and B are two dissimilar materials. Under the conditions of no temperature gradient ($\nabla T = 0$), A current I passes through materials A and B causing the absorption and release of heat Q . The rate of cooling $-q$ occurs at J_1 while heating q occurs at J_2 . (Figure adopted from [35]).	69
VI.1	Flowchart of a CASTEP calculation (Adopted from [4]).....	83
VI.2	Flowchart of a Wien2k calculation.....	85
VII.1	Crystal structure of the LiSrP hexagonal compound	92
VII.2	Pressure dependence of the normalized lattice parameters (a/a_0 and c/c_0) and unit-cell volume (V/V_0) for the LiBaP and LiSrP materials. The ‘‘0’’ subscript denotes the parameter value at zero pressure. The calculated values are shown by symbols and solid lines show the quadratic approximations.....	93
VII.3	(a) Computed pressure versus primitive-cell volume data for the LiSrP and LiBaP materials. The symbols are the calculated results and the continuous lines are Murnaghan EOS fits. (b) Unit-cell dependence of the total energy for the LiSrP and LiBaP materials. The calculated values are shown by symbols and Murnaghan EOS fits are shown by solid line.	94
VII.4	Pressure dependence of the normalized bond-lengths for the LiSrP and LiBaP materials. The calculated values are shown by symbols and the quadratic approximations are shown by solid line. ‘‘d’’ stands for the interatomic distance at a pressure P, whereas ‘‘ d_0 ’’ is the same distance at zero pressure.....	96

- VII.5** Calculated pressure dependence of the elastic constants C_{ij} and bulk modulus B for LiSrP and LiBaP materials. The symbols are the calculated results and the continuous lines are the second-order polynomial fits to the results. 103
- VII.6** 3D-directional dependence of the Young's modulus (E , in GPa) and its projection on the ab - $\{(001)\}$ and ac - $\{(010)\}$ planes for the LiSrP and LiBaP materials. 106
- VII.7** Calculated electronic energy band dispersion curves along the high symmetry directions in the Brillouin zone for the LiAeP (Ae = Sr, Ba) compounds. E_g gives the value of the fundamental energy band gap $\Gamma - M$. The Fermi level is given at 0.0 eV. 108
- VII.8** Pressure dependence of the fundamental indirect band gap Γ -M and the first direct band gap Γ - Γ for the LiAeP (Ae = Ba, Sr) compounds. The calculated values are indicated by symbols and the fits by solid lines. 109
- VII.9** Total (TDOS) and partial (PDOS) densities of states diagrams for the LiAeP (Ae = Sr, Ba) compounds. T1 (T1 \backslash), T2 (T2 \backslash), T3 (T3 \backslash) and T4 (T4 \backslash) represent the electronic transitions from the valence bands to the conduction bands. 111
- VII.10** Charge density distribution maps in the (110) plane for the LiSrP (a) and LiSrP (b) systems..... 112
- VII.11** Calculated (a) imaginary $\epsilon_2(\omega)$ and (b) real parts $\epsilon_1(\omega)$ of the dielectric function for incident radiation polarized along the two principal crystallographic directions, i.e., $E//a$ and $E//c$, for the LiAeP (Ae = Sr, Ba) crystals. The obtained spectra for the LiAeP (Ae = Sr, Ba) polycrystals are also shown..... 114
- VII.12** Calculated optical function spectra: (a) Absorption $\alpha(\omega)$, (b) Reflectivity $R(\omega)$, (c) Energy loss function $L(\omega)$, (d) Refractive index $n(\omega)$ and (e) Extinction coefficient $k(\omega)$ for incident radiation polarized along the two principal crystallographic directions i.e., $\vec{E}//a$ and $\vec{E}//c$, for the LiAeP (Ae = Sr, Ba) crystals. Obtained spectra for the LiAeP (Ae = Sr, Ba) polycrystals are also shown..... 117
- VII.13** (a) The normalized primitive-cell volume V/V_0 as a function of temperature for the LiSrP and LiBaP compounds at some fixed pressures; V is the primitive-cell volume at the considered temperature; V_0 is the primitive-cell volume at zero temperature. (b) The normalized bulk modulus B/B_0 as a function of temperature for the LiSrP and LiBaP compounds at some fixed pressures; B is the bulk modulus at the considered temperature and B_0 is the bulk modulus at the zero temperature. 119

VII.14	(a) Variations of the Debye temperature and (b) Grüneisen parameter versus temperature at some fixed pressures for the LiSrP and LiBaP compounds.....	121
VII.15	(a) Variations of the heat capacity at constant volume C_V and (b) the heat capacity at constant pressure C_P versus temperature at some fixed pressures for the LiSrP and LiBaP compounds.....	122
VII.16	Variation of the volume thermal expansion coefficient as a function of temperature at some fixed pressures for LiSrP and LiBaP.....	123
VIII.1	(colour online) one-unit cell of Sr_3AlAs_3	129
VIII.2	(colour online) 3D-directional dependence of the Young's modulus (E, in GPa) and its projection on the ab- $\{(001)\}$, ac- $\{(010)\}$ and cb- $\{(100)\}$ planes for the Sr_3AlAs_3 and Ba_3AlAs_3 compounds.....	135
VIII.3	(colour online) Electronic band dispersion curves along some high symmetry directions in the Brillouin zone for the Ae_3AlAs_3 (Ae = Sr, Ba) compounds using the GGA-PBEsol (a) and the TB-mBJ (b) functionals.....	137
VIII.4	(colour online) Total and partial densities of states (TDOS and PDOS) diagrams for the Ae_3AlAs_3 (Ae = Sr, Ba) compounds.....	139
VIII.5	(colour online) calculated imaginary ($\epsilon_2(\omega)$) and real ($\epsilon_1(\omega)$) parts of the dielectric function ($\epsilon(\omega)$) as functions of photon energy for the Ae_3AlAs_3 (Ae = Sr, Ba) single-crystals for three different polarisations: $\vec{E} \parallel [100]$, $\vec{E} \parallel [010]$ and $\vec{E} \parallel [001]$	142
VIII.6	(colour online) calculated optical function spectra: absorption coefficient $\alpha(\omega)$, reflectivity $R(\omega)$, energy loss function $L(\omega)$, refractive index $n(\omega)$ and extinction coefficient $k(\omega)$ for the Sr_3AlAs_3 and Ba_3AlAs_3 single-crystals for three different polarisations: $E \parallel [100]$, $E \parallel [010]$ and $E \parallel [001]$	145
VIII.7	(colour online) Calculated average Seebeck coefficient (S; panel a), electrical conductivity scaled by relaxation time (σ/τ ; panel b), thermal conductivity scaled by relaxation time (κ/τ ; panel c) and power-factor ($PF = S^2\sigma/\tau$ panel d) as functions of both electron and hole.....	147
VIII.8	(colour online) Calculated figure of merit ZT as a function of charge-carrier concentration of both electron and hole concentrations at 300, 600 and 900 K for the Sr_3AlAs_3 (solid lines) and Ba_3AlAs_3 (dotted lines) compounds.....	148

VII.1	Calculated optimized structural parameters for the LiBaP and LiSrP compounds at zero pressure: lattice parameters (a_0 and c_0 , in Å), equilibrium unit-cell volume (V_0 , in Å ³), bulk modulus (B, in GPa) its pressure derivative B' and cohesive energy (E_{coh} , in eV/atom). B and B' are derived from the Birch EOS fit. Available experimental results are reported for comparison.	92
VII.2	Selected bond lengths (in Å) for the LiAeP (Ae=Sr, Ba) systems.	96
VII.3	Calculated elastic constant (C_{ij} , in GPa) for the LiAeP (Ae = Sr, Ba) compounds.	98
VII.4	Acoustic wave velocities (in m/s) for some propagating directions in the LiAeP (Ae = Ba, Sr) hexagonal compounds. ρ is the mass density of material ; T and L stand to the transverse and longitudinal wave polarizations.	98
VII.5	Calculated polycrystalline elastic moduli: Reuss, Voigt and Hill bulk modulus (B_R , B_V and B_H , in GPa), Reuss, Voigt and Hill shear modulus (G_R , G_V and G_H , in GPa), Young's modulus (E, in GPa) and Poisson's ratio (σ , dimensionless) for isotropic polycrystalline LiAeP (Ae = Sr, Ba) aggregates.	100
VII.6	Calculated mass density (ρ), longitudinal, transverse and average sound velocities (v_l, v_t and v_m , respectively) and Debye temperatures (θ_D) for LiAeP (Ae = Sr, Ba).	101
VII.7	Calculated anisotropy in compression (A_B), anisotropy in shear (A_G), anisotropy factors ($A_1 = A_2$ and A_3) and the anisotropy universal index A^U for the LiAeP (Ae = Sr, Ba) compounds.	104
VII.8	Calculated electron and hole effective masses (m_e and m_h , respectively; in unit of free electron mass) for the LiSrP and LiBaP compounds.	110
VIII.1	Calculated lattice parameters (a, b and c, in Å) and unit-cell volume (V, in Å ³) for the Sr ₃ AlAs ₃ and Ba ₃ AlAs ₃ compounds, compared with the experimental data	129
VIII.2	Atomic position coordinates for the Sr ₃ AlAs ₃ and Ba ₃ AlAs ₃ compounds, compared with the experimental data.	130
VIII.3	Calculated elastic constant (C_{ij} , in GPa) for the Ae ₃ AlAs ₃ (Ae = Sr, Ba) compounds.	131
VIII.4	Calculated polycrystalline elastic moduli: Reuss, Voigt and Hill bulk modulus (B_R , B_V and B_H , in GPa), Reuss, Voigt and Hill shear modulus (G_R , G_V and G_H , in GPa),	

Young's modulus (E , in GPa) and Poisson's ratio (dimensionless) for isotropic polycrystalline Ae_3AlAs_3 ($Ae = Sr, Ba$) aggregates.	133
VIII.5 Calculated mass density (ρ), longitudinal, transverse and average sound velocities (v_l, v_t and v_m , respectively) and Debye temperatures (θ_D) for Ae_3AlAs_3 ($Ae=Sr, Ba$).	134
VIII.6 Calculated electron and hole effective masses (m_e and m_h in units of free electron mass m_0) for the Sr_3AlAs_3 and Ba_3AlAs_3 compounds.....	140
VIII.7 Calculated static dielectric constants $\epsilon_1(0)$, static refractive indexes $n(0)$ and optical anisotropy $AOPT$ for the Sr_3AlAs_3 and Ba_3AlAs_3 compounds in polycrystalline and along the principal optical axes: $[100]$, $[010]$ and $[001]$	144

I. General Introduction

I.1 Background

From the dawn of human existence, material and material development have been fundamental to the development of civilisation. The different rates of progression towards more flowered civilizations is inextricably tied to the local availability of materials and innovation of new materials that satisfy human needs from the Stone Age, to the Iron Age, to today's Silicon Age, and continue to be one of the most important factor and objectives of industrial development, thereby contributing in solving some emerging societal needs and to increase the quality of life. The demands of tomorrow's technology translate has greatly exceeded the capabilities of today's materials and chemical processes and new materials are constantly needed. The identification of new classes of materials with tailored properties can profoundly deliver greater performance, improved cost effectiveness, superior reliability and better safety, while also minimizing environmental impact.

The most inspiring developments in materials have emerged from scientific research on the structure of matter and its interaction with mechanical, electrical, magnetic and nuclear force fields, with radiation of all kinds and with chemically different species. New materials often provide opportunities for rapid technological progress, but to seize these opportunities, materials need to be adapted and integrated into economically viable products. It has not been easy; studies show that it often takes 20 years or more for a new material to create significant market penetration. Many challenges will have to be overcome to take full advantage of new materials; indispensable for a dynamic, safe and environmentally friendly economy.

One of the most advantageous and easiest ways of predicting new materials is *ab initio* calculations (i.e. the first principles). The term *ab initio* is Latin for "from the beginning". This name is given to calculations derived directly from theoretical principles without the inclusion of experimental data. The materials are composed of atoms as building units. The atoms themselves are made up of electrons. The idea behind the first principles is to apply the fundamental laws of physics to identify the behavior of a material by performing electronic structure calculations.

The so-called *ab initio* methods for electronic structure calculations are widely used in modern science. They allow us to simulate and sometimes even predict the properties of actual materials without using adjustable parameters. These methods require practically no information about the system; it is necessary to use only atomic numbers and coordinates as input to start the calculation. Then, all the properties of materials such as cohesive energy, equilibrium crystalline structure, phase transitions, transport properties, magnetism,

ferroelectricity, optical properties and others can be extracted from the calculation and sometimes directly compared to experimental data.

The ab initio study was only relatively recently possible with the development of reliable computer algorithms and the availability of high performance parallel computing facilities. Ab initio calculations can be done now on systems that only a few years ago could only be processed with semi-empirical or empirical methods.

The advantage of theoretical studies over experimental studies is that the systems studied are well defined. Therefore, the results are not obscured by undesirable effects such as those related to impurities, inhomogeneities ... Etc. In addition, theoretical studies often allow the study of properties that escape experience. The ab initio study explaining material phenomena has led to the concept of "materials by design" the idea that, for all given properties, we can predict new materials. However, Ab initio calculations are very demanding for computing resources and therefore limited in relation to small number of atoms (in the order of hundreds). On the other hand, the theoretical methods describe a real system using a similar but simpler structure, the disadvantage of these studies is that we have almost in all cases studied idealized systems, which can have only very few connections with reality. Moreover, in some situations, the neglected effects are exactly the ones of interest, but because of their complexity, they are not treated by the electronic theoretical methods. Therefore, an interaction between theoretical and experimental studies is very important and, very often, the combination of the two is greater than the sum of each study separately.

The ab initio methods for approaching the electronic structure can be classified into two classes. The simplest type of ab initio electronic structure calculation is the Hartree-Fock (HF) [1, 2] scheme, based on a wave function in the form of a Slater determinant. The Hartree-Fock (HF) program, including full exchange but no correlation, the major disadvantage is that they are intensely computational. Wave-based methods are often used to process the smallest systems. Extending HF methods to solid-state systems is difficult or impossible.

The second class of methods is density-based methods (DFTs). In these methods, the system is described by its particle density; the wave function is not taken into account. As a result, the system is reduced to fewer coordinates via its particle density. Due to its simplicity, most calculations of the electronic structure on materials are done using DFT [3, 4], and this has had a significant impact in the understanding of atoms, molecules, and solid. A number of codes implementing these methods now exist and have been used to perform simulations of several thousand atoms, such as VASP, CP-PAW, PWPAW, NWChem, EStCoMPP, Ablnit, DFT ++ and SFHInX....

I.2 Statement of the problem and research objectives

I.2.1 The ternary phosphides LiAeP ($\text{Ae} = \text{Sr}, \text{Ba}$)

Ternary compounds with a simple 1:1:1 composition—so-called 111 phase — crystallize in more than 30 structure types [5]. In recent years, these ternary compounds, especially the half Heusler structure (archetype MgAgAs), the LiGaGe structure, the ZrBeSi structure and the TiNiSi structure, have drawn increasing attention due to their interesting physical properties, which make them candidates for many technological applications. For example, the half Heusler compounds are known to be good thermoelectrics [6–8] and have been proposed as topological insulators [9, 10]. The LiGaGe structure type systems have been proposed as ferroelectrics [11]. The ZrBeSi type compounds have been proposed as Dirac semimetals [12]; three-dimensional (3D) topological Dirac semimetals (TDSs) are a recently proposed state of quantum matter [13–18] that has attracted increasing attention in physics and materials science. Generally, the 111 phases are semiconductor materials. The interest in the ternary semiconductor 111 phases is due to the attractive chemistry encountered in this class of inorganic compounds and to their excellent physical properties that are not possessed by the simple and binary semiconductors owing to the presence of three different chemical elements [19].

Recently, Dong et al. [20] synthesized several ternary phosphide single crystals, including the LiSrP and LiBaP systems. The considered LiSrP and LiBaP compounds are initially discovered in syntheses designed to explore the existence of a new class of materials containing both nitrogen and phosphorus as anions. Their crystalline structures are determined using the single-crystal X-ray diffraction. Both compounds adopt a centrosymmetric hexagonal structure, space group P63/mmc (ZrBeSi structure), with two formula units by unit-cell ($Z = 2$) [21].

Apart from the experimental results regarding the synthesis and structural parameters reported by Dong and co-authors [20], no theoretical or experimental data are available in the scientific literature for the considered systems to the best of our knowledge. Therefore, from a fundamental standpoint and in terms of eventual technological applications, we have performed the present work to obtain some of the lacking data.

Ab initio methods based on the density functional theory (DFT) have become a very powerful tool for exploring the properties of materials without requiring any experimental measurement. Thus, ab initio calculations using the pseudopotential plane-wave in the DFT

framework have been performed to investigate the electronic, optical and thermodynamic properties of the $LiAeP$ ($Ae = Sr$ and Ba) compounds.

I.2.2 The Zintl-phase Ae_3AlAs_3 ($Ae = Sr, Ba$)

Thermoelectric (TE) materials play an important role in global sustainable energy solution. These materials are investigated not only owing to their high potential of converting directly waste thermal energy to useful electrical energy but also to their capability to reduce effectively the environmental pollution. The ability of a TE material to convert heat directly into electricity is controlled by the dimensionless parameter ZT [22, 23], the so-called figure of merit. A promising TE material should have a large ZT value. However, obtaining a TE material with a high ZT value is a challenging task.

Currently, many kinds of thermoelectric materials have been widely studied, such as Zintl-phases, nanostructured compounds, zinc antimonides, oxides, half-Heusler compounds, clathrates and skutterudites [24-32]. Zintl-phases, a broad class of intermetallic compounds characterised by cations that donate their electrons to support the formation of covalency bonded anionic substrates, have emerged as a promising class of materials for thermoelectric applications due to their complex crystal structures, interesting electronic, chemical and physical properties [24,33]. The structural requirements of Zintl-phases are explained by assuming the presence of both anionic networks and electropositive cations [24]. The anionic networks are covalent and the cationic part is ionic in nature. The resulting mix of ionic and covalent bonds frequently leads to complex crystal structures with large unit cells; such a complex crystal can enable them to have low thermal conductivity [34-36]. Additionally, the Zintl-phase chemistry suggests that the fundamental transport parameters can be modified by doping to achieve a good balance between S and σ , consequently thus can lead to a high power factor [22, 37]. Therefore, Zintl-phases provide desired characteristics for high ZT and improved thermoelectric performance since their thermal conductivities are intrinsically low. This has been demonstrated in several previous studies, including Ca_3AlSb_3 [38], $Ca_5Al_2Sb_6$ [39] and $Ca_5Ga_2As_6$ [40]. This further actuates us to search for other possible new Zintl-phase materials for suitable TE candidates. In the current study, we are interested in investigating the Ae_3AlAs_3 ($Ae = Sr, Ba$) compounds that were recently synthesised [41]. These compounds crystallise in the Ba_3AlSb_3 structure type with the space group $Cmce$. The structural properties of the title compounds, including the lattice parameters and atomic position coordinates, have been investigated using single-crystal X-ray diffraction. The band structure and density of

states of Ba_3AlAs_3 have been carried out using the tight-binding linear muffin-tin orbital (TB-LMTO) method [41]. To the best of our knowledge, some basic physical properties, such as elastic, optical and thermoelectric properties of these newly synthesised compounds are not studied. Therefore, the main object of the present study is the investigation of the structural, elastic, electronic, optical and thermoelectric properties of the Ae_3AlAs_3 ($\text{Ae} = \text{Sr}, \text{Ba}$) compounds.

I.3 Organization of the thesis

The thesis is organized as follows:

In the second chapter, we present the main characteristics of the ab-initio calculations. Single-particle self-consistent field methods (Hartree and Hartree-Fock) are discussed as approximations of the multi-body Schrödinger equation. The Hohenberg-Kohn-Sham formulation of the functional theory of density is introduced. The third chapter explains the role of pseudopotential methods of the plane wave in solving Kohn-Sham equations for periodic systems. In addition, a refresher of basic solid-state physics (crystal lattices, reciprocal space, Bloch theorem . . .) is given. The fourth Chapter is devoted to the description of the Full Potential Linearized Augmented Plane Wave method. The detailed theory for investigated properties will be given in chapter five. Chapter six will focus on the computational tools used in present study. In the seventh chapter, the results of the calculations determining the properties of the LiAeP ($\text{Ae} = \text{Sr}, \text{Ba}$) phosphide ternary are presented. In the eighth chapter, we present and discuss the predicted physical properties of the Zintl-phase Ae_3AlAs_3 ($\text{Ae} = \text{Sr}, \text{Ba}$) Finally, the work is summarized in the Conclusion chapter ,the results of the calculations determining the elastic, electronic, optical and thermodynamic structural properties of the LiAeP phosphide ternary ($\text{Ae} = \text{Sr}, \text{Ba}$) are presented.

References

- [1] D. Hartree, *Proc. Cambridge Philos. Soc.* **24**, 89 (1928).
- [2] V. Fock, *Z. Phys.* **61**, 126 (1930).
- [3] P. Hohenberg and W. Kohn, *Phys. Rev.* **136**, B864 (1964).
- [4] R.G. Parr, W. Yang. *Density Functional Theory of Atoms and Molecules*, Oxford University Press, Oxford (1989).
- [5] M. L. Fornasini and F. Merlo, *J. Alloys Compd.* **219**, 63 (1995).
- [6] T. Graf, C. Felser and S. S.P. Parkin, *Prog. Solid State Chem.* **39**, 1(2011).
- [7] F. Casper, R. Seshadri and C. Felser, *Phys. Status Solidi A.* **206**, 1090 (2009).
- [8] B. Balke, J. Barth, M Schwall, G.H. Fecher and C. Felser, *J. Electron. Mater.* **40**, 702 (2011).
- [9] S. Chadov, X. Qi, J. Kübler, G. H Fecher, C. Felser and S. C. Zhang, *Nature Mater.* **9**, 541 (2010).
- [10] H. Lin, L. A. Wray, Y. Xia, S. Xu, S. Jia, R. J. Cava, A. Bansil and M. Z. Hasan, *Nature Mater.* **9**, 546 (2010).
- [11] J.W. Bennett, K. F. Garrity, K. M. Rabe and D. Vanderbilt, *Phys.Rev. Lett.* **109**, 167602 (2012).
- [12] Q. Gibson, L. M. Schoop, L. Muechler, L. S. Xie, M. Hirschberger, N. P. Ong, R. Car and R. J. Cava, arXiv.1411.0005v1, 1 (2014)
- [13] X. Wan, A.M. Turner, A. Viswanathan and S. Y. Savrasov, *Phys.Rev. B* **83**, 205101 (2011).
- [14] A. A. Burkov and L. Balents, *Phys. Rev. Lett.* **107**, 127205 (2011).
- [15] S.M. Young, S. Zaheer, J.C. Y. Teo, C. L. Kane, E. J. Mele and A. M. Rappe, *Phys. Rev. Lett.* **108**, 140405 (2012).
- [16] Z. Wang, Y. Sun, X. Q. Chen, C. Franchini, G. Xu, H. Weng, X. Dai and Z. Fang, *Phys. Rev. B* **85**, 195320 (2012).
- [17] Z.K. Liu, B. Zhou, Y. Zhang, Z. J. Wang, H. M. Weng, D. Prabhakaran, S. K. Mo, Z. X Shen, Z. Fang, X. Dai, Z. Hussain, Y. L. Chen, *Science* **343**, 864 (2014).
- [18] Z. Wang, H. Weng, Q. Wu, X. Dai and Z. Fang, *Phys. Rev. B* **88**, 125427 (2013).
- [19] M. Reffas, A. Bouhemadou, R. Khenata, T. Ouahrani and S. Bin-Omran, *Phys. B* **405**, 4079 (2010).
- [20] Y. Dong and F. J. DiSalvo, *J. Solid State Chem.* **180**, 432 (2007).
- [21] G. Brauer and E. Zintl, *Z. Phys. Chem. B* **37**, 323 (1937).
- [22] G. J. Snyder and E. S. Toberer, *Nat. Mater.* **7**, 105 (2008).

- [23] A. I. Hochbaum, R. Chen, R. D. Delgado, W Liang, E C Garnett, M. Najarian, A. Majumdar, and P. Yang, *Nature* **451**, 163 (2008).
- [24] S .M. Kauzlarich, S. R Brown, and G. J Snyder, *Dalton Trans.* **21**, 2099 (2007).
- [25] G. Chen, M. S. Dresselhaus, G. Dresselhaus, J. P. Fleurial, and T. Caillat, *Int. Mater. Rev.* **48**, 45 (2003).
- [26] M. S .Dresselhaus, G. Chen, M. Y. Tang, R. G. Yang, H. Lee, D. Z. Wang, Z. F. Ren, J. P. Fleurial and P. Gogna, *Adv. Mater.* **19**, 1043 (2007).
- [27] C. Uher, *Skutterudites: Prospective Novel Thermoelectrics, in Recent Trends in Thermoelectric Materials Research I, Semimetals and Semimetals Series*, Terry M. Tritt, eds., Vol. 69, Elsevier, Amsterdam (2001).
- [28] G. S. Nolas, J. Poon, and M. Kanatzidis, *MRS Bull.* **31**, 199 (2006).
- [29] G. J. Snyder, M. Christensen, E. Nishibori, T. Caillat, and B. B. Iversen, *Nat. Mater.* **3**, 458 (2004).
- [30] F. Casper, T. Graf, S. Chadov, B. Balke, and C. Felser, *Semicond. Sci. Technol.* **27**, 063001 (2012).
- [31] K. Koumoto, Y. Wang, R. Zhang, A. Kosuga, and R. Funahashi, *Annu. Rev. Mater. Res.* **40**, 363 (2010)
- [32] K. Koumoto, I. Terasaki, and R. Funahashi, *MRS Bull.* **31**, 206 (2006).
- [33] E. S. Toberer, A. F. May, and G. J. Snyder, *Chem. Mater.* **22**, 624 (2010).
- [34] E. S. Toberer, A. Zevalkink, N. Crisosto, and G. J. Snyder, *Adv. Funct. Mater.* **20**, 4375 (2010).
- [35] E. S. Toberer, C. A. Cox, S. R. Brown, T. Ikeda, A. F. May, S. M. Kauzlarich, and G. J. Snyder, *Adv. Funct. Mater.* **18**, 2795 (2008).
- [36] A. Zevalkink, G. Pomrehn, Y. Takagiwa, J. Swallow, and G. J. Snyder, *ChemSusChem.* **10**, 2316 (2013).
- [37] Y. Pei, A. D. LaLonde, N. A. Heinz, X. Shi, S. Iwanaga, H. Wang, L. Chen, and G. J. Snyder, *Adv. Mater.* **23**, 5674 (2011).
- [38] A. Zevalkink, E. S. Toberer, W. G. Zeier, E. Flage-Larsen, and G. J. Snyder, *Energy Environ. Sci.* **4**, 510 (2011).
- [39] Y. L. Yan and Y. X. Wang, *J. Mater. Chem.* **21**, 12497 (2011).
- [40] J. P. Perdew and A. Zunger, *Phys. Rev. B* **23**, 5048 (1981).
- [41] S. S .Stoyko, L.H. Voss, H. He, and S. Bobev, *Crystals* **5**, 433 (2015).

II. Fundamentals of the Density Functional Theory

II.1 Introduction

In this chapter, we briefly present the basic concepts such as the Born-Oppenheimer approximation that can be used to the separation of electronic and nuclear motions, the Variational Principle and Hartree-Fock (HF) that are used in all ab initio methods and which allow a considerable simplification of the solution of the Schrödinger equation. This naturally leads to the introduction of the functional theory of density, one of the most popular methods for the solution of the many-body problem.

II.2 Solving the Schrödinger equation

All materials are composed of atomic nuclei and electrons which determine the physical properties of materials and molecules: whether, for example, they are hard or soft, reactive or inert, conducting or insulating, superconducting or magnetic, good at converting solar radiation to more useful forms of energy or not. In non-relativistic quantum mechanics, the ground state of a system of atomic nuclei surrounded by electrons can be described by solving the time-independent Schrödinger equation, which has the form [1, 2]:

$$H\psi(\{R_I\}, \{r_i\}) = E\psi(\{R_I\}, \{r_i\}) \quad (\text{II. 1})$$

Where E is the total energy of the system, Ψ is the many-body wave function, $\{R_I\}$ is the set of nuclear coordinates and $\{r_i\}$ those describing the 'electrons and H is the Hamiltonian of the system composed of n electrons and N nuclei with charges Z_I . This Hamiltonian is given by

$$\widehat{H} = \widehat{T}_e + \widehat{T}_n + \widehat{V}_{ee} + \widehat{V}_{ne} + \widehat{V}_{nn} \quad (\text{II. 2})$$

In equations (II.2):

The first term $\widehat{T}_e = -\frac{\hbar^2}{2m_e} \sum_{i=1}^n \nabla_{r_i}^2$ represent the kinetic energy operator for the electrons

The second term $\widehat{T}_n = -\frac{\hbar^2}{2M_I} \sum_{I=1}^N \nabla_{R_I}^2$ represent the kinetic energy operator for the nuclei,

The third term $\widehat{V}_{ne} = -\sum_I^N \sum_i^n \frac{1}{4\pi\epsilon_0} \frac{Z_I e^2}{|R_I - r_i|}$ is the coulombic interaction between electrons and nuclei,

The fourth term $\widehat{V}_{ee} = \frac{1}{2} \sum_{i \neq j=1}^n \frac{1}{4\pi\epsilon_0} \frac{e^2}{|r_i - r_j|}$ is the electron-electron Coulomb repulsion energy,

And the last term $\widehat{V}_{nn} = \frac{1}{2} \sum_{I \neq J=1}^N \frac{1}{4\pi\epsilon_0} \frac{Z_I Z_J e^2}{|R_I - R_J|}$ is the nucleus-nucleus Coulomb repulsion energy.

Where i and I are the indices of electrons and nuclei, respectively, r_i and R_I are the coordinates of electrons and nuclei, respectively, m and e are the mass of the electron and the charge of the electron, respectively, M_I and Z_I are the mass and the charge of the I -th nucleus,

respectively, and \hbar is the Planck constant, ϵ_0 represents the permittivity of the vacuum, $|r_i - r_j|$ represents the distance between the electrons i and j , $|R_I - r_i|$ represents the distance between the i -th electron and the I -th nucleus / ion and $|R_I - R_J|$ is the distance between the I -th and the J -th nucleus / ions.

Throughout this thesis, we shall use the so-called Hartree atomic units in which mass is reckoned in units of the electron mass ($m_e = 9.1093826 \times 10^{-31}$ kg) and distance in terms of the Bohr radius ($a_0 = 5.299175 \times 10^{-2}$ nm), such that ($\hbar = e = m_e = 4\pi\epsilon_0 = 1$), the Hamiltonian is written in the most convenient form:

$$\hat{H} = -\frac{1}{2} \sum_{i=1}^n \nabla_{r_i}^2 - \frac{\hbar^2}{2M_I} \sum_{I=1}^N \nabla_{R_I}^2 - \sum_I^N \sum_i^n \frac{Z_I e^2}{|R_I - r_i|} + \frac{1}{2} \sum_{i \neq j=1}^n \frac{e^2}{|r_i - r_j|} + \frac{1}{2} \sum_{I \neq J=1}^N \frac{Z_I Z_J e^2}{|R_I - R_J|} \quad (\text{II. 3})$$

In principle, Solving Equation (II.1) is the perfect way to determine any physical property of a system of many particles. However, in practice, it is virtually impossible to solve such a complex equation, either analytically or numerically. This is due to the complexity of the above Schrödinger equation and the extremely large number of variables involved in the problem. Only for a few cases, such as hydrogen-like ions or the H_2^+ molecule, a complete analytic solution is available. The challenge posed by the many-body problem in quantum physics originates from the difficulty of describing the non-trivial correlations encoded in the exponential complexity of the many-body wave function. The many-body wave function must not only reflect the Coulomb interactions between the particles, but must also obey antisymmetry with respect to the exchange of two particles. Hence, the quantum many-body problem is centred upon finding intelligent approximations for the Hamiltonian (II.3) and the many-body wavefunction ψ , that render the Schrodinger equation tractable to numerical solution, while retaining as much of the key physics as is possible. The first approximation is to separate degrees of freedom from nuclear and electronic movements by using the Born-Oppenheimer approximation [3]

II.2.1 The Born-Oppenheimer approximation

The concept behind the Born-Oppenheimer approximation, also called adiabatic approximation [3], comes from the huge difference of mass between ions and electrons, the masses of the nuclei, being approximately two thousand times greater than those of the electrons. Typically, the ions can be considered as moving slowly in space and the electrons responding instantaneously to any ionic motion so that electrons can immediately find their ground state while the nuclei move. Hence, it seems plausible to neglect the kinetic energy of

the nuclei in zeroth order, and we take into account their kinetic energy as a classic contribution. This considerably reduces the complexity of the calculations because the presence of the kinetic term associated with the nuclear motion makes the study of the hypothetical many-body *system* into a very complex problem. It should be mentioned that the electronic properties always depend on the position of the nuclei, but not on their dynamics, such that the electronic properties depend parametrically on the position of the nuclei. The Coulomb potential describing the interaction between electrons and nuclei is therefore considered as an external potential.

Under the Born-Oppenheimer approximation, the total wave function $\Psi(\{r_i\}, \{R_I\})$ can be approximated as the product of a nuclear wavefunction and an electronic wavefunction:

$$\Psi(\{r_i\}, \{R_I\}) = \Psi_{ion}(\{R_I\})\Psi_{el}(\{r_i\}, \{R_I\}) \quad (\text{II. 4})$$

Where $\Psi_{ion}(\{R_I\})$ is the nuclear wavefunction, and $\Psi_{el}(\{r_i\}, \{R_I\})$ is the many-electron wave function that depend on the simultaneous coordinates of all the electrons. After some manipulation, we can write the Schrödinger equation only for the electrons at a given nuclear coordinates as:

$$H_e \Psi_{el}(\{r_i\}, \{R_I\}) = E_e \Psi_{el}(\{r_i\}, \{R_I\}) \quad (\text{II. 5})$$

With

$$H_e = -\frac{1}{2} \sum_{i=1}^n \nabla_{r_i}^2 - \sum_{I=1}^N \sum_{i=1}^n \frac{Z_I}{|R_I - r_i|} + \frac{1}{2} \sum_{i \neq j=1}^n \frac{1}{|r_i - r_j|} \quad (\text{II. 6})$$

For all given nuclear coordinates (R_I), the obtained electronic wave function $\Psi_{el}(\{r_i\}, \{R_I\})$ depends parametrically on (R_I), and it will change when the nuclei are moved.

The total energy of the system (electrons- nuclei) at any (static) set of (R_I) is a sum of electronic energies E_e and nuclear energies due to nucleus-nucleus interaction:

$$E_{tot}(\{R_I\}) = \langle \Psi_{el} | H_e | \Psi_{el} \rangle + V_{nn} \quad (\text{II. 7})$$

The last V_{nn} term enter only as a constant in each considered geometry.

If we know E_{tot} for many sets of nuclear coordinates, the nuclei movement can be described by the nuclear Hamiltonian H_n :

$$H_n = T_n + E_{tot}(\{R_I\}) = T_n + \langle \Psi_{el} | H_e | \Psi_{el} \rangle + V_{nn} \quad (\text{II. 8})$$

The Schrödinger equation for nuclei is given

$$\left(-\frac{\hbar^2}{2M_I} \sum_{I=1}^N \nabla_{R_I}^2 + E_{tot}(\{R_I\}) \right) \Psi_{ion}(\{R_I\}) = E_{Nu} \Psi_{ion}(\{R_I\}) \quad (\text{II. 9})$$

Note that Hamiltonian eigenvalues for nuclear motion are total energies for the system because they contain the electronic energy in their potential parts, therefore:

$$E_{tot} = E_{nuc} \quad (\text{II. 10})$$

Under the Born-Oppenheimer approximation, the dimension of the problem is reduced and the calculation is associated only with electronic degrees of freedom. However, the spatial dimension is still too important for real compounds. For a system of N electrons, the wave function $\Psi_{el}(\{r_i\}) \equiv \Psi_{el}(r_1, \dots, r_N)$ depends on $3N$ spatial variables. This causes a rapid increase in the complexity of the problem with the size of the system. Already for the small systems, which consist only of dozens of electrons, the calculation becomes unfeasible. Moreover, the equation above contains a two-particle interaction in the form of the electron-electron potential. Therefore, under the Born-Oppenheimer approach, the solution of Equation (II.5) for electrons is still a problem of many-body. We need to do more, before simulations are done. For weak interaction systems, a perturbative approach might be the best solution, but if we want good results in general, we need another method.

II.2.2 The Hartree approximation

The first approach to the problem of many electrons can be considered as that proposed by Hartree (1928) [4]. The basic assumption of this approximation is that the many-electron wave function can be written as a simple product of N monoelectronic wave functions, even when the electron-electron interactions are not neglected.

$$\Psi(r_1, r_2, \dots, r_N) = \psi(r_1)\psi(r_2) \dots \psi(r_N) \quad (\text{II. 11})$$

The $\psi(r_i)$ are the N independent electronic wave functions. This approximation defines the potential by separating it into an electron potential (V_{elec}) and an ion potential V_{ion} . During the interaction, a given electron is no longer subject to a potential depending on the instantaneous positions of all other electrons, but rather to a potential corresponding to the average electron distribution, so that the remaining electrons are treated as a regular distribution of the negative charge with their charge density. We can say that the electron moves in an average electrostatic potential $V_H(r)$ from the set of neighboring electrons, so that eventually we would be able to process a non-interacting particle system instead of processing particles in interaction. With this approximation, the energy of the system can be written as [5]:

$$\begin{aligned} E^H &= \langle \Psi | \hat{H} | \Psi \rangle \\ &= \sum_i^n \left\langle \psi(r_i) \left| \frac{1}{2} \nabla_{r_i}^2 + V_{ion}(r) \right| \psi(r_i) \right\rangle + \frac{1}{2} \sum_{i,j(i \neq j)}^n \left\langle \psi(r_i)\psi(r_j) \left| \frac{1}{|r_i - r_j|} \right| \psi(r_i)\psi(r_j) \right\rangle \end{aligned} \quad (\text{II. 12})$$

Applying the Variational principle, we obtain the Hartree equation to a single particle:

$$\left[\frac{1}{2} \nabla_{r_i}^2 + V_{ion}(r) + \sum_{i,j(i \neq j)}^n \left\langle \psi(r_j) \left| \frac{1}{|r_i - r_j|} \right| \psi(r_j) \right\rangle \right] \psi(r_i) = \varepsilon_i \psi(r_i) \quad (\text{II. 13})$$

Where $V_{ion}(r)$ represents the Coulomb potential resulting from the interaction of the electron at the position r_i with all nuclei and $\sum_{i,j(i \neq j)}^n \left\langle \psi(r_j) \left| \frac{1}{|r_i - r_j|} \right| \psi(r_j) \right\rangle$ represents the Coulomb potential resulting from the interaction of this electron with all other electrons, this term is commonly referred to as Hartree potential.

By introducing the concept of the atomic density of electrons $\rho(r_j)$, Hartree defined the potential that an electron experience by using the following relation:

$$V_H(r_i) = \left\langle \sum_{j \neq i}^n \frac{1}{|r_i - r_j|} \right\rangle = \int \frac{\rho(r_j)}{|r_i - r_j|} d^3 r_j \quad (II. 14)$$

Where the density of probability ρ at the position r_j is given by the absolute square of the wave function $\psi_j(r)$, and the integration is carried out over the coordinates of all the electrons except over the coordinate r_i of the electron i :

$$\rho(r_j) = \sum_{j \neq i}^{occ} |\psi_j(r)|^2 \quad (II. 15)$$

The Hartree potential can be obtained also from the Poisson equation:

$$\nabla^2 V_H = -4\pi e^2 n(r) \quad (II. 16)$$

The Hartree equation is written as

$$H_i \psi(r_i) = \varepsilon_i \psi(r_i) \quad (II. 17)$$

With

$$H_i = \frac{1}{2} \nabla_{r_i}^2 + V_{eff}(r_i) \quad (II. 18)$$

Where

$$V_{eff}(r_i) = V_{ion}(r_i) + V_H(r_i) \quad (II. 19)$$

Solving the equation (II.17) yields all ε_i and $\psi(r_i)$.

The total Hamiltonian is simply a sum of one-electron operators, H_i .

$$H_e = \sum_i^N H_i \quad (II. 20)$$

This implies that the total energy of the electronic system E_e is the sum of the energies of the separated electrons:

$$E_e = \sum_i^N \varepsilon_i \quad (II. 21)$$

Equation (II.17) has a very familiar form and it is similar to the Schrödinger equation for a single electron moving in an effective potential $V_{eff}(r_i)$. However, there is a big difference: in the Hartree equation, the potential depends on the solution itself, in order to solve the equation (II.17) for each wave function $\psi(r_i)$, all the other functions $\psi(r_j)$ must be known, that requires a self-consistent method. First, a set of approximate wave functions $\psi(r_j)$ is chosen as a test set from which the N one-electron functions and the V_H potential are calculated. By inserting the

potentials V_H in equation (II.17), one can obtain the solutions of the Hartree equation. Then, using these solutions, we recalculate the potentials V_H and the equation is solved again and the potential is calculated. This procedure is repeated until the input and the output potentials are very close, within a certain tolerance.

The disadvantage of Hartree approach is that he does not take into account the Pauli Exclusion Principle [6], which requires that two electrons cannot be in the same quantum state.

The introduction of this principle (the inclusion of exchange) transforms the Hartree approach into the Hartree-Fock approximation [7].

II.2.3 The Hartree-Fock approximation

The Hartree-Fock approximation [7] follows directly from what was done for the Hartree approximation, only taking into account the need for the antisymmetric character of the wave functions with respect to electron exchange, as required by the principle of exclusion of Pauli [6]. This could be achieved by adding and subtracting all possible permutations of the Hartree product. The wave function becomes the function of the $4N$ variables (the three coordinates and the spin of the electron).

In the framework of the Hartree Fock approximation [7], the many-body wave function is assumed to be a single Slater determinant of single-particle orbitals [8]:

$$\Psi_{HT} = \frac{1}{\sqrt{N!}} \begin{vmatrix} \psi_1(x_1) & \psi_2(x_1) & \dots & \psi_N(x_1) \\ \psi_1(x_2) & \psi_2(x_2) & \dots & \psi_N(x_2) \\ \vdots & \vdots & \vdots & \vdots \\ \psi_1(x_N) & \psi_2(x_N) & \dots & \psi_N(x_N) \end{vmatrix} \quad (\text{II. 22})$$

Where x_i in the wave functions represents all the coordinates (space and spin) of particle i ,

The total energy with the Hartree-Fock wave function is obtained by:

$$E^H = \langle \Psi | \hat{H} | \Psi \rangle = \sum_{i=1}^N H_i + \frac{1}{2} \sum_{i,j=1}^N (J_{ij} - K_{ij}) \quad (\text{II. 23})$$

Where

$$\begin{aligned} H_{ii} &= \int \psi_i^*(x_i) \left[\frac{1}{2} \nabla_{r_i}^2 + V_{ion}(r) \right] \psi_i(x_i) dx \\ J_{ij} &= \iint \psi_i(x_1) \psi_i^*(x_1) \frac{1}{r_{12}} \psi_j^*(x_2) \psi_j(x_2) dx_1 dx_2 \\ K_{ij} &= \iint \psi_i^*(x_1) \psi_j(x_1) \frac{1}{r_{12}} \psi_i(x_2) \psi_j^*(x_2) dx_1 dx_2 \end{aligned} \quad (\text{II.24})$$

Where the J_{ij} are called Coulomb term and K_{ij} is the exchange term. We have significant equality: $J_{ij} = K_{ij}$. The exchange term is similar to the direct Coulomb term, but for the exchanged indices

Hartree-Fock equations with a single particle are obtained by a Variational calculus [9]:

$$\hat{F}\psi_i(x) = \varepsilon_i\psi_i(x) \quad (\text{II. 25})$$

Where

$$\hat{F} = \hat{h}_i + \sum_{j=1}^N (\hat{J}_j - \hat{K}_j) \quad (\text{II. 26})$$

Where \hat{h}_i contains the kinetic energy of the electron i and its interaction with all the nuclei. The second term in equation (II.26) is the Coulomb operator \hat{J}_j and it represents the potential that an electron in position x_1 experiences due to the average charge distribution of another electron in the orbital of spin ψ_j and it is defined by its effect when it operates on a spin orbit by:

$$J_j\psi_i(x_1) = \left(\int \frac{|\psi_j(x_2)|^2}{r_{12}} dx_2 \right) \psi_i(x_1) \quad (\text{II. 27})$$

The last term K_j is the exchange operator. It stems from Pauli's exclusion principle and acts to separate electrons in the same spin state. This term has no classical analogue and is a purely quantum mechanical effect, caused by the anti-symmetric ansatz of the wave function when interchanging any two electrons, it is best represented by showing how it acts on a single particle wave function

$$K_j\psi_i(x_1) = \left(\int \frac{\psi_j^*(x_2)\psi_i(x_2)}{r_{12}} dx_2 \right) \psi_j(x_1) \quad (\text{II. 28})$$

By multiplying the equation (II.23) by ψ_i^* and integrating, we obtain for the Hartree-Fock spin-orbital energies the following expression:

$$\varepsilon_i = \langle \psi_i | \hat{F} | \psi_i \rangle = H_{ii} + \sum_{j=1}^N (J_{ij} - K_{ij}) \quad (\text{II. 29})$$

The approximate electronic energy of the electronic ground state is then calculated as:

$$E_{HF} = \sum_{i=1}^N \varepsilon_i - \frac{1}{2} \sum_{i=1}^N \sum_{j=1}^N (J_{ij} - K_{ij}) \quad (\text{II. 30})$$

And for total energy, including nuclear-nuclear repulsion [9] we obtained:

$$E_{tot} = \sum_{i=1}^N \varepsilon_i - \frac{1}{2} \sum_{i=1}^N \sum_{j=1}^N (J_{ij} - K_{ij}) + V_{nn} \quad (\text{II. 31})$$

The Hartree-Fock approach is widely used by quantum chemists today. However, it has limitations, the Hartree-Fock equation is difficult to apply in extended systems because of its exchange term, which is non-local. The computational complexity of the Hartree-Fock method grows rapidly with the number of atomic electrons, so the corresponding calculated time for heavy atoms is found to be too long even when using modern computers. For this reason, there

has been relatively few applications to solids [10]. In addition, the Hartree-Fock approximation sometimes gives unsatisfactory results because the approximation of an electron no longer takes into account the quantum effects on the electron distributions because the effect of other electrons in the system on an electron of interest is processed according to their average location. It does not consider instant Coulomb interactions between electrons. The Hartree-Fock equations neglect more detailed correlations due to many-body interactions. Much of the modern work in the field of calculating the electronic structure is designed to take electronic correlation into account.

II.3 The theory of the density functional

The alternative of HF methods is the density functional theory (DFT), which is becoming increasingly popular in condensed matter physics, quantum chemistry and materials science. The main idea of the density functional methods is that the problem is solved directly for the charge density, $\rho(\mathbf{r})$ rather than for the wave function Ψ of several particles [11]. This leads to a remarkable reduction in the difficulty because it is enough to treat a function of three variables x , y and z , rather than a problem of $3N$ variable.

Density functional theory (DFT) not only had a major impact on structural-electronic calculations, but it also makes it possible to treat properties of rather complex materials. This involves the determination of magnetic and electrical susceptibilities, spin-polarized fundamental states, superconductivity, etc. [11]. On the other hand, density functional theory (DFT) is a good compromise between the qualitative description of the electronic structure and the computational efficiency required to produce the result.

The density functional theory has its roots in Thomas and Fermi's publications in the 1920s. Thomas and Fermi [12, 13] have attempted to formulate such an approach much earlier; however, their work, suffered from inaccuracies in the processing of kinetic energy and exchange-correlation effects. Nevertheless, the method served as a starting point for the development of more advanced publications in the early 1960s [14, 15].

In their 1964 article, Hohenberg and Kohn formulated the basics of density functional theory for any system of N electrons moving in an external potential $V_{\text{ext}}(\mathbf{r})$ and whose fundamental state is nondegenerate. The Hamiltonian operator for such a system can be written as:

$$\hat{H} = \hat{F} + \hat{V}_{\text{ext}} \quad (\text{II. 32})$$

Where

$$\hat{F} = -\frac{1}{2} \sum_{i=1}^N \nabla_i^2 + \sum_{i \neq j}^N \frac{1}{|r_i - r_j|} \quad (\text{II. 33})$$

and

$$\hat{V}_{ext} = \sum_{i=1}^N V_{ext}(r_i) = - \sum_{i=1}^N \sum_{j=1}^M \frac{Z_j}{|r_i - R_j|} \quad (\text{II. 34})$$

Hohenberg and Kohn outlined DFT in terms of two theorems, proving the existence of a one-to-one mapping between the potential $V(r)$ and the density $n(r)$.

II.3.1 Hohenberg-Kohn's theorem

II.3.1.1 Hohenberg-Kohn's first theorem

The first theorem of Hohenberg and Kohn states the following: [14]

The ground state density $\rho(r)$ of a system of interacting electrons in an external potential $V_{ext}(r)$ uniquely defines this potential.

In the term "unique" we must understand "unique to an additive constant". Indeed, the charge density is not modified if a constant is added to the external potential [16].

Hohenberg and Kohn have been able to prove that there is a relation of *uniqueness* between $\rho(r)$ and the external potential: two external potentials could not give the same $\rho(r)$. This tells us that we can derive the potential External $V_{ext}(r)$ applied to an interacting N *electron system* from the electronic density of this *system*. In addition, all the properties of a system can be determined also via the electronic density of the system. This formulation can be applied to any particle system interacting in an external potential, including fixed-core problems and electrons. Originally, this theorem has been demonstrated for nondegenerate states, then it has been extended to a vast class of systems including degenerate state systems [17, 18], spin-polarized systems [19, 20]. This theorem has also been extended to finite temperature by Mermin [21], thus proving that entropy, specific heat, etc. are functionals of the equilibrium density [22].

II.3.1.2 Second theorem of Hohenberg-Kohn

The second theorem of Hohenberg-Kohn is directly related to the first and indicates that: *There exists a universal functional $F[\rho(r)]$ of the density, valid for any external potential $V_{ext}(r)$, such that the global minimum value of the energy functional $E_{tot}[\rho] = F_{HK}[\rho] + \int dr \hat{V}_{ext} \rho(r)$ is the exact ground state energy of the system and the density $n(r)$ that minimizes this functional is the exact ground state density $\rho_0(r)$. Thus, the exact ground state energy and density are fully determined by the functional $E[\rho(r)]$.*

$F_{HK}[\rho]$ is a universal functional valid for any number of electrons having an external potential, in the sense that $F_{HK}[\rho]$ does not depend on the external potential felt by the electrons (not including any information on the nuclei or on their positions).

$F_{HK}[\rho]$ contains the kinetic term of the interacting particles \hat{T}_e and the energy of the interaction between the electrons, \hat{V}_{ee}

$$F_{HK}[\rho] = \hat{T}_e + \hat{V}_{ee} \quad (\text{II. 35})$$

If the form of the "true" functional was known, we could vary the electron density until the energy functional is minimized. The electronic density that minimizes the total energy functional is the true density (the ground-state density) corresponding to the energy of the ground state of the system. This means that we can think of solving the Schrödinger equation by finding the electronic density, which is a function of three spatial variables, rather than the wave function, which is a function of $3N$ variables.

The Hohenberg-Kohn theorem does not tell us the form of the functional of energy as a function of density: it only proves that such a functional exists.

The next major step in the development of DFT came with the derivation of a set of one-electron equations from which the electron density $\rho(\mathbf{r})$ can be obtained [15].

II.3.2 Kohn and Sham's approach

Based on the fact that Hohenberg and Kohn's theorems are valid for any electronic system, whether interacting or not, Kohn and Sham (1965) [15] introduced an elegant method that became the most practical implementation of the density functional theory. Their idea is to replace formally the "real" electrons of a system by an auxiliary system of non-interacting electrons ($V_{ee} = 0$) evolving as independent particles in an effective potential so that the charge density in this auxiliary system is exactly the same as in the full interacting system [22].

The important achievement of Kohn and Sham was to write the energy functional for the real system as:

$$\begin{aligned} E_{HK}[\rho] &= \langle \Psi | \hat{T}_e + \hat{V}_{ee} + \hat{V}_{ext} | \Psi \rangle \\ &= T_e^{KS} + E_{Hartree}[\rho] + \int \rho(\mathbf{r}) V_{ext} d\mathbf{r} + E_{XC}[\rho] \end{aligned} \quad (\text{II. 36})$$

The first term T_e^{KS} is the functional of the kinetic energy for a set of N non-interacting electrons with the same ground-state density $\rho(\mathbf{r})$ as the interacting one. But T_e^{KS} is not equal to the true kinetic energy of the interacting electron system. The interest of the introduction of this fictitious system is that we can now express the functional kinetic energy as a function of the orbitals ψ_i .

If each effective electron is described by a single particle wave function ψ_i , the kinetic energy of all effective electrons is given by:

$$T_e^{KS}[\rho(r)] = \frac{1}{2} \sum_{i=1}^N |\nabla \psi_i(r)|^2 \quad (\text{II. 37})$$

Where the sum is on all occupied orbitals of Kohn-Sham (KS).

The second term is the functional of the electrostatic energy, commonly known as the Hartree contribution; it is purely classical and contains the electrostatic energy arising from the repulsion between all electronic charges,

$$E_H(\rho) = \int \frac{\rho(r_i)\rho(r_j)}{|r_i-r_j|} dr_i dr_j \quad (\text{II. 38})$$

The third term is the classical electron-nuclei Coulomb interaction with the potential $V_{ext}\rho(r)$ due to the nuclei i.e.

$$E_{ext}[\rho] = \int V_{ext}\rho(r) dr \quad (\text{II. 39})$$

$$V_{ext}(r) = -\sum_{j=1}^M \frac{Z_j}{|r-R_j|} \quad (\text{II. 40})$$

Where Z_j is the positive charge of the nucleus in R_j . The fourth term is a universal functional, termed: the exchange–correlation functional. It groups all remaining complicated electronic contributions to make the functional in Eq. (II.36) exact, however, its exact form is not known. It contains the difference between the exact kinetic energy $T[\rho(r)]$ and non-interacting kinetic energies T_e^{KS} as well as the non-classical part of $V_{ee}[\rho(r)]$:

$$E_{xc}[\rho] = T[\rho(r)] - T_e^{KS}[\rho(r)] + V_{ee}[\rho(r)] - V_H[\rho(r)] \quad (\text{II. 41})$$

As the name suggests, $Exc[n]$ arises from a combination of two quantum mechanical effects: electron exchange and correlation. The most important of these contributions is the exchange term. Briefly, electron exchange arises because a many-body wave function must be antisymmetric under exchange of any two electrons since electrons are fermions and obey the Pauli Exclusion Principle. In real space, Pauli's principle implies that in the neighbourhood of every electron with a given spin, all other electrons with the same spin tend to avoid that electron, just as it has been postulated the existence of a (Fermi) exchange hole excluding the electrons of parallel spins in the same region of space. Consequently, the exchange term reduces the Coulomb repulsion of the electronic system by increasing the spatial separation between electrons and cancels out this unwanted interaction in a sense. Likewise, a correlation hole must be "imagined" for opposite spin electrons because the motion of each individual electron is correlated with the motion of all others and electrons with opposite spins also avoid each other, helping also to keep electrons of unlike spin spatially separated. The additional many-body interaction terms between electrons of opposite spin are called correlation energy.

II.3.3 The Kohn-Sham equations

The minimization of the total energy (equation (II.36)) with respect to density, for a fixed number of electrons, produces a set of equations:

$$\left[-\frac{1}{2}\nabla^2 + V_{eff}\right]\psi_i(r) = \varepsilon_i\psi_i(r) \quad (\text{II. 42})$$

Here, the one-electron orbitals $\psi_i(r)$ are called the Kohn-Sham orbitals and the above eigenvalue equations are called the Kohn-Sham equations.

Where i refers to the i th electron, $\psi_i(r)$ is the single particle wave function of this electron. and $\hat{V}_{eff}(r)$ is the effective potential given by:

$$\hat{V}_{eff}(r) = \hat{V}_H(r) + \hat{V}_{ext}(r) + \hat{V}_{XC} \quad (\text{II. 43})$$

Where

$$\hat{V}_{XC}(r) = \left. \frac{\delta E_{XC}[\rho(r)]}{\delta \rho(r)} \right|_{\rho=\rho_0} \quad (\text{II. 44})$$

And

$$\hat{V}_H(r) = \frac{\delta E_H[\rho(r)]}{\delta \rho(r)} = \int \frac{\rho(r_j)}{|r-r_j|} dr_j \quad (\text{II. 45})$$

The Hartree potential $\hat{V}_H(r)$ namely contains a Coulomb repulsion between an electron and itself in the sense that it interacts with a charge density constructed from its own wave function. This is clearly visible in the case of one electron where the Hartree energy is non-zero. The self-interaction of the Hartree potential is exactly cancelled by exchange-correlation hole.

The set of Kohn-Sham equations is to be solved self-consistently (see subsection III.7), under the constraint that the number of particles is conserved.

Due to the dependence of the effective potential on the density via the Hartree potential. The total energy of the system is not simply equal to the sum of the eigenvalues of the Kohn-Sham equations, but it is calculated by adding the different energy contributions with corrections for double counting:

$$E = \sum_n^N \varepsilon_n + E_{XC}[\rho] - \int V_{XC}(r)\rho(r)dr - \frac{1}{2} \iint \frac{\rho(r)\rho(r_j)}{|r-r_j|} dr dr_j \quad (\text{II. 46})$$

Where the sum over the values of a single particle is often called band structure energy. The electron density is expressed according to the orbitals

$$\rho(r) = \sum_{i=1}^N |\psi_i(r)|^2 \quad (\text{II. 47})$$

Where $\psi_i(r)$ are the KS orbitals that are the lowest energy solutions of the equations (II. 42).

The full wavefunction of non-interacting is far less complicated than that of the true interacting system and it must still satisfy exchange anti-symmetry and this can be achieved by placing single-particle wavefunctions in a Slater determinant [8].

Slater Determinant constructed from a set of KS orbitals is the exact wave function for the fictional non-interacting system having the same density as the real system.

The Kohn-Sham equations seem formally very similar to the Hartree-Fock equations. They have identical contributions to the kinetic energy and from the external potential as well as from the Coulomb energy of the electrons; the only difference is the presence of exchange-correlation potential. The Kohn-Sham equations contain both parts (the exchange and the correlation), and they are treated via an approximate treatment, whereas in the Hartree-Fock equation only exchange interactions are included and it is treated exactly [23]. The Kohn-Sham equations are much easier to solve than the Hartree-Fock equations, in which the potential depends on the orbit [24]. In the Kohn-Sham equations, the effective potential is the same for each orbit in the sense that occupied and unoccupied orbitals all feel the same effective potential $\hat{V}_{eff}(r)$.

II.3.4 The exchange–correlation potential

Kohn and Sham (KS) reformulated the problem in a more familiar form and opened the way to practical applications of DFT, but the precise dependency of the exchange–correlation potential V_{XC} on the density $\rho(r)$ is not known. Nevertheless, this exchange–correlation potential can be approached and many approximations have been proposed and tested on different types of systems. The most common approximations in solid-state physics are the local density approximation (LDA), the generalized gradient approximation (GGA) and the modified Becke–Johnson (MBJ) potential.

II.3.4.1 Local density approximation (LDA)

The simplest physical way of approaching the exchange-correlation energy is Local Density Approximation (LDA) proposed by Kohn and Sham themselves [15]. The idea behind the LDA is very simple; it simply ignores the non-local aspects of the functional dependence of V_{xc} and assumes that V_{xc} only depends on the local density ρ . So that at each point in the system, the exchange and correlation energy per particle has the value that would be given by a homogeneous electronic gas that had the same electron density ρ at *this point*. Note that the LDA does not assume that the electron density in a molecule is homogeneous (uniform); this

drastic situation would be true for a "Thomas-Fermi molecule", which cannot exist. The total exchange correlation energy E_{xc} is then given by the sum of the contributions of each point in space,

$$E_{XC}[\rho] = \int dr \rho(r) \varepsilon_{xc}(\rho(r)) \quad (\text{II. 48})$$

Where $\varepsilon_{xc}(\rho(r))$ is the exchange-correlation energy per particle.

The quantity $\varepsilon_{xc}(\rho(r))$ can be divided into exchange and correlation contributions represented by the energies per particle ε_X and ε_C .

$$\varepsilon_{XC}(\rho(r)) = \varepsilon_X(\rho(r)) + \varepsilon_C(\rho(r)) \quad (\text{II. 49})$$

Both terms are negative. The exchange portion is generally larger than the correlation portion, typically by a factor of 3 to 10 in the crystallographic systems.

The exchange contribution can be evaluated analytically [22], while the correlation part is obtained by parameterizing of precise quantum Monte Carlo simulations of the homogeneous electron gas as proposed by Ceperly and Alder [25]. Depending on the analytic forms used for $\varepsilon_C(\rho(r))$, several local density approximations were have been generated, the most widely used LDA functional is that parametrized by Perdew-Zunger (PZ81) [26].

The LDA approximation is only strictly valid for interacting electron systems within the limits of a slowly varying density and very high densities. Nevertheless, experience has shown that accurate results can be obtained well beyond this expected range of validity [27]; it is surprisingly successful and even works reasonably well in systems where the electron density is rapidly varying. Typically, the LDA has proven to be a remarkable fruitful approximation in reproducing excellent numerical results for strongly bound system, which share some properties with the HEG, especially for vibrational and structural properties.

However, LDA has many short-comings mostly due to the tendency to overbind atoms (has a tendency to make chemical bindings much too strong). This leads to cell parameters being underestimated by several percent for solids. Therefore, the bulk modulus is overestimated. The main deficiency of the LDA was the large errors in predicting the energy gaps of some semi-conductors and insulators [28].

The limitations of The LDA led to the subsequent level of approximation to the exchange-correlation energy, a natural way to improve LDA is to make the exchange-correlation functional not only dependent on the local density, but also the on gradient of the density.

II.3.4.2 The generalized gradient approximation (GGA)

LDA is expected to perform well for systems with a slowly varying density. Practically, such a condition is rarely satisfied. The first logical step to go beyond LDA is the use of more sophisticated exchange-correlation potentials where the exchange-correlation energy not only depends on the charge density at a particular point r , but also of the spatial variation of this electronic density at this point in order to take into account the non-homogeneity of the true electron density [29]. This can be done by adding gradient terms of the electron density to the exchange-correlation energy and its corresponding potential.

This has led to the generalized gradient approximation (GGA) which can be put in the general form:

$$E_{XC}^{GGA}[\rho] = \int g(\rho, g) \Big|_{\substack{\rho=\rho(r) \\ g=\nabla\rho(r)}} d^3r \quad (\text{II. 50})$$

Where $g(\rho, g)$ is a function of the local density and density gradient. Function g is not unique and many different forms have been suggested because the electronic density gradient information can be included in many ways in GGA functional. The four most widely used GGAs are the forms proposed by Becke [30] (B88), Perdew et al. [31], Perdew, Burke and Enzerhof [32] (PBE) and that suggested by Perdew et al (PBESOL) [33].

Large number of test calculations showed that GGA functionals a noticeable improvement upon LDA in the description of atoms and solids [32]. Especially in systems where charge density varies rapidly, because GGA functional include more physical ingredients than the LDA functional but computationally it is more time consuming than LDA [34]. It underestimates the bulk modulus and zone center transverse optical phonon frequency of the solid [35,36], corrects the binding energy [37,36] and corrects or overcorrects the lattice constants compared to LDA [35,38-40]. However, the GGA approximation does not necessarily lead to better results than the LDA. There are several cases in which GGA gives worse results than LDA - for example, GGA sometimes overcorrects the results of LDA in ionic crystals where the lattice constants from LDA calculations agree well with the experimental data, but GGA will overestimate it. Nevertheless, LDA and GGA behave badly in materials where electrons tend to be localized and highly correlated such as transition metal oxides and rare earth elements and compounds.

In general, GGA shares the same problems with LDA in modelling a certain class of materials where electrons tend to be localized and highly correlated, so-called “strongly

correlated” systems and also like LDA, it does not give correct band gaps for semiconductors, this disadvantage leads to approximations beyond LDA and GGA.

II.3.4.3 The modified Becke–Johnson (MBJ) potential

Recently, Tran and Blaha have introduced a newly semi-local exchange-correlation functional called the modified Becke–Johnson (MBJ) potential [41], by using information from kinetic energy density in addition to the charge density as employed in standard GGA. The TB-mBJ approach can be regarded as a pragmatic approach to address the LDA/GGA band gap problem in the DFT framework. The mBJ scheme addresses only the exchange potential; the effect of correlations can be treated within the local or semi-local density approximation but according to Tran and Blaha [41, 42] has only small effect.

In this method, the exchange term is formulated by modifying the Becke-Johnson potential [43], which was proposed to model the exact exchange potential in atoms. The Becke-Johnson potential depends mainly on the total density and the kinetic-energy density (t) as given by Eq. (II.51)

$$v_x^{BJ}(r) = v_x^{BR} + \frac{1}{\pi} \sqrt{\frac{5}{12}} \sqrt{\frac{2t(r)}{\rho(r)}} \quad (\text{II.51})$$

Where $\rho(r) = \sum_{i=1}^N |\psi_i|^2$ is the electron density,

$t(r)$ is the KS kinetic energy density:

$$t(r) = \frac{1}{2} \sum_{i=1}^N \nabla \psi_i^*(r) \nabla \psi_i(r) \quad (\text{II.52})$$

, and $v_x^{BR}(r)$ is the Becke and Roussel (BR) exchange potential [44]:

$$v_x^{BR}(r) = -\frac{1}{b(r)} (1 - e^{-x(r)} - \frac{1}{2} x(r) e^{-x(r)}) \quad (\text{II.53})$$

The Becke and Roussel (BR) exchange potential was proposed to model the Coulomb potential created by the exchange hole, with $x(r)$ is determined from a nonlinear equation involving ρ ,

$\nabla \rho$, $\nabla \rho$ and t . The b is calculated with $b = \left[\frac{x^3 e^{-x}}{8\pi\rho} \right]^{\frac{1}{3}}$.

Tran and Blaha have introduced a variable prefactor ‘ c ’ (depending on the average value of $|\nabla \rho|/\rho$) that affects the relative weights of the two terms in the BJ potential.

The TB-mBJ exchange potential is defined as:

$$v_x^{TB-mBJ} = c v_x^{BR}(r) + (3c - 2) \frac{1}{\pi} \sqrt{\frac{5}{6}} \sqrt{\frac{t(r)}{\rho(r)}} \quad (\text{II.53})$$

The c parameter value showed in Eq. (II.53) is computed with

$$c = \alpha + \beta \left(\frac{1}{V_{cell}} \int \frac{|\nabla \rho(r')|}{\rho(r')} d^3 r' \right)$$

Where V_{cell} is the unit cell volume and α and β are two free parameters whose values are $\alpha = -0.012$ and $\beta = 1.023 \text{ Bohr}^{1/2}$ according to a fit to experimental results [42]. For $c=1$ the original BJ potential is recovered. The c values greater than one lead to a less negative (i.e. less attractive) potential, in particular, in low-density regions.

The TB-mBJ functionals yield remarkably accurate band gaps in a wide variety of materials [42,45-47] with a computational effort that is in general comparable to that of LDA/GGA although its self-consistency cycle converges slower and therefore requires more iterations (a factor of 2-3). It is important to point out that TB-mBJ is a potential-only functional, i.e., there is no associated TB-mBJ exchange-correlation energy. This means The TB-mBJ functionals can not be used to compute Hellmann-Feynman forces and to compare total energies, which in turn means MBJ calculations should be used only for quantities, which do not involve the total energy.

References

- [1] D. Landau and E. F. Lifshitz, *Quantum Mechanics Non-Relativistic Theory*, 3rd ed., Pergamon Press, Oxford, (1977).
- [2] A. Messiah, *Quantum Mechanics. vol. I*, North Holland Publishing Company: Amsterdam, (1964).
- [3] M. Born, J. R. Oppenheimer, *Ann. d. Physik.* **84**, 457, (1927).
- [4] D.R. Hartree, *Proc. Cambridge Phil. Soc.* **24**, 89 (1928).
- [5] E. Kaxiras, *Atomic and Electronic Structure of Solids*, Cambridge University Press, Cambridge (2003).
- [6] W. Pauli, *Zeitschrift für Physik* **.31**, 765 (1925).
- [7] V. Fock, *Z. Phys.* **61**, 126 (1930).
- [8] J. C. Slater, *Phys. Rev.* **35**, 509 (1930).
- [9] F. Jensen, *Introduction to Computational Chemistry*, Chichester, Wiley, (1999).
- [10] C. Pisany, R. Dovea, and C. Roetti, *Hartree-Fock Ab-initio Treatment of Crystalline Systems*, Springer, Berlin (1988).
- [11] W. Kohn, A. D. Becke, and R. G. Parr, *J. Phys. Chem.* **100**, 12974 (1996).
- [12] L. H. Thomas, *Proc. Cambridge Philos. Soc.* **23**, 542 (1927).
- [13] E. Fermi, *Z. Phys.* **48**, 73 (1928).
- [14] P. Hohenberg and W. Kohn, *Phys. Rev.* **136**, 864 (1964).
- [15] W. Kohn and L. Sham, *J. Phys. Rev. A* **140**, 1133 (1965)
- [16] J. Callaway, N. H. March, *Solid State Physics*, **38**, 135 (1984).
- [17] M. Levy, *Phys. Rev. A* **26**, 1200 (1982).
- [18] E. H. Lieb, *Density Functionals for Coulomb Systems, in Physics as Natural Philosophy: Essays in Honor of Laszlo Tisza on His 75th Birthday*, edited by A. Shimony and H. Feshbach, MIT Press, Cambridge, Mass., (1982),
- [19] G. Vignale and M. Rasolt, *Phys. Rev. Lett.* **59**, 2360 (1987).
- [20] G. Vignale and M. Rasolt, *Phys. Rev. B* **37**, 10685 (1988).
- [21] N. D. Mermin, *Phys. Rev. A* **137**, 1441 (1965)
- [22] R. M. Martin, *Electronic Structure Basic Theory and Practical Methods,* Cambridge University Press, Cambridge, (2004).
- [23] M. Springborg and Y. Dong, *Metallic Chains / Chains of Metals*, Elsevier, Amsterdam, (2007).

- [24] Philip L. Taylor and O. Heinonen, *A Quantum Approach to Condensed Matter Physics*, Cambridge University Press (2002).
- [25] D.M. Ceperley, B.J. Alder, *Phys. Rev. Lett.* **45**, 566 (1980).
- [26] J. P. Perdew and A. Zunger, *Phys. Rev. B* **23**, 5048 (1981)
- [27] D. S. Sholl and J. A. Steckel, *Density Functional Theory: A Practical Introduction*, John Wiley & Sons, New Jersey, (2009).
- [28] J. P. Perdew, A. Ruzsinszky, L. A. Constantin, J. Sun, and G. I. Csonka, *J. Chem. Theory Comput.* **5**, 902 (2009)
- [29] W. Koch and M. C. Holthausen, *A Chemist's Guide to Density Functional Theory*, Wiley—VCH, New York, (2000).
- [30] A. D. Becke, *Phys. Rev. A* **38**, 3098 (1988).
- [31] J. P. Perdew, J. A. Chevary, S. H. Vosko, K. A. Jackson, M. R. Pederson and C. Fiolhais, *Phys. Rev. B* **46**, 6671 (1992).
- [32] J. P. Perdew, K. Burke, and M. Ernzerhof, *Phys. Rev. Lett.* **77**, 3865 (1996).
- [33] J.P. Perdew, A. Ruzsinsky, G.I. Csonka, O.A. Vydrov, G.E. Scuseria, L.A. Constantin, X. Zhao, K. Burke, *Phys. Rev. Lett.* **100**, 136406 (2008).
- [34] El-Barbary, *First principles characterisation of defects in irradiated graphitic materials*, Ph.D. thesis, University of Sussex, 2005
- [35] C. Filippi, D.J. Singh and C.J. Umrigar, *Phys. Rev. B* **50**, 14947 (1994).
- [36] A. D. Corso, A. Pasquarello, A. Baldereschi, and R. Car, *Phys. Rev. B* **53**, 1180 (1996).
- [37] G. Ortiz, *Phys. Rev. B* **45**, 11328 (1992).
- [38] A. Khein, D. J. Singh, and C. J. Umrigar, *Phys. Rev. B* **51**, 4105 (1995).
- [39] Y. M. Juan and E. Kaxiras, *Phys. Rev. B* **48**, 14944 (1993).
- [40] A. Garcia, C. Elsaesser, J. Zhu, S. Louie, and M.L. Cohen, *Phys. Rev. B* **46**, 9829 (1992).
- [41] F. Tran, P. Blaha, and K. Schwarz, *J. Phys. Condens. Mat.* **19**, 196208 (2007).
- [42] F. Tran and P. Blaha, *Phys. Rev. Lett.* **102**, 226401 (2009).
- [43] A. D. Becke and E. R. Johnson, *J. Chem. Phys.* **124**, 221101 (2006).
- [44] A. D. Becke and M. R. Roussel, *Phys. Rev. A* **39**, 3761 (1989).
- [45] D. Koller, F. Tran, and P. Blaha, *Phys. Rev. B* **83**, 195134 (2011).
- [46] H. Dixit, R. Saniz, S. Cottenier, D. Lamoen, and B. Partoens, *J. Phys.: Condens. Matter* **24**, 205503 (2012).
- [47] D. J. Singh, *Phys. Rev. B* **82**, 155145 (2010).

III. Planes Waves and Pseudopotential Method

III.1 Introduction

In order to solve the Kohn-Sham equations, it is necessary to choose an appropriate base adapted to the studied system in order to develop the eigenstates of Kohn Sham and to express the different parts of the Hamiltonian. For the description of crystals, the set of plane wave is a good choice, because crystal lattices have periodic symmetry, which can be used to reduce the amount of atoms that must be accounted in the calculation. However, the plane wave become fast oscillation functions near the atomic nuclei, and therefore a large number of functions are needed to describe such oscillations. Nevertheless, using the pseudopotential approximation, we can reduce the size of the base set and thus reduce computational costs. The use of the plane wave basis with the pseudopotential constitutes the pseudopotential plane wave method. In this chapter, we describe the expression of the Kohn-Sham equations in the plane wave basis, then, we will represent the pseudopotential approximation, followed by a practical methodology to solve the Kohn-Sham equations.

III.1 Crystal symmetry and Bloch's theorem

III.1.1 Periodic systems

A crystal is an ordered state of matter in which the positions of the nuclei (and consequently all properties) are repeated periodically in space. It is completely described in real space in terms of non-coplanar basis vectors $\vec{b}_1, \vec{b}_2, \vec{b}_3$ and the positions of atoms inside a primitive unit cell (PUC). The lattice vectors \vec{R} are formed by all the possible combinations of primitive lattice vectors, multiplied by integers:

$$\vec{R} = n_1\vec{b}_1 + n_2\vec{b}_2 + n_3\vec{b}_3 \quad (\text{III. 1})$$

Where n_1, n_2 and n_3 are integers.

A lattice formed by such a translational operation is called the simple Bravais lattice, and the parallelepiped defined by the three basis vectors $\vec{b}_1, \vec{b}_2, \vec{b}_3$ is the unit cell of the Bravais lattice (or primitive cell); its volume is:

$$\vec{V} = \vec{b}_1 \times (\vec{b}_2 \times \vec{b}_3) \quad (\text{III. 2})$$

There are infinite possible choices for the unit cell, the cell which is the most symmetric and compact is called the Wigner-Seitz unit cell.

Since the motion of electrons in a crystal is usually described in both real space and momentum space (or k-space), it is important to introduce the concepts of reciprocal lattice,

which is the inverse of the real lattice. In a reciprocal lattice a set of reciprocal basis vectors \vec{b}_1^* , \vec{b}_2^* , \vec{b}_3^* can be defined in terms of the basis vectors \vec{b}_1 , \vec{b}_2 , \vec{b}_3 of a direct lattice. This is given by [1]:

$$\vec{b}_1^* = \frac{2\pi(\vec{b}_2 \times \vec{b}_3)}{\vec{b}_1 \cdot (\vec{b}_2 \times \vec{b}_3)}, \quad \vec{b}_2^* = \frac{2\pi(\vec{b}_3 \times \vec{b}_1)}{\vec{b}_2 \cdot (\vec{b}_3 \times \vec{b}_1)}, \quad \vec{b}_3^* = \frac{2\pi(\vec{b}_1 \times \vec{b}_2)}{\vec{b}_3 \cdot (\vec{b}_1 \times \vec{b}_2)} \quad (\text{III. 3})$$

The primitive cell of the reciprocal space does not need to be a parallelepiped, in fact we can define the Wigner-Seitz cell of the reciprocal lattice, which is also known as the first Brillouin zone in reciprocal space.

In a perfect crystal, the Hamiltonian H of the Schrödinger equation of a system of particles is invariant under any translation operation $T(\mathbf{n})$, as the effective potential has the same periodicity of the lattice and the derivative operator is invariant under the effect of translation operations [2].

III.1.2 Bloch's theorem

If we solve the Schrödinger equation for the periodic system, the solution must satisfy a fundamental property known as Bloch's theorem [3], which indicates that the eigenfunctions can be expressed by plane waves modulated by functions that have the same periodicity of the lattice. Using Bloch's theorem, the solutions of the Schrodinger equation for a periodic potential reads:

$$\psi_{n,k}(r) = \exp(ikr) u_{n,k}(r) \quad (\text{III. 4})$$

where $u_{n,k}(r)$ is a periodic wavefunction with $u_{n,k}(r) = u_{n,k}(r + R)$, R is any vector connecting equivalent Bravais lattice points, k is a reciprocal vector used to label the states and it can be always translated back to the first Brillouin zone, the subscript n is denoted as band index and distinguishes different eigen energy $\varepsilon_{n,k}$ for the same momentum k . The eigenvalues are also periodic functions in the reciprocal space, i.e.

$$\varepsilon_{n,k} = \varepsilon_{n,k+K} \quad (\text{III. 5})$$

This means that the Bloch's theorem reduces the number of electrons required for the calculation to those in the unit lattice, if the Hamiltonian of system is invariant under translation. The periodicity of $u_{n,k}(r)$ means that it can be expanded in terms of a special set of plane waves:

$$u_{n,k}(r) = \sum_G \tilde{u}_G \exp(iGr) \quad (\text{III. 6})$$

Where the summation is over all vectors defined by G :

$$\vec{G} = m_1 \vec{b}_1^* + m_2 \vec{b}_2^* + m_3 \vec{b}_3^* \quad (\text{III. 7})$$

Where m_1, m_2, m_3 are integers, and $\vec{b}_1^*, \vec{b}_2^*, \vec{b}_3^*$ are the reciprocal lattice vectors, and \tilde{u}_G are the coefficients of expansion.

By combining the equations. (III.4) and (III.6), we can find that the single-particle wave functions $\psi_{n,k}(r)$, at each point k in the BZ of a given crystal, can be developed in a discrete set of plane waves:

$$\psi_{n,k}(r) = \exp(ikr) u_{n,k}(r) = \sum_G c_{nk}(G) \exp[i(k + G) \cdot r] \quad (\text{III. 8})$$

III.2 Expression of Kohn-Sham equations in the plane wave basis

Expansion of the electron wave functions in terms of plane waves allow the Kohn-Sham equations to take a particularly simple formulation in a reciprocal space [4, 5]. Substituting the electronic wavefunction expressed in terms of all plane waves equation (II.42) into the Kohn Sham equation (II.45) and integrating over r , gives the matrix eigenvalue equation:

$$\left[\sum_{G'} \frac{1}{2} |k + G|^2 \delta_{GG'} + V_{ext}(G - G') + V_{xc}(G - G') + V_H(G - G') \right] = \varepsilon_i C_{Gnk} \quad (\text{III.9})$$

In equation (III.9), the kinetic energy is diagonal, the other three terms on the left are the Fourier components of the external potentials, exchanges correlation and Hartree term respectively.

III.3 The cut-off energy

In principle, to describe exactly the electron wave function, the dimension of the plane-wave basis set should be infinite. However, the functions appearing in the equation. (III.8) have a simple interpretation as solutions of the Schrödinger equation: they are solutions with kinetic energy:

$$E = \frac{\hbar^2}{2m} |k + G|^2 \quad (\text{III. 10})$$

Typically, the plane wave functions with higher $|G|$ have a higher kinetic energy and thus contribute less to the expansion of the wave function, because the coefficients $c_{nk}(G)$ associated with a plane wave of high kinetic energy are negligible compared to those associated with a plane wave of low kinetic energy [6].

Therefore, the size of the set of reciprocal lattice vectors can be truncated by placing an upper limit for the kinetic energy of the plane waves. This limit is called the cut-off energy such that only plane waves with a kinetic energy lower than E_{cut} are included in the expansion of Kohn-Sham functions. The infinite sum is then reduced to:

$$\psi_{n,k}(r) = \sum_{|G+k| < G_{cut}} c_{nk}(G) \exp[i(k + G) \cdot r] \quad (\text{III. 11})$$

Obviously, the value E_{cut} affects the accuracy of the calculations and depends strongly on the elements, which are present in the system under investigation. Simple convergence tests should be carefully performed in each case by varying the cut-off energy and establishing at what energy convergence is achieved. (i.e. increasing the cut-off energy does not affect the calculated energy of the system).

III.4 Sampling the Brillouin Zone

The computation of many physical quantities such as the total energy of a solid requires the knowledge of Bloch functions over infinite k points in BZ, because for each of k values exists a discrete spectrum of eigenvalues of the Kohn-Sham equation. Therefore, a finite selection of k points must be used in practice for the calculation. The electronic wave functions at k points that are very close together will be almost identical (it will not change much with small variations in k) [7]. Hence, it is possible to represent the electronic wavefunctions over a region of k space by the wavefunctions at a single k point. Thus removes the need for an infinite number of electrons and allows one to make calculations at the finite number of k points. By using the additional symmetries of the crystal, such as the rotations or reflections of the mirror, the number of points k required can be reduced, so that ψ can only be calculated at special points in the Brillouin zone and the integration can be conveniently confined in a smaller region of the BZ. The smallest possible part, that by employed all symmetries operations can be unfolded into the whole Brillouin zone is called the irreducible Brillouin zone (IBZ).

There are different methods for choosing special points in the BZ [8, 9, 10]. However, the Monkhorst-Pack approach is the most widely used [11]. The Monkhorst-Pack method is based on a representation of the integration on the BZ by a weighted sum over a number of special k -points. The error that appears in the calculations can be reduced by choosing a heavier set of k -points in the Brillouin zone.

III.5 Pseudopotential

III.5.1 The frozen core approximation

It is a well-known fact in chemistry that the core electrons, by opposition to the valence electrons, are tightly bounds to the nuclei and do not participate in the chemical bonding between atoms [12, 13]. When the atoms are transferred from one chemical environment to another, the wave functions of the core electrons do not change significantly with the

environment of the parent atom, because their wave functions overlap only very slightly with the core electron wave functions from neighboring nucleus. For this reason, they do not determine most of the electronic and optical properties of materials. [14]. It is thus justified to consider the configuration of the core electrons within the solid to be “frozen” and equal to its form of the isolated atom. Therefore, it is possible to combine the potential due to the core electrons with the Coulomb potential of the nucleus to an ionic core potential. In this way, core electrons are removed from the problem and one can focus only on the valence electrons in the calculation, this is known as the frozen core approximation [15]. The error introduced by such an approximation is quite small but savings in the computational cost is enormous.

III.5.2 Concept of pseudopotentials

The atomic wave functions are eigenstates of the atomic Hamiltonian, they must all be mutually orthogonal, so that the valence wave function must oscillate rapidly and must have some nodes in the vicinity of the nucleus in order to maintain orthogonality to the core state. But, it is difficult to develop the rapidly oscillating wavefunction with all of its radial nodes in a given basis set (e.g., Gaussian, plane waves, etc.), because an extremely large number of waves would be necessary to perform an all-electron calculation - a computationally demanding task, therefore, a further reduction of the basis set size is essential.

As the valence wave function is associated with bonding properties, a good description of valence wave function in core region is not necessary. It is therefore appropriate to attempt to replace the true potential, which includes the effects of the nucleus and the core electrons, by an effective pseudopotential acting only on valence electrons. As such, the rapid oscillations of the wave functions near the nuclei are replaced with a pseudo wave function. Pseudopotentials should be transferable between different chemical environments; ideally, a pseudopotential is constructed from an isolated atom of one element, but the resulting pseudopotential can be used for the same atomic species in another environment without further adjustment of the pseudopotential. This suggests that the pseudo-wave functions must be identical to the true valence wave functions in the region of the chemical bond (outside the ionic core region) where they overlap with other atoms [15] (see Figure III.1). An additional requirement for pseudopotentials is to be as smooth as possible in the core region [13, 16]. This is necessary to maintain the basis for the expansion of the wave functions as small as possible.

The use of pseudopotential method can reduce the size of the basis set necessary for calculations involving many atoms, therefore reduce the computational expense.

Pseudopotentials requiring high cut-off energies are called to be hard, while more computationally efficient pseudopotentials with low cut-off energies are soft.

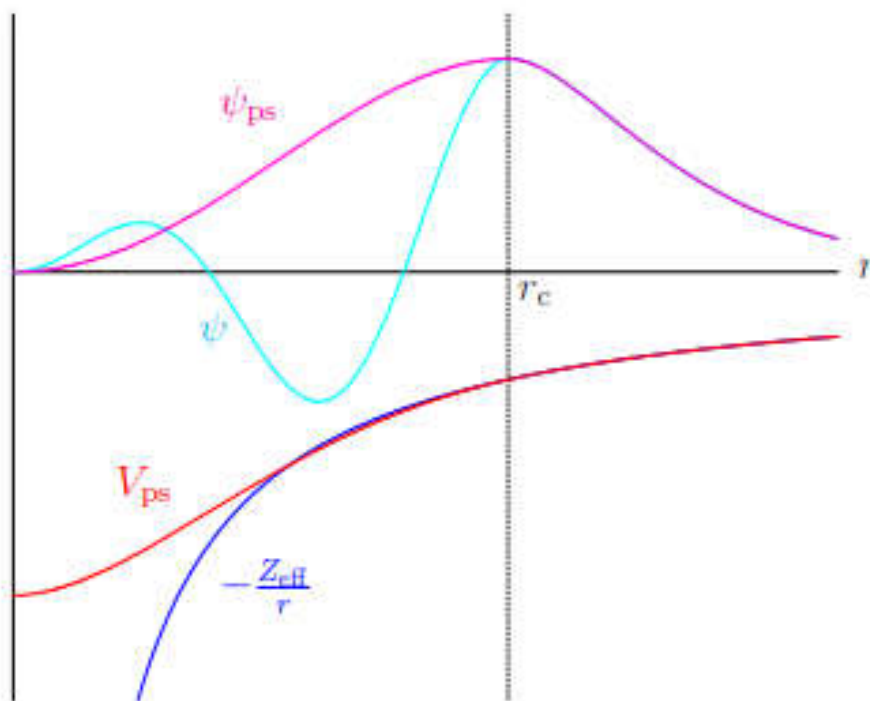


Figure III.1 Schematic diagram of the relationship between all-electron and pseudopotentials and wave functions.

III.5.3 Ab initio Pseudopotentials

There is no single way to build a pseudopotential for a particular chemical element; there is an enormous freedom in constructing pseudopotentials [17-19].

In past, empirical pseudopotentials (they do not come from the first principles) constructed by fitting to the experimental data have been adopted [20, 21]. Although, these empirical pseudopotentials are simple to use, they lack a very important property, the transferability. They can be used for some specific environment but not in a different environment.

At present, there are many pseudopotentials that are constructed with non-empirical approaches. Pseudopotentials generated by calculations on atoms and are not fitted to experiments are called ab initio pseudopotentials. The ab initio pseudopotential method is now

a well-established tool in condensed matter physics, computational chemistry and material science.

The use of pseudopotentials dates back to Fermi's work in the 1930s to study high-lying atomic levels [22]. However, the most elegant way to present a non-empirical pseudopotential is due to Phillips and Kleinman [23, 24] who developed a rigorous formulation of the pseudopotential approach.

III.5.3.1 Method of Philips and Kleinman

To illustrate the pseudopotential idea suggested by Phillips and Kleinman, we distinguish between the states of the valence electrons $|\psi_v\rangle$ and the states of the core electrons $|\psi_c\rangle$ of a given Hamiltonian (for example the Fock operator in the Hartree-Fock theory or the Kohn-Sham operator in density-functional theory.)

The core electrons wave functions are defined by:

$$\hat{H}|\psi_c\rangle = \varepsilon_c|\psi_c\rangle \quad (c = 1, N_c) \quad (\text{III. 12})$$

The valence electron wave functions for this same Hamiltonian is given by,

$$\hat{H}|\psi_v\rangle = \varepsilon_v|\psi_v\rangle \quad (v = 1, N_v) \quad (\text{III. 13})$$

$|\psi_v\rangle$ has a number of radial nodes because it must be orthogonal to the core orbitals.

Phillips and Kleinman showed that one can construct a smooth valence wave function $|\hat{\psi}_v\rangle$, that is not orthogonal to the core state ($\langle\hat{\psi}_v|\psi_c\rangle \neq 0$), by combining the core wave functions $|\psi_c\rangle$ and the function of the real valence wave function $|\psi_v\rangle$ in the following way :

$$|\hat{\psi}_v\rangle = |\psi_v\rangle + \sum_{c=1}^{N_c} b_c |\psi_c\rangle \quad (\text{III. 14})$$

b_c is some (yet) unknown constants, and $|\psi_c\rangle$ is the core wavefunctions. The constants b_c can be determined by using that the core wave functions are orthonormal, and that $|\psi_v\rangle$ is orthogonal to the core wavefunctions. We multiply Eq. (III. 14) by any of the core wavefunctions, $|\psi_{c_0}\rangle$, and integrate, we obtain :

$$\langle\psi_{c_0}|\hat{\psi}_v\rangle = \langle\psi_{c_0}|\psi_v\rangle + \sum_c b_c \langle\psi_{c_0}|\psi_c\rangle \quad (\text{III. 15})$$

Where

$$\langle\psi_{c_0}|\hat{\psi}_v\rangle = b_{c_0} \quad (\text{III. 16})$$

By using the fact that $|\psi_v\rangle$ and $|\psi_c\rangle$ are solutions of the Schrodinger equation with eigenvalues ε_v and ε_c , respectively, one easily obtains the following equation for $|\hat{\psi}_v\rangle$:

$$[\hat{H} + \sum_{c=1}^{N_c} (\varepsilon_v - \varepsilon_c) |\psi_c\rangle\langle\psi_c|] |\hat{\psi}_v\rangle = \varepsilon_v |\hat{\psi}_v\rangle \quad (\text{III. 17})$$

$$[\hat{T} + \hat{V} + \sum_{c=1}^{N_c} (\varepsilon_v - \varepsilon_c) |\psi_c\rangle \langle \psi_c|] |\hat{\psi}_v\rangle = \varepsilon_v |\hat{\psi}_v\rangle \quad (\text{III. 18})$$

The above result suggests to construct a pseudo-Hamiltonian:

$$\hat{H}_{PS} = \hat{T} + \hat{V}_{ps} \quad (\text{III. 19})$$

With a pseudopotential

$$V_{PS} = V + \sum_{c=1}^{N_c} (\varepsilon_v - \varepsilon_c) |\psi_c\rangle \langle \psi_c| \quad (\text{III. 20})$$

So,

$$\hat{H}_{PS} |\hat{\psi}_v\rangle = \varepsilon_v |\hat{\psi}_v\rangle \quad (\text{III. 21})$$

This equation indicates that states $|\hat{\psi}_v\rangle$ satisfy a Schrodinger-like equation with an additional contribution, \hat{V}_{ps} to the Hamiltonian.

Since \hat{V}_{ps} is not a usual potential, it is called pseudopotential. i.e., a function depending on a position r . It is important to note that the operator \hat{V}_{ps} is energy-dependent because it depends on ε_v , and it is nonlocal because it depends $|\psi_v\rangle$.

Since valence electron energies always lie above the core energies (i.e., $\varepsilon_v > \varepsilon_c$), the second term in Equation (III. 20) is always positive. Since $V(r)$ is attractive, the first term will be negative, which will be partially cancelled by the second term.

The pseudopotential acts differently on wave functions of different angular momentum, thereby expressing its energy dependence. The most general form of a pseudopotential of this kind is:

$$V_{ps}(r) = \sum_{\ell=0}^{\infty} \sum_{m=-\ell}^{\ell} V_{\ell}^{PS}(r) |\ell m\rangle \langle \ell m| = \sum_{\ell=0}^{\infty} V_{\ell}^{PS}(r) \hat{P}_{\ell} \quad (\text{III. 22})$$

Where $|\ell m\rangle$ are the spherical harmonics $\langle r | \ell m \rangle = Y_{\ell m}(\theta, \phi)$, V_{ℓ}^{PS} is the pseudopotential corresponding to the angular component l , and the operator $\hat{P}_l = \sum_{m=-l}^l |\ell m\rangle \langle \ell m|$ is a projection operator onto the l th angular momentum subspace.

The meaning of the expression for V_{ℓ}^{PS} in Eq. (III. 22) is that when V_{ℓ}^{PS} operator acts on the electronic wave function, the projection operator \hat{P}_l selects the different angular momentum components of the wave function, which are then multiplied by the corresponding pseudopotential V_{ℓ}^{PS} . Next, the contributions of all the angular momentums are added up to form the total pseudopotential contribution to the Hamiltonian matrix elements that enter Schrödinger equation.

Since V_{ℓ}^{PS} acts as a local operator in the radial coordinate that depends on ℓ , it can be called a angular-dependent or semi local pseudopotential. A local pseudopotential is a function only of the distance from the nucleus [25].

The work of Phillips and Kleinman first established the theoretical basis of the

pseudopotential method which can broadly be assigned into two categories: norm-conserving pseudopotentials and the ultra-soft pseudopotential.

III.5.3.2 Norm conserving pseudopotentials

III.5.3.2.1 Concept of Norm conserving pseudopotentials

A major step forward in the attempts to produce transferable first principles pseudopotentials came with the advent of norm conserving pseudopotentials by Hamann, Schlüter and Chiang [26] in 1979 and developed by Kleinman and Bylander [27]. Within this approximation, the all-electron and the pseudo wave function must have the same norm in the ionic core region delimited by a certain radius chosen called cut-off radius r_c to guarantee that both wave functions generate identical electron densities in the outside region. The pseudo and all-electron wave functions are identical outside the core radius but they are different inside the region of the ionic core delimited by the cut-off radius r_c . The charge conservation property of norm-conserving pseudopotentials simplifies the application of the pseudopotentials and makes them more accurate and transferable, they can be used to predict the physicochemical properties of an atom in a wide range of situations (volume, surface, etc.). However, the use of norm-conserving pseudopotentials is very expensive, due to the requirement of conservation of the norm below the r_c . They require large plane-wave basis sets or a large energy cut-off for elements with strongly localized orbitals such as the case of transition metals and rare earths, thus requiring much more computational effort.

III.5.3.2.2 The construction of the norm-conserving pseudopotential

The construction of a pseudopotential ('ab initio') is an inverse problem. However, there are important rules that help to solve the problem. We present here briefly the main stages of construction formulated first by Hamann et al [26] and exploited by Bachelet, Hamann and Schlüter (BHS) [28] who applied this methodology to all atoms from hydrogen to plutonium.

The following is the process of constructing the norm-conserving pseudopotential:

First, the real radial wave function $R_{n\ell}(r)$ of the atom is obtained by solving the radial equation of Kohn-Sham

$$\left[-\frac{1}{2r} \frac{\hbar^2}{m_e} \frac{d^2}{dr^2} r + \frac{\hbar^2}{2m_e} \frac{\ell(\ell+1)}{r^2} + v(r) \right] R_{n\ell}(r) = e_{n\ell} R_{n\ell}(r) \quad (\text{III. 23})$$

Where

$$V(r) = -\frac{1}{r} + V_H(r) + V_{XC}(r) \quad (\text{III. 24})$$

Here, $V_{XC}(r)$ is the exchange correlation potential and $V_H(r)$ is given by:

$$V_H(r) = \int \frac{\rho(r')}{|r-r'|} d^3r' \quad (\text{III. 25})$$

Where $\rho(r')$ is the total electron density.

Once the true radial wave function $R_{n\ell}(r)$ is obtained, we choose a cut-off radius r_c (generally between the outermost node and the outermost extremum of the all-electron radial wavefunction) to construct a pseudo radial function $R_{n\ell}^{PS}(r)$ satisfying five general criteria:

- The pseudowave function must be identical to the true valence wave function beyond the chosen cut-off radius:

$$R_{n\ell}^{PS}(r) = R_{n\ell}(r) \text{ pour } r \geq r_c \quad (\text{III. 26})$$

- The pseudowave function $R_{n\ell}^{PS}(r)$ must not contain no nodes and be continuous at r_c , as well as its first and second derivatives. Since the pseudowave function is constructed only for valence electrons, we omit the principal quantum number n .
- The normalized atomic radial pseudowave function $R_{n\ell}^{PS}(r)$ and normalized radial true wave function $R_{n\ell}(r)$ must be equal beyond a suitably chosen cut-off radius r_c

$$|R_{n\ell}^{PS}(r)|^2 = |R_{n\ell}(r)|^2 \text{ pour } r \geq r_c \quad (\text{III. 27})$$

- The eigenvalues of pseudowave function must be equal to the true eigenvalues.
- The charge enclosed within r_c for the pseudowave function and true wave function must be equal, that is

$$\int_0^{r_c} |R_{n\ell}^{PS}(r)|^2 r^2 dr = \int_0^{r_c} |R_{n\ell}(r)|^2 r^2 dr \quad (\text{III. 28})$$

The last condition is commonly referred to as the norm-conservation condition and if a pseudopotential meets this condition, it is called a “norm-conserving pseudopotential” (NCPP). Note that a pseudowave function fulfilling these conditions can be constructed arbitrarily in many ways. This freedom is further exploited to produce a smooth pseudopotential. Once a particular pseudo-wavefunction is created, the screened pseudopotential can be recovered by inverting the radial Schrodinger equation (III.24):

$$V_{\ell SC}^{PS}(r) = e_{n\ell} - \frac{\ell(\ell+1)}{2r^2} + \frac{1}{2rR_{n\ell}^{PS}} \frac{d^2}{dr^2} [rR_{n\ell}^{PS}(r)] \quad (\text{III. 29})$$

We call the resulting pseudopotential $V_{\ell SC}^{PS}(r)$ screened, because it still includes the potential due to the nucleus and all electrons, not just the core electrons. The screened pseudopotential $V_{\ell SC}^{PS}(r)$ thus obtained lacks transferability as the screening from the valence electrons depends

strongly on the environment in which they are placed. To improve the transferability and generate a pseudopotential "ionic" (not screened) independent of the chemical environment, the interaction among the valence electrons (and their self-interaction) is removed from the screened PP by the so-called unscreening procedure. This is achieved by subtracting the screening Hartree and exchange–correlation potential, calculated solely by the pseudo valence orbitals (or rather their densities), from the screened pseudopotential.

By subtracting the effect of the valence electrons, one obtains an (unscreened) ‘ionic’ pseudopotential that does not depend on the chemical environment and, it should be transferable from the atom to a molecular state or to a solid state or liquid state. The ionic pseudopotential we are looking for is given by:

$$V_\ell^{PS}(r) = V_{\ell,sc}^{PS}(r) - \int dr' \frac{\rho_v^{PS}(r')}{|r-r'|} - V_{xc}[\rho_v^{PS}(r)] \quad (\text{III. 30})$$

With

$$\rho_v^{PS}(r) = \sum_{\ell m}^{occ} |rR_\ell^{PS}(r)|^2 \quad (\text{III. 31})$$

When such ionic potential is placed in a different environment, $V_H(r)$ and $V_{xc}(r)$ are recalculated for that environment and again added to the potential. Note that this does not guarantee that the pseudopotential is transferable to any environment. It can be used only in an environment in which eigenvalues do not change significantly from the eigenvalues used in its construction. The property that makes this energy range wider is loosely called smoothness, that is, the smoother the pseudopotential, the weaker the energy dependence.

The norm-conserving pseudopotentials, constructed from equation (III.30), have a general semi-local form, because although the potentials are local in r , they depend in a non-local way on the angular variables. Through the orbital moment, each component of the angular momentum of the wave function sees a different potential [29]. The ionic pseudopotential can be expressed as follows [30]:

$$V^{PS} = \sum_{\ell=0}^{\infty} V_\ell^{PS} \hat{P}_\ell \quad (\text{III. 32})$$

\hat{P}_ℓ is the operator defined in equation (III.21).

In general, we can express the non-local pseudopotential in semi-local form [25]:

$$\begin{aligned} V^{PS}(r) &= \sum_{\ell=0}^{\infty} V_{loc}^{PS}(r) \hat{P}_\ell + \sum_{\ell=0}^{\ell_{max}} [V_\ell^{PS}(r) - V_{loc}^{PS}(r)] \hat{P}_\ell \\ &= \sum_{\ell=0}^{\infty} V_{loc}^{PS}(r) \hat{P}_\ell + \sum_{\ell=0}^{\ell_{max}} [\Delta V_\ell^{PS}(r)] \hat{P}_\ell \end{aligned} \quad (\text{III. 33})$$

With

$$\Delta V_\ell^{PS}(r) = V_\ell^{PS}(r) - V_{loc}^{PS}(r) \quad (\text{III. 34})$$

Here $V_{loc}^{PS}(r)$ and $\Delta V_{\ell}^{PS}(r)$ are the local and semi-local potentials respectively. The semi-local potential in equation (III.34) can be transformed into a completely non-local form using a general form suggested by Kleinman-Bylander (KB) [27] as:

$$V_{PP}^{KB} = V_{loc}^{PS} + \sum_{l,m} \frac{|\Delta V_{\ell}^{PS} \psi_{lm}^{PS}\rangle \langle \psi_{lm}^{PS} \Delta V_{\ell}^{PS}|}{\langle \psi_{lm}^{PS} | \Delta V_{\ell}^{PS} | \psi_{lm}^{PS} \rangle} \quad (\text{III. 35})$$

Where ψ_{lm}^{PS} is a proper state of the atomic pseudo-Hamiltonian. The operator V_{PP}^{KB} acts on the reference state identically to the original semi-local operator $V^{PS}(r)$, so that it is conceptually well justified, but now the number of projections that must be made varies only linearly with the number of basic states, whereas for semi-local forms, this number varies quadratically. This separable form can be seen as a "correction" to the local pseudopotential in the core region.

III.5.3.3 Vanderbilt Pseudopotential (Ultrasoft)

III.5.3.3.1 Concept of Vanderbilt Pseudopotential (Ultrasoft)

The "norm conserving pseudopotentials" approach has been extended by David Vanderbilt [31], by creating ultra-soft pseudopotentials. In this approximation, Vanderbilt [31] showed that then much smoother, but still highly transferable, non-norm-conserving pseudopotentials can be obtained by relaxing the norm-conserving constraint, which is the main factor responsible for the hardness of the norm conserving pseudopotentials. The only restriction remaining is, then, the matching of the pseudo and the all-electron functions for $r \geq r_c$, and this gives the possibility to choose a much larger value for r_c . Consequently, the kinetic energy is reduced, the valence electrons experience a smoother potential and the number of plane waves required for its description decreases. It is for this reason that Vanderbilt ultra-soft pseudopotentials are amongst the most widely used in the condensed matter community. Pseudopotentials can be made softer by moving the cut-off radius outward, however, there is an upper bound to the cut-off radius, if it is increased beyond this bound, the transferability of the pseudopotential reduces. The relaxation of the norm-conservation constraint causes a charge-density deficit between the pseudo wavefunction and the exact one that should be taken into account in the generation of the ultrasoft pseudopotential. This can be done by dividing the pseudo wave functions into two parts: Ultrasoft valence wave function that do not fulfil the norm conservation criteria plus, a core augmentation charge functions which are defined as the charge density difference between the all-electron and pseudo wave functions and are strictly localized in the core region.

$$Q_{nm}(r) = \psi_n^*(r) \psi_m(r) - \psi_n^{pp*} \psi_m^{pp} \quad (\text{III. 36})$$

Therefore, the norm-conservation will be satisfied when the $Q_{nm}(r) = 0$.

III.5.3.3.2 The construction of ultrasoft pseudopotential

The generation of ultrasoft pseudopotential start out in the same way as norm-conserving pseudopotentials. For a given species, the atomic Kohn-Sham system is solved self-consistently, resulting the screened all-electron potential, V_{AE} . Then for each angular momentum channel, a few energy values, τ are chosen (τ =number of such energies, usually max 3). For the V_{AE} already obtained, the Schrödinger equation is found

$$[T + V_{AE}]|\psi_n\rangle = \varepsilon_n|\psi_n\rangle \quad (\text{III. 37})$$

Here n is a composite index holding l for the angular momentum quantum number, m for the projection and τ . $n = \{\tau\ell m\}$.

Next, we choose three cut-off radii:

1. A smooth local (ℓ -independent) potential is created which matches V_{AE} after the radius r_c^{loc} .
2. A second cut-off radius r_{cl} , is chosen for each angular momentum channel and a pseudofunction, ψ_n^{pp} is constructed which matches the real wave function $|\psi_n\rangle$ at r_{cl} .
3. Finally a diagnostic radius R_c . is chosen such that it is slightly greater than the maximum of all radius r_c^{loc} and r_{cl} , so that all the quantities of PS and AE agree beyond R_c .

Then a smooth pseudofunction wave is determined for each angular momentum only with the constraint that it corresponds to the real wave functions outside the chosen cut-off radius r_{cl} .

The Kohn-Sham equations are then inverted to obtain the total effective V_{KS}^{PP} pseudopotential satisfying the following equations:

$$(\hat{T} + V_{eff}^{ps})\psi_n^{pp} = \varepsilon_n\psi_n^{pp} \quad (\text{III. 38})$$

The total effective pseudopotential is then separated into a local and non-local contribution,

$$V_{KS}^{PP} = V_L + V_{NL} \quad (\text{III. 39})$$

The local potential V_L is chosen to be smooth, this potential agrees with the all-electron potential beyond cut-off radii chosen r_c . By inserting the equation (III.40) in the equation (III.39), we can construct for each wave pseudofunction the following orbital [32]:

$$|\chi_n\rangle = [\varepsilon_n - T - \hat{V}_L]|\psi_n^{pp}(r)\rangle \quad (\text{III. 40})$$

The orbitals $|\chi_n\rangle$ are local and disappear beyond R where $V_{lo} = V_{AE}$ and $\psi_n^{PP} = \psi_n$ Then, an auxiliary matrix of interior products is determined

$$(B^{-1})_{mn} = \langle\psi_n^{pp}|\chi_m\rangle \quad (\text{III. 41})$$

The projectors needed to define the non-local part of the potential are defined by:

$$|\beta_n\rangle = \sum_n |\chi_n\rangle \langle\chi_m|\psi_n^{pp}\rangle = \sum_n (B^{-1})_{mn} |\chi_m\rangle \quad (\text{III. 42})$$

The total non-local operator is then rewritten as:

$$\hat{V}_{NL} = \sum_{n,m} B_{nm} |\beta_n\rangle \langle \beta_m| \quad (\text{III. 43})$$

Provided that the norm-conserving constraint of the pseudo-wave function is respected. The norm-conservation will be satisfied when:

$$Q_{nm}(r) = \psi_n^*(r)\psi_m(r) - \psi_n^{pp*}\psi_m^{pp} = 0 \quad (\text{III. 44})$$

We note that for the particular case where a single reference energy is chosen by angular momentum, the equation (III.42) simply returns to the Kleinman-Bylander form of the separable non-local potential [32]. Vanderbilt has shown that the norm-conserving constraint of equation (III.44) can be abandoned by introducing a generalized Hermitian overlap operator S :

$$S = 1 + \sum_{nm} q_{nm} |\beta_n\rangle \langle \beta_m| \quad (\text{III. 45})$$

So that the orthonormality condition to satisfy in the solution of the KS equations is:

$$\langle \psi_n | S | \psi_m \rangle = \delta_{nm} \quad (\text{III. 46})$$

In the expression (III.45) q_{nm} is the integral of the augmentation function $Q_{nm}(r)$ over the sphere defined by r_c :

$$q_{nm} = \int dr Q_{nm}(r) \quad (\text{III. 47})$$

The new non-local operator V_{NL} becomes:

$$V_{NL} = \sum_{nm} D_{nm} |\beta_n\rangle \langle \beta_m| \quad (\text{III. 49})$$

Where the new coefficients are:

$$D_{nm} = B_{nm} + \varepsilon_m q_{nm} \quad (\text{III. 50})$$

With all these descriptions, we can verify that the pseudo functions obey the equation

$$\begin{aligned} (\hat{T} + V_{loc} + \sum_{nm} D_{nm} |\beta_n\rangle \langle \beta_m|) |\psi_n^{pp}\rangle &= \varepsilon_i (1 + \sum_{nm} q_{nm} |\beta_n\rangle \langle \beta_m|) |\psi_n^{pp}\rangle \\ (\hat{T} + V_{loc} + \sum_{nm} D_{nm} |\beta_n\rangle \langle \beta_m|) |\psi_n^{pp}\rangle &= \varepsilon_i S |\psi_n^{pp}\rangle \end{aligned} \quad (\text{III. 51})$$

It can be verified that the pseudopotentials ultrasoft generated with the above steps have excellent transferability; this means that the pseudo-wave functions and their logarithmic derivatives correspond to each reference energy and for small variations around it.

To compensate for the charge deficit, the valence charge density is defined as

$$\rho(r) = \sum_n \left[|\psi_n^{ps}(r)|^2 + \sum_{i,j} Q_{ji}(r) \langle \psi_n^{ps} | \beta_i \rangle \langle \beta_j | \psi_n^{ps} \rangle \right] \quad (\text{III. 52})$$

III.6 Resolution of Kohn-Sham equations

In order to set up and solve the Kohn–Sham equations, we need to define both the Hartree operator V_H and the exchange-correlation operator V_{xc} which depend on the density $\rho(r)$. But to construct the electron density, we must know the single-electron wave functions, and to find these wave functions we must solve the Kohn–Sham equations. Thus means the estimated solution of the Kohn-Sham problem must be known before it can be solved, so an iterative procedure is needed to escape from this paradox (See [Figure III.2](#)). The Kohn-Sham equations of the system can be constructed for a trial electron density and for a given set of atomic coordinates. The geometries of the system for density functional calculation are constructed using experimental data such as bulk lattice constants, previous first principle calculations or semi-empirical methods, or from intuition. Once trial electron density and is defined, the Poisson’s equation is constructed and solved in order to obtain the electrostatic Coulomb potential. Subsequently explicit form of the exchange-correlation potential is used and the exchange correlation operator is constructed. All these terms are added together to give the full Hamiltonian of equation (II.42)

Following standard mathematical techniques for solving eigenvalue problems, one can expand the unknown solutions $\psi_i(r)$ of the equation ((II.42)) for each k-point in a set of known functions, $\phi_j(r)$, with unknown linear coefficients, c_{ij} ,

$$\psi_i(r) = \sum_j c_{ij} \phi_j(r) \quad (\text{III. 53})$$

There are many possible choices that could be made for the basis set, although Gaussians²⁵ have dominated the molecular community while plane waves have been the de facto standard for solid-state physics. In principle, $\phi_j(r)$ has an infinite dimension, i.e., but in practice one works with a limited set of basis functions that can generate a function that is ‘close’ to $\phi_j(r)$ by using the technique discussed in section (III.4).

The coefficients that determine how much these functions contribute to the development of the Kohn-Sham function are found by constructing the energy functional (i.e. the expectation value of the Hamiltonian) and applying the Variational principle This transforms the partial differential equation to a discrete matrix problem that can then be solved:

$$\begin{aligned} \sum [\langle \phi_{ik} | H | \phi_{jk} \rangle - \varepsilon_{nk} \langle \phi_{ik} | \phi_{jk} \rangle] c_{ink} &= 0 \\ \sum [H_{ij} - \varepsilon_{nk} S_{ij}] c_{ink} &= 0 \end{aligned} \quad (\text{III. 54})$$

where

$$H_{ij} = \langle \phi_{ik} | H | \phi_{jk} \rangle \quad (\text{III. 55})$$

And

$$S_{ij} = \langle \phi_{jk} | \phi_{ik} \rangle \quad (\text{III. 56})$$

Where H_{ij} is the matrix elements of the Kohn-Sham Hamiltonian in the basis states, and S_{ij} is the overlap matrix elements.

The diagonalization of the matrix (III. 54) at each k point produces a set of eigenvalues of a particle and the variational coefficients of expansion corresponding to each eigenvalue.

The initial wave functions at each k-point in the irreducible wedge of the Brillouin zone could in principle be obtained by using the expansion coefficients. The occupation of each state is obtained by using Fermi-Dirac statistics. This indicates that the eigenvalues are generated with increasing energy and all states are filled until the total number of electrons of the system is exhausted.

The electron density at a specific point k is thus:

$$\rho^k(r) = \sum_{i=1}^N |\phi_i^k|^2 \quad (\text{III. 57})$$

Therefore, the new total electron density ("output") can be calculated via the summation of the densities at the sampled k-points,

$$\rho(r) = \frac{\Omega}{(2\pi)^3} \sum_k^{1^{emeBz}} \rho^k(r) \Delta k \quad (\text{III. 58})$$

Where Δk is the k-point sampling spacing which could be manually determined. It is easy to see that the smaller Δk is selected, the more accurate the calculation of $\rho(r)$ would be, but as the number of electrons in the system increases, the computational cost will also increase, making almost impossible to solve systems with more than a few electrons. The constructed electron density is called the output electron density. If the output electron density is not equal to the input one, it will be used as an input and this process is repeated several times until the new-evaluated electron density can be equated to the old density. This is known as the self-consistent field cycle SCF. In practice, one iterates sufficiently long until the residual difference between the input and output densities does not cause any significant errors in the total energy or other properties of interest. The found electron density also corresponds to the ground state density, since this is the only density that can be correctly solved from the Kohn-Sham equation.

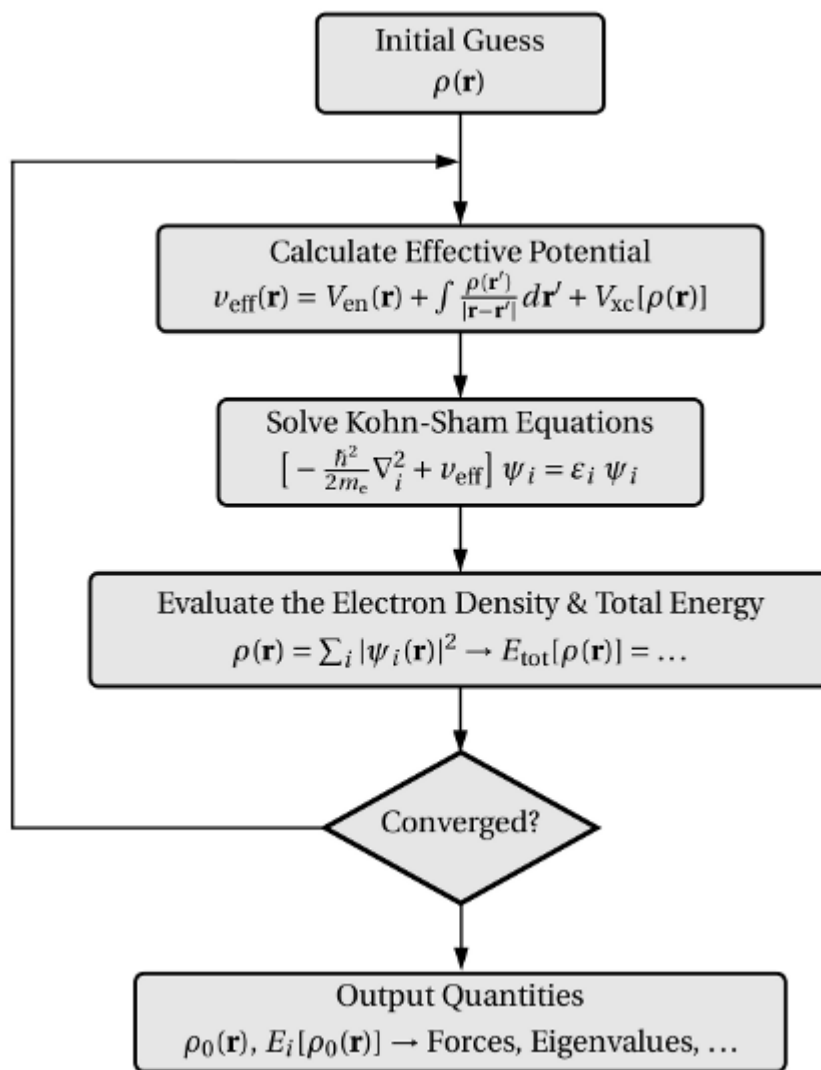


Figure III.2 : A flow chart of a typical DFT calculation within the Kohn Sham method.

References

- [1] E. Kaxiras, *Atomic and Electronic Structure of Solids*, Cambridge University Press, Cambridge (2003).
- [2] N.W. Ashcroft, N.D. Mermin: *Solid State Physics*, Holt Rinehart and Winston, New York (1976).
- [3] F. Bloch, *Z. Physik* **52**, 555 (1928).
- [4] M. C. Payne, M. P. Teter, D. C. Allan, T. A. Arias, and J. D. Joannopoulos, *Rev. Mod. Phys.* **64**, 1045 (1992).
- [5] J. Ihm, A. Zunger, M.L. Cohen, *J. Phys. C* **12**, 4409 (1979).
- [6] D. S. Sholl and J. A. Steckel, *Density Functional Theory: A Practical Introduction*, John Wiley & Sons, Hoboken, New Jersey (2009).
- [7] L. P. Bouckaert, R. Smoluchowski, and E. Wigner. *Phys. Rev.* **50**, 58 (1936).
- [8] D. J. Chadi and M. L. Cohen, *Phys. Rev. B* **8**, 5747 (1973).
- [9] J. D. Joannopoulos and M. L. Cohen, *J. Phys. C* **6**, 1572 (1973).
- [10] R.A. Evarestov and V.P. Smirnov, *Phys. Status Solidi* **119**, 9 (1983).
- [11] H. J. Monkhorst and J. D. Pack, *Phys. Rev. B* **13**, 5188 (1976).
- [12] R. M. Martin, “*Electronic Structure Basic Theory and Practical Methods*,” Cambridge University Press, Cambridge, (2004).
- [13] W. E. Pickett, *Comput. Phys. Rep.* **9**, 115 (1989).
- [14] U. von Barth and C. D. Gelatt, *Phys. Rev. B* **21**, 2222 (1980).
- [15] S. Goedecker and K. Maschke, *Phys. Rev. A* **45**, 88 (1992).
- [16] V. Heine. *The pseudopotential concept. In Solid State Physics, Vol. 24*, Academic Press, New York (1970).
- [17] M. L. Cohen and V. Heine. *The fitting of pseudopotentials to experimental data and their subsequent application, volume 24 of Solid State Physics*. Academic Press, New York, (1970).
- [18] M.L. Cohen, J.R. Chelikowsky, *Electronic Structure and Optical Properties of Semiconductors*, Springer, Berlin, (1988).
- [19] W. A. Harrison, “*Pseudopotentials in the Theory of Metals*,” Benjamin, New York, (1966).
- [20] B. J. Austin, V. Heine and L. J. Sham, *Phys. Rev.* **127**, 276 (1962).
- [21] R.W. Shaw, Jr. and W.A. Harrison, *Phys. Rev.* **163**, 604 (1967).
- [22] E. Fermi, *Nuovo Cimento* **11**, 157 (1934).
- [23] J. C. Phillips, *Phys. Rev.* **112**, 685 (1958).
- [24] J. C. Phillips and L. Kleinman, *Phys. Rev.* **116**, 287 (1959).

- [25] J. Kohanoff, *Electronic structure calculations for solids and molecules: theory and computational methods*, Cambridge University Press, New York (2006).
- [26] D. H. Hamann, M. Schlüter, and C. Chiang, *Phys. Rev. Lett.* **43**, 1494 (1979).
- [27] L. Kleinman and D. M. Bylander, *Phys. Rev. Lett.* **48**, 1425 (1982).
- [28] G. B. Bachelet, D. R. Hamann, and M. Schlüter, *Phys. Rev. B* **26**, 4199 (1982).
- [29] N. Troullier and J. L. Martins, *Phys. Rev. B* **43**, 1993 (1991)
- [30] X. Gonze, R. Stumpf, and M. Scheffler, *Phys. Rev. B* **44**, 8503 (1991).
- [31] D. Vanderbilt, *Phys. Rev. B* **41**, 7892 (1990).
- [32] G. Kresse and J. Hafner, *J. Phys. Condens. Matter* **6**, 8245 (1994).

IV. Full-Potential Linearized Augmented Plane Wave Method

IV.1 Introduction

One of the most accurate methods for solving the KS equations, when aiming to maintain a full-potential description, is the separation of real space into regions close to the nuclei and in between them in the sense that all the charge inside the solid is taken into account not only that of the valence states. This method is well known to enable most accurate calculations of the electronic structure and magnetic properties of crystals and surfaces. In this chapter, the augmented plane waves (APW), the linearized augmented plane waves (LAPW) method and the effect of local orbitals on the efficiency of the basis set will be introduced.

IV.2 The augmented plane wave (APW)

The augmented plane wave (APW) method was developed by Slater (1937) as possible basis functions to solve one-electron equations [1- 3]. The basic assumption of this method is the partitioning of real space into two regions: near the nuclei and away from them, so-called muffin-tin or atomic spheres, and interstitial region as shown in [Figure. IV.1](#).

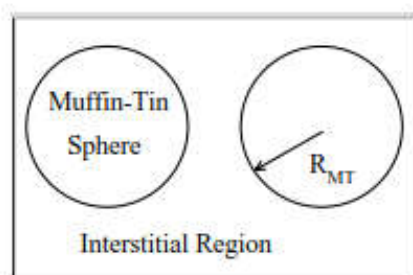


Figure IV.1 :Division of the unit cell into two parts: The Muffin-Tin spheres, with radius R , around the nucleus and an interstitial region.

The potential is assumed to be spherically symmetric in the muffin tin region and constant away from the atom in the interstitial region.

The potential in the whole space can be defined as

$$V(r) = \begin{cases} V(r) & (r \in MT) \\ Constant & (r \in I) \end{cases} \quad (IV. 1)$$

The advantage of this partitioning is that the problem can be solved using a divide-and-conquer strategy and allows for dramatic simplifications. Inside the atomic spheres electrons behave almost as if they were in a free atom and therefore we can describe their behavior by atomic-like wavefunctions evaluated at a predefined energy ϵ_ℓ . Outside the muffin tin spheres between

atoms, electrons are almost free and, as we know, the plane waves are efficient to describe the behavior of the electrons in this region. The boundary conditions are set by requiring continuity of the wavefunctions and their first and second derivatives at the muffin tin borders. The wave function for the wave vector k is now taken to be:

$$\varphi_{k+G}(r, \epsilon_\ell) = \begin{cases} \frac{1}{\sqrt{\Omega}} e^{i(k+G).r}, & r \in I \\ \left(\sum_{\ell, m} A_{\ell m}^{k+G} u_\ell(r, \epsilon_\ell) Y_{\ell m}(\hat{r}) \right), & r \in MT \end{cases} \quad (IV. 2)$$

Here, Ω is the unit cell volume, $Y_{\ell m}$ are spherical harmonics with the azimuthal quantum number ℓ and magnetic quantum number m , k and G are vectors belonging to the reciprocal space, α the muffin tin labelling index and u_ℓ is the numerical solution to the radial wave equation of a free atom and it is a function of the energy parameter ϵ_ℓ :

$$\left\{ -\frac{d^2}{dr^2} + \frac{\ell(\ell+1)}{r^2} + V(r) - \epsilon_\ell \right\} r u_\ell(r) = 0 \quad (IV. 3)$$

The coefficients $A_{\ell m}^{\alpha, k+G}$ are determined from the requirement that the wave function in the MT must match smoothly with the plane-wave solution at the surface of the muffin-tin sphere.

In order to realize this requirement, we use the expansion of plane waves into spherical harmonics Y_{lm} about the origin of the sphere of atom α and equating the basis functions inside and outside the sphere for each value of k :

$$\frac{1}{\sqrt{\Omega}} e^{i(k+G).r} = \frac{4\pi}{\sqrt{\Omega}} e^{i(k+G).r} \sum_{\ell, m} i^\ell j_\ell(|k+G|R) Y_{\ell m}^*(\widehat{k+G}) Y_{\ell m}(\hat{r}) \quad (IV. 4)$$

Where j_ℓ are the ℓ th-order Bessel functions.

The coefficient of each (ℓ, m) component is then matched at the sphere boundary. Thus, after some algebra, it yields:

$$A_{\ell m}^{\alpha, k+G} = \frac{4\pi i^\ell e^{i(k+G).\vec{r}}}{\Omega^2 u_\ell^\alpha} j_\ell(|k+G|R) Y_{\ell m}^*(\widehat{k+G}) \quad (IV. 5)$$

Which uniquely defines $A_{\ell m}^{\alpha, k+G}$ coefficients. Thus, we are now left with the only undetermined parameter being the energy ϵ_ℓ .

Thus, each plane wave is augmented by an atomic-like function in every atomic sphere and constitutes thus the basis set used to expand the Kohn- Sham wave function (ψ),

The sum appearing in Eq. (IV.4) contains, in principle, an infinite number of terms, which would force us to use an infinite number of $A_{\ell m}^{k+G}$ in order to have the matching between the two functions. In practice, one cut the sum in Eq. (IV.4) at a finite value ℓ_{max} . This cut-off can be calculated following the reasoning of Cottenier [4].

The APW functions are not exact solutions to the Schrodinger equation, but they are appropriate basis functions for expanding the Kohn-Sham eigenstates:

$$\psi_i(\mathbf{r}) = \sum_K C_K^i \varphi_K(\mathbf{r}) \quad (\text{IV. 6})$$

Where the sum is over the reciprocal lattice vectors, which has the proper form.

The wave function (IV.6) is used as a trial wave function and the expansion coefficients C_K^i , can be determined variationally [3]. This requires a Variational expression for energy with respect into the linear combination of APW basis set:

$$\frac{\delta \langle \psi_i | H | \psi_i \rangle}{\delta C_K^i} = 0 \quad (\text{IV. 7})$$

The final result has a very interesting form, very much similar to the one we got for the plane wave expansion method, the main disadvantage of the APW method that it cannot get the eigenvalues from a single diagonalization because the basis functions are energy dependent, as apparent in the definition of the radial functions (IV.3). Since this energy depends on the function $u_\ell(\mathbf{r}, \epsilon_\ell)$, the resulting eigenvalue problem is non-linear in energy. Instead of performing a single diagonalization to solve the KS equation, it is necessary to find the secular determinant as a function of ϵ and then find its roots. One repeatedly needs to obtain (for many trial energies) the APW basis, set up the matrix elements, and compute the determinant of the secular equation in order to find its zeros and thus the single particle eigenvalues ϵ_i , this makes the APW method very demanding and numerically even unstable.

The number of augmented plane waves is commonly determined by the parameter $R_{MT} K_{max}$, where R_{MT} is the smallest muffin-tin (MT) radius, and K_{max} is the maximal value of the plane wave vector.

IV.3 The linearized augmented plane wave method (LAPW)

In order to overcome the problem of the energy dependence of the Hamiltonian matrix in the APW method, Andersen [5] and Koelling and Arblman [6] in two different works developed the linearized augmented plane wave method (LAPW). Within LAPW approach, the basis functions are defined as the linear combination of the radial solutions u_ℓ (inside each atomic sphere and for azimuthal quantum number ℓ) of the KS equation and its energy derivative and both of them are evaluated at fixed energy ϵ_ℓ .

This formulation is achieved by calculating an energy independent radial solution u_ℓ at some energy ϵ_ℓ and then performing a Taylor expansion in the neighbourhood of a fixed energy ϵ_ℓ^1 . Such a Taylor expansion of u_ℓ around fixed energy value ϵ_ℓ^1 is given by:

$$u_\ell(\mathbf{r}, \epsilon_\ell) = u_\ell(\mathbf{r}, \epsilon_\ell^1) + (\epsilon_\ell - \epsilon_\ell^1) \frac{\partial u_\ell(\mathbf{r}, \epsilon_\ell)}{\partial \epsilon_\ell} + O((\epsilon_\ell - \epsilon_\ell^1)^2) \quad (\text{IV. 7})$$

The additional term $O((\epsilon_\ell - \epsilon_\ell^1)^2)$ denotes the errors. It turns out that the resulting wavefunctions are affected by an error of second order in $(\epsilon_\ell - \epsilon_\ell^1)$ as a result of the linearization. Taking into account the Variational principle, this leads to an error of fourth order, $(\epsilon_\ell - \epsilon_\ell^1)^4$, in the band energy.

The energy derivatives of the radial solution within the muffin tins satisfies the equation (in atomic units).

$$\left[\frac{1}{2} \left\{ -\frac{d^2}{dr^2} + \frac{\ell(\ell+1)}{r^2} \right\} + v(r) - \epsilon_\ell^1 \right] r \dot{u}_\ell(r, \epsilon_\ell^1) = r u_\ell(r, \epsilon_\ell^1) \quad (\text{IV. 8})$$

Where $u_\ell(r, \epsilon_\ell^1)$ satisfies equation (IV. 3), same as in the APW method.

Substituting Eq. (IV. 8) into Eq.(IV. 2), we get the formulation of the LAPW basis set:

$$\psi_{k+G}(r, \epsilon_\ell^1) = \begin{cases} \sum_{\ell m} [A_{\ell m}^{k+G} u_\ell(r, \epsilon_\ell^1) + B_{\ell m}^{k+G} \dot{u}_\ell(r, \epsilon_\ell^1)] Y_{\ell m}(\hat{r}) & (r \in MT) \\ \frac{1}{\sqrt{\Omega}} e^{i(k+G).r} & (r \in I) \end{cases} \quad (\text{IV. 9})$$

the two parameters, $A_{\ell m}^{k+G}$ and $B_{\ell m}^{k+G}$ are determined by requiring that this basis function inside the sphere matches the plane waves both in value and in slope at the sphere boundary.

In the interstitial region, the basis set is the same as in the APW method but in the Muffin-Tin spheres, the basis functions have more Variational freedom compared to the APWs. This is because if ϵ_ℓ^1 differs slightly from the band energy, ϵ_ℓ , a linear combination will reproduce the APW radial function constructed at the band energy.

The big advantage of LAPW method is that the radial functions $u_\ell(r, \epsilon_\ell^1)$ and $\dot{u}_\ell(r, \epsilon_\ell^1)$ and the respective overlap and Hamilton matrix elements need to be evaluated only for energies in some range around the pivot energy. Moreover, one can get all KS energies at each k-point by a single diagonalization, thus saving much computational cost compared to the APW method.

IV.4 Local Orbitals

In the LAPW method, there is only one linearization energy ϵ_ℓ^1 for every ℓ quantum number. This leads to a problem, which occurs mainly for systems with so-called semi-core states. The semi-core states have usually the same angular quantum number ℓ as the valence states and a different principal quantum number of another higher valence state. They are too delocalized to be described as core states and too deep in energy to be described as valence or conduction states. When applying LAPW on these states, it is thus hard to use single set of reference energies ϵ_ℓ^1 to determine the two same ℓ in Eq. (IV. 9). The dilemma is solved by introducing local orbitals (LO) inside of the augmentation sphere. Local Orbitals are called local, since they are completely localized inside the muffin-tin spheres under consideration and

thus zero in the interstitial. They are not connected to plane waves in the interstitial region, hence they have no k - or G -dependence.

Inside the muffin-tin spheres, local orbitals consists of adding to the linear combination of $u_\ell(r, \epsilon_\ell^1)$ and $\dot{u}_\ell(r, \epsilon_\ell^1)$ an additional orbital $u_\ell(r, \epsilon_\ell^2)$ evaluated at a new reference energies. This new radial function is constructed in the same way as $u_\ell(r, \epsilon_\ell^1)$, but with different energy parameter ϵ_ℓ^2 . A Local Orbital for a given ℓ and m and for a particular atom α is defined as [7, 8]:

$$\phi_{LAPW}^{LO}(r) = \begin{cases} \sum_{lm} \left[A_{\ell m}^{k+G} u_\ell(r, \epsilon_\ell^1) + B_{\ell m}^{k+G} \dot{u}_\ell(r, \epsilon_\ell^1) + C_{\ell m}^{LO} u_\ell(r, \epsilon_\ell^2) \right] Y_{\ell m}(\hat{r}) & (r \in MT) \\ 0 & (r \in I) \end{cases} \quad (IV.11)$$

The three parameters $A_{\ell m}^{LO}$, $B_{\ell m}^{LO}$, and $C_{\ell m}^{LO}$ are evaluated by requiring that the LO is normalized, and has zero value and zero slope at the augmentation sphere radius.

Local Orbitals can treat two principle quantum numbers per ℓ channel. This way, semi-core and valence states with same ℓ value, but different n value can be treated more adequately.

The resulting LAPW+LO basis set can be used to describe both the valence region and the already quite localized semi-core states appropriately.

IV.5 The APW+ local orbitals

An alternative method to linearize the APW method is the APW+ local orbitals method developed by Sjostedt et al [9-11]. In this method, the basis functions belong to two complementary basis sets:

The principal basis set consists of the original APW basis functions but with the crucial difference that each radial function is evaluated at a fixed energy in order to remove the energy dependence of the original APW basis functions:

$$\psi_{k+G}(r, E) = \begin{cases} \frac{1}{\sqrt{\Omega}} e^{i(k+G) \cdot r}, & r \in I \\ \sum_{\ell, m} A_{\ell m}^{k+G} u_\ell(r, \epsilon_\ell) Y_{\ell m}(\hat{r}), & r \in MT \end{cases} \quad (IV.12)$$

The APW basis set is therefore augmented with a new set to gain enough Variational flexibility in the radial basis functions and to recover the effect of the missing derivative of the radial wave functions. The new energy-independent basis set called "local orbitals", which is different from the LOs used to describe semicore states. Here, we shall label these local orbitals as "lo".

Local orbitals are completely confined within the MT sphere and expressed in the following form:

$$\psi_{lo}^{\ell m}(r, E) = \begin{cases} \sum_{\ell m} [A_{\ell m}^{lo} u_{\ell}(r, \epsilon_{\ell}^1) + B_{\ell m}^{lo} \dot{u}_{\ell}(r, \epsilon_{\ell}^1)] Y_{\ell m}(\hat{r}) & (r \in MT) \\ 0 & (r \in I) \end{cases} \quad (IV.13)$$

The same set of energies ϵ_{ℓ}^1 is used as for the corresponding APW's (although this is not strictly needed). By choosing the same linearization energies for the lo as for the principal APW basis functions, the number of energy parameters will be limited to one ϵ_{ℓ}^1 per ℓ quantum number.

The coefficients $A_{\ell m}^{lo}$ and $B_{\ell m}^{lo}$ are determined by the requirement that the lo is zero on the muffin-tin sphere and normalized but not zero slope. Hence, both the APW and the local orbital are continuous at the sphere boundary, but their first derivative is discontinuous for both of them.

The advantage of the APW+lo method is that it has the same small basis set size as the original APW method, they (the local orbitals), neither impose extra boundary condition of the APW basis set, and the number of plane waves in the interstitial is therefore unaffected.

The APW+lo method has also the same accuracy compared to the LAPW method, since it removes the energy dependence of the original APW basis functions (which is the characteristic of LAPW functions). The new APW+lo basis set includes the radial solutions of the Schrodinger equation in their original APW form, which efficiently describes the eigenfunctions at energies close to ϵ_{ℓ}^1 , but also a (less restricted) linear combination of $u_{\ell}(r, \epsilon_{\ell}^1)$ and $\dot{u}_{\ell}(r, \epsilon_{\ell}^1)$, which improves the description of states away from ϵ_{ℓ}^1 .

In this case the problem with semi-core states when different states with the same ℓ (semicore states) have to be treated. The solution is, once more, to use a second set of local orbitals as described above, which now (i.e., for the APW+lo basis set) reads:

$$\phi_{\alpha, LO}^{\ell m}(r) = \begin{cases} \sum_{\ell m} \begin{bmatrix} A_{\ell, m}^{LO} u_{\ell}(r, \epsilon_{\ell}^1) + \\ C_{\ell, m}^{LO} u_{\ell}(r, \epsilon_{\ell}^2) \end{bmatrix} Y_{\ell m}(\hat{r}) & (r \in MT) \\ 0 & (r \in I) \end{cases} \quad (IV.14)$$

That is, it is the same LO as the one used for LAPW, but without the term representing the derivative energy of u_{ℓ} .

IV.6 The Full Potential (L)APW+lo Method

The accuracy of the (L)APW+lo method can be further improved by using the full potential (FP), i.e. developed by Hamann and Wimmer in [12, 13]. In the full-potential LAPW method (FLAPW), any shape approximations in the interstitial region and inside the muffin-tins spheres are dropped, in the sense that all the charge inside the solid is taken into account not only that of the valence states. In FP-LAPW approach. The potential and charge density,

are expanded into plane waves in the interstitial region and as radial functions times spherical harmonics inside each atomic sphere (in the same manner than the wave function in the MT - zone and I-region). For the two regions, the electron potential $V(\vec{r})$ is expanded as :

$$V(\vec{r}) = \begin{cases} \sum_{LM} V_{LM}(r) Y_{LM}(\hat{r}), & r < R \\ \sum_{\vec{G}} V_{\vec{G}} e^{i\vec{G}\cdot\vec{r}}, & r > R \end{cases} \quad (\text{IV.15})$$

The charge density is represented in the same way as the potential:

$$\rho(r) = \begin{cases} \sum_G \rho_I^G e^{iGr} & (r \in I) \\ \sum_L \rho_{MT}^L(r) Y_L(\hat{r}) & (r \in MT) \end{cases} \quad (\text{IV.16})$$

These corrections are also called non-muffin-tin corrections. The choice of basis functions in the interstitial is not effected by the non-muffin-tin corrections.

References

- [1] J.C. Slater, *Phys. Rev.* **51**, 846 (1937).
- [2] J. C. Slater, *Advances in Quantum Chemistry* **1**, 35 (1964)
- [3] T. L. Loucks, *Augmented Plane Wave Method: A Guide to Performing Electronic Structure Calculations*, W. A. Benjamin, New York (1967).
- [4] S. Cottenier, *Density Functional Theory and the family of (L)APW-methods: a step-by-step introduction*, Instituut voor Kern- en Stralingsfysica, K.U. Leuven, Belgium, (2002).
- [5] O. K. ANDERSEN, *Phys. Rev. B* **12**. 3060 (1975).
- [6] D. D. Koelling and G. O. Arbman, *J. Phys. F: Metal Phys.* **5**, 2041 (1975).
- [7] D. J. Singh, *Planewaves, Pseudopotentials, and the LAPW Method*, Kluwer Academic, Boston, (1994).
- [8] D. J. Singh, *Phys. Rev. B* **43**, 6388 (1991).
- [9] E. Sjöstedt, L. Nordström, and D. J. Singh, *Solid State Comm.* **114**, 15 (2000).
- [10] E. Sjöstedt, *Augmented Planewaves, Developments and Applications to Magnetism*, PhD thesis, Uppsala University (2002).
- [11] G. K. H. Madsen, P. Blaha, K. Schwarz, E. Sjöstedt, and L. Nordström, *Phys. Rev. B* **64**, 195134 (2001).
- [12] D. R. Hamann, *Phys. Rev. Lett.* **212**, 662, (1979).
- [13] E. Wimmer, H. Krakauer, M. Weinert, and A. J. Freeman, *Phys. Rev. B* **24**, 864 (1981).

V. Theory of the Investigated Properties

V.1 Introduction

The objective of the present chapter is to present an overview of the theory applied to study the different properties of LiAeP ($\text{Ae}=\text{Sr}, \text{Ba}$) and Ae_3AlAS_3 ($\text{Ae}=\text{Sr}, \text{Ba}$) compounds. In the present work, the aim is fixed to calculate the ground state crystal energy and from this the equilibrium lattice parameters, unit cell volume, bulk modulus, elastic constants, band structure, total and partial density of states are evaluated. The optical properties (such as dielectric function, refractive index, extinction coefficient, absorption spectrum, energy loss function, reflectivity and photoconductivity), thermodynamic properties (such as bulk modulus, Debye temperature, specific heats and volumetric thermal expansion coefficient) and thermoelectric properties (such as Seebeck coefficient, electric conductivity, and thermal conductivity) are also calculated.

V.2 Ground State Energy

For structure optimization one searches for the equilibrium positions corresponding to the lowest energy. This is done by performing an iterative process in which the coordinates of the atoms and possibly the parameters of the cell are adjusted so that the total energy of the structure is minimized with respect to the positions of the nuclei. This total minimum energy is the energy of the ground state of the system. The structure optimization makes it possible to obtain a stable structure. Virtually all effective minimization techniques based on knowledge of the forces applied to each nucleus, since the equilibrium position is found when all the forces disappear. The physical force acting on an ion is simply the classical electrostatic force due to electrons and other nuclei. The force acting on an ion can be given using the Hellman-Feynman theorem [1] which states that the ionic forces can be directly calculated taking the partial derivative of the total energy of the system with respect to the positions of ions:

$$F_I = - \frac{dE}{dR_I} \quad (\text{V. 1})$$

For numerical reasons, the knowledge of the forces helps significantly, since finding the equilibrium position of an atom, for which the forces vanish, often can be easier than looking for the total energy minimum.

V.3 Elastic constants

Elastic constants of a material describe its response to an externally applied stress and play an important role in providing valuable information on the bonding characteristic between

adjacent atomic planes, anisotropy and hardness, and so on. [2]. If a crystal is subjected to a very small mechanical stress, the balance of the inter-particle forces gets disturbed and as a result, lattice spacing changes. Macroscopic changes in lattice spacing manifest themselves as elastic deformations described by a strain tensor.

In the theory of linear elasticity, the studied material is supposed to be homogeneous. Likewise, the applied stress as well as resultant strain are also assumed to be uniform.

Elastic deformation involves a temporary change in an object's shape or size, which self-reverses after force is no longer exerted on it (the elastic deformation is a reversible deformation)

An elastic material regains its original shape and size when the deforming force (stress tensors) is no longer exerted up to a specific limit, called the 'elastic limit' of the solid. If a material is loaded beyond its elastic limit, the material will remain in a deformed condition after the deforming force is removed. At larger deformations, elasticity becomes non-linear for some materials.

The most general linear relationship, which connects stress to strain, is provided by the generalized version of the well-known Hooke's law [3].

$$\sigma_{ij} = C_{ijkl}\varepsilon_{kl} \quad (\text{V. 2})$$

Where ε_{kl} is the strain tensor, σ_{ij} the stress tensor, the C_{ijkl} are the elastic moduli (usually called "elastic constants", although in fact variable according to the conditions to which the studied solid is subjected [4])

By reversing equation (V.2), the strain can be expressed in terms of the stress as follows:
of the stress components

$$\varepsilon_{ij} = S_{ijkl}\sigma_{kl} \quad (\text{V. 3})$$

Where S_{ijkl} are the deformability coefficients.

The tensor C_{ijkl} contains 81 elastic constants; the number of independent coefficients is reduced to 21 because of the symmetry [5]. Taking into account additional symmetry arguments imposed by the crystal lattice, the number of elastic constants decreases further.

Generally, there are two approaches for calculating monocrystalline elastic constants from ab-initio methods [6, 7]: the energy-strain approach and the stress-strain approach. The stress-based method is more efficient than the energy-based method.

V.4 Diagram of band structure and density of states

V.4.1 Electronic band structure

In solid-state physics, the electronic band structure of a material describes the range of energy that an electron is forbidden or allowed to have. In principle, the number of bands is large, generally infinite, but only the lowest are occupied by electrons. The filling of the energy levels at $T = 0$ follows Pauli's principle, starting with the lowest energy states which, according to the Fermi-Dirac statistics. The lower filled bands are called the valence band and they are occupied with certainty. The upper empty bands represent the conduction band. The different bands are well separated from each other and each band comes from a well-determined atomic level. The two permitted energy bands are separated by a band of forbidden energy (the gap) that appears at the edges of the Brillouin zone.

A complete knowledge of the band structure requires the solution of the Kohn-Sham equations for each vector k of the primitive cell of the reciprocal lattice (or the Brillouin zone) and must be represented in the different directions of the wave vector k in the reciprocal space. In practice, we represent the energies of the valence band and the conduction band between points of high symmetry in the different directions of the wave vector k in the Brillouin zone.

From the structure of the band and the number of electrons filling the bands, one can predict the type of material that one has:

- If the valence band is completely filled, the conduction band is empty, and the width of the forbidden band is of the order of several eV, one has an insulator. Semiconductors translate in the same way, except that the forbidden band is smaller. Insulators and semiconductors having their Fermi level in a forbidden band.
- If the Fermi level is in a permissible band but in a region of low density of states, one has semi-metals. The properties of these conductors are quite special; this is the case, for example, of bismuth (Bi).
- We have a metal, if the width of the forbidden band is zero, then, there is an overlap between the conduction band and the valence band. Thus, the conduction band is partially filled with free electrons that come from the valence band. In this case, the Fermi level is within a permitted band.

The fundamental band gap (the gap of an interacting system) is defined as the difference between the ionization energy and electron affinity [8]. The ionization potential is the energy

necessary to transfer an electron from the top of the valence band to the vacuum level energy. Similarly, the electron affinity is introduced as the energy difference between the vacuum energy level and the bottom of the conduction band. In the calculation DFT, the energy gap is defined as the difference between the highest occupied state and the lowest unoccupied state:

$$E_{gap}^{DFT} = [\varepsilon_{BC}(k)]_{min} - [\varepsilon_{BV}(k)]_{max} \quad (V.4)$$

However, the eigenvalues obtained from Kohn-Sham equation do not have the physical meaning with the exception of the last occupied level, which coincides with the exact ionization-energy of the system as shown by Janak's theorem [9]. The density functional theory (DFT) calculations provide the structure of the band without account for electron-electron interactions. Sham and Schlüter [10] and Perdew and Levy [11] have shown that the gap obtained by a DFT calculation (which is commonly known as the gap energy of the DFT) does not coincide with the gap of an interacting system. It is often a bad approximation of the electronic band structure observed in the experiments. Generally, a DFT calculation systematically underestimates the band gap in semiconductors. An extreme case is germanium; whose experimental bandgap is 0.7 eV [12] whereas the LDA predicts that it is metallic [13]. In the case of diamond, the LDA gives a direct band gap of 5.5 eV [14] against 7.3 eV experimentally [15, 16]. Other problems, for example with Mott-Hubbard insulators and magnetic materials, reduce the range of systems for which the LDA can make useful predictions. Typically, the DFT calculation underestimates the energy gaps of the solids from 30% to 100% compared to the experiment [13, 17, 18]. This comes from the use of formula (V.4) to calculate the gap. The energy of the forbidden band calculated from the eigenvalues obtained from Kohn-Sham equation differs from the real gap energy by a term Δ called "discontinuity of the exchange-correlation potential" [19, 20]. Moreover, the calculated energy dispersions $\varepsilon(k)$ within the BV and the BC are often found to be in good agreement with the experimental.

V.4.2 Density of electronic states

In the physics of the solid state and condensed matter, the electronic density of the states of a system is defined the number of electronic states per unit volume of the solid, per unit energy in the range $[E, E + dE]$ [21]. The DOS shows both the occupied and unoccupied available states, a high DOS at a specific energy level means that there are many states available for occupation. A DOS of zero means that no state can be occupied at this energy level.

The density of the states for a given band n , $N_n(E)$, is given in three dimensions by:

$$N_n(E) = 2 \int \frac{d^3k}{(2\pi/L)^3} \delta(E - E_n(k)) \quad (\text{V. 5})$$

Where $(2\pi/L)^3$ is the volume of space k for a state. Factor 2 concerns the spin degeneracy, $E_n(k)$ describes the dispersion of the given band and the integral is carried on the first Brillouin zone and selects only the states that are at E .

The total energy density of the states, $N(E)$, is obtained by summation over all bands

$$N(E) = \sum N_n(E) = \sum \int \frac{d^3k}{4\pi^3} \delta(E - E_n(k)) \quad (\text{V. 6})$$

DOS is often used for a quick visual analysis of the electronic structure. Characteristics such as the width of the valence band, the energy gap and the number and intensity of the main features are helpful in qualitatively interpreting experimental spectroscopic data. The importance of the density of states can be found also in the calculation of the speed of any process in a solid, from the diffusion of an electron to the absorption and emission of light.

The contributions of the individual orbitals can be calculated (partial DOS) to reveal information on which the orbitals are occupied or involved in bonding. This also gives the Fermi level (E_F) at 0 K, or the electrochemical potential, which is defined at the thermodynamic equilibrium as the energy level with a 50% probability of being filled (i.e. halfway between the conduction and valence bands). PDOS calculations are based on Mulliken population analysis, which allows the contribution from each energy band to a given atomic orbital to be calculated. The summation of these contributions over all bands produces a weighted DOS. But, only the valence band and lower part of the conduction band are meaningful in the PDOS plot.

V.5 Optical properties

The optical properties of solids relate to the interaction of solids with electromagnetic radiation whose wavelength is in the infrared to the ultraviolet. When electromagnetic radiation interacts with matter, it affects, with its oscillating electromagnetic field, the charges in the material, exchanging energy with that material. From a macroscopic point of view, when light impinges on matter, it can be scattered (elastically or inelastically), absorbed, or transmitted. The interaction depends on the physical, chemical and structural properties of the matter, as well as the intensity and energy of the photons. The optical properties of solids are an important tool to understand the main fundamental physical properties such as electronic structure, recombination mechanisms, impurity levels, excitons, localized defects, lattice vibrations and certain magnetic excitations.

In the linear response range, the optical properties of a matter can be characterized by an understanding of response functions such as the complex dielectric coefficient $\varepsilon(\omega) = \varepsilon_1(\omega) + i\varepsilon_2(\omega)$ [22], with $\varepsilon_2(\omega)$ is the imaginary component of the complex dielectric coefficient, it relate to absorption and describes the energy losses that occur in a medium due to electronic transitions. The imaginary component of the complex dielectric coefficient can be calculated with the momentum matrix elements between the occupied and unoccupied wave functions within the selection rules [23]:

$$\varepsilon_2(\omega) = \frac{2e^2\pi}{\Omega\varepsilon_0} \sum_{k,v,c} |\langle \psi_k^c | u \cdot r | \psi_k^v \rangle|^2 \delta(E_k^c - E_k^v - E) \quad (V. 7)$$

Where ω is the light frequency, e is the electronic charge, u is the vector defining the polarization of the incident electric field, $\langle \psi_k^c |$ and $|\psi_k^v \rangle$ are the conduction and valence band wave functions at k , respectively.

$\varepsilon_1(\omega)$ is the real part of the dielectric function and it can be calculated by Kramer-Kroning relations [24].

$$\varepsilon_1(\omega) = 1 + \frac{2}{\pi} P \int_0^\infty \frac{\omega' \varepsilon_2(\omega')}{\omega'^2 - \omega^2} d\omega' \quad (V. 8)$$

Where P represents the main integral.

All other optical constants on the energy dependence of the absorption spectrum can be derived from $\varepsilon_2(\omega)$ and $\varepsilon_1(\omega)$. This includes the refractive index, the extinction coefficient, the energy-loss spectrum, and the reflectivity.

The complex refractive index is related to the complex dielectric function via:

$$N(\omega) = \sqrt{\varepsilon(\omega)} \quad (V. 9)$$

Given that $N(\omega)$ is written as:

$$N(\omega) = n(\omega) + ik(\omega) \quad (V. 10)$$

Where $n(\omega)$ is the refractive index, and $k(\omega)$ the extinction coefficient.

The real and imaginary components of both the refractive index and the dielectric function are therefore related by:

$$n(\omega) = \frac{1}{\sqrt{2}} [(\varepsilon_1^2(\omega) + \varepsilon_2^2(\omega))^{1/2} + \varepsilon_1(\omega)]^{1/2} \quad (V. 11)$$

$$k(\omega) = \frac{1}{\sqrt{2}} \left[(\varepsilon_1^2(\omega) + \varepsilon_2^2(\omega))^{1/2} - \varepsilon_1(\omega) \right] \quad (V. 12)$$

The remaining optical properties, such as optical absorption $\alpha(\omega)$, the energy loss function $L(\omega)$, the real part of the optical conductivity $\sigma(\omega)$ and the reflectivity $R(\omega)$ are calculated from $\varepsilon_1(\omega)$ and $\varepsilon_2(\omega)$ as follows:

$$\alpha(\omega) = \sqrt{2}\omega [(\varepsilon_1^2(\omega) + \varepsilon_2^2(\omega))^{1/2} + \varepsilon_1(\omega)]^{1/2} \quad (V. 13)$$

$$L(\omega) = \frac{\varepsilon_2(\omega)}{[(\varepsilon_1^2(\omega) + \varepsilon_2^2(\omega))]} \quad (\text{V. 14})$$

$$\sigma(\omega) = \frac{\omega \varepsilon_2}{4\pi} \quad (\text{V. 15})$$

$$R(\omega) = \left| \frac{(\varepsilon_1(\omega) + i\varepsilon_2(\omega))^{1/2} - 1}{(\varepsilon_1(\omega) + i\varepsilon_2(\omega))^{1/2} + 1} \right|^2 \quad (\text{V. 16})$$

V.6 The Thermodynamic properties

Thermodynamic properties are observable characteristics of the thermodynamic system. Pressure, temperature, volume, viscosity, modulus of elasticity etc. are the examples of property. All thermodynamic quantities of a crystal can be obtained from the vibrational density of states, $g(\omega)$. This function gives the number of normal modes of vibration between ω and $\omega + d\omega$. In equilibrium, at finite temperatures, the atoms are not exactly at their equilibrium positions, they oscillate around their position. The energy of a vibration is quantized and the quantum of vibration is called a phonon (in analogy with the photon). As the temperature is increased, more and more thermal energy is injected into the crystal, the kinetic energy of atoms increases and the atoms vibrate with greater and greater amplitude. As the amplitude of atomic oscillations increases, so does the average separation between the atoms and thus thermal expansion, i.e., the vibrational origin of thermal expansion.

Theoretically, to understand this situation, one can take a potential that is a function of atomic positions. If we take the harmonic potential model where the vibrations of the atoms are represented as a set of harmonic oscillator, we can expand the potential energy of interaction between the atoms to give an expression, which is quadratic in the atomic displacements from their equilibrium positions. In this case, the lattice vibrations will be independent of the interatomic distance and there will be no lattice expansion due to the symmetrical displacements of the atoms around their equilibrium positions. Thus means that the vibrational energy does not depend on the volume and that there is therefore no relation between the temperature and the geometry of the system (volume). Currently, nothing depends on temperature, since temperature is not at all included in the harmonic approximation.

To overcome this deficiency, one must introduce an interdependence between T and V in the model, this can be obtained only from the anharmonic lattice potential models, but this is not a reasonable task. A simple way to take some anharmonic effects into account for calculations of the free energy is the Quasiharmonic Approximation, which has been successfully applied to study the thermodynamic properties of several materials [25-27]. The Quasiharmonic approximation assumes harmonic vibrations, at positions different from the

equilibrium positions and it uses the harmonic partition function but it assumes that the frequencies depend on a global static constraint X , usually the volume.

This model allows us to obtain all the thermodynamics quantities from the calculated energy-volume points, in which the non-equilibrium Gibbs function $G^*(V; P; T)$ is expressed as follows [28]:

$$G^*(V; P, T) = E(V) + PV + A_{Vib}(\Theta(V); T) \quad (V. 17)$$

where $E(V)$ is the total energy per unit cell, PV is the constant hydrostatic pressure condition, A_{Vib} is the vibrational Helmholtz free energy, and $\Theta(V)$ is the Debye temperature.

According to the quasi-harmonic Debye model of the phonon density of states, one can write [29, 30]:

$$A_{Vib}(\Theta(V); T) = nkT \left[\frac{9}{8} \frac{\theta_D}{T} + 3 \ln \left(1 - \exp \left(-\frac{\theta_D}{T} \right) \right) - D \left(\frac{\theta_D}{T} \right) \right] \quad (V. 18)$$

Where θ_D is the Debye temperature, n is the number of atoms per formula unit, $D \left(\frac{\theta_D}{T} \right)$ represents the Debye integral, which is defined as:

$$D \left(\frac{\theta_D}{T} \right) = \frac{3}{(\theta_D/T)^3} \int_0^{\theta_D/T} \frac{x^3}{e^x - 1} dx \quad (V. 19)$$

For an isotropic solid with a Poisson ratio σ , the characteristic Debye temperature θ_D can be expressed as:

$$\theta_D = \frac{\hbar}{k} \left[6\pi^2 V^{\frac{1}{2}} n \right]^{\frac{1}{3}} f(\sigma) \sqrt{\frac{B_S}{M}} \quad (V. 20)$$

Where M is the molecular mass per unit of formula, B_S is the adiabatic bulk modulus measuring the compressibility of the crystal for fixed quantum state populations and can be approximated by the static compressibility:

$$B_S \approx B(V) = V \left(\frac{d^2 E(V)}{dV^2} \right) \quad (V. 21)$$

and the $f(\sigma)$ is defined as [25, 26]:

$$f(\sigma) = \left\{ 3 \left[2 \left(\frac{2}{3} \frac{1+\sigma}{1-2\sigma} \right)^{3/2} + \left(\frac{1}{3} \frac{1+\sigma}{1-\sigma} \right)^{3/2} \right]^{-1} \right\}^{1/3} \quad (V. 22)$$

Consequently, the non-equilibrium Gibbs function $G^*(V; P, T)$ as a function of $(V; P, T)$ can be minimized with respect to volume V as:

$$\left(\frac{\partial G^*(V; P, T)}{\partial V} \right)_{P, T} = 0 \quad (V. 23)$$

By solving equation (IV.23), one can obtain the thermal equation of the state (EOS) $V(P, T)$. Then, the isothermal bulk modulus B_T , the constant-volume heat capacity C_V , the constant-pressure heat capacity C_P , and the volumetric thermal expansion α_V , can be derived as

$$B_T(P, T) = V \left(\frac{\partial^2 G^*(V; P, T)}{\partial V^2} \right) \quad (\text{V.24})$$

$$C_V = 3nk \left[4D(\theta_D/T) - \frac{3\theta_D/T}{\exp(\theta_D/T)-1} \right] \quad (\text{V.25})$$

$$C_P = C_V(1 + \alpha\gamma T) \quad (\text{V.26})$$

$$\alpha_V = \frac{\gamma C_V}{B_T V} \quad (\text{V.27})$$

Where γ is the Grüneisen parameter, which is defined as:

$$\gamma = - \frac{d \ln \Theta(V)}{d \ln V} \quad (\text{V.28})$$

V.7 Thermoelectric proprieties

V.7.1 The Seebeck effect

The Seebeck effect, is the rise of an electromotive force in a thermocouple, under zero electric current, on other words, it is the conversion of a temperature difference into an electric current. The Seebeck effect was discovered in 1821 by Thomas Johann Seebeck who found that when two dissimilar materials are joined together via two junctions in an open circuit and these junctions between the materials are held at the same time at different temperatures ΔT , an electrical potential difference could be generated across the junctions between them [31, 32], as shown in Figure V.1. The generated voltage ΔV is directly related to the temperature difference ΔT by a proportionality coefficient, which is best known as Seebeck coefficient:

$$V = S_{AB} \Delta T \quad (\text{V.29})$$

Where S_{AB} is the relative Seebeck coefficient which is given by the difference between the absolute Seebeck coefficients S_A and S_B of the individual materials A and B by [33] :

$$S_{AB} = S_B - S_A \quad (\text{V.30})$$

The Seebeck coefficient has units of $V.K^{-1}$ and its magnitude varies with material and temperature of operation. In materials where dominant charge carriers are holes (p-type), the Seebeck coefficient has a positive sign, whereas a negative Seebeck coefficient results in electrons being the dominant charge carriers (n-type).

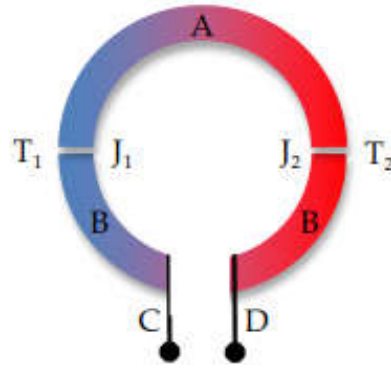


Figure V.1: An open circuit that displays the Seebeck effect; A and B are two dissimilar conductors. The terminals C and D are assumed to be at the same temperature, J_1 and J_2 are junctions held at two different temperatures, T_1 and T_2 , resulting in the formation of a voltage across points C and D. (Figure adopted from [34])

V.7.2 The Peltier effect

In 1834, the second thermoelectric effect was discovered by Jean-Charles Peltier; it is called the Peltier effect [34, 35]. This effect is the conversion of electricity into heat transfer, which can be regarded as the reverse phenomenon of the Seebeck effect. Jean Peltier discovered that when current flows across a junction connecting two dissimilar materials maintained at the same temperature, a certain amount of heat could be emitted at one junction and absorbed at the other junction, depending on the direction of the current (If the direction of the current is reversed, the heat output and input occur at the opposite junctions). This is because an isothermal electric current in a metal is accompanied by a thermal current.

Peltier effects occur only at junctions between dissimilar conductors, it is quite different from Joule heating, where electrons energy is loss through scattering with the lattice. In contrast to Peltier effect, Joule heat occurs along the length of the conductor and does not require a junction of dissimilar materials.

The rate of heat liberated or absorbed is proportional to the electric current induced in a sample by a weak electric field with the proportionality coefficient that was subsequently named after J. Peltier.

For a circuit made up of two dissimilar materials A and B the heat liberated or absorbed at the junction is given by [36]:

$$Q = \Pi_{AB}I \quad (\text{V.31})$$

Where I is the electrical current and Π_{AB} is the relative Peltier coefficient of the junction between two conductors. The relative Peltier coefficient is given by the difference between the absolute Peltier coefficients Π_A and Π_B of the individual materials A and B by

$$\Pi_{AB} = (\Pi_A - \Pi_B) \quad (\text{V.32})$$

The Peltier coefficient is related with the Seebeck coefficient or the thermopower by the first Thomson (Kelvin) relation

$$\Pi = ST \quad (\text{V.33})$$

Where T denotes the absolute temperature. The origin of the Peltier effect resides in the transport of heat by an electric current as is shown in [Figure. V.2](#).

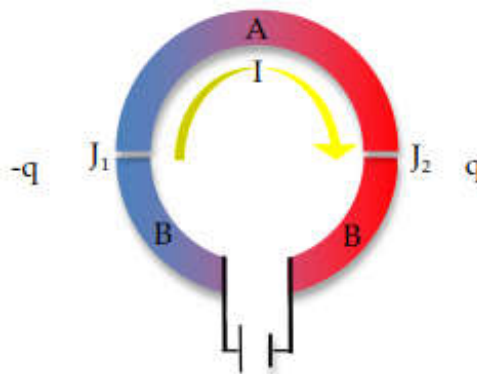


Figure V.2 Schematic representation of the Peltier effect; A and B are two dissimilar materials. Under the conditions of no temperature gradient ($\nabla T = 0$), A current I passes through materials A and B causing the absorption and release of heat Q . The rate of cooling $-q$ occurs at J_1 while heating q occurs at J_2 . (Figure adopted from [34]).

V.7.3 The Thomson effect

The third thermoelectric effect was predicted in 1854 and found experimentally in 1856 by Thomson [37]. By applying the first and second laws of thermodynamics to a reversible thermoelectric circuit Thomson could establish a relationship between the Seebeck and Peltier effects and predicting a third thermoelectric effect which is called the Thomson effect. In the Thomson effect, heat is absorbed or produced in a wire of single homogeneous material having a temperature gradient along its length and exposed to a difference in voltage. The main difference with the Peltier and Seebeck effects is that the Thomson effect involves only one material and no junction is required. The Thomson effect can occur even in the same solid if the Seebeck coefficient depends on temperature, balancing for the flowing Peltier heat. The generation or absorption of heat depending on the direction of current and on the nature of the

material; if the direction of current is reversed, the Thomson effect also changes sign (contrary to the Joule heating effect).

The heat generated by the Thomson effect is called the Thomson heat. It was found that the Thomson heat in the material is proportional to the electrical current and the temperature gradient through a proportionality coefficient (Thomson coefficient):

$$Q_T = \beta I \Delta T \quad (\text{V. 34})$$

Where β is the Thomson coefficient of material in units (V.K^{-1}), I is the current, which passes through the materials, and ΔT is change in temperature.

V.7.4 The Boltzmann transport Equation

The classical theory of transport processes is based on the Boltzmann transport Equation, which arises from considering what can happen to a collection of particles as they flow through a volume of phase space. A single particle is identified by its three spatial coordinates and three momentum values.

The Boltzmann theory introduces the so-called transport distribution function, which describes the carrier density at a point r , with a particular momentum $p = \hbar k$ and at a certain time t .

In absence of any external force at equilibrium, the electrons (Fermions) adopt the Fermi-Dirac distribution (Equation V.35):

$$f_0(\epsilon, T) = \frac{1}{1 + e^{(\epsilon_k - \mu)/k_B T}} \quad (\text{V. 35})$$

Where ϵ_k is the quasi-particle energy, μ is the chemical potential, k_B is the Boltzmann constant and T is the temperature.

For our transport problem, we want to describe a non-equilibrium distribution function since transport is an inherently non-equilibrium problem.

The distribution function $f(r, k, t)$ of electrons with a wave vector k at the position r at time t can vary due to the following three distinct physical processes namely,

(a) Due to Diffusion associated with temperature gradients or concentration gradients, carriers can move from one region of space to another.

(b) Due to the influence of external fields, carriers are accelerated and their wave vector is affected, according to $\hbar dk/dt = F_{ext}$

(c) Due to scattering processes, electrons will change their momentum states from one k -state to another, this motion is not included in the Fermi-Dirac function.

The variation in time of the total distribution can be expressed as the sum of these three contributions:

$$\frac{\partial f}{\partial t} = \left(\frac{\partial f}{\partial t}\right)_{diff} + \left(\frac{\partial f}{\partial t}\right)_{field} + \left(\frac{\partial f}{\partial t}\right)_{scat} \quad (V.36)$$

In order to find an explicit form of the Boltzmann equation, we shall consider these processes separately by evaluating the partial time derivative of the function $f(r, k, t)$ due to each source.

i. Diffusion-Induced Evolution of $f(r, k, t)$

First of all, one can consider an electron is not subject to scattering but experiences an external perturbation (concentration gradient, temperature gradients). In the presence of a temperature or concentration gradient, diffusion takes place in the conductor, therefore the carriers will be moving into and out of any volume element around r .

If v_k is the velocity of a carrier in the state k , in a time interval Δt , the electron moves a distance $\Delta r = v(k)\Delta t$. In accordance with the Liouville theorem on the invariance of the volume occupied in phase space [38- 42], the number of carriers in the region of the point r at time t must equal to their number in the region of the point $r + v(k)\Delta t$ at time $t + \Delta t$, i.e.,

$$f(r, k, t) = f(r + \Delta r, k, t + \Delta t) \quad (V.37)$$

By taking the Taylor expansion up to first order of the right-hand side close to r , inserting

$\Delta r = v(k)\Delta t$ and making $\Delta t \rightarrow 0$ we obtain:

$$\left(\frac{\partial f}{\partial t}\right)_{diff} = -v(k)\frac{\partial f}{\partial r} = -v(k)\nabla_r f \quad (V.38)$$

ii. External Field-Induced Evolution of $f(r, k, t)$

When external force F are applied to the sample, the crystal momentum k of the electron evolves under the action of external forces, according to the semiclassical dynamics of carriers, their momentum is expressed as:

$$F = \hbar \frac{dk}{dt}. \quad (V.39)$$

If the same considerations as for the diffusion term are used for the k -space, we can argue that particles at time t with momentum k will have momentum $k + \Delta k$ at time $t + \Delta t$.

$$f(r, k, t) = f(r, k + \Delta k, t + \Delta t) \quad (V.40)$$

Which leads to

$$\left(\frac{\partial f}{\partial t}\right)_{field} = -\frac{\partial k}{\partial t} \cdot \frac{\partial f}{\partial k} = -\hbar^{-1} F \nabla_k f \quad (V.41)$$

iii. Scattering-Induced Evolution of $f(r, k, t)$

In the absence of collisions, the probability to find the particle in such trajectory remains constant with time. It is therefore can be written [41]:

$$f(r, k, t) = f(r + \Delta r, k + \Delta k, t + \Delta t) \quad (V.42)$$

However, collisions cannot be neglected because they significantly change the population of carriers. During the motion, electrons may also be scattered to or from r and k in time dt . Under steady-state conditions, there will be no net change in the distribution function because the changes due to diffusion and acceleration have to be in equilibrium with the changes of the distribution function through scattering,

According to the Liouville theorem on the invariance of the phase space volume, an additional term must be added to the equation (V.42). If we express the change in f due to scattering by the term $\left[\frac{\partial f}{\partial t}\right]_{Coll}$, it can be found that [41] :

$$f\left(r + vdt, k + \frac{F}{\hbar} dt, t + dt\right) \equiv f(r, k, t) + \left[\frac{\partial f}{\partial t}\right]_{Coll} dt \quad (V.43)$$

The left member of Eq. (V.43) can be expanded in Taylor series up to first order, and we obtain the Boltzmann equation

$$\nabla_r f \cdot v + \nabla_k f \frac{F}{\hbar} + \frac{\partial f}{\partial t} = \left[\frac{\partial f}{\partial t}\right]_{Coll} \quad (V.44)$$

V.7.5 The relaxation time

In its most general form, the Boltzmann equation (V.44) is a complicated equation for determining the non-equilibrium distribution $f(r, k, t)$. In particular, it requires the evaluation of scattering mechanisms, which are rendering the equation a non-linear integro-differential equation of a complicated kind [38,43]. A simple approach to the solution is that of using the relaxation time approximation, which is a plausible postulate for many problems. The central assumption of this approximation is the existence of a relaxation time τ governed the relaxation of the system to equilibrium when the external fields or thermal gradients are switched off. The relaxation time characterizes the velocity of recovery of the equilibrium state: for a short relaxation time, many scatterings help the system to relax toward equilibrium and conversely for a long relaxation time.

Within the relaxation time approximation, it is assumed that the scattering term, which will bring the system to equilibrium, is proportional to the deviation of the distribution function from its equilibrium value

$$\left(\frac{\partial f}{\partial t}\right)_s = -\frac{f(k) - f_0(k)}{\tau(k)} \quad (V.45)$$

Where $f_0(k)$ is the equilibrium distribution, $f(k)$ is the non-equilibrium distribution before the collision.

Integrating (V.45) gives:

$$f - f_0 = Ae^{-t/\tau} \quad (\text{V. 46})$$

Which simply says that in the absence of external perturbations, any system will reach its equilibrium value when t becomes infinite. The relaxation time approximation is valid only for the elastic-scattering case, which requires that the change of electron energy before and after each scattering process must be small compared to the energy of electrons. Moreover, the scattering is considered to occur instantaneously. In other words, upon scattering electrons change their state k but not their position r .

By the combination of equations (V.44) and (V.45), we get the Boltzmann transport equation with the collision term within the relaxation time approximation:

$$\nabla_r f \cdot v + \nabla_k f \frac{F}{\hbar} + \frac{\partial f}{\partial t} = -\frac{f-f_0}{\tau} \quad (\text{V. 47})$$

We obtain the following simple form of the stationary Boltzmann equation in the absence of a magnetic field,

$$\nabla_r f \cdot v - \nabla_k f \frac{eE}{\hbar} + \frac{\partial f}{\partial t} = -\frac{f-f_0}{\tau} \quad (\text{V. 48})$$

Thus, by using the notion of relaxation time the integro-differential Equation (V.44) can be formally reduced to the differential Equation (V.48) for the nonequilibrium distribution function $f(r, k)$.

Further considerable simplification of the transport problem is achieved by linearized Boltzmann equation, which is done simply by replacing the steady-state carrier distribution in the gradient $\nabla_r f(r, k, t)$ and $\nabla_k f(r, k, t)$ to the equilibrium distribution function as $\nabla_r f_0(r, k)$ and $\nabla_k f_0(r, k)$ [41]:

$$f(k) = f_0(\epsilon_k) + \left(-\frac{\partial f_0}{\partial \epsilon}\right) \tau v_k \left[eE + \frac{\epsilon - \mu}{T} (-\nabla T)\right] \quad (\text{V. 49})$$

V.7.6 The transport coefficients

The various transport coefficients that govern the thermopower, electric and thermal conductivity can be expressed in terms the electrical current j or thermal current J_Q . These "currents" arise due to external fields such as an electric field and temperature gradient which are referred to as "forces". At macroscopic level and within the linear response regime, the electric current density components J and the thermal current components j_Q are related to the electric field components E and the temperature gradient components ΔT in the following way [44]:

$$J = \sigma E - S\sigma \Delta T \quad (\text{V. 50})$$

$$j_Q = S\sigma E - \kappa\Delta T \quad (\text{V. 51})$$

Where σ is the electrical conductivity, S is the Seebeck coefficient and κ is the thermal conductivity.

To evaluate these transport coefficients, it is customary to introduce both the electrical current J_e and the thermal current density J_Q in terms of microscopic variables.

At microscopic level, the electric current density and the thermal current density are written as:

$$J_e = \frac{2e}{8\pi^3} \int v_k f_k dk \quad (\text{V. 52})$$

$$J_Q = \frac{2}{8\pi^3} \int v_k (\epsilon_k - \mu) f_k dk \quad (\text{V. 53})$$

where e is the charge of the carriers, v_k is the group velocity associated with state k , which can be found from the slope of the dispersion relation $E(k)$ at k : $v_k = \frac{1}{\hbar} \frac{\partial \epsilon_k}{\partial k}$, μ is the chemical potential and f_k it is the population of the quantum state labeled with k . The analytical expression of the distribution function is given by the solution of the Boltzmann transport theory.

Substituting the perturbed distribution function in Eq. (V.49) into Equations (V.52) and (V.53) causes the integral containing the equilibrium distribution to vanish because there can be no flow of charge or heat when $f = f_0$. The remaining terms are:

$$J_e = \frac{2e}{8\pi^3} \int v_k v_k \tau \left(-\frac{\partial f_0}{\partial \epsilon} \right) \left[eE + \frac{\epsilon - \mu}{T} (-\nabla T) \right] dk \quad (\text{V. 54})$$

$$J_Q = \frac{2}{8\pi^3} \int v_k v_k \tau \left(-\frac{\partial f_0}{\partial \epsilon} \right) \left[eE + \frac{\epsilon - \mu}{T} (-\nabla T) \right] (\epsilon - \mu) dk \quad (\text{V. 55})$$

Defining now the integral:

$$K_n = \frac{2}{8\pi^3} \int v_k v_k \tau \left(-\frac{\partial f_0}{\partial \epsilon} \right) (\epsilon - \mu)^n dk \quad (\text{V. 56})$$

we can express Equations. (V.54) and (V.55) in terms of K_n as:

$$J_e = e^2 K_0 E + \frac{e}{T} K_1 (-\nabla T) \quad (\text{V. 57})$$

$$J_Q = e K_1 E - \frac{e}{T} K_2 \Delta T \quad (\text{V. 58})$$

The above equations serve to define transport coefficients in zero magnetic, let us begin with the conductivity tensor.

V.7.6.1 Electrical conductivity

In general terms, the electrical conductivity, σ , is a measure of how well a system conducts electrons due to an applied electric field. In absence of magnetic field and temperature

gradients, the distribution function is given by just the field streaming term and the scattering term as:

$$f(k) = f_0(\epsilon_k) + e \left(-\frac{\partial f_0}{\partial \epsilon} \right) \tau_k v_k E \quad (\text{V. 59})$$

Then, the equation (V. 57) become:

$$J_e = \frac{2e}{8\pi^3} \int v_k v_k \tau \left(-\frac{\partial f_0}{\partial \epsilon} \right) e E dk = e^2 K_0 E \quad (\text{V. 60})$$

From equation (V.50), it is easy to see that in the absence of a gradient of temperature, the macroscopic expression of the electrical current is reduced to its electric field contribution

$J = \sigma E$, therefore, the electrical conductivity can then be expressed as [41]:

$$\sigma = e^2 K_0 = \frac{e^2}{4\pi^3} \int v_k v_k \tau \left(-\frac{\partial f_0}{\partial \epsilon} \right) dk \quad (\text{V. 61})$$

V.7.6.2 Seebeck coefficient

The Seebeck coefficient is one of the key quantities of thermoelectric materials. The Seebeck coefficient of a material is a measure of the magnitude of an induced thermoelectric voltage in response to a temperature difference across that material, as induced by the Seebeck effect. Under conditions of zero current flow through the sample ($j=0$), we can found[41] :

$$S = \frac{1}{eT} \frac{K_1}{K_0} = \frac{1}{eT} \frac{\int v_k^2 \tau \left(-\frac{\partial f_0}{\partial \epsilon} \right) (\epsilon - \mu) dk}{\int v_k^2 \tau \left(-\frac{\partial f_0}{\partial \epsilon} \right) dk} \quad (\text{V. 62})$$

V.7.6.3 The thermal conductivity

The thermal conductivity κ is a measure of the rate at which heat flows through a sample when its two ends are held at different temperatures and it has two contributions.

$$\kappa = \kappa_e + \kappa_L \quad (\text{V. 63})$$

Here, κ_e is called the electron thermal conductivity and κ_L is called the lattice thermal conductivity. κ_e is due to a charge carrier flux and κ_L is due to a phonon flux through the lattice. In order to estimate the electronic contribution to the thermal conductivity, we now consider that the sample is electrically insulated to prevent any electric current flowing through it and a thermal gradient ∇T is maintained. Thus, we set the current $J_e = 0$ in Eq. (V.57) and express an electric field in terms of a thermal gradient:

$$E = \frac{K_0^{-1} K_1}{eT} \nabla T \quad (\text{V. 64})$$

Substituting Eq. (V.64) into Eq. (V.58) yields

$$j_Q = \frac{1}{T} [K_2 - K_1 K_0^{-1} K_1] (-\nabla T) \quad (\text{V. 65})$$

Macroscopically, heat conduction in a solid is governed by the Fourier law:

$$j_Q = -\kappa \nabla T \quad (\text{V. 66})$$

So, that from Eq. (V.65) and (V.66) one gets

$$\kappa = \frac{1}{T} [K_2 - K_1 K_0^{-1} K_1] \quad (\text{V. 67})$$

The second term in (V.67) is often negligible as compared to the first one and in this case, the thermal conductivity is therefore [41]:

$$\kappa = \frac{K_2}{T} = \frac{2}{8\pi^3 T} \int v_k v_k \tau \left(-\frac{\partial f_0}{\partial \epsilon} \right) (\epsilon - \mu)^2 dk \quad (\text{V. 68})$$

V.7.6.4 The Figure of merit

In principle, the thermoelectric effect is present in all materials, but only few are suitable and only those comprise the material group of thermoelectric. The efficiency of a thermoelectric depends on the transport coefficients of the material. Already in 1909 and 1911, Altenkirch was showed that good thermoelectric materials must have a high electrical conductivity, to ensure high carrier mobility, a low thermal conductivity to retain heat at the junctions and maintain a large temperature gradient, which helps to generate a large voltage and a high Seebeck coefficient for maximum conversion of heat to electrical power (or electrical power to cooling performance) [45, 46]. These requirements are summarized in what is called the Figure of merit (FOM) ZT [47]:

$$ZT = \frac{S^2 \sigma}{\kappa_e + \kappa_L} T \quad (\text{V. 69})$$

Where T is the temperature, S the Seebeck coefficient, σ the electrical conductivity, κ_L the lattice thermal conductivity and κ_e the electronic part of the thermal conductivity. The larger the figure of merit, the better the efficiency of the thermoelectric cooler or power generator.

It is obvious that a higher ZT is obtained by decreasing the denominator or by increasing the numerator, the latter being called the power factor $PF = \sigma S^2$. Unfortunately, it is difficult in practical systems to improve the thermoelectric figure of merit because the transport coefficients are interdependent and the optimization of each coefficient individually is limited, increasing the electrical conductivity results in a decrease of Seebeck coefficient and an increase in σ leads to a comparable increase in the electronic contribution to κ because of the Wiedemann–Franz law [48], so that the resulting ZT does not vary significantly, this limits the enhancement of the thermoelectric performances of materials.

There are several attempts, which are currently done by researches in order to enhance the ZT value of thermoelectric materials [49-53]. The main strategy for improving the figure of merit has been based on the reduction of lattice thermal conductivity. They include the rattling atom approach in clathrates [54] and skutterudites [55, 56], introducing atomic disorder at transition metal sites in half-Heusler alloys [57], structural complexity in Zintl phases [58, 59].

References:

- [1] R. P. Feynman, *Phys. Rev.*, **56**, 340 (1939).
- [2] M. Rabah, S. Benalia, D. Rached, B. Abidri, H. Rached, and G. Vergoten, *Comput. Mater. Sci.* **48**, 556 (2010).
- [3] D. Royer, E. Dieulesaint, *Elastic Waves in Solids*, Springer, New York (1996).
- [4] T. H. K. Barron and M. L. Klein, *Proc. Phys. Soc.* **85**, 523 (1965).
- [5] J. F. Nye, *Physical Properties of Crystals*. Oxford University Press, Oxford (1993).
- [6] Y. Le Page and P. Saxe, *Phys. Rev. B* **63**, 174103 (2001).
- [7] Y. Le Page and P. Saxe, *Phys. Rev. B* **65**, 104104 (2002).
- [8] J. P. Perdew, *Int. J. Quantum Chem. S* **19**, 497 (1986).
- [9] J. F. Janak, *Phys. Rev. B* **18**, 7165 (1978).
- [10] L.J. Sham and M. Schlüter, *Phys. Rev. B* **32**, 3883 (1985).
- [11] J. P. Perdew and M. Levy, *Phys. Rev. Lett.* **51**, 1884 (1983).
- [12] C. Kittel, *Introduction to Solid State Physics*, 8th Edition, John Wiley & Sons, New York (2005).
- [13] M. S. Hybertsen and S. G. Louie, *Phys. Rev. B* **34**, 5390 (1986).
- [14] M.S. Hybertsen and S.G. Louie, *Phys. Rev. Lett.* **55**, 1418 (1985).
- [15] R. A. Roberts and W. C. Walker, *Phys. Rev.* **161**, 730 (1967).
- [16] S. Logothetidis, J. Petalas, H. Polatoglou, and D. Fuchs, *Phys. Rev. B* **46**, 4483 (1992).
- [17] C.S. Wang and W.E. Pickett, *Phys. Rev. Lett.* **51**, 597 (1983).
- [18] R. Godby and R. Needs, *Phys. Rev. Lett.* **62**, 1169 (1989).
- [19] J. P. Perdew, R. G. Parr, M. Levy, and J. L. Balduz, Jr, *Phys. Rev. Lett.* **49**, 1691 (1982).
- [20] L.J. Sham and M. Schlüter, *Phys. Rev. Lett.* **51**, 1888 (1983).
- [21] J. Calloway and G. G. Johnson Jr, "Energy band theory," *Physics Today*. **17**, (1964).
- [22] P. W. Tasker, *J. Phys. C: Solid State Phys.* **12**, 4977 (1979).
- [23] L. Makinistian and E.A. Albanesi, *Phys. Rev. B* **74**, 045206 (2006).
- [24] M. Alouani and J. M. Wills, *Phys. Rev. B* **54**, 2480 (1996).
- [25] S. Daho, M. Ameri, Y. Al Douri, D. Bensaid, D. Varshney and I. Ameri, *Mater. Sci.Semicond. Process.* **41**,102 (2016).
- [26] Q.Y. Fan, Q. Wei, C.C. Chai, Y.T. Yang, X.H. Yu, Y. Liu, J.P. Zheng, P.K. Zhou, D.Y. Zhang, *Acta Phys. Pol. A* **129**, 103 (2016).
- [27] Q. Wei, M. Zhang, L. Guo, H. Yan, X. Zhu, Z. Lin, and P. Guo, *Chem. Phys.* **415**, 36 (2013).

- [28] E. W. Montroll, G. H. Weiss and I. P. Ipatova., *Theory of Lattice Dynamics in the Harmonic Approximation*, Academic Press, New York (1971).
- [29] M. Flórez, J. M. Recio, E. Francisco, M. A. Blanco, and A. M. Pendás, *Phys. Rev.* **B 66**, 144112 (2002).
- [30] M.A. Blanco, A.M. Pendás, E. Francisco, J.M. Recio, R. Franco, *J. Mol. Struct. Theochem.* **368**, 245 (1996).
- [31] T. J. Seebeck, *Ann. Phys.* **82**, 133 (1826).
- [32] E. Velmre, *Proc. Estonian Acad. Sci. Eng.* **13**, 276 (2007).
- [33] D. D. Pollock, *Thermocouples: Theory and Properties*, CRC Press, Boca. Raton, FL (1991).
- [34] H. J. Goldsmid, *Introduction to Thermoelectricity*, Springer, Heidelberg (2009).
- [35] J.C. A. Peltier, *Annales de Chimie et de Physique.* **56**, 371 (1834).
- [36] D. M. Rowe, *Ed.*, *CRC Handbook of Thermoelectrics*, Boca Raton, Florida: CRC Press, (1995).
- [37] W. Thomson, *Proc. R. Soc. Edinb.* **3**, 91 (1851).
- [38] J. M. Ziman. *Electrons and Phonons, The Theory of Transport Phenomena in Solids*, Oxford University Press, London, (1960).
- [39] F. Seitz, D. Turnbull, Editors. *Solid State Physics, Advances in Research and Applications, Vol. 5*, Academic Press, New York, (1957).
- [40] M. Balkanski and R F Wallis, *Semiconductor Physics and Applications*, Oxford University Press, New York (2000).
- [41] T. M. Tritt, *Thermal Conductivity: Theory, Properties and Applications*, Kluwer Academic/Plenum Publishers, New York (2004)
- [42] P. Y. Yu and M. Cardona, *Fundamentals of Semiconductors: Physics and Materials Properties*, Springer: Heidelberg, New York (2010).
- [43] C. Cercignani, *The Boltzmann Equation and Its Applications*, Springer, New York (1988).
- [44] J. I. Gersten and F. W. Smith, *The Physics and Chemistry of Materials*, New York, John Wiley & Sons, Inc (2001).
- [45] E. Altenkirch, *Physikalische Zeitschrift* **10**, 560 (1909)
- [46] E. Altenkirch, *Physikalische Zeitschrift* **12**, 920 (1911).
- [47] A .F. Ioffe, *Semiconductor Thermoelements and Thermoelectric Cooling*, Info search, London (1957).
- [48] M. Dresselhaus, G. Dresselhaus, S. B. Cronin, A. Gomes Souza Filho, *Solid State Properties: From Bulk to Nano*, Springer, Berlin, (2018).

- [49] A. J. Minnich, M. S. Dresselhaus, Z. F. Ren, and G. Chen, *Energy & Environmental Science* **2**, 466 (2009).
- [50] J. F. Li, W. S. Liu, L. D. Zhao, and M. Zhou, *NPG Asia Mater.* **2**, 152 (2010).
- [51] J.R. Sootsman, D.Y. Chung, and M.G. Kanatzidis, *Angew. Chem. Int. Ed.* **48**, 8616 (2009).
- [52] C. J. Vineis, A. Shakouri, A. Majumdar, and M. G. Kanatzidis, *Advanced Materials* **22**, 3970 (2010).
- [53] Y. Lan, A. J. Minnich, G. Chen, and Z. Ren, *Advanced Functional Materials.* **20**, 357 (2010)
- [54] C.L. Condron, J. Martin, G.S. Nolas, P.M.B. Piccoli, A.J. Schultz, S.M. Kauzlarich, *Inorg. Chem.* **45**, 9381 (2006).
- [55] G. S. Nolas, D. T. Morelli, and T. M. Tritt, *Annual Review of Materials Science* **29**, 89 (1999).
- [56] D. T. Morelli, G. P. Meisner, B. Chen, S. Hu, and C. Uher, *Physical Review B.* **56**, 7376 (1997).
- [57] Q. Shen, L. Chen, T. Goto, T. Hirai, J. Yang, G. P. Meisner, and C. Uher, *Applied Physics Letters.* **79**, 4165 (2001).
- [58] M. Tsutsui, L. T. Zhang, K. Ito, and M. Yamaguchi, *Intermetallics* **12**, 809 (2004).
- [59] G. J. Snyder, M. Christensen, E. Nishibori, T. Caillat, and B. B. Iversen, *Nature Materials* **3**, 458 (2004).

VI. Computational Tools

VI.1 Introduction

The aim of this chapter is to provide an overview of the different computational tools used in present investigation. We have carried out the first-principles calculations of structural, elastic, electronic and optical properties of LiAeP (Ae=Sr, Ba) using CASTEP code. The thermodynamic properties are investigated by implementation of Gibbs program. First-principles calculations for Ae_3AlAs_3 (Ae=Sr, Ba) were performed by employing two code. The elastic properties were evaluated using the pseudopotential plane wave (PP-PW) method as implemented in the CASTEP code, while the electronic and optical properties were carried out using the WIEN2k suite of programs. The thermoelectric properties of are investigated by using Boztrap program.

VI.2 Cambridge serial total energy package (CASTEP)

The Castep code is a modern implementation of density-functional theory; it can be used to simulate a wide range of materials, including crystalline solids, surfaces, molecules, liquids and amorphous materials; the properties of any material that can be considered as an assembly of cores and electrons can be calculated with the only limitation being the finite speed and the memory of the computers used. CASTEP [1] uses the pseudopotential plane wave method where ionic potentials are replaced by effective potentials that act only on the valence electrons in the system. The electronic wave functions are developed by a set of plane waves and the exchange-correlation effects in the electron-electron interactions can be included in the local density (LDA) [2], or generalized gradient (GGA) approximations [3], CASTEP takes the number and type of atoms in a system and predicts properties such as lattice constants, molecular geometry, elastic constants, band structures, state density, charge densities, and lattice functions. waves and optical properties. Flowchart of a CASTEP calculation is shown in [Figure VI.1](#).

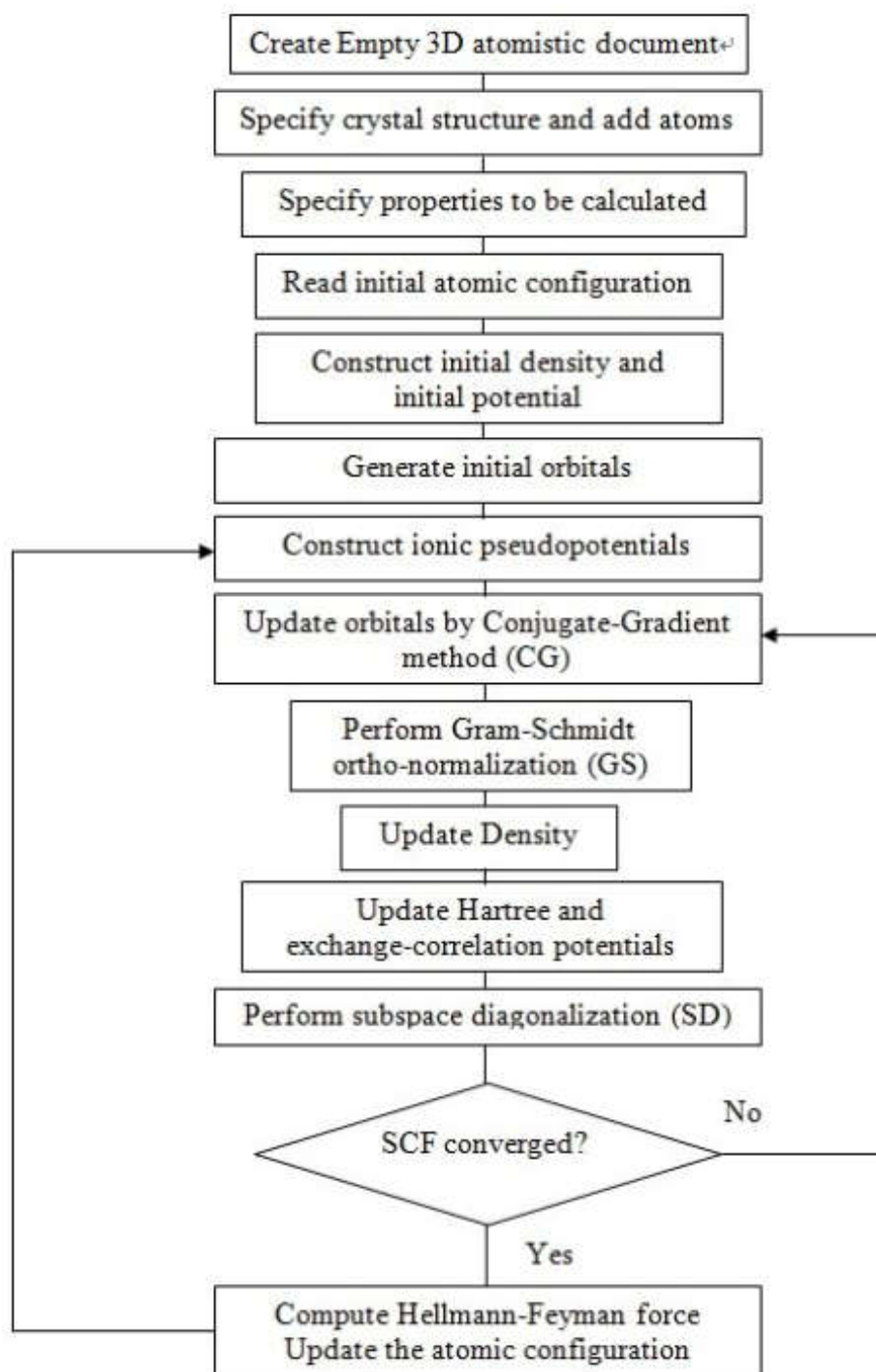


Figure VI.1 :Flowchart of a CASTEP calculation (Adopted from [4])

VI.3 The WIEN2k code

The WIEN2k [5], code is developed by P. Blaha and K. Schwarz et al. It allows an accurate estimation of the ground state properties for a given system with periodic boundary conditions and therefore mainly it is used for crystal calculations.

The code is based on KS formalism of the DFT using the full-potential (linearized) augmented plane-wave ((L) APW) + local orbitals (lo) method. There are two distinct parts in the program, the initialization and the self-consistent field [(SCF)] cycle. Each part again is composed of several separated subroutines, which are linked together via C-shell scripts.

The initialization part works starting from a structure file containing information on the atomic configuration of the system: lattice parameters, atomic species, atomic positions, muffin-tin radii, etc. Based on this file, the SGROUP and SYMMETRY routine checks for overlap between the different muffin-tin spheres and determines through different steps respectively the symmetries of the unit cell. In the next step, LSTART generate from the input files the atomic densities for all atoms in the unit cell, generates the suitable k-mesh, i.e. the sample of point k in the irreducible Brillouin zone (IBZ). Finally, the DSTART routine superimpose the atomic densities to obtain the input trial density $\rho(\mathbf{r})$, for the SCF cycle. Once the input procedure has been performed, one can proceed with the self-consistent (SCF) calculation.

In the self-consistent calculation, there are five major subroutines, namely LAPW0 LAPW1, LAPW2, LCORE and MIXER. The first one, LAPW0 generate the Coulomb and the exchange-correlation potential for the calculation from the charge density. The second, LAPW1 solves the secular equation for all the k-values in the k-mesh and gives rise to the eigenvectors and eigenvalues for the valence band by diagonalization of the Kohn-Sham equation. The third, LAPW2 integrates all valence states and constructs the valence electron density (ρ_{val}). Separately, LCORE solves the atomic calculation and gets the core state eigenvalues, eigenstates and consequently the core charge density for a spherical symmetric potential (ρ_{core}). Finally, the MIXER subroutine mixes the two electron densities with the old total electron density (ρ_{old}) and gets the input for the next cycle and checks the convergence criteria. Flowchart of a Wien2K calculation is shown in [Figure VI.2](#).

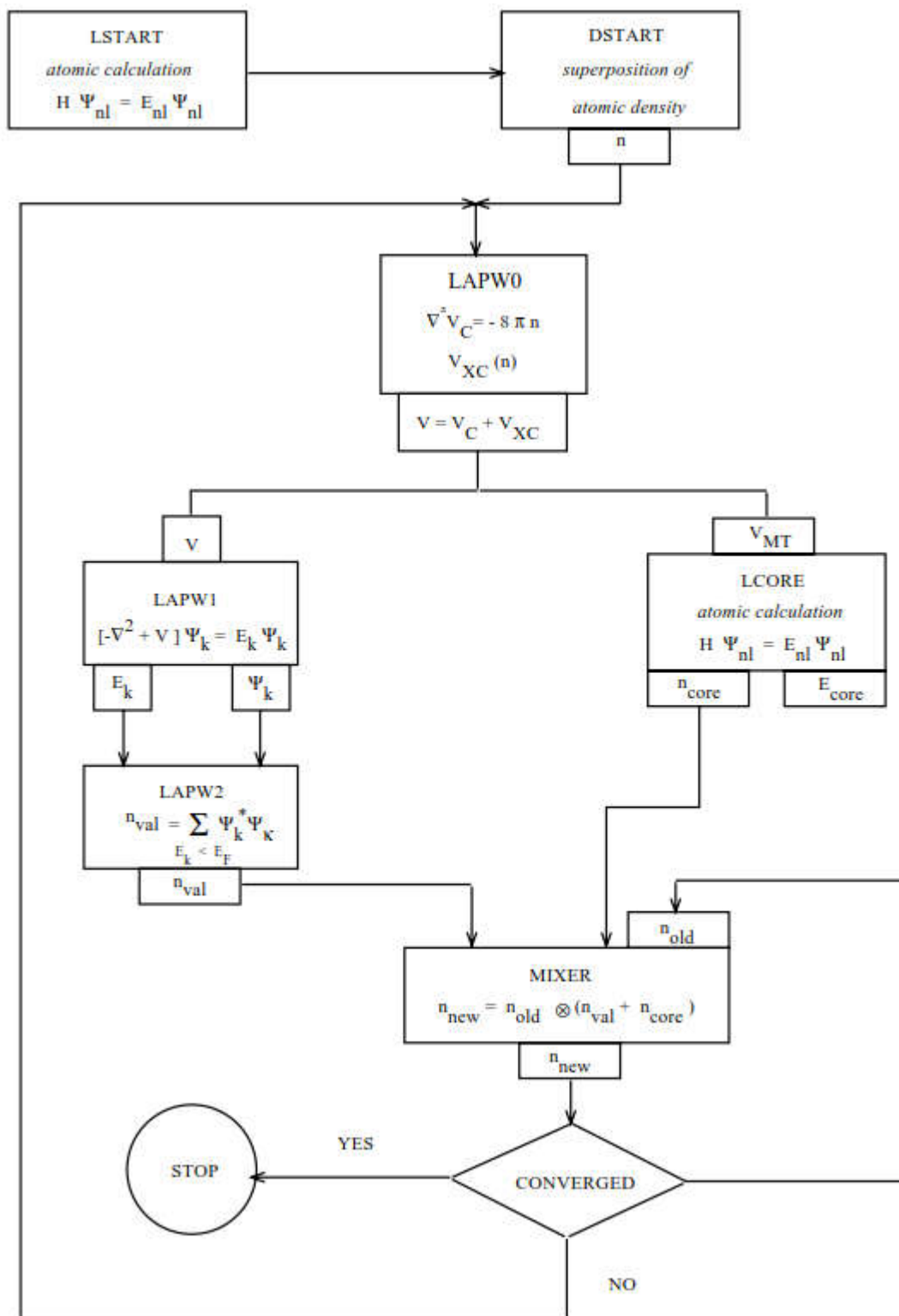


Figure VI.2 :Flowchart of a Wien2k calculation

VI.4 Gibbs program

Gibbs is a program for calculating the thermodynamic properties of solids as a function of pressure and temperature from ab initio data [6]. This program requires only a set of data (Volume, Energy) and the basic properties of the crystal to generate automatically the thermodynamic properties of any selected pressure and temperature. Taking into account the energy of a solid (E) as a function of the molecular volume (V), the Gibbs program uses a quasi-harmonic Debye model to generate the Debye $\Theta(V)$ temperature, obtains the Gibbs function out of equilibrium $G^*(V; p, T)$ and minimizes G^* to derive the thermal equation of the state (EOS) $V(p, T)$ and the chemical potential $G(p, T)$ of the corresponding phase. The other macroscopic properties are also derived as a function of p and T from standard thermodynamic relationships. Three EOS are incorporated in the Gibbs program to determine the thermodynamic properties of solids: Vinet et al. EOS [7], Birch-Murnaghan EOS [8, 9], and the spinodal EOS [10]. In this study, third-order EOS Birch-Murnaghan is used to calculate the thermodynamic properties.

VI.5 The BoltzTrap

The BoltzTrap [11] is an open-source program for computing the semi-classical transport coefficients based on solving the Boltzmann equation in the relaxation time approximation. The relaxation time τ_e , in principle, is dependent on both the band index and the κ direction. To facilitate the computation of the transport coefficients, the relaxation time is by default assumed as constant in BoltzTraP, so, BoltzTraP can only output the electrical conductivities time the inverse of the relaxation time τ , whereas we have direct access to the Seebeck coefficient. For use of an energy and temperature dependent relaxation times, one needs to modify the code (subroutine FERMIINTEGRALS).

To calculate the TE transport coefficients by use of the BTE, the group velocity of electrons should be known. It is therefore essential that the band energies are exactly computed before using BoltzTraP. This code expands the band energies in a Fourier series such that it reproduces a smooth analytical representation of the bands; therefore, the group velocities are calculated as derivatives of this interpolated band structure straightforwardly for evaluating transport properties. The code of BoltzTraP is interfaced to the band-structure code WIEN2k, but can also be easily interfaced to any other band-structure codes.

References

- [1] S. J. Clark, M. D. Segall, C. J. Pickard, P. J. Hasnip, M. J. Probert, K. Refson and M. C. Payne, *Zeitschrift fuer Kristallographie*. **220**, 567 (2005).
- [2] W. Kohn and L. Sham, *J. Phys. Rev. A* **140**, 1133 (1965).
- [3] W. Koch and M. C. Holthausen, *A Chemist's Guide to Density Functional Theory*, 2nd edition. Wiley-VCH Verlag GmbH, Weinheim, Germany (2001).
- [4] T. Collis: Porting the DFT code CASTEP to GPGPUs
(<http://www.ccs.tsukuba.ac.jp/eng/wordpress/wp-content/uploads/2013/06/13-Toni-Collis.pdf>) (Updated: 2013) (Accessed: Apr 2015).
- [5] P. Blaha, K. Schwarz, G. K. H. Madsen, D. Kvasnicka, and J. Luitz, *WIEN2k: An Augmented Plane Wave Plus Local Orbitals Program for calculating Crystal Properties*, Vienna University of Technology, Austria (2001).
- [6] M. A. Blanco, E. Francisco, and V. Luaña, *Comput. Phys. Commun.* **158**, 57 (2004).
- [7] P. Vinet, J.H. Rose, J. Ferrante, J.R. Smith, *J. Phys. Condens. Matter.* **1**, 1941 (1989).
- [8] F. D. Murnaghan, *Proc. Natl. Acad. Sci.* **30**, 244 (1944).
- [9] F. Birch, *Phys. Rev.* **71**, 809 (1947).
- [10] V. García Baonza, M. Caceres, J. Nuñez, *Phys. Rev. B* **51**, 28 (1995).
- [11] G.K.H. Madsen, D.J. Singh, *Comput. Phys. Commun.* **175**, 67 (2006).

**VII. Ab initio study of the Structural,
Elastic, electronic, optical and
thermodynamic properties of ternary
phosphides LiAeP (Ae=Sr, Ba)**

VII.1 Computational details

All calculations were carried out using the pseudopotential plane-wave method based on the DFT, as implemented in the CASTEP (Cambridge Serial Total Energy Package) code [1]. The exchange–correlation potential was modelled using the generalized gradient approximation of Perdew et al. (so-called GGA-PBEsol) [2]. The interactions between the valence electrons and the ion cores were described by means of the Vanderbilt ultrasoft pseudopotentials [3]. The Li $1s^2 2s^1$, P $3s^2 3p^3$, Ba $4d^{10} 5s^2 5p^6 6s^2$ and Sr $3d^{10} 4s^2 4p^6 5s^2$ states are treated as valence electrons. The cut-off energy, which determines the size of the plane-wave basis set, was 400 eV. The integration over the Brillouin zone (BZ) was carried out using the Monkhorst–Pack sampling method [4] with a $9 \times 9 \times 6$ k-points grid. The self-consistent field was considered to be converged when the change in total energy was less than 1×10^{-6} eV/atom.

The structural optimizations were performed using the Broyden–Fletcher–Goldfarb–Shanno (BFGS) minimization scheme [5], which minimizes the enthalpy of unit cell by minimizing the force on the nuclei and the stress on the unit cell simultaneously. In principle, the total energy is obtained from a charge density according to the assumed shape of the unit cell and the atomic positions, we then calculate the force on each atom and the stress on the unit cell, which will move the atoms and cell parameters to a certain new geometry. The new geometry can then be used to recalculate the electronic structure. The procedure is repeated until the total force acting on the atoms and the stress is below the required thresholds, which indicates that the optimization has been achieved. The tolerances were set as the difference in total energy being within 5×10^{-6} eV/atom, the maximum ionic Hellmann–Feynman force within 0.01 eV/Å, the maximum ionic displacement within 5×10^{-4} Å, and the maximum stress within 0.02 GPa.

The elastic stiffness constants of LiBaP and LiSrP systems were obtained using the stress-strain method according to Hooke's law [1, 6]. The stress-strain approach implemented in the CASTEP code is based on the construction of a set of linear equations for several deformations of the unit cell. During the simulation, each stress-strain curve was determined by uniformly increasing the amount of strain and allowing the relaxations of all the internal atomic coordinates, then the resulting stresses are calculated. Applying a given homogeneous deformation (strain) and calculating the resulting stress requires far less computational effort, since the unit cell is fixed and does not require optimization. The strain amplitude is appropriately selected so that its value is not too high or low. If the value is too high, the material cannot remain in the linear elasticity regime, i.e. in the approximation of the harmonic

oscillator. On the other hand, a low value does not produce enough distortion to generate dissimilar structures. The convergence tolerances were selected as follows: difference on total energy within 1×10^{-6} eV/atom, maximum ionic displacement within 1×10^{-4} Å and maximum ionic force within 0.002 eV/Å.

VII.2 Results and discussion

VII.2.1 Structural parameters

The examined LiSrP and LiBaP systems crystallize in a hexagonal crystal structure, space group $P6_3/mmc$ (No.194) with two formula units per unit-cell. The Wyckoff positions of atoms are as follows: Li: 2c (1/3, 2/3, 1/4), Sr, Ba: 2a (0, 0, 0) and P: 2d (1/3, 2/3, 3/4) [7]. The unit-cell crystalline structure of the LiSrP compound is depicted in Figure VII.1 as representative. So, the crystalline structure of these systems is characterized by two lattice parameters, a and c , which are not fixed by the symmetry. The equilibrium lattice parameters, a_0 and c_0 , for LiSrP and LiBaP are tabulated in Table VII.1 together with the available experimental data for comparison. One can appreciate that the relative deviations of the calculated equilibrium lattice parameters a_0 and c_0 from the measured ones do not exceed 0.26 and 0.96 %, respectively, in LiSrP and 0.12 and 0.65 %, respectively, in LiBaP. This good consistency proves the reliability of the calculation method. The lattice parameters (a_0 and c_0) of LiBaP are larger than those of LiSrP. This trend can be explained by considering the atomic radii of Ba and Sr atoms as follows: $R(\text{Ba}) = 215 \text{ pm} > R(\text{Sr}) = 200 \text{ pm}$.

In order to determine the pressure dependence of the lattice parameters of the considered materials, their geometries were optimized at different ascending pressure from 0 to 20 GPa with a step of 3 GPa. Variations of the normalized lattice parameters a/a_0 and c/c_0 versus applied hydrostatic pressure P (in GPa) are depicted in Figure VII. 2 (a) (symbols). It is clearly seen that these data are well fitted to the following second order polynomials:

$$\left\{ \begin{array}{l} \left(\frac{a}{a_0}\right)^{\text{LiSrP}} = 1 - 0.00484P + 9.7637 \times 10^{-5}P^2 \\ \left(\frac{c}{c_0}\right)^{\text{LiSrP}} = 1 - 0.0083P + 9.62202 \times 10^{-5}P^2 \\ \left(\frac{a}{a_0}\right)^{\text{LiBaP}} = 1 - 0.0059P + 1.28412 \times 10^{-4}P^2 \\ \left(\frac{c}{c_0}\right)^{\text{LiBaP}} = 1 - 0.00747P + 6.75316 \times 10^{-5}P^2 \end{array} \right. \quad (\text{VII.1})$$

The compressibility of both examined materials along c -axis is larger than that along a -axis, indicating that the chemical bonding along the c -axis is weaker than that along the a -axis. The relationship between normalized volume V/V_0 and pressure P is shown in [Figure VII.2\(b\)](#). It is found that the volume–pressure data are well fitted to the following second order polynomials:

$$\begin{cases} \left(\frac{V}{V_0}\right)^{\text{LiSrP}} = 1 - 0.0174P + 3.10915 \times 10^{-4}P^2 \\ \left(\frac{V}{V_0}\right)^{\text{LiBaP}} = 1 - 0.01858P + 3.44909 \times 10^{-4}P^2 \end{cases} \quad (\text{VII.2})$$

To calculate the bulk modulus B and its pressure derivative B' , the calculated pressure-volume (P - V) and total energy-volume (E - V) data were fitted to the following $P(V)$ and $E(V)$ Murnaghan equations of states (EOS) [8]:

$$\frac{V}{V_0} = \left(1 + B' \frac{P}{B}\right) \quad (\text{VII.3})$$

$$E(V) = E_0 + BV_0 \left[\frac{1}{B'(B'-1)} \left(\frac{V}{V_0}\right)^{1-B'} + \frac{V}{B'V_0} - \frac{1}{B_0-1} \right] \quad (\text{VII.4})$$

Here, V_0 is the unit-cell volume at zero pressure, E_0 is the equilibrium total energy and B and B' are the bulk modulus and its pressure derivative, respectively. [Figure.VII.3](#) shows the calculated P - V and E - V data (symbols) and their fits to the corresponding Murnaghan EOS s. The obtained bulk modulus B and its pressure derivative B' for the title compounds are listed in [Table VII.1](#). The calculated bulk modulus at the theoretical equilibrium volume does not find experimental or theoretical findings in the scientific literature for comparison. The bulk modulus of LiSrP is slightly larger than that of LiBaP, which is in agreement with the known relation: $B \sim 1/V_{\text{unit-cell}}$; the unit-cell volume of LiSrP is smaller than that of LiBaP.

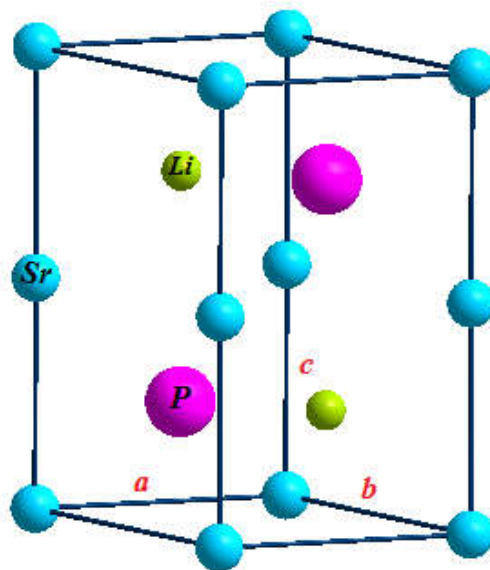


Figure VII.1 :Crystal structure of the LiSrP hexagonal compound

Table VII.1 :Calculated optimized structural parameters for the LiBaP and LiSrP compounds at zero pressure: lattice parameters (a_0 and c_0 , in Å), equilibrium unit-cell volume (V_0 , in Å³), bulk modulus (B , in GPa) its pressure derivative B' and cohesive energy (E_{coh} , in eV/atom). B and B' are derived from the Birch EOS fit. Available experimental results are reported for comparison.

	a_0	c_0	$(c/a)_0$	V_0	B	B'	E_{coh}
LiSrP							
Present work	4.3557	7.9031	1.81	129.85	48.29 ^a 44.64 ^b	3.34 ^a 4.07 ^b	-2.798
Expt. [7]	4.3674	7.9802	1.83	131.82			
LiBaP							
Present work	4.4945	8.5483	1.90	149.54	44.32 ^a 41.23 ^b	3.37 ^a 3.91 ^b	-3.170
Expt. [7]	4.5003	8.6049	1.91	150.92			

^a from Murnaghan $V(P)$ EOS

^b from Murnaghan $E(V)$ EOS

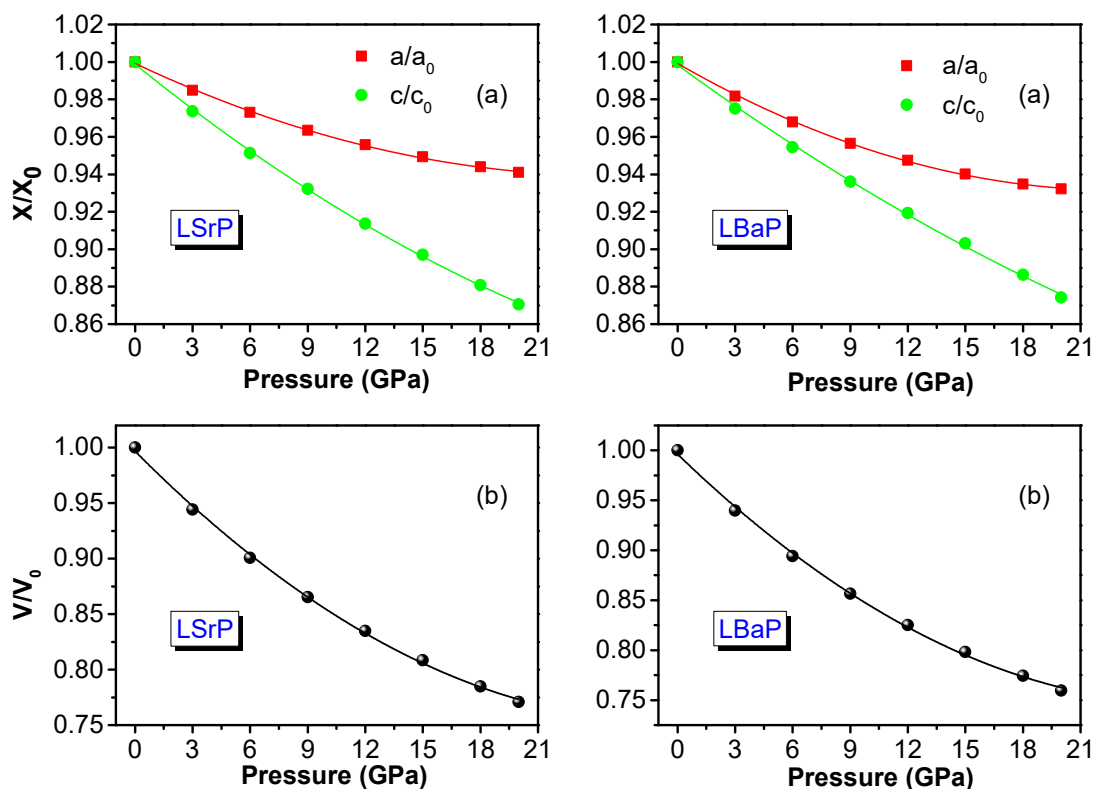


Figure VII.2 : Pressure dependence of the normalized lattice parameters (a/a_0 and c/c_0) and unit-cell volume (V/V_0) for the LiBaP and LiSrP materials. The “0” subscript denotes the parameter value at zero pressure. The calculated values are shown by symbols and solid lines show the quadratic approximations.

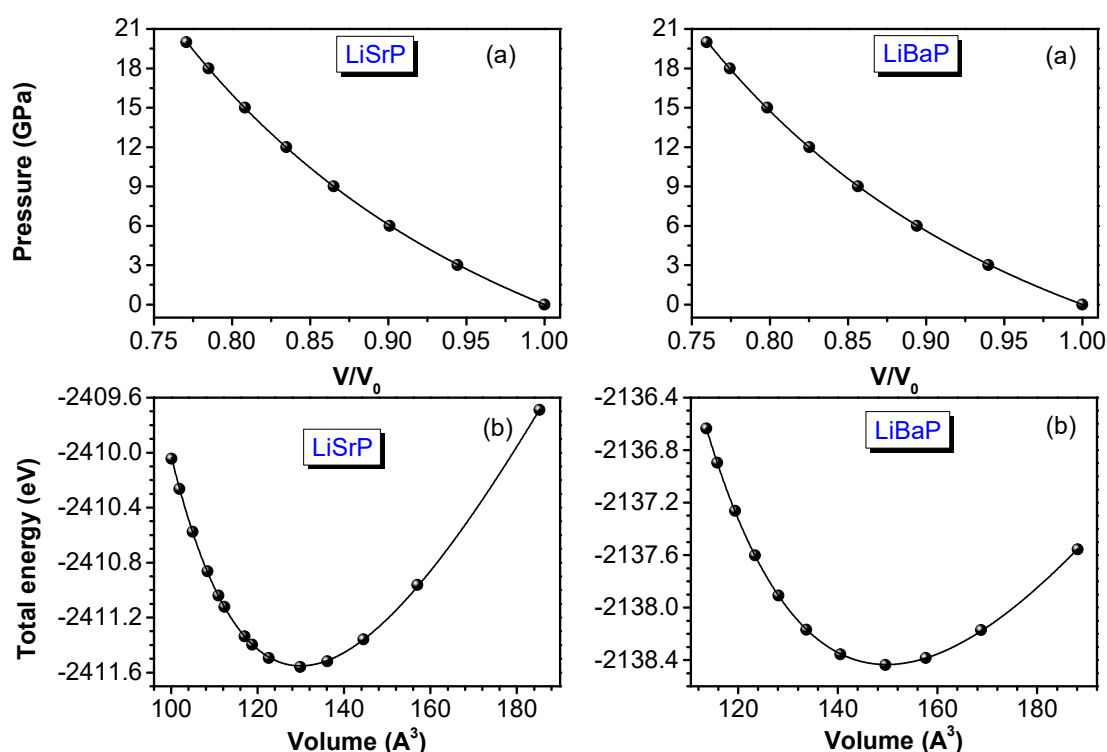


Figure VII.3 : (a) Computed pressure versus primitive-cell volume data for the LiSrP and LiBaP materials. The symbols are the calculated results and the continuous lines are Murnaghan EOS fits. (b) Unit-cell dependence of the total energy for the LiSrP and LiBaP materials. The calculated values are shown by symbols and Murnaghan *EOS* fits are shown by solid line.

The chemical stability of crystal is determined by its cohesive energy, which can be defined as the energy needed to form the crystal from free atoms or the work needed to decompose the crystal into isolated atoms. Lower the cohesive energy is; better the stability is. The cohesive energy E_{Coh} of LiSrP and LiBaP per atom were calculated using the following expression [9]:

$$E_{Coh} = \frac{E_{Tot}^{LiAeP} - (2E_{Tot}^{Li(atom)} + 2E_{Tot}^{Ae(atom)} + 2E_{Tot}^P)}{6} \quad (\text{VII.5})$$

Here, E_{Tot}^{LiAeP} is the total energy corresponding to the unit-cell of the considered material, $E_{Tot}^{Li(atom)}$, $E_{Tot}^{Ae(atom)}$ and E_{Tot}^P are the total energies of the isolated Li, Ae and P atoms in the free state, respectively. The calculated cohesive energies of LiSrP and LiBaP are listed in [Table VII.1](#). The negative cohesive energies of LiSrP and LiBaP show their energetic stabilization.

Finally, to fully characterize the pressure-induced structural changes, we turn our attention to the analysis of the interionic distances. The bond-lengths at zero pressure of the considered bonds are listed in [Table VII.2](#) along with the existing experimental data [7]. Our results are in good agreement with the reported experimental results. Pressure dependence of some normalized bond-lengths for the investigated materials are plotted in [Figure VII.4](#) (symbols). Pressure dependence of the examined normalized bond-lengths are fitted to the following second-order polynomials:

$$LiSrP \left\{ \begin{array}{l} \left(\frac{L}{L_0}\right)_{Li-P}^{LiBaP} = 1 - 0.00484P + 9.76321 \times 10^{-5}P^2 \\ \left(\frac{L}{L_0}\right)_{P-Sr}^{LiSrP} = \left(\frac{L}{L_0}\right)_{Li-Sr}^{LiSrP} = 1 - 0.00616P + 9.87577 \times 10^{-5}P^2 \\ \left(\frac{L}{L_0}\right)_{Sr-Sr}^{LiSrP} = 1 - 0.0083P + 9.62413 \times 10^{-5}P^2 \\ \left(\frac{L}{L_0}\right)_{P-P}^{LiSrP} = 1 - 0.0073P + 9.8145 \times 10^{-5}P^2 \end{array} \right. \quad (VII.6)$$

$$LiBaP \left\{ \begin{array}{l} \left(\frac{L}{L_0}\right)_{Li-P}^{LiBaP} = 1 - 0.0059P + 1.28421 \times 10^{-4}P^2 \\ \left(\frac{L}{L_0}\right)_{P-Ba}^{LiBaP} = \left(\frac{L}{L_0}\right)_{Li-Ba}^{LiBaP} = 1 - 0.00655P + 1.05374 \times 10^{-4}P^2 \\ \left(\frac{L}{L_0}\right)_{Ba-Ba}^{LiBaP} = 1 - 0.00747P + 6.75254 \times 10^{-5}P^2 \\ \left(\frac{L}{L_0}\right)_{P-P}^{LiBaP} = 1 - 0.00706P + 8.52373 \times 10^{-5}P^2 \end{array} \right. \quad (VII.7)$$

From [Figure VII.4](#), it is clearly that the Li-P and Li-Sr (Li-Ba) bonds are less compressible than the others bonds in both crystals. Whereas the Sr-Sr (Ba-Ba) bonds along the *c*-axis are the most easily compressible, which explains why the *c*-axis is more compressible than the *a*-axis.

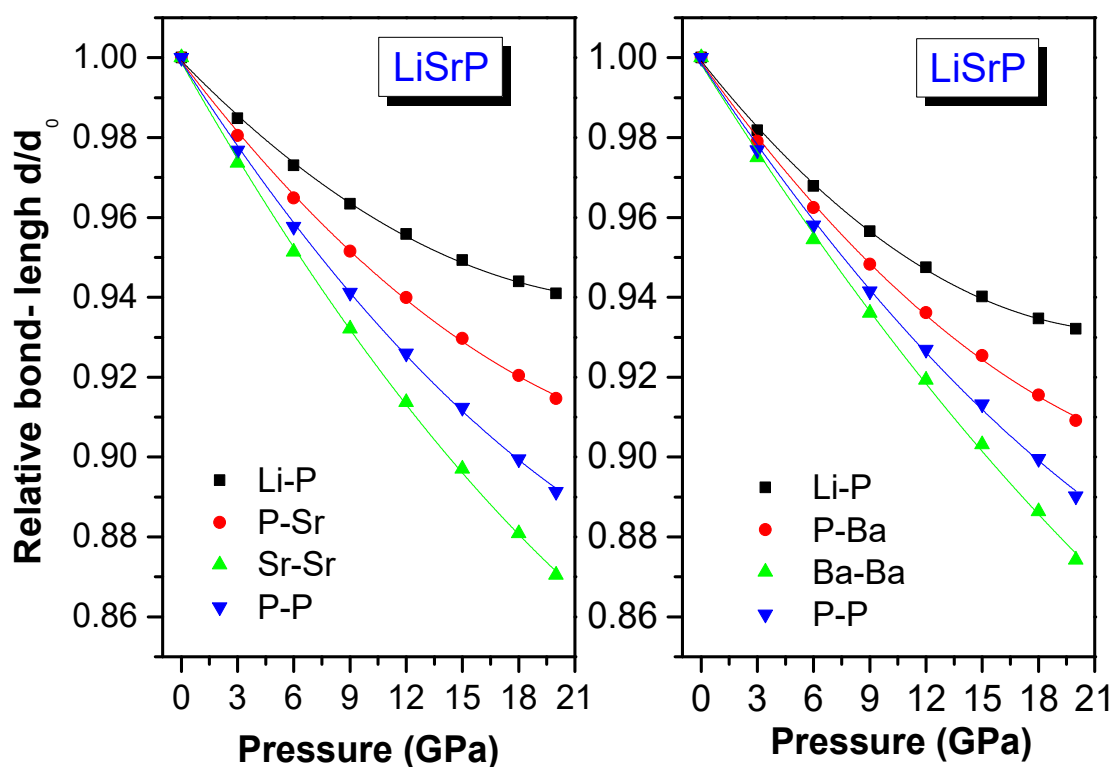


Figure VII.4 : Pressure dependence of the normalized bond-lengths for the LiSrP and LiBaP materials. The calculated values are shown by symbols and the quadratic approximations are shown by solid line. “d” stands for the interatomic distance at a pressure P, whereas “ d_0 ” is the same distance at zero pressure.

Table VII.2 : Selected bond lengths (in Å) for the LiAeP (Ae= Sr, Ba) systems.

Bonds	LiSrP		LiBaP	
	Present work	expt. [7]	Present work	expt. [7]
Li-P	2.5148	2.5215	2.5949	2.5983
Li-Ae	3.1981	3.2153	3.3617	3.3732
Ae-P	3.1981	3.2153	3.3617	3.3732

VII.2.2 Elastic properties

VII.2.2.1 Elastic constants and related properties

Five independent elastic constants, namely C_{11} , C_{12} , C_{13} , C_{33} and C_{44} , for the hexagonal LiSrP and LiBaP were calculated using the strain-stress method [1] at the equilibrium lattice parameters. The obtained data are listed in Table VII.3; no experimental or theoretical data for the elastic constants of LiBaP and LiSrP are available in the scientific literature to be compared with our results. From Table VII. 3 data, one can make the following conclusions:

1. To be mechanically stable, a hexagonal crystal should satisfy the known mechanical stability criteria [10]:

$$\check{C}_{44} > 0, \check{C}_{11} - |\check{C}_{12}| > 0, (\check{C}_{11} + \check{C}_{12})\check{C}_{33} - 2\check{C}_{13}^2 > 0 \quad (\text{VII.8})$$

Here, $\check{C}_{\alpha\alpha} = C_{\alpha\alpha} - P$, $\check{C}_{\alpha\beta} = C_{\alpha\beta} + P$ and P is the applied hydrostatic pressure

The calculated C_{ij} at zero pressure for both considered materials (Table VII.3) verify these required criteria, implying their mechanical stability.

2. One can appreciate that the C_{11} , which represents the unidirectional resistance to the compressional deformation along the [100] crystallographic direction, is larger than the C_{33} , which measures the resistance to the compressional deformation along the [001] direction. These results are in concordance with the pressure dependence of the lattice parameters discussed in Section VII.2.1.

3. The C_{ii} ($i = 1, 3$) are larger than the C_{ij} ($i, j = 4, 4; 1, 2; 1, 3$), indicating that the resistance to the compressional deformation is larger than that to shear deformation.

4. The C_{ij} of LiSrP are larger than those of LiBaP, which confirm that the LiSrP is more resistant to the applied deformation than LiBaP.

5. For a hexagonal crystal, the parameter, the ratio between the linear compressibilities of the c - and a -axis (k_c and k_a , respectively) is given by the following relationship [11]:

$$\frac{k_c}{k_a} = \frac{C_{11} + C_{12} - 2C_{13}}{C_{33} - C_{13}} \quad (\text{VII.9})$$

This ratio is found to be equal 1.69 for LiSrP and 1.44 for LiBaP. These results confirm the results obtained from the pressure dependence of the lattice parameters indicating that the linear compressibility along c -axis is greater than along a -axis for both examined crystals.

Table VII.3 Calculated elastic constant (C_{ij} , in GPa) for the LiAeP (Ae = Sr, Ba) compounds.

Compounds	C_{11}	C_{33}	C_{44}	C_{12}	C_{13}
LiSrP	109.2	72.12	40.12	20.5	25.02
LiBaP	89.2	65.02	34.62	18.2	24.22

6. It is important to evaluate the sound velocity in a crystal because they are related to some physical properties of the material such as its thermal conductivity. The sound wave velocities of pure transverse and longitudinal modes of crystals can be calculated from the Cristoffel equation [12]. The calculated sound wave velocities propagating in the [100], [001] and [120] crystallographic directions for the examined crystals reproduced from the calculated elastic constants C_{ij} at zero pressure are listed in Table VII.4. One can note that the longitudinal sound velocities and the first transverse sound velocities are quite different along [100] and [001] directions for each structures. The anisotropic properties of sound velocities indicate the elastic anisotropy in these crystals. The longitudinal sound wave along the [100] direction travels faster than shear sound wave since the square root of C_{11} is larger than C_{44} and C_{33} .

Table VII.4 Acoustic wave velocities (in m/s) for some propagating directions in the LiAeP (Ae = Ba, Sr) hexagonal compounds. ρ is the mass density of material ; T and L stand to the transverse and longitudinal wave polarizations.

Acoustic wave velocities	LiSrP	LiBaP
$V_L^{[100]} = V_L^{[120]} = \sqrt{C_{11}/\rho}$	5832.6	4787.2
$V_{T1}^{[100]} = V_{T1}^{[120]} = \sqrt{(C_{11} - C_{12})/2\rho}$	3717.7	3020.32
$V_{T2}^{[100]} = V_{T2}^{[120]} = \sqrt{C_{44}/\rho}$	3535.92	2982.22
$V_L^{[001]} = \sqrt{C_{33}/\rho}$	4740.5	4087.75
$V_{T1}^{[001]} = V_{T2}^{[001]} = \sqrt{C_{44}/\rho}$	3535.95	2982.25

7). From the single-crystal independent elastic constants C_{ij} of solids it is possible to calculate useful elastic moduli characterizing the mechanical properties for their polycrystalline phases, such as the bulk modulus B and shear modulus G . The bulk modulus B , which depicts the contraction of an object when a pressure is imposed and the shear modulus G , which reflects the resistance of an object to the shear deformation, for polycrystals can be computed from the C_{ij} via the Voigt-Reuss bounds [13,14]. According to Voigt approximation, the bulk (B_V) and shear (G_V) moduli for a hexagonal structure can be calculated from the C_{ij} through the following relationships [13]:

$$B_V = \frac{2}{9} \left(C_{11} + C_{12} + C_{33} + 2C_{13} + \frac{1}{2}C_{33} \right) \quad (\text{VII.10})$$

$$G_V = \frac{1}{30} (7C_{11} - 5C_{12} + 12C_{44} + 2C_{33} - 4C_{13}) \quad (\text{VII.11})$$

In the Reuss approximations, the bulk (B_R) and shear (G_R) moduli for a hexagonal lattice can be evaluated from the C_{ij} via the following expressions [14]:

$$B_R = C(C_{11} + C_{12} + 2C_{33} - 4C_{13})^{-1} \quad (\text{VII.12})$$

$$G_R = \frac{5}{2} \{ (C_{44}C_{66}) \} \{ 3B_V C_{44}C_{66} + C(C_{44} + C_{66}) \}^{-1} \quad (\text{VII.13})$$

$$C = (C_{11} + C_{12})C_{33} - 2C_{13}^2; \quad C_{66} = \frac{C_{11} - C_{12}}{2}. \quad (\text{VII.14})$$

The Voigt and Reuss yield the limits of the values that can take B and G . Hill [15] suggested that the effective B_H and G_H for polycrystals are approximated by the arithmetic mean of these mentioned limits –Voigt and Reuss-:

$$B_H = (B_V + B_R)/2 \quad (\text{VII.15})$$

$$G_H = (G_V + G_R)/2 \quad (\text{VII.16})$$

Other elastic moduli characterizing the mechanical properties of solids, such as the Young's modulus and Poisson's ratio, can be derived from the B and G using the well-known relationships [16]:

$$E = \frac{9BG}{3B+G} \quad (\text{VII.17})$$

$$\sigma = \frac{3B-2G}{2(3B+G)} \quad (\text{VII.18})$$

The calculated aforementioned elastic moduli are presented in Table VII.5. These findings allow us to make the following conclusions:

7.1). The calculated bulk modulus from the elastic constants via the Voigt-Reuss-Hill approximations (Table VII.5) is in agreement with that obtained from the fit to Murnaghan's EOS (Table VII.1). This might be an estimate of the reliability and accuracy of our calculated elastic constants for LiBaP and LiSrP.

7.2). The isotropic Young's modulus E , defined as the ratio of linear stress to linear strain averaged over all directions, is an important elastic parameter that can provide useful information about the stiffness of solids. The moderate values of the isotropic Young's modulus of the studied materials ($E \approx 77-92$ GPa) suggest that they will show a rather moderate stiffness. From the present results of E , we can state that LiSrP is stiffer than LiBaP.

7.3). Poisson's ratio σ provides more information about the chemical bonding than any other elastic constant. Poisson's ratios of covalent systems are known to be small ($\sigma \sim 0.1$), while those of ionic solids are $\sigma \sim 0.25$ [17], From the data presented in Table VII.5, one can conclude that the chemical bonding in the studied materials shows a mixed ionic-covalent character.

7.4). According to Pugh's empirical criterion [18], the ratio of the shear modulus to bulk modulus (G/B) can predict the brittle/ductile behaviour of materials. The critical value separating ductility from Brittleness is about 0.57. If the G/B ratio is over 0.57 the material behaves as a ductile material, otherwise, it will demonstrate brittleness. The obtained B and G values (Table VII. 5) yield $G/B = 0.82$ for LiSrP and 0.78 for LiBaP. According to this indicator, LiAeP ($Ae = \text{Ba, Sr}$) must behave as a plastic material.

Table VII.5 :Calculated polycrystalline elastic moduli: Reuss, Voigt and Hill bulk modulus (B_R , B_V and B_H , in GPa), Reuss, Voigt and Hill shear modulus (G_R , G_V and G_H , in GPa), Young's modulus (E , in GPa) and Poisson's ratio (σ , dimensionless) for isotropic polycrystalline LiAeP ($Ae = \text{Sr, Ba}$) aggregates.

System	B_V	G_V	B_R	G_R	B_H	G_H	E_j		E	σ
							E_x	E_z		
LiSrP	47.95	39.60	46.60	38.35	47.28	38.97	99.16	62.50	91.72	0.176
LiBaP	41.85	32.73	41.33	31.78	41.59	32.26	79.12	54.11	76.887	0.191

7.5). From computed bulk and shear moduli, we can evaluate the longitudinal (v_l) and transverse (v_t) and the average (v_m) velocities of the sound wave in polycrystals in terms of the following relationships [19]:

$$v_l = \sqrt{(B_H + 4G_H/3)/\rho}; \quad v_t = \sqrt{G_H/\rho}; \quad v_m = [(2/v_t^3 + 1/v_l^3)/3]^{-1/3} \quad (\text{VII.19})$$

Then the Debye temperature, a suitable parameter to describe phenomena of solid-state physics that are associated with lattice vibration, elastic constants, specific heat and melting point, can be predicated by using the following common relation [19]:

$$\theta_D = \frac{h}{k_B} \left[\frac{3n}{4\pi} \left(\frac{N_A \rho}{M} \right) \right]^{\frac{1}{3}} v_m \quad (\text{VII.20})$$

Here, h is the Planck's constant, k_B is the Boltzmann's constant, n is the number of atoms per one formula unit, N_A is the Avogadro's number, ρ is the mass density, M is the molecular mass. The calculated values of v_l , v_t , v_m and θ_D for the LiAeP ($Ae=\text{Sr, Ba}$) compounds at zero pressure and temperature are given in Table VII. 6. It can be seen that LiSrP has a larger Debye temperature than LiBaP which can explain by the higher elastic constant of LiSrP compared to those of LiBaP. Up to now, there are no available data for these parameters in the scientific literature to be compared with our present findings.

Table VII.6 : Calculated mass density (ρ), longitudinal, transverse and average sound velocities (v_l , v_t and v_m , respectively) and Debye temperatures (θ_D) for LiAeP ($Ae = \text{Sr, Ba}$).

System	$\rho(\frac{g}{cm^3})$	$v_l(\frac{m}{s})$	$v_t(\frac{m}{s})$	$v_m(\frac{m}{s})$	$\theta_D(\text{K})$
LiSrP	3.21	5559.8	3484.2	3837.1	410.0
LiBaP	3.89	4662.3	2878.9	3175.5	323.7

The required semiconductors for technical applications are generally thin monolayers or multilayers grown on substrates. The lattice mismatch and difference in the thermal expansion coefficients between the epitaxial layers and substrates can cause large stresses in the epitaxial layers. Hence, in this context, it is of more than fundamental interest to estimate the numerical values of the elastic constants of these materials, which describe their responses to externally applied strains and their evolution with pressure. Therefore, in the present work, we evaluated the pressure dependence of the elastic constants in the range from 0 GPa to 15 GPa with a step of 3 GPa and the obtained results are depicted in Figure VII.5. The elastic constant C_{11} and C_{33} reflect the elasticity in length; a longitudinal strain produces a change in C_{11} and C_{33} . The elastic constants C_{12} , C_{13} and C_{44} are associated with the elasticity in shape; they are shear constants. A transverse strain causes a change in shape, but no change in volume. All elastic constants of both considered materials increase monotonically with the increasing pressure. From Figure.VII.5, one can observe that the C_{11} is more sensitive to the pressure variation compared to C_{33} , C_{12} , C_{13} and C_{44} . The variations of the C_{ij} with pressure are well fitted to second-order polynomials as follows:

$$\text{LiSrP} \left\{ \begin{array}{l} C_{11} = 109.65073 + 7.31957P - 0.08358P^2 \\ C_{33} = 72.56983 + 3.60684P - 0.06493P^2 \\ C_{44} = 40.21167 + 2.67115P - 0.0197P^2 \\ C_{12} = 20.26029 + 2.37587P + 0.00336P^2 \\ C_{13} = 25.02782 + 3.77388P - 0.02159P^2 \\ C_{66} = 44.69522 + 2.47185P - 0.04347P^2 \\ B = 46.72509 + 4.07335P - 0.04447P^2 \end{array} \right. \quad (\text{VII.21})$$

$$\text{LiBaP} \left\{ \begin{array}{l} C_{11} = 89.36627 + 6.09836P - 0.07386P^2 \\ C_{33} = 63.56769 + 4.14229P - 0.09602P^2 \\ C_{44} = 34.66454 + 2.40093P - 0.02466P^2 \\ C_{12} = 18.10315 + 2.40808P + 0.01444P^2 \\ C_{13} = 23.21626 + 4.39061P - 0.03079P^2 \\ C_{66} = 35.63156 + 1.84514P - 0.04415P^2 \\ B = 40.51837 + 4.36429P - 0.05052P^2 \end{array} \right. \quad (\text{VII.22})$$

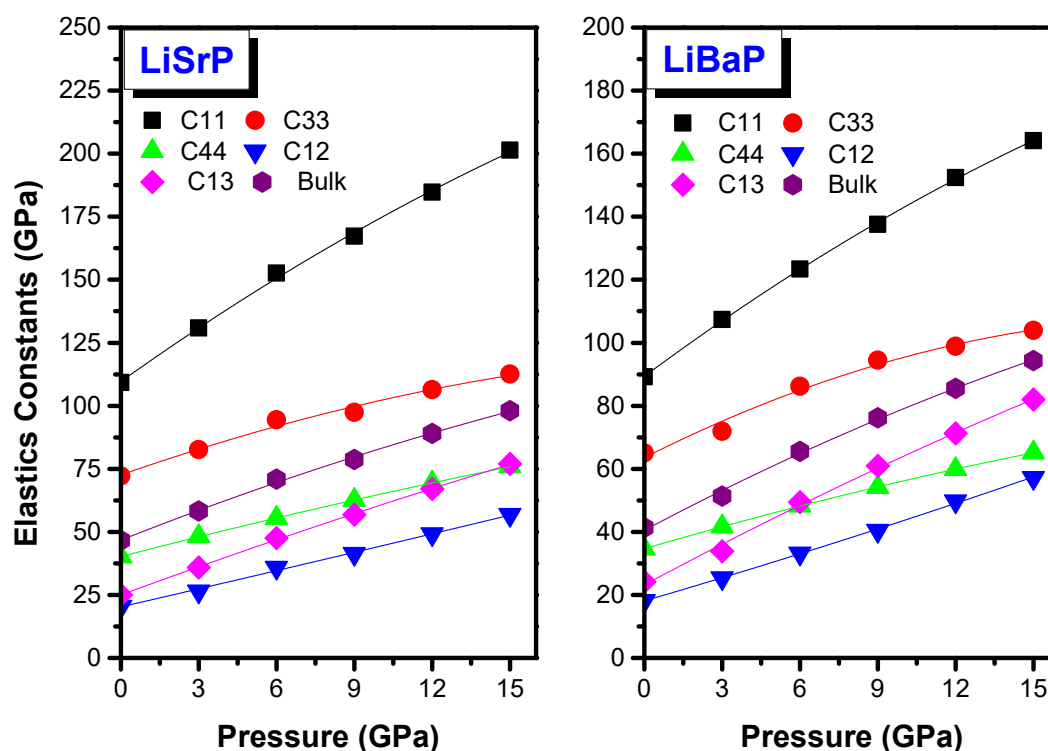


Figure VII.5: Calculated pressure dependence of the elastic constants C_{ij} and bulk modulus B for LiSrP and LiBaP materials. The symbols are the calculated results and the continuous lines are the second-order polynomial fits to the results.

VII.2.2.2 Elastic anisotropy

The elastic anisotropy of crystals is an important mechanical parameter, which is highly correlated with the possibility to induce microcracks in the materials [20]. Furthermore, recent study [21] has reported that the elastic anisotropy has a significant influence on the nanoscale precursor textures in alloys. Owing to these, it becomes necessary and significant to estimate the elastic anisotropy of crystals for a better understanding of this property and hopefully find mechanisms that will help to improve its durability and resistivity to microcracks. Thus, different indicators have been developed to estimate the elastic anisotropy in solids. Four different indexes were used in the present work to explore the elastic anisotropy of the LiAeP phosphides.

1. The degree of anisotropy in bonding between atoms in different crystallographic planes can be estimated from the calculated independent elastic constants C_{ij} via the shear anisotropic factors A_1 , A_2 and A_3 . For hexagonal crystals, the shear factors A_1 , A_2 and A_3 are given by the following expressions [22]:

$$A_1 = A_2 = \frac{4C_{44}}{C_{11} + C_{33} - 2C_{13}} \text{ for the } \{100\} \text{ and } \{010\} \text{ planes} \quad (\text{VII.23})$$

$$A_3 = \frac{2(C_{11} - C_{12})}{C_{11} + C_{22} - 2C_{12}} \text{ for the } \{001\} \text{ plane} \quad (\text{VII.24})$$

For an isotropic crystal A_{1-3} are equal to unity and any value either smaller or greater than unity indicates presence of a certain degree of elastic anisotropy; the degree of elastic anisotropy possessed by a crystal is estimated in terms of the magnitude of deviations of the shear factors A_1 , A_2 and A_3 from unity. The calculated shear anisotropic factors for the considered crystals are given in Table VII.7. The obtained results reveal that A_3 is equal to 1 for both studied crystals, indicating that bonding in the $\{001\}$ plane is isotropic. Both systems exhibit anisotropic bonding in the $\{100\}$ and $\{010\}$ planes. We can see also that the deviation of A_1 (A_2) from the unity in LiBaP is larger than that in LiSrP indicating that the degree of elastic anisotropy in LiBaP is larger than in LiSrP.

Table VII.7: Calculated anisotropy in compression (A_B), anisotropy in shear (A_G), anisotropy factors ($A_1 = A_2$ and A_3) and the anisotropy universal index A^U for the LiAeP ($Ae = \text{Sr, Ba}$) compounds.

System	A_1	A_2	A_3	$A_B\%$	$A_G\%$	A^U
LiSrP	1.222	1.222	1	1.613	1.429	0.193
LiBaP	1.308	1.308	1	0.624	1.476	0.162

2. The so-called percentage of elastic anisotropy in compression A_B and shear A_G , usually used to estimate the elastic anisotropy of crystals, are defined the following formulas [23]

$$A_B = \frac{B_V - B_R}{B_V + B_R} \times 100 \quad (\text{VII.25})$$

$$A_G = \frac{G_V - G_R}{G_V + G_R} \times 100 \quad (\text{VII.26})$$

Zero value for A_B and A_G corresponds to elastic isotropy, while a value of 100% is associated with the largest possible anisotropy. According to Table VII.7 data, both materials exhibit a small anisotropy in shear and compression.

3. A truest representative of the elastic anisotropy is the so-called universal anisotropic index A^U . It is defined by the following expression [24]:

$$A^U = 5 \frac{G_V}{G_R} + \frac{B_V}{B_R} - 6 \quad (\text{VII.27})$$

A^U is zero for isotropic crystals; deviations of A^U from zero define the extent of crystal anisotropy. In our case, according to this indicator, both LiSrP and LiBaP will exhibit a certain elastic anisotropy (Table VII. 7).

4. The degree of elastic anisotropy of crystals can be bestly visualized by plotting a three dimensional (3-D) representation of its crystallographic direction dependence of the Young's modulus E . The Young's modulus E in an arbitrary direction for a hexagonal crystal can be determined by the following equation [25]:

$$E = \frac{1}{S_{11} - \left[l_3^2 (S_{11} - S_{33}) + (2S_{11} - 2S_{13} - S_{44})(l_1^2 + l_2^2) \right] l_3^2} \quad (\text{VII.28})$$

l_1 , l_2 and l_3 are the cosines directors and S_{ij} are the elastic compliance. The distance from the origin of the coordinate system to this surface is equal to the Young's modulus in a given direction. For elastic isotropy, the 3D-surface representation of the Young's modulus exhibits a spherical shape, while the magnitude of deviation of its shape from a sphere indicates the degree of elastic anisotropy in the considered crystal. The obtained 3D direction dependence of Young's modulus for $LiAeP$ ($Ae=\text{Sr, Ba}$) is given in Figure VII.6, which shows that the shape of the 3D-resurface representation show a certain deviation from the spherical shape, indicating that these crystals possess a certain degree of elastic anisotropy. For more visualizing the elastic anisotropy, the cross-section of the 3D-surface representation in the (010) and (001) planes are also depicted in Figure VII. 6. For isotropic materials, the cross-section curve is circular. From the 2D-plane projection, we can see that the Young's modulus in the ab -plane ((001)-plane) is isotropic in both considered compounds but there is a clear deviation of the cross-section in the ac -plane ((010)-plane) from the circular form, indicating the anisotropic of the Young's modulus in this plane. The difference between the maximal value of the Young's modulus $E_{\max} = 99.72 \text{ GPa}$ (79.12 GPa) for LiSrP (LiBaP) in the ac -plane and its minimal value $E_{\min} = 62.50 \text{ GPa}$ (54.11 GPa) is about 37.22 GPa (25.01 GPa); i.e. $E_{\max} = 159\% E_{\min}$, indicates a consistent elastic anisotropy.

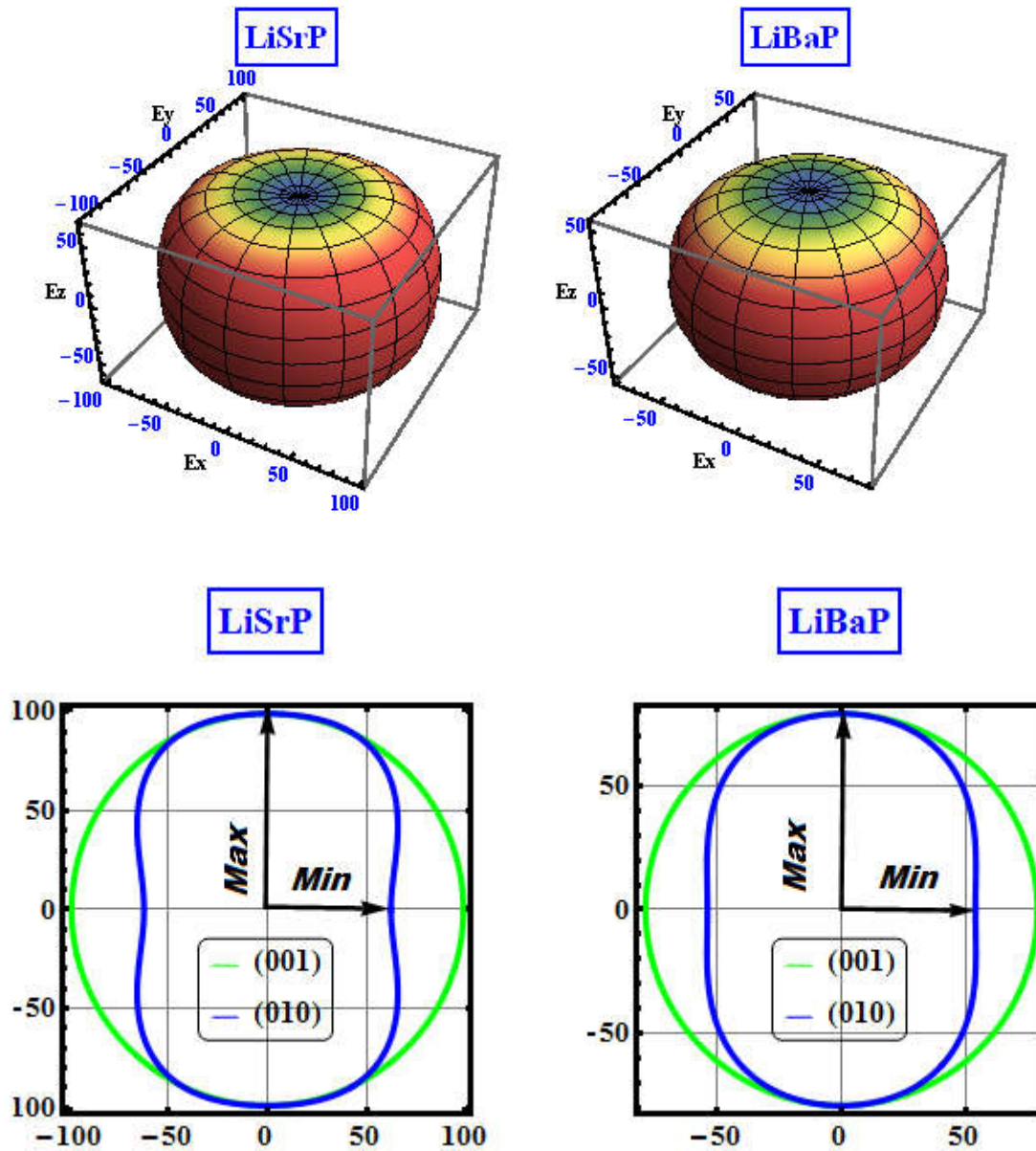


Figure VII.6 : 3D-directional dependence of the Young's modulus (E, in GPa) and its projection on the ab- $\{(001)\}$ and ac- $\{(010)\}$ planes for the LiSrP and LiBaP materials.

VII.2.3 Electronic structure and chemical bonding

Investigation of the electronic energy bands of the LiBaP and LiSrP ternary compounds would be very useful to better understand their electronic and optical properties. The electronic energy band dispersions along the high symmetry lines in the first Brillouin zone of both examined crystals are depicted in [Figure. VII.7](#) The topmost of the valence bands (VB) is located at the Γ -point in the Brillouin zone and the bottommost of the conduction bands (CB) is positioned at the M-point. Hence, both investigated systems are indirect band gap (Γ -M) semiconductors. The fundamental band gap of LiSrP (LiBaP) is equal to 1.16 eV (0.80 eV). No experimental or theoretical data are available in the scientific literature for the band gaps of LiSrP and LiBaP for comparison with our findings. Bearing in mind that the DFT within the common GGA underestimates the band gaps of semiconductors and isolators, the predicted values in the present work can serve as minimum estimates of the true band gaps of the considered crystals. The band gap calculated using the DFT with the common GGA is likely to be approximately 30-50 % smaller than the experimental values [26]. Therefore, the real fundamental band gap of LiSrP (LiBaP) is expected to be in the range 1.50–1.73 eV (1.04–1.20 eV). The replacement of Sr with Ba in the LiAeP series (Ae: Sr, Ba) leads to the narrowing of the band gap by approximately 31 %.

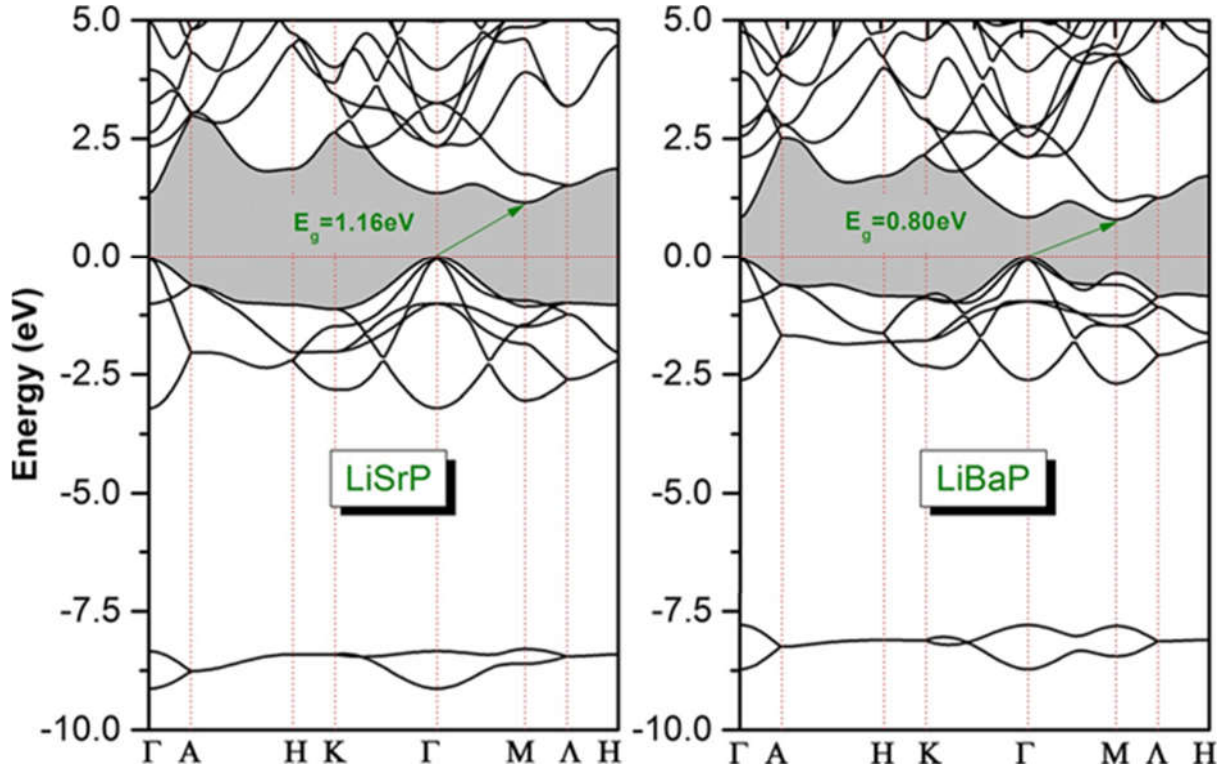


Figure VII.7 : Calculated electronic energy band dispersion curves along the high symmetry directions in the Brillouin zone for the $LiAeP$ ($Ae = Sr, Ba$) compounds. E_g gives the value of the fundamental energy band gap $\Gamma - M$. The Fermi level is given at 0.0 eV.

Figure VII.8 shows the pressure dependencies of the fundamental band gap $\Gamma - M$ ($E_g^{\Gamma - M}(p)$) and the first direct band gap $\Gamma - \Gamma$ ($E_g^{\Gamma - \Gamma}(p)$) of LiSrP and LiBaP in a pressure range between 0 and 15 GPa. First, the fundamental band gap remains between the topmost of the valence bands at the Γ -point and the bottommost of the conduction bands at the M-point for both examined compounds in the considered pressure range. Second, both considered gaps, i.e. $\Gamma - M$ and $\Gamma - \Gamma$, are characterized by a quadratic decrease with increasing pressure in both compounds ; the CB bottommost moves down with increasing pressure. When the pressure increases from 0 to 15 GPa, the fundamental band gap $\Gamma - M$ decreases from 1.16 to 0.44 eV in LiSrP and from 0.80 eV to 0.13 eV in LiBaP. The first direct band gap, $\Gamma - \Gamma$, decreases from 1.35 to 0.82 eV in LiSrP and from 0.83 to 0.27 eV in LiBaP.

Pressure dependences of the studied gaps induced are given by the following quadratic relationships:

$$LiSrP \begin{cases} E_g^{\Gamma - M}(P) = 1.153 - 0.04969P + 1.19048 \times 10^{-4}P^2 \\ E_g^{\Gamma - \Gamma}(P) = 1.3539 - 0.02736P - 5.49028 \times 10^{-4}P^2 \end{cases} \quad (VII.29)$$

$$\text{LiBaP} \begin{cases} E_g^{\Gamma-M}(p) = 0.799 - 0.04738p + 2.04365 \times 10^{-4}p^2 \\ E_g^{\Gamma-\Gamma}(p) = 0.83146 - 0.033p + -3.17679 \times 10^{-4}p^2 \end{cases} \quad (\text{VII.30})$$

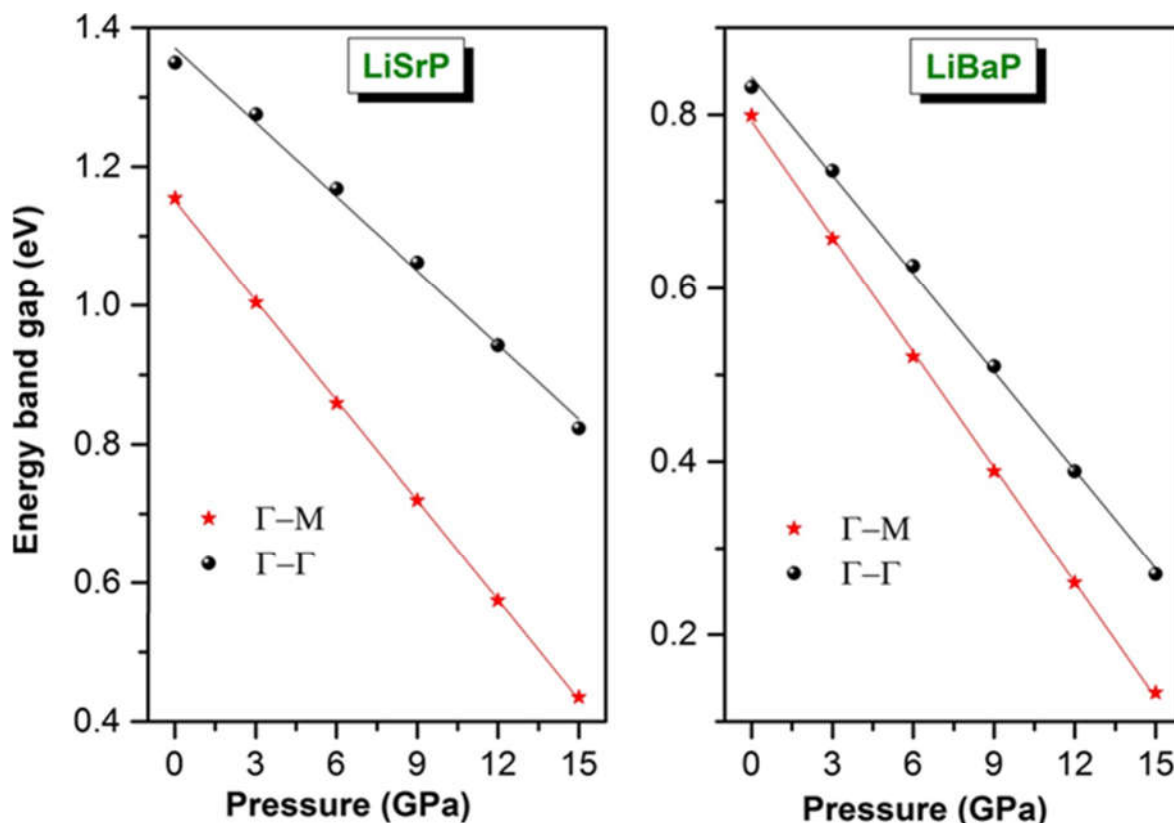


Figure VII.8 :Pressure dependence of the fundamental indirect band gap Γ -M and the first direct band gap Γ - Γ for the LiAeP ($Ae = \text{Ba, Sr}$) compounds. The calculated values are indicated by symbols and the fits by solid lines.

VII.2.4 The effective mass

In general, the theoretical effective mass is a tensor with nine components. However, for the very idealized simple case in which the energy $E(k)$ data are represented by a parabola curve, such as at the valence band maximum (VBMa) and the conduction band minimum (CBMi), the effective mass becomes a scalar that can be evaluated from the $E(k)$ curve around the VBMa and CbMi by fitting the $E(k)$ data to the following well-known equation: $E = \frac{\hbar^2 k^2}{2m^*} E$ is the band-edge energy as a function of the wave vector k and m^* is the effective mass. The calculated effective masses of the holes at the VBMa along the Γ -K and Γ -M directions and those of the electrons at the CbMi along the M- Γ and M- Λ directions are tabulated in [Table VII 8](#). The results indicate that the electron effective mass has a relevant dependence on the k

direction in both compounds, indicating its anisotropy, while the hole effective mass is quite isotropic. In addition, the hole effective mass value is close to that of the electron, suggesting that their mobilities will be fairly similar.

Table VII.8 :Calculated electron and hole effective masses (m_e and m_h , respectively; in unit of free electron mass) for the LiSrP and LiBaP compounds.

System	m_e^* ($\Gamma \rightarrow M$)	m_e^* ($M \rightarrow \Lambda$)	m_h^* ($K \rightarrow \Gamma$)	m_h^* ($\Gamma \rightarrow M$)
LiSrP	0.0668	0.0492	0.0437	0.0438
LiBaP	0.0579	0.0390	0.0337	0.0337

VII.2.5 Densities of states

The total and atomic-resolved l-projected densities of states (TDOS and PDOS) corresponding to the energy bands of the LiSrP and LiBaP compounds are calculated to obtain information regarding the orbital character of the electronic states and the chemical bonding. The obtained DOS diagrams are depicted in [Figure. VII.9](#). For the LiSrP compound, the lowest valence band group, located between approximately -10.0 and -8.0 eV, is essentially dominated by the P-3s orbitals with a small contribution from the Li-1s, Sr-4s and Sr-3d states. The lower part of the valence band group, ranging from -3.13 eV up to the Fermi level, consists mainly of the Sr-3d-4p and P-3p states, whereas the upper part is due to the hybridized Li-1s, Sr-3d and P-3p states. The conduction bands ranging from 0 to 10 eV are composed principally of the Li-2s, Sr-3d and Sr-5s states, with a minor contribution from the P-3s states. For the LiBaP compound, the lowest valence band group, located between approximately -10.0 and -7.4 eV, is essentially dominated by the P-3s orbitals, with a small presence of the Ba-5s and Ba-4d states. The lower part of the upper valence band group, ranging from -2.98 eV up to the Fermi level, is formed mainly from the Ba-4d-5p and P-3p states, whereas the upper part is due to the hybridized Li-1s, Ba-d and P-3p states. The conduction bands ranging from 0 to 10 eV are composed primarily of the Ba-4d and Li-2s states with a small contribution from the Ba-6s and P-3p states.

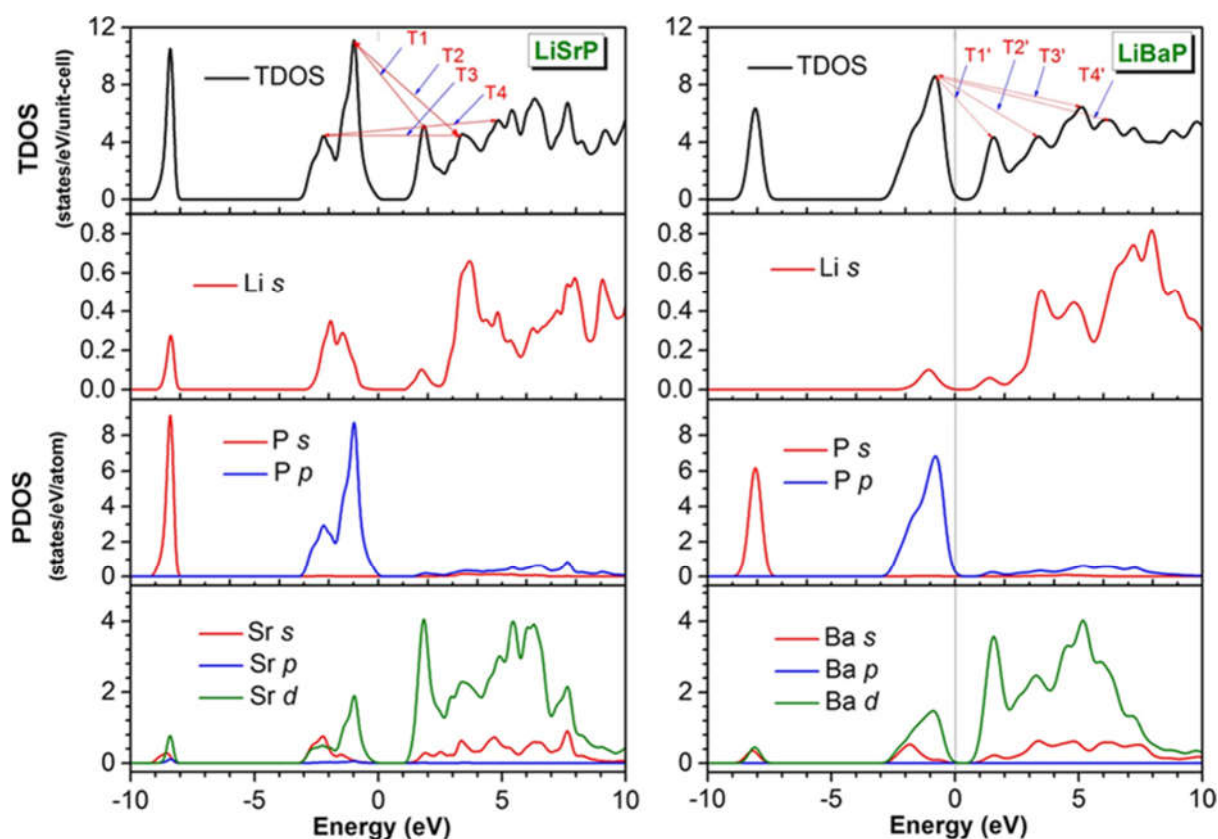


Figure VII.9 : Total (TDOS) and partial (PDOS) densities of states diagrams for the $LiAeP$ ($Ae = Sr, Ba$) compounds. T1 (T1 \backslash), T2 (T2 \backslash), T3 (T3 \backslash) and T4 (T4 \backslash) represent the electronic transitions from the valence bands to the conduction bands.

To visualize the character of the chemical bonding between the constituent atoms, the valence charge density distribution maps of the investigated systems in the (110) plane are plotted in [Figure VII.10](#). The figure shows that a certain accumulation of electrons occurs between the P and Sr/Ba and between the P and Li atoms, indicating that the chemical bonding between those atoms is mostly covalent. The covalent bonding between P and Sr/Ba is due to the hybridization between the P-3p and Sr-3d/Ba-4d states, and the covalent bonding between P and Li is due to the hybridization between the P-3p and Li-2s states.

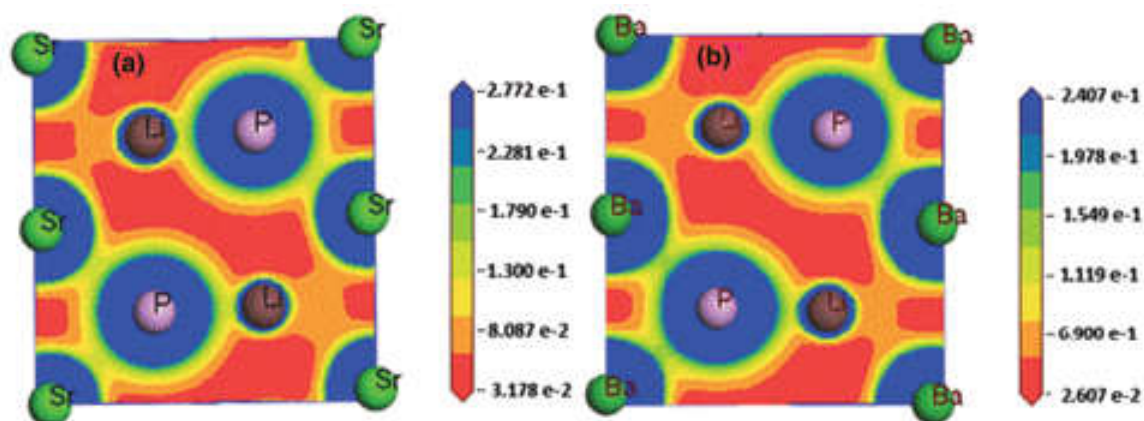


Figure VII.10 :Charge density distribution maps in the (110) plane for the LiSrP (a) and LiBaP (b) systems

VII.2.6 Optical properties

Calculations of the optical properties require more k-points than ordinary self-consistent field calculations; a $20 \times 20 \times 20$ k-points grid is used in the present work. The LiSrP and LiBaP compounds have a hexagonal structure and are thus optically biaxial systems. For this reason, the optical functions of the considered crystals are calculated for polarized incident radiation with electric field vector \vec{E} parallel to the principal crystallographic axes, i.e., $\vec{E} // a$ ($\vec{E} // [100]$) and $\vec{E} // c$ ($\vec{E} // [001]$). Because some of the synthesized samples are polycrystalline, the optical spectra are also predicted for the polycrystalline phase.

VII.2.6.1 The dielectric function

The absorptive $\varepsilon_2(\omega)$ and dispersive $\varepsilon_1(\omega)$ parts of the dielectric function for both LiSrP and LiBaP are shown in [Figure VII.11](#). The figure displays noticeable differences between the magnitudes, shapes and locations of the main features and peaks in the $\varepsilon_2(\omega)$ and $\varepsilon_1(\omega)$ spectra corresponding to, $\vec{E} // a$ and $\vec{E} // c$, demonstrating a strong anisotropy of the dielectric response of these materials to the incident radiation. The absorption edge is slightly shifted toward lower energies for the $\vec{E} // c$ polarization in both compounds; the absorption edge starts at 1.003 eV (0.510 eV) for $\vec{E} // a$ and at 0.960 eV (0.4680 eV) for $\vec{E} // c$ in LiSrP (LiBaP). Now we try to determine the origin of the occupied and unoccupied states involved in the direct interband transitions that caused the main peaks in the $\varepsilon_2(\omega)$ spectra based on the calculated electronic structure discussed in Sect. VII.2.4. The absorptive part $\varepsilon_2(\omega)$ of the dielectric function $\varepsilon(\omega)$ of LiSrP exhibits four structures labeled A, B, C and D. The lowest energy peak, A, centred at

approximately 2.77 eV for $\vec{E} // a$ and 2.72 eV for $\vec{E} // c$, is caused by the interband transition T1 (see Figure.VII.9), which is due mostly to the electronic transitions from the Sr-3d and P-3p valence states to the Sr-3d conduction states. Structure B, centred at approximately 4.37 eV for $\vec{E} // a$ and 4.19 eV for $\vec{E} // c$, is due to the direct interband transition T2. Peak C, centred at approximately 5.23 eV for $\vec{E} // a$ and 6.68 eV for $\vec{E} // c$, is attributable to the direct interband transition T3, which is due mostly to the electronic transitions from the Sr-3d, P-3p and Li-2s valence states to the Sr-3d and Li-2s conduction states. The fourth peak, D, centred at approximately 5.66 eV for $\vec{E} // a$ and absent for $\vec{E} // c$, is caused by the direct interband transition T4.

The $\varepsilon_2(\omega)$ spectrum of LiBaP also exhibits four structures labeled A \backslash , B \backslash , B \backslash and D \backslash . Peak A \backslash , centered at approximately 2.23 eV for $\vec{E} // a$ and 2.67 eV for $\vec{E} // c$, is caused by the direct interband transition T1 \backslash (see Figure.VII.9) (mostly Ba-4d and P-3p \rightarrow Ba-4d). Peak B \backslash , centered at approximately 4.13 eV for $\vec{E} // a$ and 3.97 eV for $\vec{E} // c$, is due to the direct interband transition T2 \backslash . Peak B \backslash , centred at approximately 4.92 eV for $\vec{E} // a$ and 4.93 eV for $\vec{E} // c$, is attributable to the direct interband transition T3 \backslash (mostly Ba-4d, P-3p and Li-2s \rightarrow Ba-4d and Li-2s]). The fourth peak, D \backslash , centered at approximately 9.28 eV for $\vec{E} // a$ and absent for $\vec{E} // c$, is caused by the direct interband transition T4 \backslash .

The zero frequency limit $\varepsilon_1(0) = \varepsilon_1(\omega \rightarrow 0)$, the electronic part of the static dielectric constant is the most important quantity in the $\varepsilon_1(\omega)$ spectrum. The calculated value of $\varepsilon_1(0)$ for LiSrP (LiBaP) is equal to 8.569 (11.530) for $\vec{E} // a$ and 10.694 (13.498) for $\vec{E} // c$. The values of $\varepsilon_1(0)$ for both considered light polarizations in LiSrP are larger than their corresponding ones in LiBaP; i.e., $\varepsilon_1(0)$ increases with decreasing band gap. This trend can be explained based on the Penn model [27]: $\varepsilon(0) \approx 1 + (\hbar\omega_p / E_g)^2$.

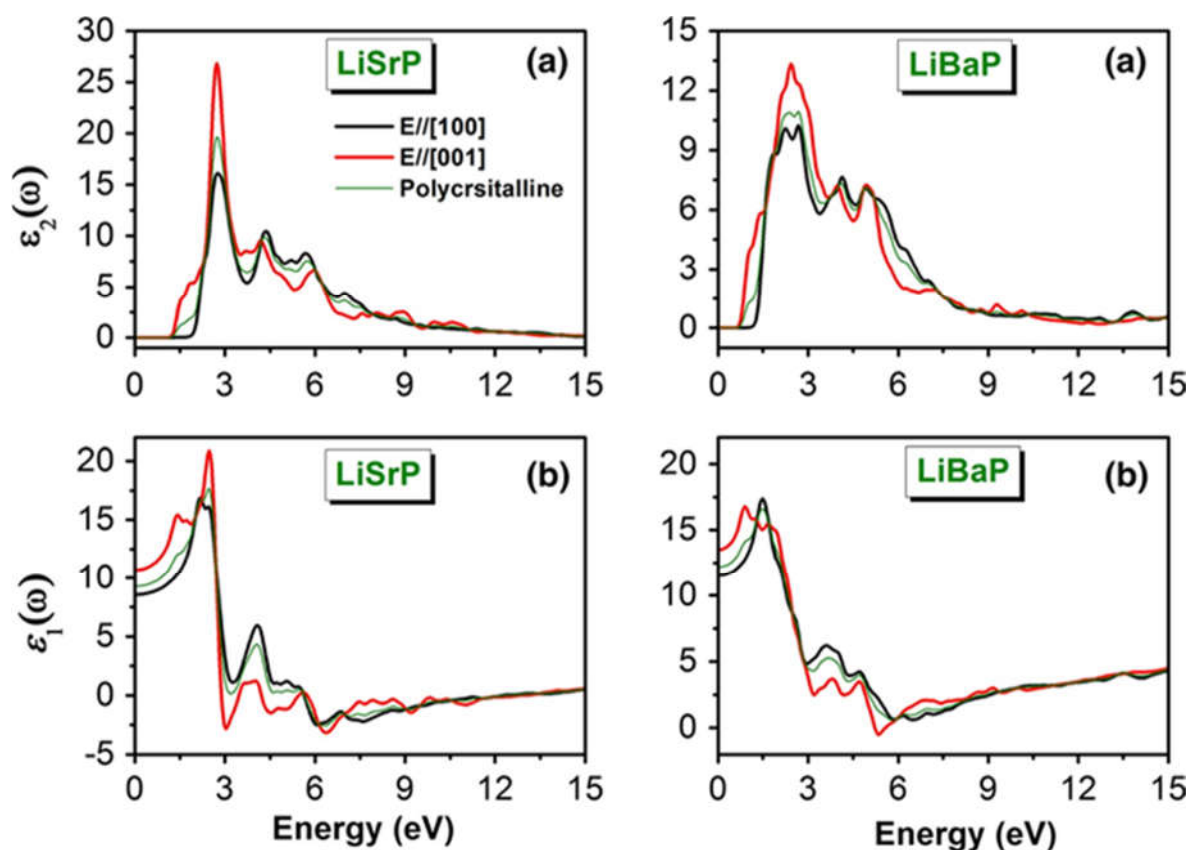


Figure VII.11 : Calculated (a) imaginary $\epsilon_2(\omega)$ and (b) real parts $\epsilon_1(\omega)$ of the dielectric function for incident radiation polarized along the two principal crystallographic directions, i.e., $\vec{E} // a$ and $\vec{E} // c$, for the $LiAeP$ ($Ae = Sr, Ba$) crystals. The obtained spectra for the $LiAeP$ ($Ae = Sr, Ba$) polycrystals are also shown.

VII.2.6.2 The absorption coefficient

The absorption coefficient $\alpha(\omega)$ is a basic way to measure how far light with a specific energy can penetrate a material before being absorbed. The absorption coefficient depends on the incident photon energy and expresses the ratio between the number of photons actually absorbed by the crystal per unit volume per second and the number of incident photons per unit area per second. From the point of view of the structure of electron bands, we are interested in the probability that, under the influence of the radiation field, an electron makes a transition between two energy levels. The absorption coefficient (α) is determined from:

$$I = I_0 \exp(-\alpha t) \quad (V. 31)$$

Where I is the intensity transmitted at a particular wavelength, t is the thickness of the material and I_0 is the maximum intensity transmitted (assumed to be 100%).

The calculated absorption coefficients for LiSrP and LiBaP for both considered light polarizations, i.e., $\vec{E} // a$ and $\vec{E} // c$, are displayed in [Figure VII.12 \(a\)](#), in which the fundamental absorption edge starts approximately at 1.003 eV (0.510 eV) for $\vec{E} // a$ and 0.960 eV (0.468 eV) for $\vec{E} // c$ in LiSrP (LiBaP). The absorption coefficient increases with increasing photon energy, reaching a maximum and then decreasing to reach its minimum. The absorption spectrum shows some peaks that can be explained by the interband transitions using the band structure results. LiSrP has an absorptive energy region larger than that of LiBaP. The LiSrP compound can be used as an absorptive layer in the energy range from 1.37 to 12 eV, whereas LiBaP can be used in the energy range from 0.84 to 9 eV.

VII.2.6.3 The reflectivity

The reflectivity is the ratio of the energy of a wave reflected from a surface to the energy of the wave incident on it. The frequency-dependent reflectivity $R(\omega)$ spectra of the considered systems for both polarizations of the incident radiation are depicted in [Figure VII.12 \(b\)](#). The zero frequency limit $R(0)$ is equal to 24 % (30 %) for $\vec{E} // a$ and 28 % (32 %) for $\vec{E} // c$ in LiSrP (LiBaP). The reflectivity $R(\omega)$ increases from $R(0)$ with increasing photon energy to attain a maximum, and then a rapid decrease of $R(\omega)$ occurs at approximately 13.85 eV (5.88 eV) for $\vec{E} // a$ and 13.34 eV (5.41 eV) for $\vec{E} // c$. [Figure VII.12 \(b\)](#) shows that the maximum reflectivity in LiSrP (LiBaP) occurs at approximately 7.7 eV (1.62 eV) for $\vec{E} // a$ and at approximately 2.85 eV (2.44 eV) for $\vec{E} // c$. The maximum reflectivity is approximately 47 % (39 %) for $\vec{E} // a$ and 56 % (41 %) for $\vec{E} // c$ in LiSrP (LiBaP).

VII.2.6.4 The energy-loss function

The energy-loss spectrum $L(\omega)$ describes the energy loss of a fast electron passing through a material [28]. The main peak in the $L(\omega)$ spectrum represents the characteristic associated with the plasma resonance; the corresponding frequency is called plasma frequency ω_p , which occurs when $\epsilon_2(\omega) < 1$ and $\epsilon_1(\omega)$ reaches a zero value [29]. From the energy-loss spectrum [Figure VII.12 \(c\)](#), the plasma frequency ω_p for LiSrP (LiBaP) is equal to approximately 13.85 eV (7.43 eV) for $\vec{E} // a$ and approximately 13.34 eV (6.05 eV) for $\vec{E} // c$. When the frequency of the incident light is higher than the plasma frequency, the material

becomes transparent and hence an abrupt reduction of the reflectivity $R(\omega)$ occurs at the plasma frequency.

VII.2.6.5 The refractive index

The refractive index $n(\omega)$ of a substance is the ratio of the speed of an electromagnetic wave in a vacuum to its speed in the substance. Knowledge of the refractive index of an optical material is important because its use in optical devices, such as photonic crystals and waveguides. The calculated refractive index spectra of LiSrP and LiBaP are shown in [Figure VII.12 \(d\)](#). The static refractive index $n(0)$ (the refractive index at zero energy) of LiSrP (LiBaP) is equal to 2.94 (3.39) for $\vec{E} // a$ and 3.27 (3.67) for $\vec{E} // c$. In both considered compounds, the refractive index increases with increasing energy, shows some peaks for the two polarization directions of the incident radiation and then decreases at high energy. Moreover, the refractive index for LiSrP goes below unity in certain energy ranges. When the refractive index is lower than unity, it indicates that the group velocity $V_g = c/n$ of the incident radiation is greater than the speed of light c , which means that the group velocity shifts to the negative domain and the nature of the medium changes from linear to non-linear. It is known that the refractive index has the same trend of variation with photon energy as the real part of the dielectric function, which means that all peaks appearing in the spectrum of the refractive index are related to the ones appearing in the real part of the dielectric function, whereas the extinction coefficient $k(\omega)$ [[Figure VII.12 \(e\)](#)] follows the imaginary part of the dielectric function. The polycrystalline sample optical behavior for both materials closely mimics the optical behavior observed for the [100] polarized incident light.

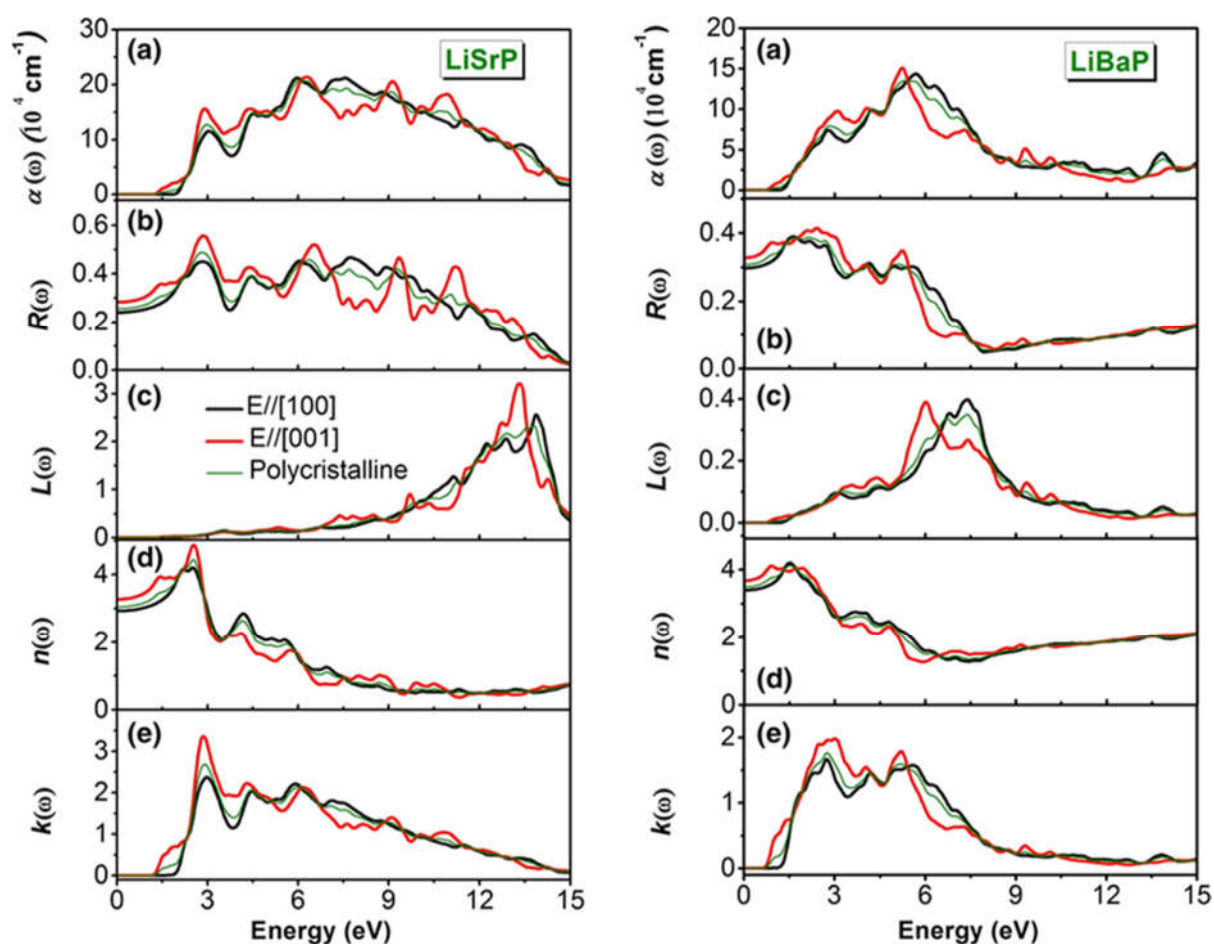


Figure VII.12 : Calculated optical function spectra: (a) Absorption $\alpha(\omega)$, (b) Reflectivity $R(\omega)$, (c) Energy loss function $L(\omega)$, (d) Refractive index $n(\omega)$ and (e) Extinction coefficient $k(\omega)$ for incident radiation polarized along the two principal crystallographic directions i.e., $\vec{E} // a$ and $\vec{E} // c$, for the LiAeP ($\text{Ae} = \text{Sr}, \text{Ba}$) crystals. Obtained spectra for the LiAeP ($\text{Ae} = \text{Sr}, \text{Ba}$) polycrystals are also shown.

VII.2.7 Thermodynamic properties

We have investigated the thermodynamic properties of the LiAeP ($\text{Ae} = \text{Sr}, \text{Ba}$) systems in the temperature range from 0 to 800 K and the pressure range from 0 to 15 GPa using the quasi-harmonic Debye model as implemented in the Gibbs program [30]. A detailed description of the quasi-harmonic Debye model can be found elsewhere [31–35].

VII.2.7.1 The lattice parameter under temperature

The relationship between the normalized unit-cell volume and temperature at some fixed pressures for LiSrP and LiBaP is shown in [Figure VII.13 \(a\)](#), which shows that the normalized volume V/V_0 is nearly constant at low temperature and that an abrupt change occurs with increasing temperature. The normalized volume increases more rapidly at a high temperature for both compounds; however, the rate becomes a little slower with increasing pressure; these materials become less expandable at 15 GPa than at 0 GPa.

VII.2.7.2 The Bulk modulus

The variation of the Bulk modulus versus temperature at four fixed pressures (0, 5, 10 and 15 GPa) is depicted in [Figure VII.13 \(b\)](#). It can be seen that the Bulk modulus remains nearly constant at a low temperature for both compounds and then decreases rapidly with increasing temperature; the increasing temperature causes a decrease in the hardness of materials due to the increase of the unit-cell volume. The bulk modulus values of LiSrP (LiBaP) at 0, 5, 10 and 15 GPa decrease by 29.43 % (32.70 %), 16.37 % (17.19 %), 10.75 % (10.86 %) and 7.92 % (7.62 %), respectively, when the temperature increases from 0 to 800 K. At zero pressure and zero temperature, our calculated bulk moduli for LiSrP and LiBaP are 45.12 GPa and 41.09 GPa, respectively. LiSrP is slightly more resistant to the compression of volume.

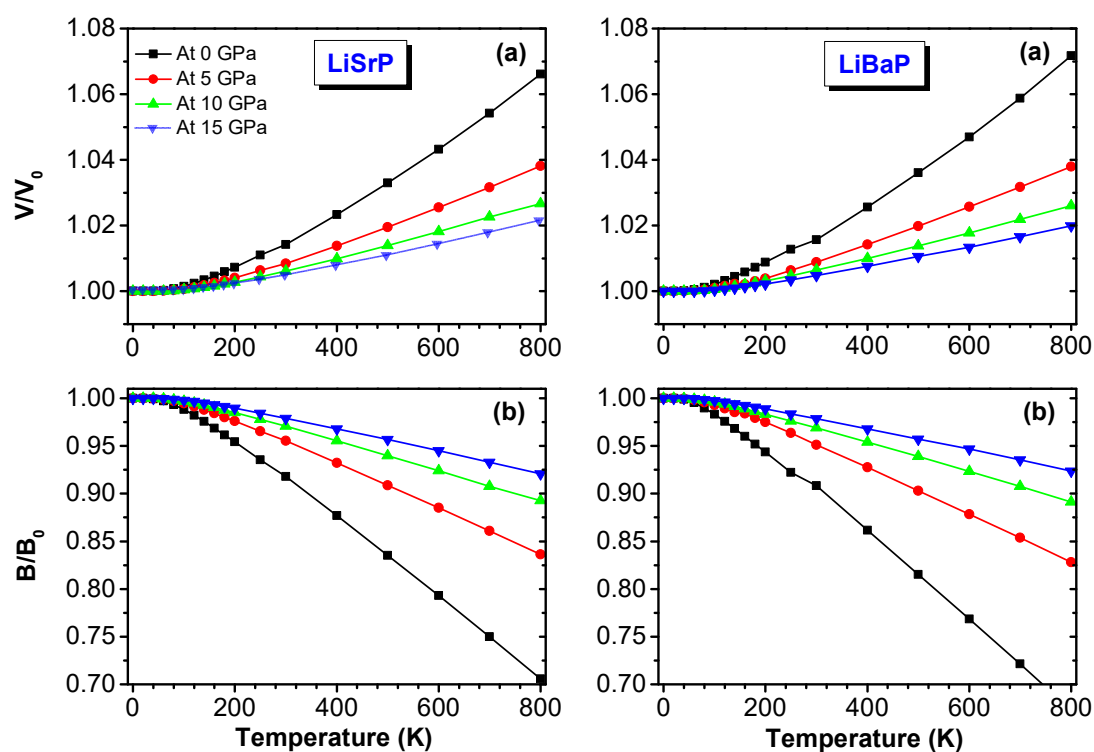


Figure VII.13 (a) :The normalized primitive-cell volume V/V_0 as a function of temperature for the LiSrP and LiBaP compounds at some fixed pressures; V is the primitive-cell volume at the considered temperature; V_0 is the primitive-cell volume at zero temperature. **(b)** The normalized bulk modulus B/B_0 as a function of temperature for the LiSrP and LiBaP compounds at some fixed pressures; B is the bulk modulus at the considered temperature and B_0 is the bulk modulus at the zero temperature.

VII.2.7.3 The Debye temperature

The Debye temperature is a characteristic temperature of the behavior of the heat capacity and the hardness of the solids. It is the highest temperature that can be reached due to a single normal vibration. Figure VII.14 (a) illustrates the variation in the Debye temperature θ_D as a function of temperature at some fixed pressures for LiSrP and LiBaP. It can be seen that θ_D decreases slightly with increasing temperature in both considered compounds. When the temperature increases from 0 to 800 K, the Debye temperature θ_D is reduced by 12.04 % (13.82 %) at 0 GPa, 6.11 % (6.24 %) at 5 GPa, 3.85 % (3.80 %) at 10 GPa and 2.82 % (2.65 %) at 15 GPa in LiSrP (LiBaP). This indicates that the reduction rate of θ_D with temperature becomes small at higher pressure; the high pressure suppresses the temperature effect on the Debye

temperature. The calculated Debye temperatures θ_D at zero pressure and zero temperature are 398.27 K for LiSrP and 320.47 K for LiBaP.

VII.2.7.4 The Grüneisen parameter

The Grüneisen parameter describes the change in the vibrational properties of a crystal lattice due to the increase or decrease of its volume as a result of temperature change.

The variation of the Grüneisen parameter γ as a function of temperature is shown in [Figure VII.14 \(b\)](#). At a given pressure, the Grüneisen parameter γ increases slowly with temperature. Moreover, the Grüneisen parameter γ increases more slowly at high pressure than at low pressure. At 300 K and zero pressure, our calculations yield a γ equal to 1.94 (2.073) for LiSrP (LiBaP).

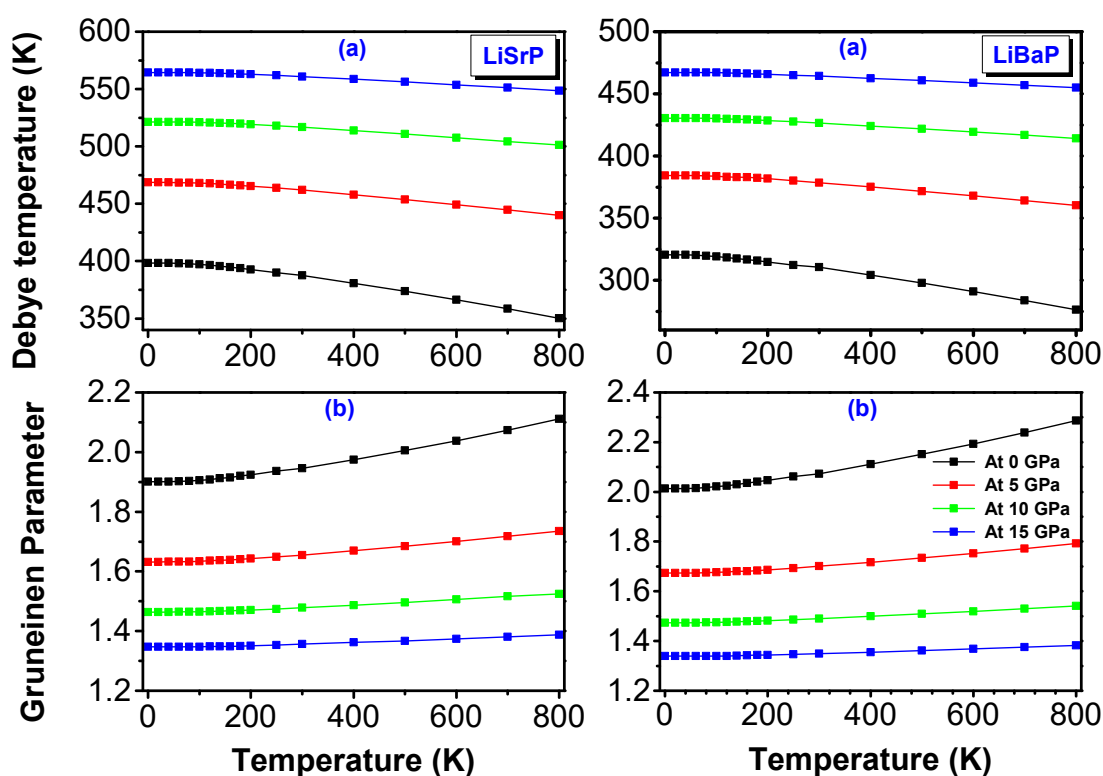


Figure VII.14: (a) Variations of the Debye temperature and (b) Grüneisen parameter versus temperature at some fixed pressures for the LiSrP and LiBaP compounds.

VII.2.7.5 The heat capacity

The heat capacity of a solid quantifies the relationship between the temperature of a body and the energy supplied to it. If a large amount of heat (energy) supplied to a body produced only a slight increase in temperature, the solid would have a large heat capacity. The heat capacity of a solid usually increases with temperature. The measured value of the heat capacity depends on the measurement carried out at constant volume C_V , or at constant pressure C_P . Figures VII.15 (a) and VII.15 (b) show the temperature dependencies of the constant pressure heat capacity C_P and the constant volume heat capacity C_V , respectively, at some fixed pressures. One can see that the constant volume heat capacity C_V and the constant pressure capacity C_P are very similar for the temperature range from 0 to approximately 300 K; C_V and C_P increase rapidly with temperature at a fixed pressure. When the temperature is higher than 300 K, the anharmonic effect on the heat capacity C_V is suppressed and increases slowly with increasing temperature to approach a constant value—the so-called Dulong–Petit limit [36] which is common for all solids at high temperatures—whereas C_P still increases monotonously

with increasing temperature. At high temperature, C_V approaches approximately $147.71 \text{ J mol}^{-1} \text{ K}^{-1}$ ($148.77 \text{ J mol}^{-1} \text{ K}^{-1}$) in LiSrP (LiBaP). At zero pressure and ambient temperature, C_V and C_P of LiSrP (LiBaP) are $137.88 \text{ J mol}^{-1} \text{ K}^{-1}$ ($141.94 \text{ J mol}^{-1} \text{ K}^{-1}$) and $144.37 \text{ J mol}^{-1} \text{ K}^{-1}$ ($149.47 \text{ J mol}^{-1} \text{ K}^{-1}$), respectively.

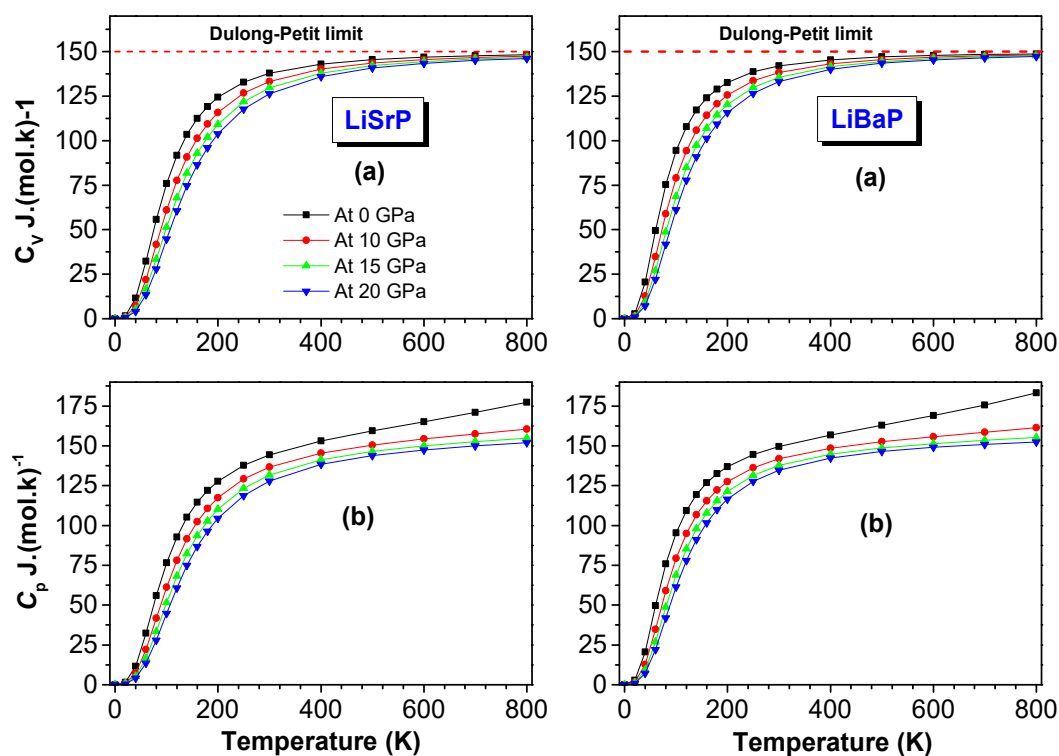


Figure VII.15 : (a) Variations of the heat capacity at constant volume C_V and (b) the heat capacity at constant pressure C_P versus temperature at some fixed pressures for the LiSrP and LiBaP compounds.

VII.2.7.6 The coefficient of thermal expansion

The coefficient of thermal expansion measures the relative increase in volume of a system when only one parameter is changed, usually pressure or temperature. Variations in the volume thermal expansion coefficient α of LiSrP and LiBaP as a function of temperature T at certain fixed pressures are shown in Figure VII.16. For $T \leq 250 \text{ K}$, the thermal expansion coefficient α increases rapidly with increasing temperature at fixed pressure in both considered compounds. For $T > 250 \text{ K}$, the increase of α with increasing temperature becomes more gradual and approaches a linear behavior. The rate of increase of α with increasing temperature

decreases with increasing pressure. Figure VII.16 shows that the pressure effect on α is small at low temperature and becomes substantial at high temperature. This means that there is a large volume thermal expansion coefficient at low pressure, which is in accordance with the variation of the unit-cell volume with pressure and temperature. At zero pressure and room temperature, α is approximately equal to 8.0672 K^{-1} for LiSrP and 8.5318 K^{-1} for LiBaP.

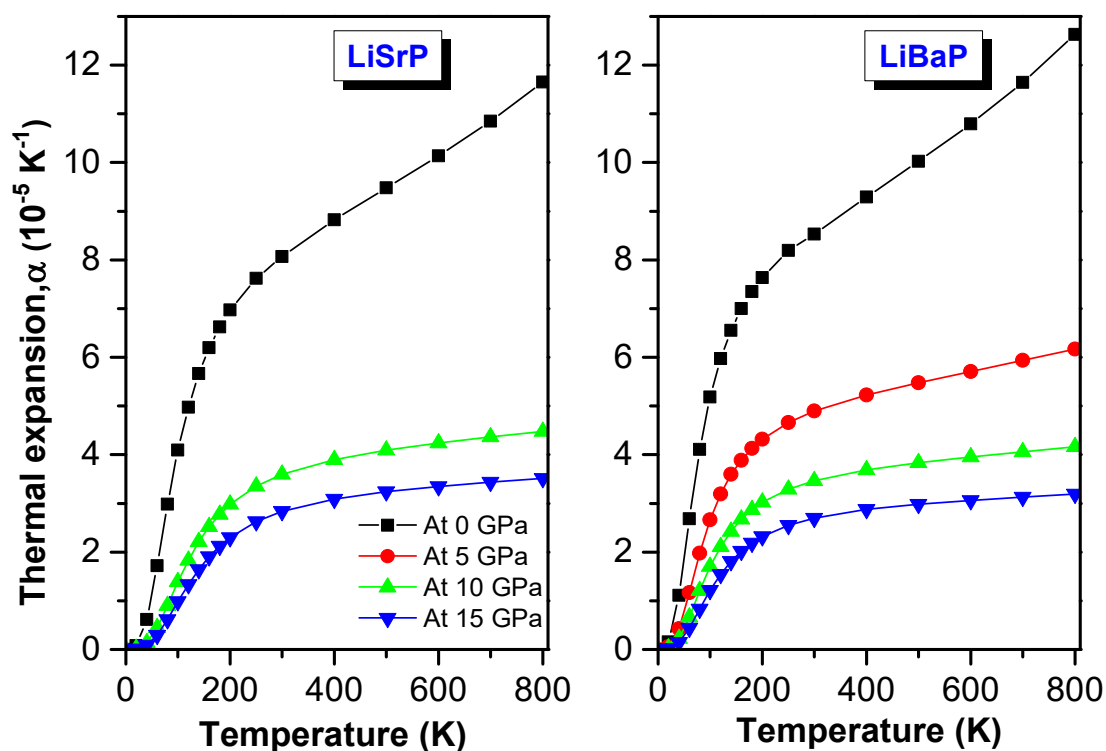


Figure VII.16 :Variation of the volume thermal expansion coefficient as a function of temperature at some fixed pressures for LiSrP and LiBaP.

References

- [1] S. J. Clark, M. D. Segall, C. J. Pickard, P. J. Hasnip, M. J. Probert, K. Refson and M. C. Payne, *Zeitschrift fuer Kristallographie*. **220**, 567 (2005).
- [2] J. P. Perdew, A. Ruzsinszky, G. I. Csonka, O. A. Vydrov, G. E. Scuseria, L. A. Constantin, X. Zhou, and K. Burke, *Phys. Rev. Lett.* **100**, 136406 (2008).
- [3] D. Vanderbilt, *Phys. Rev. B* **41**, 7892 (1990).
- [4] H. J. Monkhorst and J. D. Pack, *Phys. Rev. B* **13**, 5188 (1976).
- [5] T. H. Fischer and J. Almlof, *J. Phys. Chem.* **96**, 9768 (1992).
- [6] Daniel Royer, *Ondes élastiques dans les solides*. Masson, Paris (1996).
- [7] Y. Dong and F.J. DiSalvo, *J. Solid State Chem.* **180**, 432 (2007).
- [8] F. D. Murnaghan, *Proc. Natl. Acad. Sci.* **30**, 244 (1944).
- [9] M.M. Wu, L. Wen, B.Y. Tang, L.M. Peng, W.J. Ding, *J. Alloys Compd.* **506**, 412 (2010).
- [10] J.F. Nye, *Physical Properties of Crystals: Their Representation by Tensors and Matrices*, Oxford University Press, New York (1985).
- [11] L.D. Landau, E.M. Lifschitz, *Theory of Elasticity, Course of Theoretical Physics*, Pergamon Press, New York, (1980).
- [12] J.Y. Wang, Y.C. Zhou, T. Liao, Z.J. Lin, *Appl. Phys. Lett.* **89**, 021917 (2006).
- [13] W. Voigt, *Lehrbuch der Kristallphysik*, Taubner, Leipzig, (1928).
- [14] A. Reuss, *Z. Angew. Math. Mech.* **9**, 49 (1929).
- [15] R. Hill, *Proc. Phys. Soc., London, Sect. A* **65**, 349 (1952).
- [16] S. Aydin and M. Simsek, *J. Alloys Compd.* **509**, 5219 (2011).
- [17] M. Mattesini, M. Magnuson, F. Tasnádi, C. Höglund, A. Abrikosov Igor, L. Hultman, *Phys. Rev. B* **79**, 125122 (2009).
- [18] S. F. Pugh, *Philos. Mag.* **45**, 823 (1954).
- [19] O. L. Anderson, *J. Phys. Chem. Solids* **24**, 909 (1963).
- [20] P. Ravindran, L. Fast, P. A. Korzhavyi, B. Johansson, J. Wills, and O. Eriksson, *J. Appl. Phys.* **84**, 4891 (1998).
- [21] P. Lloveras, T. Castán, M. Porta, A. Planes, A. Saxena, *Phys. Rev. Lett* **100**, 165707 (2008).
- [22] Y. Mo, M. Pang, W. Yang, Y. Zhan, *Comput. Mater. Sci.* **69**, 160 (2013).
- [23] D.H. Chung and W.R. Buessem, *The Elastic Anisotropy of Crystals, in Proceeding of International Symposium 2, F.W. Vahldiek and S.A. Mersol, eds.*, Plenum Press, New York, NY, (1968).
- [24] S. I. Ranganathan, M. Ostoja-Starzewski, *Phys. Rev. Lett.* **101**, 055504 (2008).

- [25] A. Cazzani, *Appl. Math. Comput.* **238**, 397 (2014).
- [26] S. Zh. Karazhanov, P. Ravindran, H. Fjellvag, and B. G. Svensson, *J. Appl. Phys.* **106**, 123701 (2009).
- [27] D. R. Penn, *Phys. Rev.* **128**, 2093 (1962).
- [28] A. Bouhemadou and R. Khenata, *Comput. Mater. Sci.* **39**, 803 (2007).
- [29] R. Saniz, L. H. Ye, T. Shishidou, and A. J. Freeman, *Phys. Rev. B* **74**, 014209 (2006).
- [30] M. A. Blanco, E. Francisco, and V. Luaña, *Comput. Phys. Commun.* **158**, 57 (2004).
- [31] A. Bouhemadou, R. Khenata, B. Amrani, *Physica B: Condensed Matter* **404**, 3534 (2009).
- [32] M. Flórez, J.M. Recio, E. Francisco, M.A. Blanco, A.M. Pendás, *Phys. Rev. B* **66**, 144112 (2002).
- [33] E. Francisco, J.K.M. Recio, M.A. Blanco and A. Martin Pends, *J.Phys.Chem.* **102**, 1595 (1998).
- [34] E. Francisco, M. A. Blanco, and G. Sanjurjo, *Phys. Rev. B* **63**, 049107 (2001).
- [35] A.-T. Petit and P. L. Dulong, *Ann. Chim. Phys.* **10**, 395 (1819).

**VIII. Structural, elastic, electronic,
optical and Thermoelectric properties of
the Zintl-phase Ae_3AlAs_3 ($Ae=$ Sr, Ba)**

VIII.1 Computational details

First-principles calculations were performed by employing two complementary methods based on density functional theory. The elastic properties were evaluated using the pseudopotential plane wave (PP-PW) method as implemented in the CASTEP code [1], while the electronic and optical properties were carried out using the full potential linearised augmented plane wave method (FP-LAPW) as incorporated in the WIEN2k suite of programs [2]. The structural properties were evaluated using both the aforementioned methods. The structural data from Ref. [3] were taken as initial input for our calculations. For the pseudopotential plane wave approach, Vanderbilt ultra-soft pseudo-potentials [4] were used to describe the interactions between core and valence electrons of each atom. The Ba: $5s^25p^66s^2$, Sr: $4s^24p^65s^2$, Al: $3s^23p^1$ and As: $4s^24p^3$ states were treated as valence electrons. The electronic exchange and correlation effects were treated through the generalised gradient approximation functional in the version of Perdew et al. [5], the so-called GGA-PBEsol. The plane-wave basis set energy cut-off was set at 350 eV. The Brillouin zone integration was replaced by a summation over a $6 \times 6 \times 3$ k-point mesh generated according to Monkhorst-Pack scheme [6]. This set of parameters assures a total energy tolerance of 1×10^{-5} eV/atom, a maximum force tolerance of 0.01 eV/Å, a maximum stress of 0.02 GPa and a maximum displacement of 5.0×10^{-4} Å. It is well known that the first-principles methods with the common generalised gradient approximation (GGA) yield good values for the ground state structures but they underestimate the band gaps of semiconductors and insulators typically by 30–50% [7-9] when compared to experiments. The underestimation of the band gaps of semiconductors and insulators when using GGA is because this approximation cannot describe exactly the exchange–correlation potential. Some sophisticated approaches, such as the weighted density approximation (WDA) [10], the GW approximation [11] and the Tran-Blaha modified Becke-Johnson (TB-mBJ) potential [12], have been developed in order to overcome this insufficiency and to obtain reliable band gap values for semiconductors and insulators compared to the measured ones. The TB-mBJ is computationally cheaper than the other aforementioned methods and produces energy band gaps almost comparable with the corresponding measured ones with a reasonable computation time. Therefore, in addition to the GGA-PBEsol, the electronic, optical and thermoelectric properties of the investigated compounds were calculated using the TB-mBJ functional as implemented in the WIEN2k package [2]. The WIEN2k code is an implementation of the full-potential linearised augmented plane wave (FP-LAPW). In the FP-LAPW method, the unit cell

is divided into non-overlapping spheres centred at the atomic sites (labelled muffin-tin spheres (MTS)) and the space between the MTS (labelled interstitial region (IR)). A linear combination of radial atomic functions time spherical harmonics is used inside the MTS to expand the wave functions, whereas a plane wave basis set is used in the IR. In order to achieve the energy convergence of the eigenvalues, the wave functions in the interstitial regions were expanded in plane waves with a cut-off parameter $K_{Max} = 4$ (a.u.)⁻¹. The Brillouin zone integration was replaced by a $6 \times 6 \times 3$ k-point mesh. The iteration process was repeated until the calculated total energy of the crystal converged to less than 10^{-5} Ry. The muffin-tin radii were selected as 2.35 a.u. for Sr, 2.40 a.u. for Ba, 2.18 a.u. for Al and 2.44 a.u. for As..

VIII.2 Results and discussion

VIII.2.1 Structural parameters

Single-crystal X-ray diffraction technique reveals that the Ae_3AlAs_3 ($Ae = Sr, Ba$) compounds crystallise in the orthorhombic Ba_3AlSb_3 -type structure, space group $Cmce$, with eight formula units in one-unit cell [3] (Figure VIII.1). There are two kinds of Ae (Ae1 and Ae2) and As (As1 and As2) atoms. The Wyckoff atomic positions in the Ae_3AlAs_3 unit cell are Ae1: 8f (0, y_{Ae1} , z_{Ae1}); Ae2: 16 g (x_{Ae2} , y_{Ae2} , z_{Ae2}); Al: 8d (x_{Al} , 0, 0); As1: 8f (0, y_{As1} , z_{As1}) and As2: 16 g (x_{As2} , y_{As2} , z_{As2}). The fully optimised crystal structure, including lattice parameters and atomic positions, for the orthorhombic Sr_3AlAs_3 and Ba_3AlAs_3 crystals, using both the PP-PW and FP-LAPW methods, are collected in Table VIII.1 and VIII.2 in comparison with experimental findings. The inspection of Table VIII.1 data indicates a good agreement between the calculated values for the lattice parameters (a, b and c) and the corresponding measured ones. Using the PP-PW (FP-LAPW) method, the deviations between the theoretical values of a, b and c and the corresponding experimental ones do not exceed +2.03% (-0.51%), -0.72% (-3.27) and +0.67% (-0.01%), respectively, in Sr_3AlAs_3 , and -0.03% (-1.38%), -0.34% (-7.48%) and -0.107% (-0.51%), respectively, in Ba_3AlAs_3 .

Table VIII.2 data show also a very good agreement between the calculated atomic position coordinates (x, y, z) and the corresponding measured ones, indicating the reliability of the performed calculations.

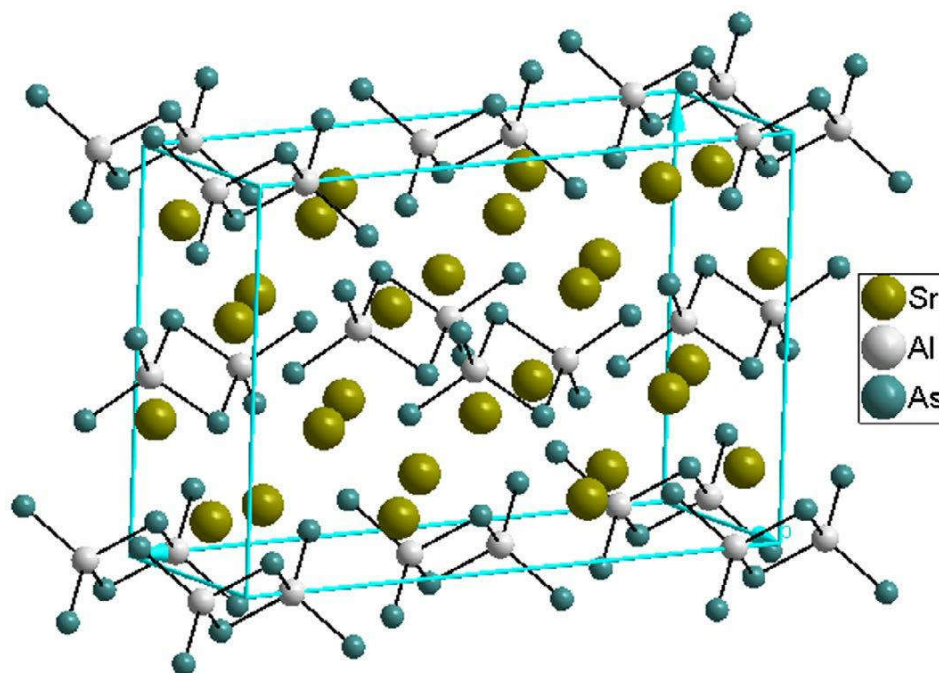


Figure VIII.1 :(colour online) one-unit cell of Sr_3AlAs_3 .

Table VIII.1: Calculated lattice parameters (a , b and c , in Å) and unit-cell volume (V , in Å³) for the Sr_3AlAs_3 and Ba_3AlAs_3 compounds, compared with the experimental data.

	a	b	c	V
Sr_3AlAs_3				
Present work ^a	19.0503	6.3501	12.7002	1587.22
Present work ^b	19.5368	6.5174	12.7729	1626.39
Expt. [3]	19.149	6.5652	12.6871	1595.0
Ba_3AlAs_3				
Present work ^a	19.5795	6.3501	13.2294	1737.92
Present work ^b	19.8475	6.8406	13.2741	1802.22
Expt. [3]	19.854	6.8636	13.2849	1810.3

^a using FP-LAPW method within GGA-PBEsol

^b using PP-PW method within GGA-PBEsol

Table VIII.2 : Atomic position coordinates for the Sr_3AlAs_3 and Ba_3AlAs_3 compounds, compared with the experimental data.

Atom	X			Y			Z		
	Present work ^a	Present work ^b	Expt ^c	Present work ^a	Present work ^b	Expt ^c	Present work ^a	Present work ^b	Expt ^c
Sr_3AlAs_3									
Sr1	0	0	0	0.17601	0.17924	0.17463	0.34919	0.34707	0.34891
Sr2	0.17701	0.17755	0.17691	0.31155	0.30838	0.31222	0.13114	0.13009	0.13126
Al	0.08477	0.08377	0.08500	0	0	0	0	0	0
As1	0	0	0	0.21042	0.21277	0.20879	0.10330	0.10079	0.10250
As2	0.34107	0.34207	0.34135	0.29518	0.29326	0.29606	0.12081	0.11794	0.12022
Ba_3AlAs_3									
Ba1	0	0	0	0.17027	0.17109	0.17015	0.34671	0.34766	0.34685
Ba2	0.17572	0.17535	0.17563	0.31309	0.31201	0.31318	0.13024	0.12975	0.13014
Al	0	0.08316	0.08294	0	0	0	0	0	0
As1	0	0	0	0.20320	0.20566	0.20319	0.09628	0.09791	0.09613
As2	0.34335	0.34294	0.34345	0.30899	0.30728	0.30905	0.11818	0.11954	0.11805

^a using FP-LAPW method within GGA-PBEsol

^b using PP-PW method within GGA-PBEsol.

^c Ref. [23].

VIII.2.2 Elastic constants and related properties

Accurate calculations of the elastic constants C_{ij} are very helpful to understand many physical properties of solids. The elastic constants C_{ij} provide valuable information on the stability and stiffness of crystals against externally applied strain, bonding characteristics, specific heat, thermal expansion, Debye temperature, Grüneisen parameter and so on [13–15]. In general, the elastic behaviour of a completely asymmetric material is specified by 21 independent elastic constants C_{ij} but due to the presence of some symmetries, this number can be reduced. Only nine independent elastic constants, namely $C_{11}, C_{22}, C_{33}, C_{44}, C_{55}, C_{66}, C_{12}, C_{13}$ and C_{23} , are required to characterise the elastic properties of an orthorhombic crystal. The elastic constants C_{ij} were evaluated via the calculation of three stress tensors

corresponding to three different deformation patterns applied to the equilibrium lattice. The calculated elastic constants C_{ij} using the strain–stress method [1] for the title compounds are reported in Table VIII.3. There are no theoretical or experimental results for the elastic constants C_{ij} in the scientific literature to be compared with the present results. Then, our results can serve as a prediction for future investigations.

The elastic constants C_{11} , C_{22} and C_{33} reflect the resistance to the linear compression along the [100], [010] and [001] crystallographic directions, respectively. From Table VIII.3, one can note that the values of the three aforementioned elastic constants are not remarkably different, suggesting that the resistance to the compression deformation along the [100], [010] and [001] directions are approximately equal. The values of C_{11} , C_{22} and C_{33} are higher than those of the other elastic constants C_{ij} , demonstrating that the resistance of the two studied compounds to the shear distortion is lower than their resistance against the compressional deformation.

The mechanical stability of crystals leads to some restrictions on their elastic constants. For orthorhombic crystals, these mechanical stability criteria are [16]:

$$C_{11} + C_{22} - 2C_{12} > 0, \quad C_{11} + C_{33} - 2C_{13} > 0, \quad C_{22} + C_{33} - 2C_{23} > 0, \quad C_{11} > 0, C_{22} > 0, \\ C_{33} > 0, C_{44} > 0, C_{55} > 0, C_{66} > 0, C_{11} + C_{22} + C_{33} + 2C_{12} + 2C_{13} + 2C_{23} > 0 \quad (\text{VIII.1})$$

The calculated elastic constants of the two studied compounds (Table VIII.3) satisfy the aforementioned criteria. This indicates that these compounds are mechanically stable.

Table VIII.3: Calculated elastic constant (C_{ij} , in GPa) for the Ae_3AlAs_3 ($Ae = Sr, Ba$) compounds.

Compounds	C_{11}	C_{22}	C_{33}	C_{44}	C_{55}	C_{66}	C_{12}	C_{13}	C_{23}
Sr_3AlAs_3	61.69	74.61	76.58	32.37	28.62	30.29	27.10	22.58	31.30
Ba_3AlAs_3	80.24	71.14	81.49	17.07	4.65	14.05	21.60	15.32	23.99

It is not possible to measure the individual elastic constants C_{ij} when single-crystal samples cannot be obtained. In this case, polycrystalline elastic moduli, such as the bulk modulus B and the shear modulus G , can be measured. Theoretically, we can deduce the polycrystalline (aggregates of single-crystals with random orientations) elastic moduli, which are more desirable for technological characterisation of materials, from the calculated single-crystal elastic constants C_{ij} . The isotropic shear and bulk moduli (G and B) can be calculated

from the anisotropic single-crystal elastic constants C_{ij} using the Hill approximation [17], which takes the arithmetic average of the Voigt [18] and Reuss [19] approximations. The Voigt approach determines the upper limit of the actual effective moduli, while the Reuss approach determines the lower limit of these parameters. The expression of the Voigt bulk and shear moduli (B_V and G_V) and the Reuss bulk and shear moduli (B_R and G_R) can be found in Ref. [20]. The Young's modulus E and Poisson's ratio σ can be obtained from B and G using the well-known relationships [21, 22]. The calculated values of the aforementioned elastic moduli are given in Table VIII.4. The obtained results allow us to make the following conclusions:

- (i) Due to the low value of the bulk modulus, which represents the resistance to volume change by external applied pressure, one can conclude that the considered materials are characterised by a weak resistance to the volume change; i.e. by a high compressibility. The lower value of the shear modulus, which characterises the resistance to shear deformation, demonstrates that Ba_3AlAs_3 and Sr_3AlAs_3 have also a weak resistance to shape change. Besides, the bulk modulus B is larger than the shear modulus G in both considered compounds, indicating a better capability of resistance to volume change than to shape change.
- (ii) The Young's modulus E , defined as the ratio of linear stress to linear strain, can be used to provide a measure of the stiffness of a material. It is found that E of the two studied compounds is weak, indicating that these compounds will show a rather small stiffness. The results also demonstrate that Sr_3AlAs_3 is stiffer than Ba_3AlAs_3 in terms of B , G and E moduli.
- (iii) The most widely used criterion to distinguish between ductile and brittle materials is the Pugh's one (B/G ratio) [23]. According to this criterion, a material can be classified as ductile if the B/G ratio is greater than 1.75; otherwise, it demonstrates brittleness. The obtained data foretell that Sr_3AlAs_3 ($B/G = 1.55$) should behave as brittle material, while Ba_3AlAs_3 should demonstrate ductility. The classical criteria of Cauchy pressure can also be used to examine the brittle/ductile character of materials [24]. Pettifor [25] indicated that Cauchy pressure can be adopted to capture the nature of the bonding. Materials with a positive Cauchy pressure possess metallic like bonds, thereby holding ductile characteristics. On the other hand, brittle materials would hold a negative Cauchy pressure. In orthorhombic materials, the Cauchy pressure in the three lattice directions can be expressed as follows [26]:

$$\begin{cases} P_a^{Cauchy} = C_{22} - C_{44} \\ P_b^{Cauchy} = C_{13} - C_{55} \\ P_c^{Cauchy} = C_{12} - C_{66} \end{cases} \quad (VIII.2)$$

Based on calculated single-crystal C_{ij} (Table VIII.3) :

$P_a^{Cauchy} = -1.10GPa(6.90GPa)$, $P_b^{Cauchy} = -6.0GPa(10,60GPa)$ and $P_c^{Cauchy} = -3.0GPa(7.50GPa)$ for Sr_3AlAs_3 (Ba_3AlAs_3). These results confirm the brittleness of Sr_3AlAs_3 and ductility of Ba_3AlAs_3 .

Table VIII.4 : Calculated polycrystalline elastic moduli: Reuss, Voigt and Hill bulk modulus (B_R , B_V and B_H , in GPa), Reuss, Voigt and Hill shear modulus (G_R , G_V and G_H , in GPa), Young's modulus (E , in GPa) and Poisson's ratio (dimensionless) for isotropic polycrystalline Ae_3AlAs_3 ($Ae = Sr, Ba$) aggregates.

System	B_V	G_V	B_R	G_R	B_H	G_H	E_j			E	σ
							E_x	E_x	E_x		
Sr_3AlAs_3	41.65	39.60	40.92	26.15	41.29	26.60	72.80	60.30	72.52	65.70	0.23
Ba_3AlAs_3	39.41	32.73	39.39	12.02	39.40	15.32	72.80	60.30	72.52	40.69	0.32

From the computed bulk and shear moduli, we can evaluate the longitudinal (V_l), transverse (V_t) and average (V_m) sound wave velocities in a polycrystalline material through the following relationships [27]:

$$v_l = \sqrt{(B_H + 4G_H/3)/\rho} , v_t = \sqrt{G_H/\rho} \text{ and } v_m = [(2/v_t^3 + 1/v_l^3)/3]^{-1/3} \quad (VIII.3)$$

Debye temperature θ_D , which is associated with the lattice vibration, elastic constants, specific heat and melting point, can be predicated via the following common relation [27]:

$$\theta_D = \frac{h}{k_B} \left[\frac{3n}{4\pi} \left(\frac{N_A \rho}{M} \right) \right]^{\frac{1}{3}} v_m \quad (VIII.4)$$

Here, h and k_B are the constants of Planck and Boltzmann, respectively, n is the number of atoms per one formula unit, N_A is Avogadro's number, ρ denotes the mass density, M is the molecular mass. The calculated values of ρ , v_l , v_t , v_m and θ_D for the Ae_3AlAs_3 ($Ae = Sr, Ba$) compounds are collected in Table VIII.5. Sr_3AlAs_3 has a larger Debye temperature than Ba_3AlAs_3 ; this is a predicted result because the bulk modulus of Sr_3AlAs_3 is somewhat larger

than that of Ba_3AlAs_3 . Up to now, there are no available data for these parameters in the scientific literature to be compared with our present findings.

Table VIII.5: Calculated mass density (ρ), longitudinal, transverse and average sound velocities (v_l , v_t and v_m , respectively) and Debye temperatures (θ_D) for Ae_3AlAs_3 ($Ae=Sr, Ba$).

System	$\rho(\frac{g}{cm^3})$	$v_l(\frac{m}{s})$	$v_t(\frac{m}{s})$	$v_m(\frac{m}{s})$	$\theta_D(K)$
Sr_3AlAs_3	4.20332	4273.50	2331.94	2600.81	251.95
Ba_3AlAs_3	4.89248	3961.10	1769.79	1996.65	186.91

An isotropic material displays the same physical properties irrespective of the direction in which those properties are measured. In general, the elastic response of a single-crystal is seldom isotropic; almost all the known crystals are elastically anisotropic, so their elastic moduli depend on the orientation of the applied force in respect of the crystallographic axes. The description of elastic anisotropy in materials is important because it influences various physical properties, such as unusual phonon modes, phase transformations, precipitation, dislocation dynamics, anisotropic plastic deformation, anomalous bcc slip, mechanical yield points, crack behaviour, elastic instability and internal friction [28]. The anisotropy in mechanical properties might be estimated using various anisotropy indexes and factors [29–34]. An even detailed picture of the elastic anisotropy can be emerged by plotting a three-dimensional surface representation showing the variation of the Young's modulus with the crystallographic directions. This directional dependence of the Young's modulus E for an orthorhombic crystal in an arbitrary direction is defined as [35]:

$$Y = [S_{11}l_1^4 + 2S_{12}l_1^2l_2^2 + S_{22}l_2^4 + 2S_{23}l_2^2l_3^2 + S_{33}l_3^4 + 2S_{13}l_1^2l_3^2 + S_{44}l_2^2l_3^2 + S_{55}l_1^2l_3^2 + S_{66}l_1^2l_2^2]^{-1} \quad (VIII.5)$$

Here, l_1 , l_2 and l_3 are the direction cosines, which determine the angles between the axes a , b and c , respectively, and a given direction, and S_{ij} is the elastic compliance constants, which can be acquired from the inverse of the matrix of elastic constants. The distance from the origin of the coordinate system to this surface is equal to the Young's modulus in a given direction. For a perfectly isotropic medium, this surface would be a sphere, while the deviation of this surface from the spherical shape indicates the presence of a certain degree of elastic anisotropy. [Figure](#).

VIII. 2 illustrates the directional dependence of the Young's modulus of the Sr_3AlAs_3 and Ba_3AlAs_3 compounds. Figure. VIII. 2 shows that the degree of elastic anisotropy of Ba_3AlAs_3 is much more appreciable than that of Sr_3AlAs_3 . A deeper look into the peculiar features of elastic anisotropy can be gauged by plotting the cross-section of the closed surface of E in the principal planes. For isotropic crystal, the plane projection curves are circular. From the cross sections plotted separately in Figure VIII.2, we can see that there is a clear deviation from circular shape.

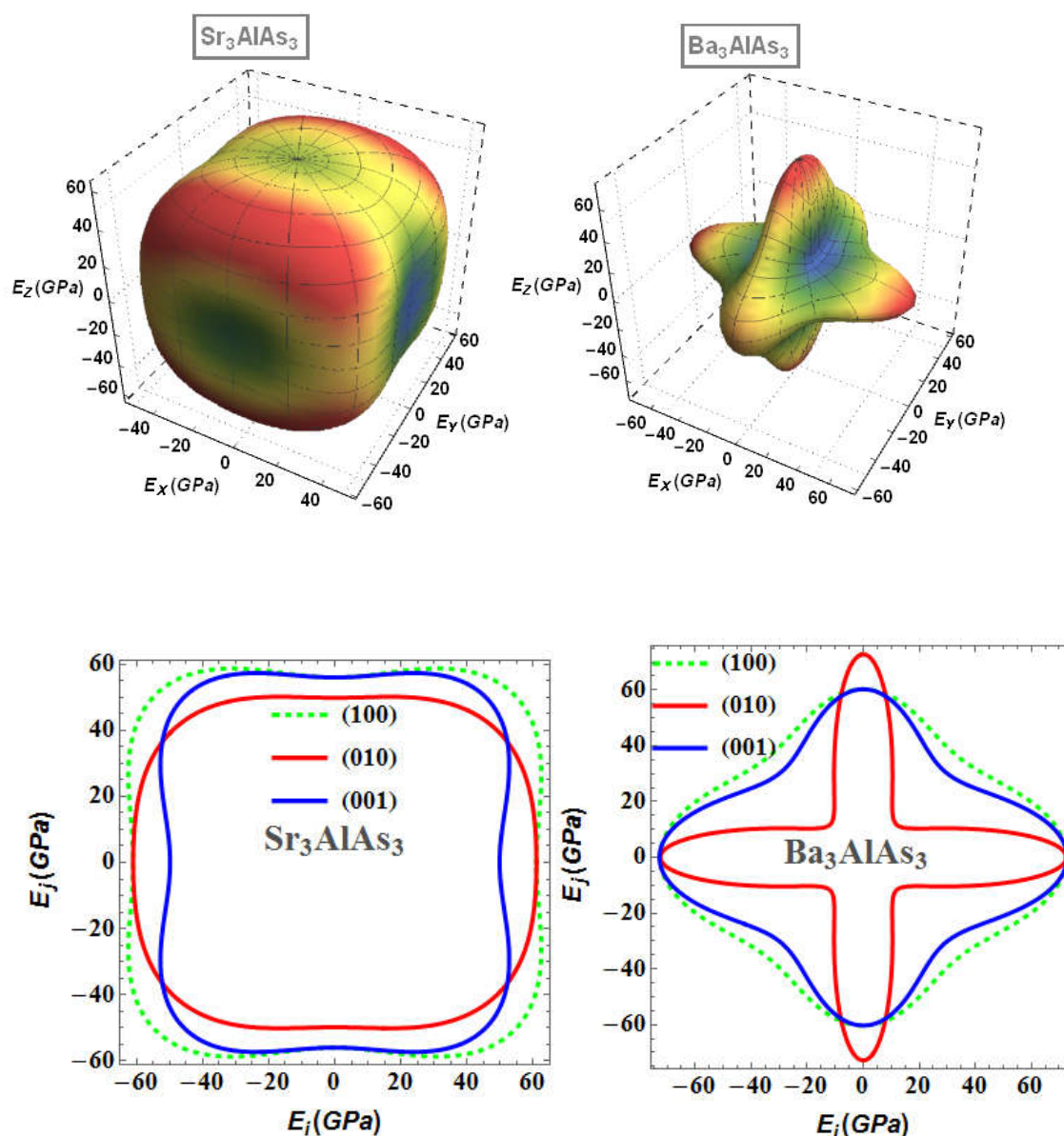


Figure VIII.2 :(colour online) 3D-directional dependence of the Young's modulus (E , in GPa) and its projection on the ab- $\{(001)\}$, ac- $\{(010)\}$ and cb- $\{(100)\}$ planes for the Sr_3AlAs_3 and Ba_3AlAs_3 compounds.

VIII.2.3 Electronic properties

VIII.2.3.1 Band structure

The electronic energy band dispersions along the high-symmetry directions in the Brillouin zone (BZ) for the Sr_3AlAs_3 and Ba_3AlAs_3 compounds, performed at the optimised structural parameters, using the FP-LAPW method with both the GGA-PBEsol and TP-mBJ approaches, are depicted in [Figure VIII.3](#). The Γ , Z, T, Y, S and R letters indicate the high symmetry points in the BZ of the Ae_3AlAs_3 ($Ae = Sr, Ba$) compounds and their coordinates are respectively $(0,0,0)$, $(0,0,0.5)$, $(-0.5,0.5,0.5)$, $(-0.5, 0.5, 0)$, $(0,0.5,0)$ and $(0,0.5,0.5)$ in the unit vectors of the reciprocal lattice. From [Figure VIII.3](#), one can note that Sr_3AlAs_3 has a direct band gap; the top of the valence band (VB) and the bottom of the conduction band (CB) are located at the Γ -point, while Ba_3AlAs_3 has an indirect band gap; the top of the VB is located at the Y-point and the bottom of the CB is at the Γ -point. The calculated band structures using the TB-mBJ and GGA-PBEsol functionals have practically same features except the band gap values that are disparate. The calculated Sr_3AlAs_3 (Ba_3AlAs_3) energy band gap is 1.51 eV (1.28 eV) when using the TB-mBJ formalism, and is 0.90 eV (0.61 eV) when using the GGA-PBEsol. We note that the GGA and LDA functionals usually underestimate the energy band gap by 30–50% [30–32]. Therefore, one can appreciate that the TB-mBJ considerably improves the band gap values. There are no experimental values for the gaps of the studied compounds. The GGA-PBEsol band gap value for Ba_3AlAs_3 is in good agreement with the one predicted by Stanislav et al. [3] using the tight-binding linear muffin tin orbital (TB-LMTO) method within the LDA.

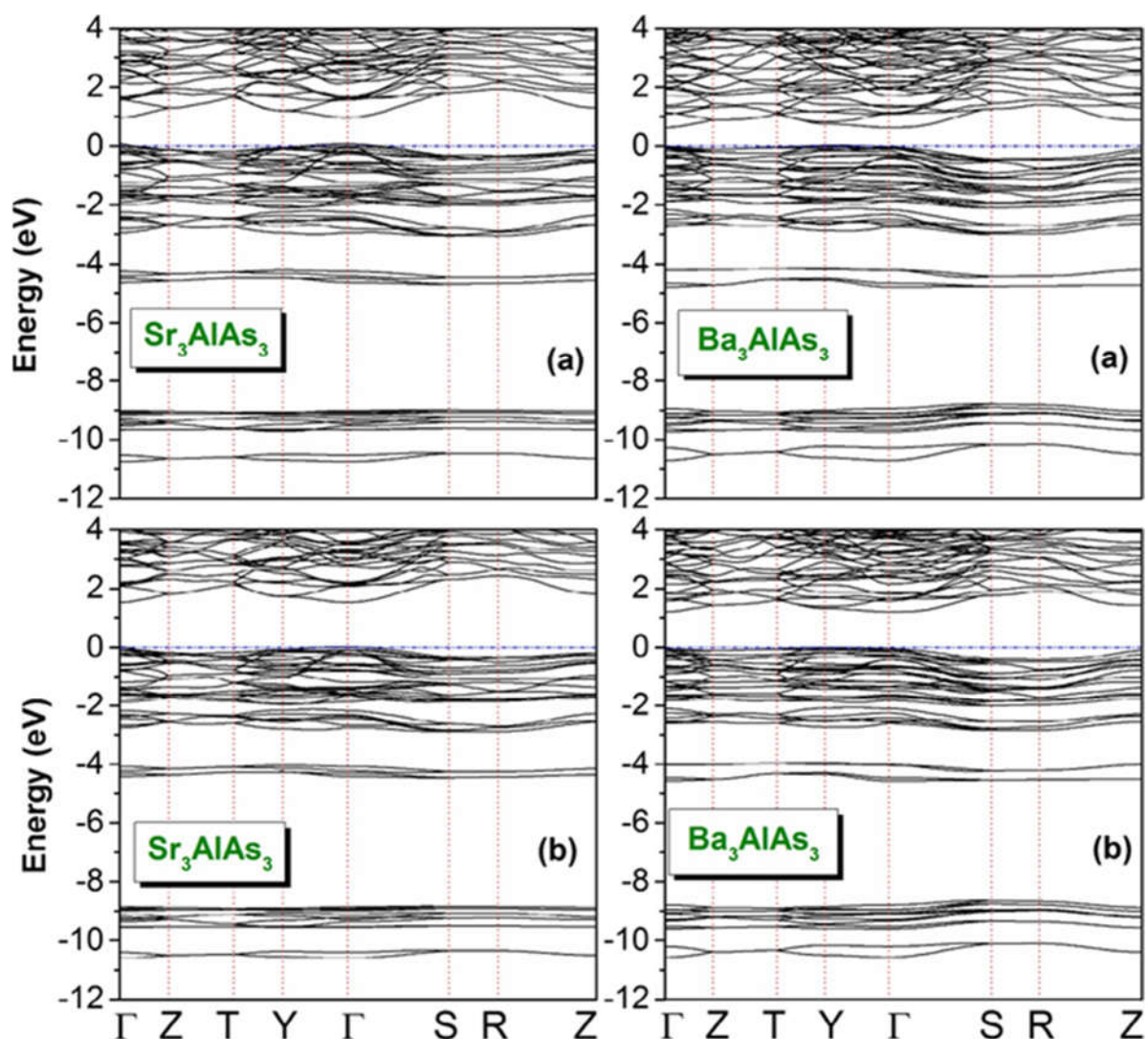


Figure VIII.3 : (colour online) Electronic band dispersion curves along some high symmetry directions in the Brillouin zone for the Ae_3AlAs_3 ($Ae = Sr, Ba$) compounds using the GGA-PBEsol (a) and the TB-mBJ (b) functionals.

VIII.2.3.2 Density of states

Assignment of the electronic states composing the electronic energy bands of the considered systems can be made with the help of the total and atomic decomposed partial densities of states (TDOS and PDOS) diagrams, which are shown in [Figure VIII.4](#). The Sr_3AlAs_3 and Ba_3AlAs_3 valence bands located in the energy range from -12 eV up to Fermi level (E_F) can be separated into four groups that are labelled V1, V2, V3 and V4 in the [Figure VIII.4](#). For Sr_3AlAs_3 , the lowest energy group V1, which is stretched from approximately -10.6 to -9.9 eV, is mainly formed of the As1-4s and As2-4s states. The second group V2, which

spreads approximately from -9.7 to -8.5 eV, is mainly due to the As1-4p and Al-3s states with a very small contribution from an admixture of the Al-3s, Al-3p, Sr1-4p and Sr2-4p orbitals. The third group V3, located in the energy range from -4.6 to -3.97 eV, is mainly due to the As1-4p and Al-3s states. The fourth valence band group V4, which lays approximately from -3.0 eV up to Fermi level (EF), is completely dominated by the As1-4p and As2-4p states with a small contribution from the Al-3p, Sr1-4s, Sr2-4s, Sr1-4p, Sr2-4p, Sr1-3d and Sr2-3d states. The bottom of the conduction band (C1) comes from the Sr1-3d and Sr2-3d states with a small contribution from the Al-3p and Al-3s states. For the Ba_3AlAs_3 compound, the V1 valence band group, from -10.7 to -9.97 eV, is mainly occupied by the As1-4s states with a small contribution from an admixture of the Ba1-5p, Ba2-5p, As2-4d and Al-3s states. The second group V2, from -9.7 to -8.5 eV, is mainly formed of the As1-4s states with a small contribution from an admixture of the Ba1-5p, Ba2-5p, As2-4d and Al-3sp states. The third group V3, from -4.7 to -3.82 eV, is mainly composed of the As2-4d and As1-4p states with a small contribution from the Ba1-4p, Ba1-4d, Ba2-4p and Ba2-4d. The upper valence band group V4, from -3.05 eV up to Fermi level, is mainly due to the As1-4p and As2-4sd states with a small contribution from the Al-3p and Ba1-4pd orbitals. The bottom of the conduction band C1 is made up basically of the As2-4d, Ba1-4d and Ba2-4d states with a small contribution from the Al-3s and Al-3p states.

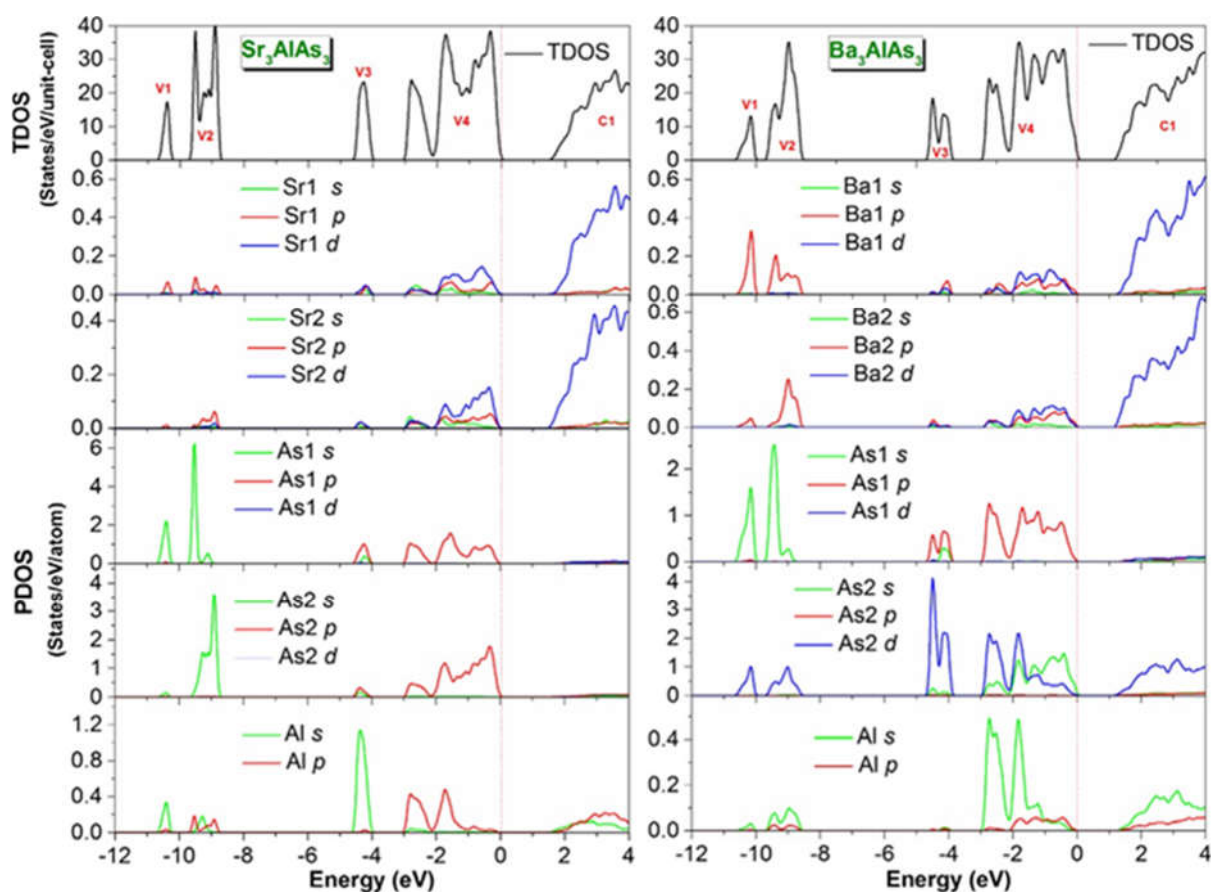


Figure VIII.4 : (colour online) Total and partial densities of states (TDOS and PDOS) diagrams for the Ae_3AlAs_3 ($Ae = Sr, Ba$) compounds.

VIII.2.3.3 Effective mass

The effective mass of charge-carrier provides an opposite contribution to the Seebeck coefficient and electrical conductivity. A large effective mass of charge-carrier is favourable to improve the Seebeck coefficient; however, the high charge-carrier mobility requires a lighter effective mass. To further understand the electrical behaviour of the Ae_3AlAs_3 ($Ae = Sr, Ba$) compounds, it is necessary to estimate their effective masses of the charge-carries in various electron and hole pockets at the band edges. For Ba_3AlAs_3 , the effective masses of the holes (m_h^*) at the VBMA were calculated along the $Y \rightarrow T$ and $Y \rightarrow \Gamma$ directions and those of the electrons m_e^* at the CBMi were evaluated along the $\Gamma \rightarrow S$ and $\Gamma \rightarrow Y$ directions. For Sr_3AlAs_3 , the effective masses of holes and electrons are calculated along the $\Gamma \rightarrow S$ and $\Gamma \rightarrow Y$ directions. The obtained results are listed in Table VIII.6. From Table VIII.6, it is clear that the electrons and holes effective masses show a relevant dependence on the k-direction in the two considered compounds, implying the anisotropy of this physical property. It is found also that

the effective mass of electron at the conduction band minimum is small than that of the hole at the valence band maximum. Consequently, the p-type Ae_3AlAs_3 ($Ae = Sr, Ba$) compounds would have the highest Seebeck coefficient, while the n-type Ae_3AlAs_3 ($Ae = Sr, Ba$) compounds would have the largest electrical conductivity. In addition, we can predict that the charge-carrier mobility of the p-type Sr_3AlAs_3 (Ba_3AlAs_3) compound along the $\Gamma \rightarrow S$ ($\Gamma \rightarrow Y$) direction should be larger than that in the $\Gamma \rightarrow Y$ ($Y \rightarrow T$) direction.

Table VIII.6 : Calculated electron and hole effective masses (m_e and m_h in units of free electron mass m_0) for the Sr_3AlAs_3 and Ba_3AlAs_3 compounds.

System	m_e^* ($\Gamma \rightarrow S$)	m_e^* ($\Gamma \rightarrow Y$)	m_h^* ($\Gamma \rightarrow S$)	m_h^* ($\Gamma \rightarrow Y$)
Sr_3AlAs_3	0.2007	0.2202	0.3225	4.0226
	m_e^* ($\Gamma \rightarrow S$)	m_e^* ($\Gamma \rightarrow Y$)	m_h^* ($Y \rightarrow T$)	m_h^* ($Y \rightarrow \Gamma$)
Ba_3AlAs_3	0.2158	0.3738	0.6161	0.551399

VIII.2.4 Optical properties

Since the investigated compounds belong to the orthorhombic system, space group $Cmce$, it is necessary to calculate the three non-zero components of the dielectric tensor that correspond to the three polarisations of the electric field \vec{E} of the incident electromagnetic radiation along the three principal crystallographic directions: a ([100]), b ([010]) and c ([001]).

VIII.2.4.1 The dielectric functions

The calculated imaginary parts of the Sr_3AlAs_3 and Ba_3AlAs_3 dielectric functions for the three different polarisations, i.e. $\vec{E} \parallel [100]$, $\vec{E} \parallel [010]$ and $\vec{E} \parallel [001]$, are presented in [Figure VIII. 5\(a\)](#). It is clear from [Figure VIII.5\(a\)](#) that the optical properties of the considered compounds exhibit a noticeable anisotropy. To account for the features observed in the optical spectra, it is customary to consider transitions from occupied to unoccupied states in the electronic energy band structure, especially at the high symmetry points in the Brillouin zone.

Our scrutiny of the $\varepsilon_2(\omega)$ curve of Sr_3AlAs_3 indicates that it rises speedily with practically the same rate for the three different polarisations of the incident radiation. The $\varepsilon_2(\omega)$ spectrum exhibits two peaks centred at approximately 3.99 and 4.56 eV when the incident radiation is polarised parallel to the [100] crystallographic direction, at 4.01 and 4.91 eV for \vec{E}

// [010] and at 4.53 and 4.97 eV when $\vec{E} // [001]$. Based on the calculated band structure and density of states diagrams, one can conclude that these peaks are mainly originated from the direct transitions between the Sr1-4p and Sr2-4p or As1-4p and As2-4p states in the valence band and the Sr-3d states in the conduction band. The absorptive part of the dielectric function of the single-crystal Ba_3AlAs_3 exhibits one peak centred at approximately 4.20 eV for $\vec{E} // [100]$, at 4.97 eV for $\vec{E} // [010]$ direction and at approximately 4.23 eV for $\vec{E} // [001]$. This peak is mainly due to the electronic direct transitions from the occupied state As1-4p or As2-4s to the unoccupied states Ba1-3d or Ba2-3d.

The dispersive parts $\varepsilon_1(\omega)$ of the Sr_3AlAs_3 and Ba_3AlAs_3 dielectric functions are shown in Figure VIII.5 (b). The most important quantity in $\varepsilon_1(\omega)$ spectrum is the static dielectric constant, which is defined as the zero-energy value of the real part of the complex dielectric function: $\varepsilon_1(0) = \varepsilon_1(\omega \rightarrow 0)$. The $\varepsilon_1(0)$ is a parameter of fundamental importance in many aspects of material properties. Calculated $\varepsilon_1(0)$ value for Sr_3AlAs_3 (Ba_3AlAs_3) is found to be equal 8.048 (8.683) when $\vec{E} // [100]$, 7.566 (8.255) when $\vec{E} // [010]$ and 7.810 (8.361) when $\vec{E} // [001]$. One can note that the $\varepsilon_1(0)$ values corresponding to the three different polarisation directions are larger than the corresponding ones for Ba_3AlAs_3 . This demonstrates that $\varepsilon_1(0)$ value is inversely proportional with the band gap; a smaller energy gap yields a larger $\varepsilon_1(0)$ value. This is consistent with the Penn's model [36] based on the expression $\varepsilon_1(0) \approx 1 + \left(\frac{\hbar\omega_p}{E_g}\right)^2$.

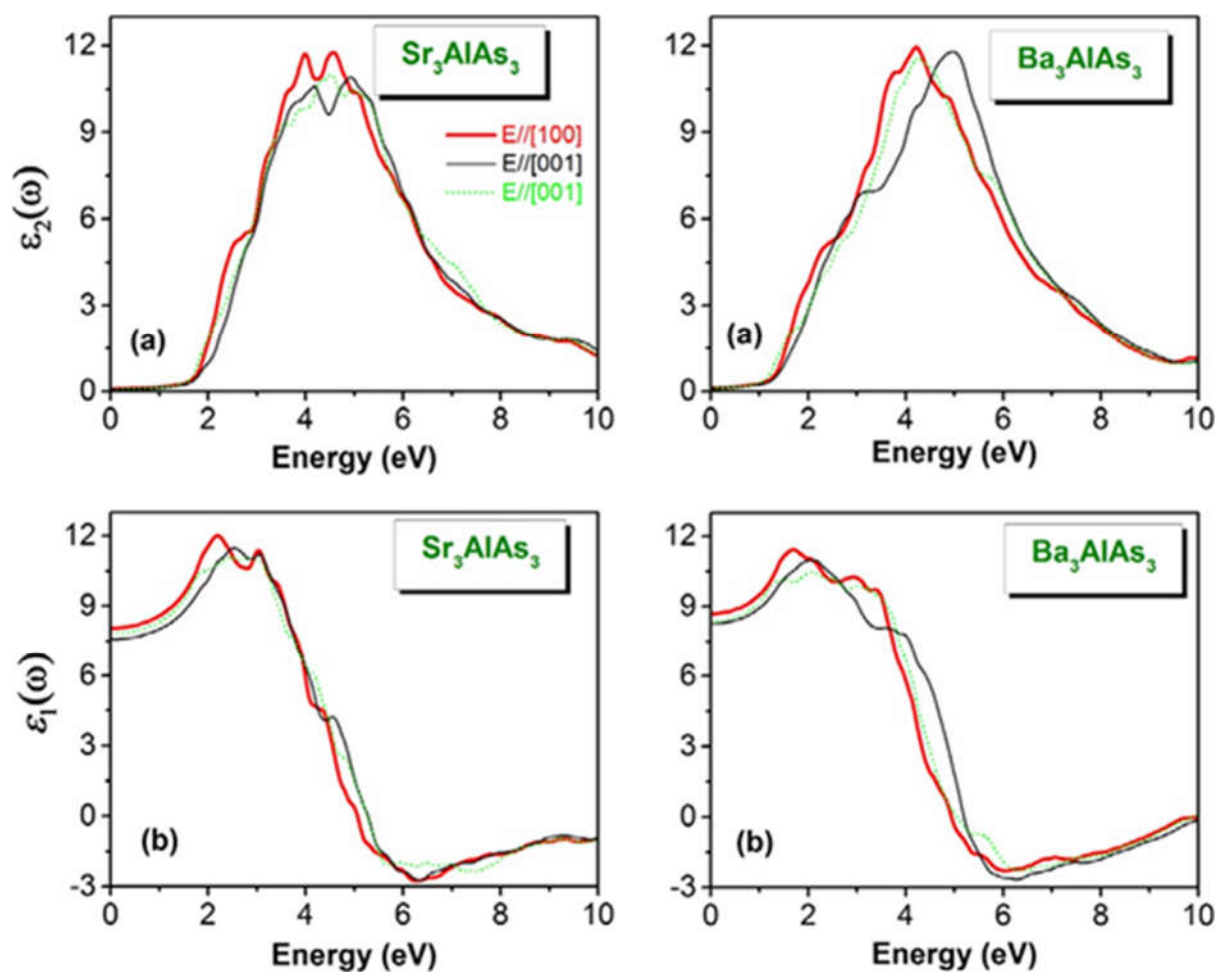


Figure VIII.5 : (colour online) calculated imaginary ($\epsilon_2(\omega)$) and real ($\epsilon_1(\omega)$) parts of the dielectric function ($\epsilon(\omega)$) as functions of photon energy for the Ae_3AlAs_3 ($Ae = Sr, Ba$) single-crystals for three different polarisations: $\vec{E} // [100]$, $\vec{E} // [010]$ and $\vec{E} // [001]$.

VIII.2.4.2 The absorption coefficient

The absorption coefficient $\alpha(\omega)$ describes the relative decrease in the incident radiation intensity when it passes through a medium. The calculated Sr_3AlAs_3 and Ba_3AlAs_3 absorption coefficients in a wider spectral region up to 15 eV for three different polarisations of the incident radiation: $\vec{E} // [100]$, $\vec{E} // [010]$ and $\vec{E} // [001]$ are displayed in [Figure VIII.6\(a\)](#). The absorption edge in the Sr_3AlAs_3 compound starts at approximately 1.51 eV for the three different polarisations of the incident radiation. For the Ba_3AlAs_3 compound, the absorption edge begins approximately at 1.28 eV for the three different polarisations of the incident radiation. A wide absorption band, located between 2 and 12 eV, characterises the considered compounds

VIII.2.4.3 The reflectivity

Figure VIII.6 (b) displays the calculated dependence of the reflectivity on the incident photon energy for three different polarisations for the Sr_3AlAs_3 and Ba_3AlAs_3 single-crystals. The zero frequency limit $R(0)$ of the Sr_3AlAs_3 (Ba_3AlAs_3) compound is equal to 23% (24%) for $\vec{E} \parallel [100]$, 21% (23%) for $\vec{E} \parallel [010]$ and 22% (23%) for $\vec{E} \parallel [001]$. The reflectivity $R(\omega)$ enhances from $R(0)$ with increasing photon energy to acquire a maximum and then it decreases rapidly. From Figure VIII.6 (b), one can note that the maximum reflectivity in Sr_3AlAs_3 (Ba_3AlAs_3) arises approximately at 6.27 eV (6.00 eV) for $\vec{E} \parallel [100]$, 6.35 eV (5.75 eV) for $\vec{E} \parallel [010]$ and 7.60 eV (6.35 eV) for $\vec{E} \parallel [001]$. This maximum attains 46% (44%) for $\vec{E} \parallel [100]$, 46% (46%) for $\vec{E} \parallel [010]$ and 43% (42%) for $\vec{E} \parallel [001]$ in Sr_3AlAs_3 (Ba_3AlAs_3).

VIII.2.4.4 The energy-loss function

The energy-loss function $L(\omega)$ describes the energy-loss of a fast electron passing through a material [37]. The main peak of the $L(\omega)$ spectrum is generally defined as the bulk plasma frequency (ω_p), which occurs when $\epsilon_2(\omega) < 1$ and $\epsilon_1(\omega)$ reaches the zero point [38]. The plasma frequency for Sr_3AlAs_3 (Ba_3AlAs_3) is approximately equal to 13.15 eV (11.68 eV) for $\vec{E} \parallel [100]$, 13.34 eV (11.87 eV) for $\vec{E} \parallel [010]$ and 12.77 eV (11.60 eV) for $\vec{E} \parallel [001]$ (Figure VIII.6 (c)). When the frequency of incident light is higher than the plasma frequency, the material becomes transparent, and hence an abrupt reduction of the reflectivity occurs at the corresponding energy.

VIII.2.4.5 The refractive index

The refractive index $n(\omega)$ of a material describes the difference between the propagation of an electromagnetic wave through vacuum and in a material. The knowledge of the refractive index of an optical compound is important for its use in optical devices, such as photonic crystals and waveguides. Figure VIII. 6(d) shows the refractive index of Sr_3AlAs_3 and Ba_3AlAs_3 in relation with the energy of incident radiation. It is found that the static refractive index $n(0)$ (the value of refraction index at zero energy) for Sr_3AlAs_3 (Ba_3AlAs_3) compound is 2.83 (2.94) for $\vec{E} \parallel [100]$, 2.75 (2.87) for $\vec{E} \parallel [010]$ and 2.79 (2.89) for $\vec{E} \parallel [100]$. Static optical anisotropy for the title compounds can be quantified by an anisotropy rate, which can be expressed as follows [39,40]:

$$A_{OPT} = \left[\frac{\varepsilon_1(o)^{[direction]}}{\varepsilon_1(o)^{[polycrystalline]}} - \frac{n(o)^{[direction]}}{n(o)^{[polycrystalline]}} \right] \quad (VIII.6)$$

A material is optically isotropic if $A_{OPT} = 1$; otherwise, it is optically anisotropic. The degree of deviation of A_{OPT} from unity reveal the extent of the optical anisotropy. The calculated values of A_{OPT} are shown in Table VIII.7. The calculated A_{OPT} values reveal that the two studied compounds exhibit a certain optical anisotropy. The maximum optical anisotropy occurs along the [010] crystallographic direction.

Table VIII.7 Calculated static dielectric constants $\varepsilon_1(0)$, static refractive indexes $n(0)$ and optical anisotropy A_{OPT} for the Sr_3AlAs_3 and Ba_3AlAs_3 compounds in polycrystalline and along the principal optical axes: [100], [010] and [001].

System		$\varepsilon_1(0)$	$n(0)$	A_{OPT}
Sr_3AlAs_3	Polycrystallines	7.808	2.79	
	[100]	8.048	2.82	[1.031,1.011]
	[010]	7.566	2.75	[0.969,0.986]
	[001]	7.810	2.79	[1.0,1.0]
Ba_3AlAs_3	Polycrystallines	8.433	2.90	
	[100]	8.683	2.94	[1.030,1.014]
	[010]	8.255	2.87	[0.979,0.990]
	[001]	8.361	2.89	[0.991,0.997]

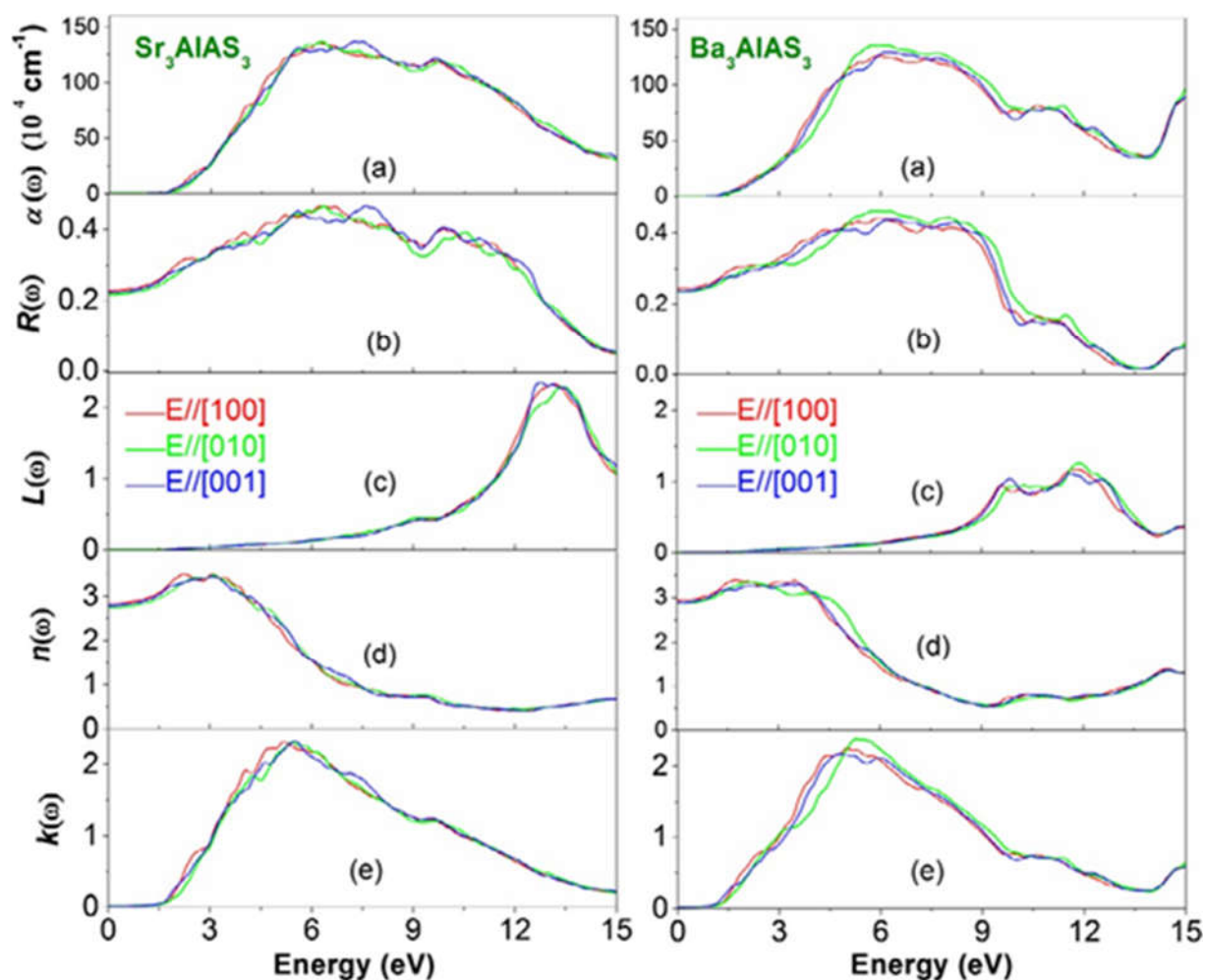


Figure VIII.6:(colour online) calculated optical function spectra: absorption coefficient $\alpha(\omega)$, reflectivity $R(\omega)$, energy loss function $L(\omega)$, refractive index $n(\omega)$ and extinction coefficient $k(\omega)$ for the Sr_3AlAs_3 and Ba_3AlAs_3 single-crystals for three different polarisations: $\vec{E} \parallel [100]$, $\vec{E} \parallel [010]$ and $\vec{E} \parallel [001]$.

VIII.2.5 Thermoelectric properties

In order to study the thermoelectric properties of the orthorhombic Ae_3AlAs_3 ($Ae = Sr, Ba$) compounds, we have calculated the basic transport parameters, e.g. Seebeck coefficient (S , in $\mu V K^{-1}$), electrical conductivity scaled by relaxation time (σ/τ , in $\Omega^{-1} m^{-1} s^{-1}$), thermal conductivity scaled by relaxation time (κ/τ , in $W K^{-1} m^{-1} s^{-1}$), power-factor ($PF = S^2 \frac{\sigma}{\tau}$, in $W K^{-2} m^{-1} s^{-1}$) and factor of merit ($ZT = \frac{\sigma S^2}{\kappa}$, dimensionless), as function of both charge-carrier concentration and temperature. The thermoelectric properties of the examined compounds were calculated for temperature between 300 and 900 K and for charge-carrier concentration between

1×10^{18} and $1 \times 10^{21} \text{cm}^{-3}$, which is an optimum charge-carrier concentration range for better thermoelectric performance, using the semi classical Boltzmann theory as implanted in the BoltzTraP computer package [41] with a dense k-mesh of $50 \times 50 \times 50$. As the investigated compounds crystallise in an orthorhombic system, we have first investigated the directional dependence of the thermoelectrical parameters. We find that the two considered compounds exhibit almost isotropic behaviour in the TE parameters along the three principal crystallographic directions. Since there is no significant anisotropy observed in the TE parameters, we have presented only their average values.

Figure VIII.7 shows the variation of the Seebeck coefficient S (thermopower), electrical conductivity scaled by relaxation time σ/τ , electronic thermal conductivity scaled by relaxation time κ/τ and power-factor PF with charge-carrier concentration for both n-type and p-type Sr_3AlAs_3 and Ba_3AlAs_3 compounds at 300, 600 and 900 K. Panel (a) of Figure VIII.7 demonstrates that the absolute value (magnitude) of S decreases with an increasing charge-carrier concentration for both n-type and p-type doping at a fixed temperature. The magnitude of S increases with an increasing temperature due to the increase of charge-carrier concentration for both charge-carrier types; this is a common trend in thermoelectric materials. One can note that the considered compounds possess larger thermopower for the holes compared with the electrons throughout the considered temperature range. For the same carrier concentration, the difference in Seebeck coefficient between electrons and holes is of the order of $200 \mu\text{V/K}$. This result is consistent with the calculated charge-carrier masses; large Seebeck coefficient translates to large effective masses of charge-carriers. The thermopower shows practically the same behaviour regarding the variation of charge-carrier concentration and temperature for the two title compounds. This comportment is might be due to the similarity of their band dispersions around the Fermi level and their effective masses, which are close to each other. For the same concentration and same type of charge-carrier, the two studied compounds have almost equal value for the thermopower at the same fixed temperature. To have an idea about the thermopower efficiency of the title compounds, we have compared their Seebeck coefficient S with a traditional thermoelectric material, Bi_2Te_3 . It was reported that at 300 K and charge-carrier concentration of $4 \times 10^{18} \text{cm}^{-3}$, Bi_2Te_3 has a thermopower of $313 \mu\text{VK}^{-1}$ for p-doping and of $196 \mu\text{VK}^{-1}$ for n-doping [42, 43], while our investigated compound Sr_3AlAs_3 (Ba_3AlAs_3), at the same conditions, has a Seebeck coefficient S equal to approximately 442 (472) μVK^{-1} for p-doping and -327 (-404) μVK^{-1} for n-doping. From this, one can appreciate that the thermopower value of the examined materials is larger than that of the traditional thermoelectric compound. This allows us to claim that the Sr_3AlAs_3 and Ba_3AlAs_3 systems are

potential candidates for thermoelectric applications if one can more reduce their thermal conductivity by some techniques, such as alloying, nano-structuring or superlattice growth.

Panels (b) and (c) of Figure VIII.7 demonstrate that the electrical and thermal conductivities scaled by relaxation time (σ/τ and κ/τ) increase with an increasing charge-carrier concentration in the two considered compounds for both n -type and p -type doping at a fixed temperature. It is found that the σ/τ value of the electrons is larger than that of the holes.

Figure VIII. 8 depicts the variation of the figure of merit (ZT) as function of hole and electron concentrations at 300, 600 and 900 K for Sr_3AlAs_3 and Ba_3AlAs_3 . One can note that at the same temperature and same charge-carrier concentration, the maximum figure of merit (ZT) is found in the hole-doped systems. At 900 K, the ZT is equal 1.02 (1.00) in the p -doped Sr_3AlAs_3 (Ba_3AlAs_3) and 0.93 (0.89) in the n -doped Sr_3AlAs_3 (Ba_3AlAs_3).

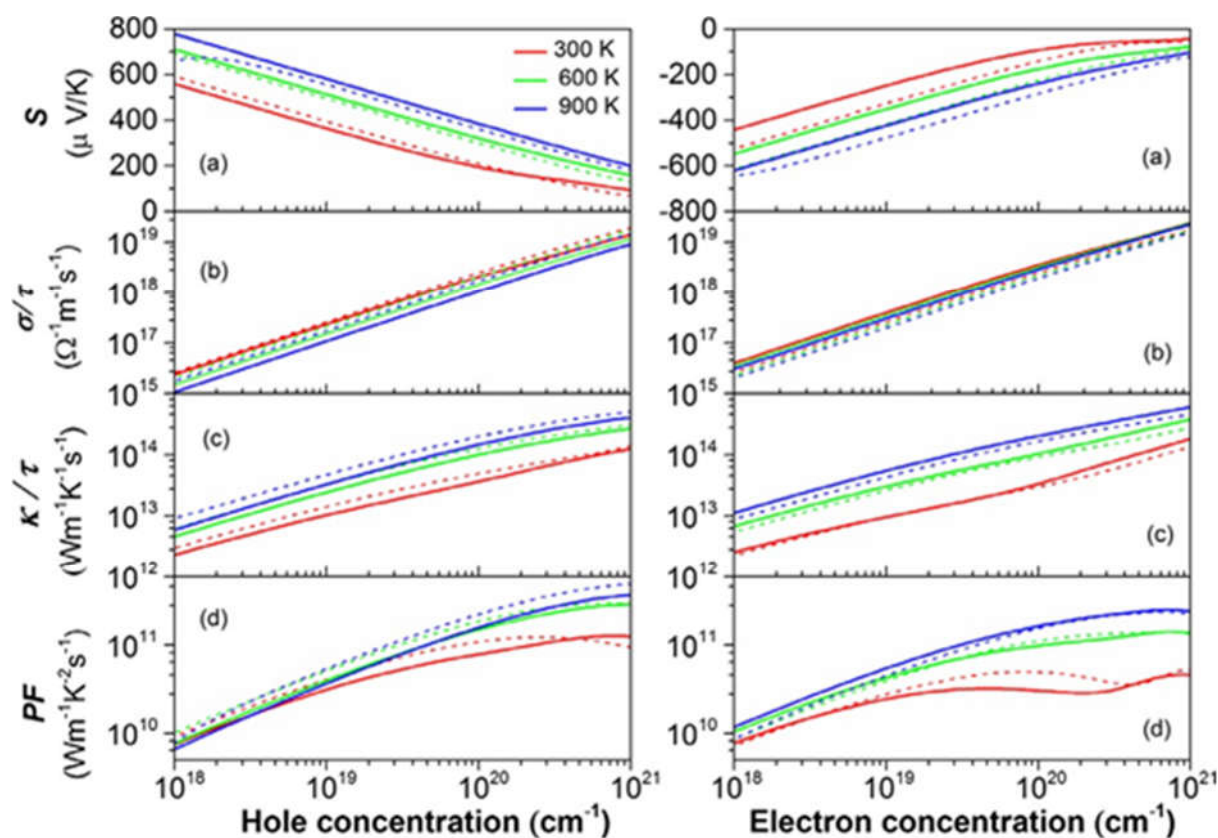


Figure VIII.7: (colour online) Calculated average Seebeck coefficient (S ; panel a), electrical conductivity scaled by relaxation time (σ/τ ; panel b), thermal conductivity scaled by relaxation time (κ/τ ; panel c) and power-factor ($PF = S^2\sigma/\tau$; panel d) as functions of both electron and hole.

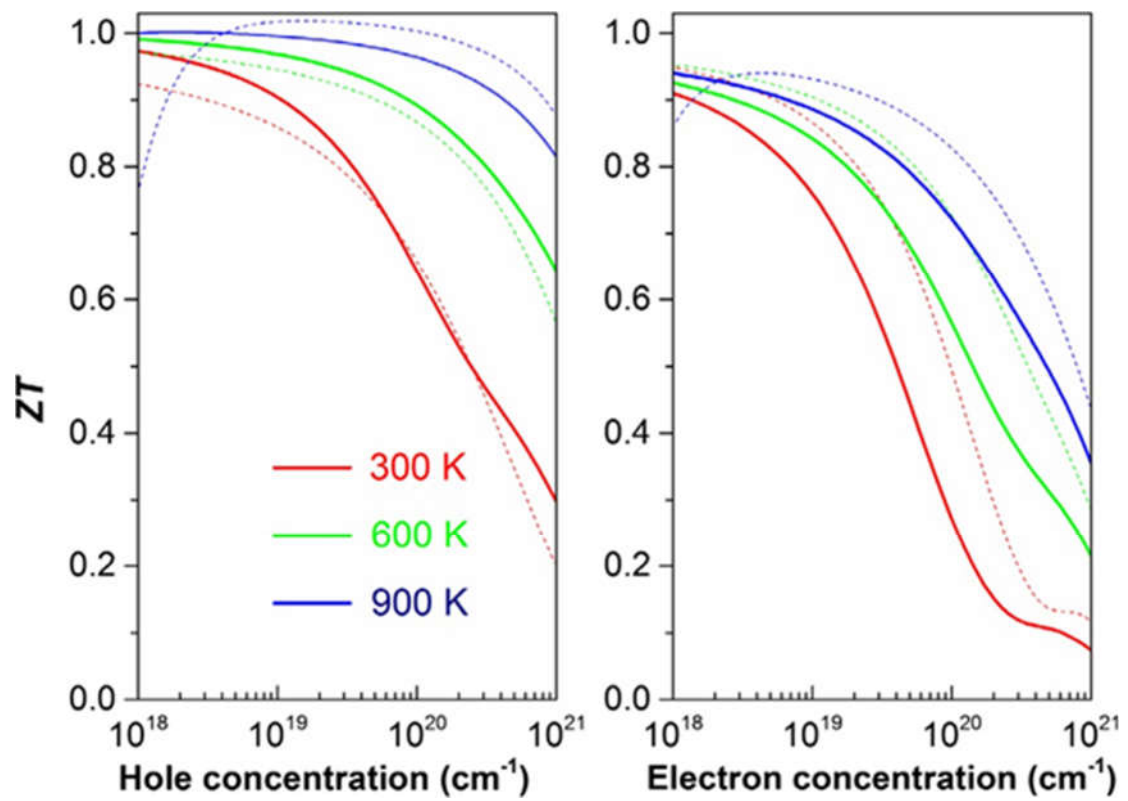


Figure VIII.8 :(colour online) Calculated figure of merit ZT as a function of charge-carrier concentration of both electron and hole concentrations at 300, 600 and 900 K for the Sr_3AlAs_3 (solid lines) and Ba_3AlAs_3 (dotted lines) compounds.

References

- [1] S. J. Clark, M. D. Segall, C. J. Pickard, P. J. Hasnip, M. J. Probert, K. Refson and M. C. Payne, *Zeitschrift fuer Kristallographie*. **220**, 567 (2005).
- [2] P. Blaha, K. Schwarz, G. K. H. Madsen, D. Kvasnicka, and J. Luitz, *WIEN2k: An Augmented Plane Wave Plus Local Orbitals Program for calculating Crystal Properties*, Vienna University of Technology, Austria, (2001).
- [3] S.S. Stoyko, L.H. Voss, H. He, and S. Bobev, *Crystals* **5**, 433 (2015).
- [4] D. Vanderbilt, *Phys. Rev. B* **41**, 7892 (1990).
- [5] J. P. Perdew, A. Ruzsinszky, G. I. Csonka, O. A. Vydrov, G. E. Scuseria, L. A. Constantin, X. L. Zhou, and K. Burke, *Phys. Rev. Lett.* **100**, 136406 (2008).
- [6] H. J. Monkhorst and J. D. Pack, *Phys. Rev. B* **13**, 5188 (1976).
- [7] P. Dufek, P. Blaha, and K. Schwarz, *Phys. Rev. B* **50**, 7279 (1994).
- [8] E. Engel and S. H. Vosko, *Phys. Rev. B* **47**, 13164 (1993).
- [9] X. ZHU, S. FAHY, and S. G. LOUIE, *Phys. Rev. B* **39**, 7840 (1989).
- [10] P. P. Rushton, D. J. Tozer, and S. J. Clark, *Phys. Rev. B* **65**, 235203 (2002).
- [11] B. Kralik, E. K. Chang and S. G. Louie, *Phys. Rev. B* **57**, 7027 (1998).
- [12] F. Tran and P. Blaha, *Phys. Rev. Lett.* **102**, 226401 (2009).
- [13] P.E. Blöchl, O. Jepsen, and O.K. Andersen, *Phys. Rev. B* **49**, 16223 (1994).
- [14] C.A. Ponce, R.A. Casali, M.A. Caravaca, *J. Phys. Condens. Matter* **20**, 045213 (2008).
- [15] A. Bouhemadou, R. Khenata, M. Chegaar, S. Maabed, *Phys. Lett. A* **371**, 337 (2007).
- [16] D.C. Wallace, *Thermodynamics of Crystals*, John Wiley, New York, NY, 1972.
- [17] R. Hill, *Proc. Phys. Soc. Lond. A* **65**, 349 (1952).
- [18] W. Voigt, *Lehrbuch der Kristallphysik*, Taubner, Leipzig, (1928).
- [19] A. Reuss, *Z. Angew. Math. Mech.* **9**, 49 (1929).
- [20] A. Bedjaoui, A. Bouhemadou, S. Aloumi, R. Khenata, S. Bin-Omran, Y. Al-Douri, F. Saad Saoud, and S. Bensalem, *Solid State Sci.* **70**, 21 (2017).
- [21] E. Schreiber, O.L. Anderson, and N. Soga, *Elastic Constants and Their Measurements*, McGraw-Hill, New York, NY, (1973).
- [22] J.W. Soh, H.M. Lee, and H.-S. Kwon, *J. Alloys Compd.* **194**, 119 (1993).
- [23] S. F Pugh, *Phil. Mag.* **45**, 823 (1954).
- [24] S. Chen, Y. Sun, Y. H. Duan, B. Huang and M. J. Peng, *J. Alloys Compd.* **630**, 202 (2015).
- [25] D. G. Pettifor, *Mater. Sci. Technol.* **8**, 345 (1992).

- [26] P. Jund, R. Viennois, X. Tao, K. Niedziolka, and J.-C. Tédénac, *Phys. Rev. B* **85**, 224105 (2012).
- [27] O. L. Anderson, *J. Phys. Chem. Solids* **24**, 909 (1963).
- [28] V. Tvergaard and J. W. Hutchinson, *J. Am. Ceram. Soc.* **71**, 157 (1988).
- [29] B. Xiao, J. Feng, C.T. Zhou, Y.H. Jiang and R. Zhou, *J. Appl. Phys.* **109**, 023507 (2011).
- [30] K. Lau and A. K. McCurdy, *Phys. Rev. B* **58**, 8980 (1998).
- [31] P. Ravindran, L. Fast, P. A. Korzhavyi, and B. Johansson, *J. Appl. Phys.* **84**, 4891(1998).
- [32] D.H. Chung and W.R. Buessem, *The Elastic Anisotropy of Crystals, in Proceeding of International Symposium 2, F.W. Vahldiek and S.A. Mersol, eds.*, Plenum Press, New York, NY, (1968).
- [33] K. B. Panda and K. S. R. Chandran, *Comput. Mater. Sci.* **35**, 134 (2006).
- [34] S. Ranganathan and M. Ostoja-Starzewski, *Phys. Rev. Lett.* **101**, 055504 (2008).
- [35] J.F. Nye, *Physical Properties of Crystals: Their Representation by Tensors and Matrices*, Oxford University Press, Great Britain, (1957).
- [36] M. Alouani and J. M. Wills, *Phys. Rev. B* **54**, 2480 (1996).
- [37] A. Bouhemadou and R. Khenata, *Comput. Mater. Sci.* **39**, 803 (2007).
- [38] R. Saniz, L. H. Ye, T. Shishidou, and A. J. Freeman, *Phys. Rev. B* **74**, 014209 (2006).
- [39] D. Yonghua, M. Lishi, L. Ping, and C. Yong, *Ceram. Internat.* **43**, 6312 (2017).
- [40] D. Cherrad, D. Maouche, M. Boudissa, M. Reffas, L. Louail, M. Maamache, K. Haddadi, and Y. Medkour, *Physica B* **429**, 95 (2013).
- [41] G.K.H. Madsen, D.J. Singh, *Comput. Phys. Commun.* **175**, 67 (2006)
- [42] P. C. Sreeparvathy, V. Kanchana and G. Vaitheeswaran, *J. Appl. Phys* **119**, 085701(2016).
- [43] T. J. Scheidemantel, C. Ambrosch-Draxl, T. Thonhauser, J. V. Badding, and J. O. Sofo, *Phys. Rev. B* **68**, 125210 (2003).

IX. General Conclusions

In this chapter, we have reported the results of the computations of some physical properties for two groups of systems: the first group is related to the two novel ternary phosphides LiSrP and LiBaP, while the second group includes both the Zintl Phase Sr_3AlAs_3 and Ba_3AlAs_3 . The obtained results for each group are summarized separately as follows:

IX.1 The ternary phosphides LiAeP ($\text{Ae} = \text{Sr, Ba}$)

Ab initio calculations based on the DFT within the GGA-PBEsol are performed to investigate the systematic trends for the structural, electronic, optical and thermodynamic properties of the LiAeP family, depending on the type of the alkaline earth (Ae) elements (Ae are Sr and Ba). First, the optimized structural parameters are obtained and compared with the available data in the scientific literature. The good agreement between our calculated structural parameters and their corresponding measured ones confirms the reliability of the used calculation approaches. Calculated pressure dependence of the lattice parameters reveals that the [100] crystallographic direction is more resistant to compressional deformation than the [001] direction. After the geometry optimization, single-crystals and polycrystals elastic moduli and the related properties were predicted. It is found that the investigated materials are mechanically stable, with a ductile behaviour and exhibiting noticeable elastic anisotropy. Sound wave propagating velocities and Debye temperature were predicted. The good concordance between the bulk modulus calculated via two different methods constitutes a second proof for the reliability of the present reported results. The examined materials have an indirect band gap. The value of the fundamental energy gap decreases when the Ae atom in the isostructural LiAeP series is substituted in the sequence: Sr, Ba. Analysis of the bonding properties via the density of states and charge density maps reveals that the considered materials are rather covalent. Optical functions are predicted for two different polarizations of the incident radiations for an energy range up to 20 eV. The obtained optical spectra exhibit a strong optical anisotropy. LiSrP is more absorptive than LiBaP. The static dielectric function of LiBaP is larger than that of LiSrP, which can be explained on the basis of the Penn model. The obtained results through the quasi-harmonic Debye model show that at a fixed pressure the increase of temperature leads to an increase in the unit-cell volume, heat capacity and volume thermal expansion coefficient, but it leads to a decrease in the bulk modulus and Debye temperature. At a fixed temperature, the increase of pressure leads to the increase of the bulk modulus and Debye temperature whereas it leads to the decrease of the unit-cell volume, volume thermal expansion coefficient and heat capacity. There are no available experimental data for the

electronic, optical and thermodynamic properties of the examined materials; our results are therefore purely theoretical predictions and must be tested experimentally in the future.

IX.2 The Zintl-phase Ae_3AlAs_3 ($Ae = Sr, Ba$)

we have investigated structural, electronic, optical properties of new ternary arsenides: Ae_3AlAs_3 ($Ae = Sr$ and Ba) by using The full potential linear augmented plane wave plus local orbitals method, within the GGA and mBJ approaches as implemented in WIEN2k code. We have additionally estimated the elastic constants using GGA-Pbsol as implanted in Castep. Our obtained lattice constants, free internal parameters are in good accordance with the available experimental data. To our knowledge, elastic constants, orthorhombic Ae_3AlAs_3 ($Ae = Sr, Ba$) are reported for the first time in this work and the results satisfy all of the mechanical stability criteria. The aggregate elastic moduli (B, G, E) have been deduced using the Voigt–Reuss–Hill approximations and deduced computed Poisson’s and B/G ratios the B/G ratio indicates that Sr_3AlAs_3 is brittle in nature and Ba_3AlAs_3 as ductile manner. The elastic anisotropy was investigated by several different anisotropic indexes and it was illustrated by plotting the three dimensional visualization of the Young’s modulus. Electronic band gap calculations reveal that Sr_3AlAs_3 is a direct band gap semiconductor with a gap of 0.89 eV with GGA-PbSol, whereas Ba_3AlAs_3 is an indirect band gap semiconductor with a GGA gap of 0.58 eV. In order to provide a more accurate description of the electronic structure, we have also used the mBJ approximation to the exchange-correlation potential. The value of the band gap with mBJ approximation in Sr_3AlAs_3 and Ba_3AlAs_3 is found to be 1.51 eV and 1.28 eV, respectively. We have determined the photon-energy dependent dielectric function and optical constant such as extinction coefficient, reflective index, reflectivity and energy-loss spectrum for the first time. Using the band structure, we have discussed the origin of the features that appear in the optical properties. Further, the static dielectric constants $\epsilon(0)$ and refractive index $n(0)$ and the Plasmon energy have been estimated, for the (100), (010) and (001) polarizations. Our study show that the compounds show weak optical anisotropy in in the photon energy range 0–15 eV for all the calculated optical properties. Based on the calculated band structure, the semi-classical Boltzmann theory as implemented in the BoltzTraP code was used to study the thermoelectric properties. The Seebeck coefficient of Sr_3AlAs_3 is higher at room temperature than that of Ba_3AlAs_3 , while Ba_3AlAs_3 possess the largest thermal conductivity.

Published Papers

1. Ab initio study of the electronic, optical and thermodynamic properties of the ternary phosphides LiAeP (Ae = Sr, Ba), A. Benahmed, A. Bouhemadou, R. Khenata, S. Bin-Omran, Indian Journal of Physics, Volume 91, Issue 22, Pages 157–167. (2016).
2. Structural, elastic, electronic, optical and thermoelectric properties of the Zintl-phase Ae_3AlAs_3 (Ae = Sr, Ba), A. Benahmed, A. Bouhemadou, B. Alqarni, N. Guechi, Y. Al-Douri, R. Khenata & S. Bin-Omran, Philosophical Magazine, Part B: Condensed Matter Physics, Volume 98, Issue 13, Pages 1217-1240 (2018)

Ab initio study of the electronic, optical and thermodynamic properties of the ternary phosphides LiAeP (Ae = Sr, Ba)

**A. Benahmed, A. Bouhemadou,
R. Khenata & S. Bin-Omran**

Indian Journal of Physics

ISSN 0973-1458

Volume 91

Number 2

Indian J Phys (2017) 91:157-167

DOI 10.1007/s12648-016-0909-7



Your article is protected by copyright and all rights are held exclusively by Indian Association for the Cultivation of Science. This e-offprint is for personal use only and shall not be self-archived in electronic repositories. If you wish to self-archive your article, please use the accepted manuscript version for posting on your own website. You may further deposit the accepted manuscript version in any repository, provided it is only made publicly available 12 months after official publication or later and provided acknowledgement is given to the original source of publication and a link is inserted to the published article on Springer's website. The link must be accompanied by the following text: "The final publication is available at link.springer.com".

Ab initio study of the electronic, optical and thermodynamic properties of the ternary phosphides LiAeP (Ae = Sr, Ba)

A Benahmed¹, A Bouhemadou^{1*}, R Khenata² and S Bin-Omran³

¹Laboratory for Developing New Materials and Their Characterization, University of Setif 1, 19000 Sétif, Algeria

²Laboratoire de Physique Quantique de la Matière et de Modélisation Mathématique (LPQ3M), Université de Mascara, 29000 Mascara, Algeria

³Department of Physics and Astronomy, College of Science, King Saud University, P.O. Box 2455, Riyadh 11451, Saudi Arabia

Received: 25 December 2015 / Accepted: 05 July 2016 / Published online: 23 August 2016

Abstract: We report the results of an ab initio study of the electronic, optical and thermodynamic properties of the LiBaP and LiSrP compounds using the pseudopotential plane-wave method within the framework of the density functional theory with the GGA-PBEsol. The calculated equilibrium structural parameters are in good agreement with the available experimental data. The energy band dispersions along the high symmetry directions in the k -space and the density of states diagrams are computed and analyzed. The obtained energy bands show that both examined crystals are indirect band gap semiconductors. The chemical bonding character is examined via electron density map plots. The optical properties are predicted for an incident radiation in an energy range up to 15 eV, and the origins of the main peaks in the optical spectra are discussed in terms of the calculated electronic band structure. We have also predicted the temperature and pressure dependencies of the unit-cell volume, thermal expansion coefficient, heat capacity, Debye temperature and Grüneisen parameter.

Keywords: Ternary phosphides; Ab initio calculations; Electronic structure; Optical properties; Thermal effect

PACS Nos.: 71.15.Mb; 71.20.Nr; 78.20.-e; 71.20.-b; 65.40.-b

1. Introduction

Ternary compounds with a simple 1:1:1 composition—so-called 111 phase—crystallize in more than 30 structure types [1]. In recent years, these ternary compounds, especially the half Heusler structure (archetype MgAgAs), the LiGaGe structure, the ZrBeSi structure and the TiNiSi structure, have drawn increasing attention due to their interesting physical properties, which make them candidates for many technological applications. For example, the half Heusler compounds are known to be good thermoelectrics [2–4] and have been proposed as topological insulators [5, 6]. The LiGaGe structure type systems have been proposed as ferroelectrics [7]. The ZrBeSi type compounds have been proposed as Dirac semimetals [8]; three-dimensional (3D) topological Dirac semimetals (TDSs) are a recently proposed state of quantum matter

[9–14] that has attracted increasing attention in physics and materials science. Generally, the 111 phases are semiconductor materials. The interest in the ternary semiconductor 111 phases is due to the attractive chemistry encountered in this class of inorganic compounds and to their excellent physical properties that are not possessed by the simple and binary semiconductors owing to the presence of three different chemical elements [15].

Recently, Dong et al. [16] synthesized several ternary phosphide single crystals, including the LiSrP and LiBaP systems. The considered LiSrP and LiBaP compounds are initially discovered in syntheses designed to explore the existence of a new class of materials containing both nitrogen and phosphorus as anions. Their crystalline structures are determined using the single-crystal X-ray diffraction. Both compounds adopt a centrosymmetric hexagonal structure, space group $P6_3/mmc$ (ZrBeSi structure), with two formula units by unit-cell ($Z = 2$) [17]. Apart from the experimental results regarding the synthesis and structural parameters reported by Dong and co-authors

*Corresponding author, E-mail: a_bouhemadou@yahoo.fr

[16], no theoretical or experimental data are available in the scientific literature for the considered systems to the best of our knowledge. Therefore, from a fundamental standpoint and in terms of eventual technological applications, we have performed the present work to obtain some of the lacking data.

Ab initio methods based on the density functional theory (DFT) have become a very powerful tool for exploring the properties of materials without requiring any experimental measurement. Thus, ab initio calculations using the pseudopotential plane-wave in the DFT framework have been performed to investigate the electronic, optical and thermodynamic properties of the LiAeP ($Ae = Sr$ and Ba) compounds.

2. Calculation details

All calculations were carried out using the pseudopotential plane-wave method based on the DFT, as implemented in the CASTEP (Cambridge Serial Total Energy Package) code [18]. The exchange–correlation potential was modeled using the generalized gradient approximation of Perdew et al. (so-called GGA-PBEsol) [19]. The interactions between the valence electrons and the ion cores were described by means of the Vanderbilt ultrasoft pseudopotentials [20]. The Li: $1s^2 2s^1$, P: $3s^2 3p^3$, Ba: $4d^{10} 5s^2 5p^6 6s^2$ and Sr: $3d^{10} 4s^2 4p^6 5s^2$ states were treated as valence electrons. The cut-off energy, which determines the size of the plane-wave basis set, was 400 eV. The integration over the Brillouin zone (BZ) was carried out using the Monkhorst–Pack sampling method [21] with a $9 \times 9 \times 6k$ -points grid. The self-consistent field was considered to be converged when the change in total energy was less than 1×10^{-6} eV/atom. The structural optimizations were performed using the Broyden–Fletcher–Goldfarb–Shanno (BFGS) minimization scheme [22]. The tolerances were set as the difference in total energy within 5×10^{-6} eV/atom, the maximum ionic Hellmann–Feynman force within 0.01 eV/Å, the maximum ionic displacement within 5×10^{-4} Å and the maximum stress within 0.02 GPa.

3. Results and discussion

3.1. Structural parameters

The examined LiSrP and LiBaP systems crystallize in a hexagonal crystal structure, space group $P6_3/mmc$ (no. 194), with two formula units per unit-cell. The Wyckoff positions of atoms are as follows: Li: $2c$ ($1/3, 2/3, 1/4$), Sr, Ba: $2a$ ($0, 0, 0$) and P: $2d$ ($1/3, 2/3, 3/4$) [16]. The calculated equilibrium lattice parameters, a_0 and c_0 , for LiSrP

and LiBaP are tabulated in Table 1, together with the available experimental data for comparison. One can appreciate that the relative deviations of the calculated equilibrium lattice parameters a_0 and c_0 from the measured ones do not exceed 0.26 and 0.96 %, respectively, in LiSrP and 0.12 and 0.65 %, respectively, in LiBaP. This good consistency proves the reliability of the calculation method. The lattice parameters (a_0 and c_0) of LiBaP are larger than those of LiSrP. This trend can be explained by considering the atomic radii of Ba and Sr atoms as follows: $R(Ba) = 215pm > R(Sr) = 200pm$.

3.2. Electronic band structure and chemical bonding

Investigation of the electronic energy bands of the LiBaP and LiSrP ternary compounds would be very useful to better understand their electronic and optical properties. The electronic energy band dispersions along the high symmetry lines in the first Brillouin zone of both examined crystals are depicted in Fig. 1. The topmost of the valence bands (VB) is located at the Γ -point in the Brillouin zone and the bottommost of the conduction bands (CB) is positioned at the M-point. Hence, both investigated systems are indirect band gap (Γ –M) semiconductors. The fundamental band gap of LiSrP (LiBaP) is equal to 1.16 eV (0.80 eV). No experimental or theoretical data are available in the scientific literature for the band gaps of LiSrP and LiBaP for comparison with our findings. Bearing in mind that the DFT within the common GGA underestimates the band gaps of semiconductors and isolators, the predicted values in the present work can serve as minimum estimates of the true band gaps of the considered crystals. The band gap calculated using the DFT with the common GGA is likely to be approximately 30–50 % smaller than the experimental values [23]. Therefore, the real fundamental band gap of LiSrP (LiBaP) is expected to be in the range 1.50–1.73 eV (1.04–1.20 eV). The replacement of Sr with Ba in the LiAeP series (Ae : Sr, Ba) leads to the narrowing of the band gap by approximately 31 %.

Table 1 Calculated equilibrium lattice parameters (a_0 and c_0 , in Å), equilibrium unit-cell volume (V_0 , in Å³)

	a_0	c_0	c_0/a_0	V_0
LiSrP				
Present work	4.3557	7.9031	1.81	129.85
Expt. [3]	4.3674	7.9802	1.83	131.82
LiBaP				
Present work	4.4945	8.5483	1.90	149.54
Expt. [3]	4.5003	8.6049	1.91	150.92

Available experimental results are reported for comparison

Fig. 1 Calculated electronic energy band dispersion curves along the high symmetry directions in the Brillouin zone for the LiAeP ($\text{Ae} = \text{Sr}, \text{Ba}$) compounds. E_g gives the value of the fundamental energy band gap Γ -M. The Fermi level is given at 0.0 eV

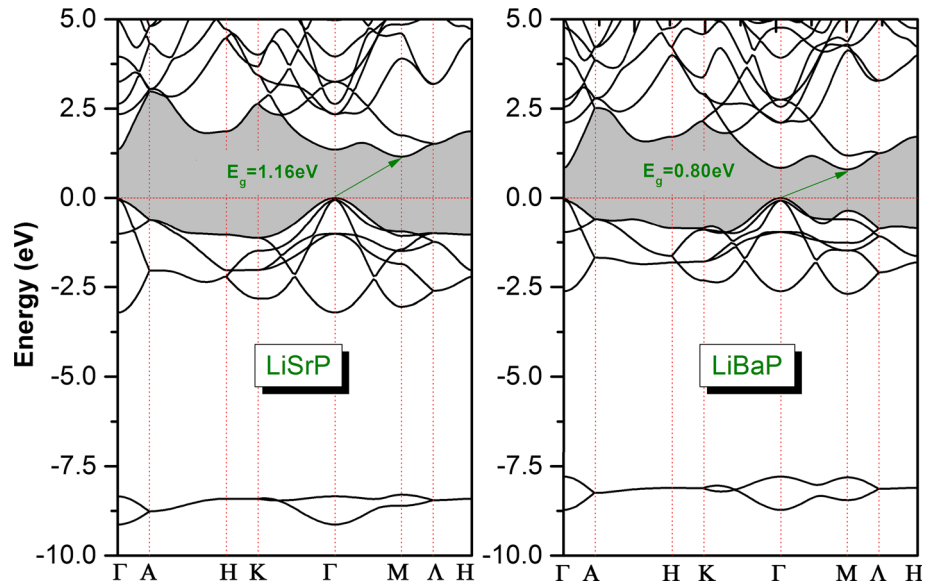


Fig. 2 Pressure dependence of the fundamental indirect band gap Γ -M and the first direct band gap Γ - Γ for the LiAeP ($\text{Ae} = \text{Ba}, \text{Sr}$) compounds. The calculated values are indicated by *symbols* and the fits by *solid lines*

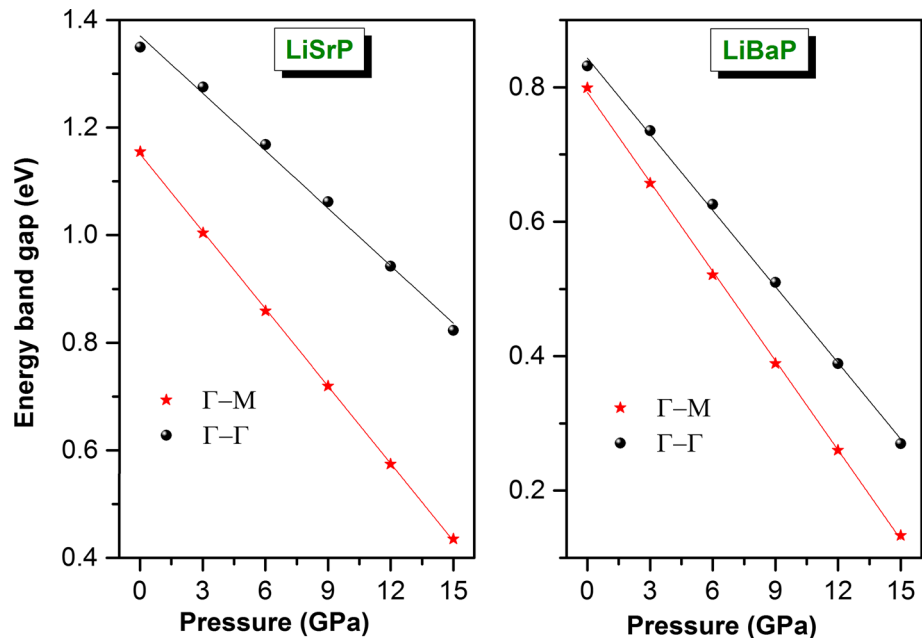


Figure 2 shows the pressure dependencies of the fundamental band gap Γ -M ($E_g^{\Gamma-M}(P)$) and the first direct band gap Γ - Γ ($E_g^{\Gamma-\Gamma}(P)$) of LiSrP and LiBaP in a pressure range between 0 and 15 GPa. First, the fundamental band gap remains between the topmost of the valence bands at the Γ -point and the bottommost of the conduction bands at the M-point for both examined compounds in the considered pressure range. Second, both considered gaps, i.e., Γ -M and Γ - Γ , are characterized by a quadratic decrease with increasing pressure in both compounds; the CB bottommost moves down with increasing pressure. When the pressure increases from 0 to 15 GPa, the fundamental band gap Γ -M decreases from 1.16 to 0.44 eV in LiSrP and from

0.80 eV to 0.13 eV in LiBaP . The first direct band gap, Γ - Γ , decreases from 1.35 to 0.82 eV in LiSrP and from 0.83 to 0.27 eV in LiBaP .

Knowledge of the effective mass values of the charge-carriers is necessary to determine the transport properties and electrical conductivity of materials; the conductivity is inversely proportional to the effective mass. In general, the theoretical effective mass is a tensor with nine components. However, for the very idealized simple case in which the energy $E(k)$ data are represented by a parabola curve, such as at the valence band maximum (VBMA) and the conduction band minimum (CBMi), the effective mass becomes a scalar that can be evaluated from the $E(k)$ curve

around the VB_{Ma} and CB_{Mi} by fitting the $E(k)$ data to the following well-known equation: $E = \frac{\hbar k^2}{2m^*}$, where \hbar is Planck's constant, E is the band-edge energy as a function of the wave vector k and m^* is the effective mass. The calculated effective masses of the holes at the VB_{Ma} along the Γ -K and Γ -M directions and those of the electrons at the CB_{Mi} along the M- Γ and M- Γ directions are tabulated in Table 2. The results indicate that the electron effective mass has a relevant dependence on the k direction in both compounds, indicating its anisotropy, while the hole effective mass is quite isotropic. In addition, the hole effective mass value is close to that of the electron, suggesting that their mobilities will be fairly similar.

The total and atomic-resolved l -projected densities of states (TDOS and PDOS) corresponding to the energy bands of the LiSrP and LiBaP compounds are calculated to obtain information regarding the orbital character of the electronic states and the chemical bonding. The obtained DOS diagrams are depicted in Fig. 3. For the LiSrP compound, the lowest valence band group, located between approximately -10.0 and -8.0 eV, is essentially dominated by the P-3s orbitals with a small contribution from the Li-1s, Sr-4s and Sr-3d states. The lower part of the valence band group, ranging from -3.13 eV up to the Fermi level, consists mainly of the Sr-3d4p and P-3p states, whereas the upper part is due to the hybridized Li-1s, Sr-3d and P-3p states. The conduction bands ranging from 0 to 10 eV are composed principally of the Li-2s, Sr-3d and Sr-5s states, with a minor contribution from the P-3s states. For the LiBaP compound, the lowest valence band group, located between approximately -10.0 and -7.4 eV, is essentially dominated by the P-3s orbitals, with a small presence of the Ba-5s and Ba-4d states. The lower part of the upper valence band group, ranging from -2.98 eV up to the Fermi level, is formed mainly from the Ba-4d5p and P-3p states, whereas the upper part is due to the hybridized Li-1s, Ba-d and P-3p states. The conduction bands ranging from 0 to 10 eV are composed primarily of the Ba-4d and Li-2s states with a small contribution from the Ba-6s and P-3p states.

To visualize the character of the chemical bonding between the constituent atoms, the valence charge density distribution maps of the investigated systems in the (110) plane are plotted in Fig. 4. The figure shows that a certain accumulation of electrons occurs between the P and Sr/Ba

and between the P and Li atoms, indicating that the chemical bonding between those atoms is mostly covalent. The covalent bonding between P and Sr/Ba is due to the hybridization between the P-3p and Sr-3d/Ba-4d states, and the covalent bonding between P and Li is due to the hybridization between the P-3p and Li-2s states.

3.3. Optical properties

In the linear response range, the macroscopic optical response functions of solids can usually be described by the frequency-dependent dielectric function $\epsilon(\omega) = \epsilon_1(\omega) + i\epsilon_2(\omega)$ or by the frequency-dependent complex refractive index $\tilde{n}(\omega) = n(\omega) + ik(\omega)$ [24], which are related mainly to the electronic structures. The optical functions reflect the fine structure of the electron energy dispersions in the valence and conduction bands. It is well-known that the imaginary part, i.e., $\epsilon_2(\omega)$, of the dielectric function $\epsilon(\omega)$ constructs the bridge between the electronic structure and the interband transitions. The imaginary part $\epsilon_2(\omega)$ can be calculated from the momentum matrix elements between the occupied and unoccupied wave functions with respect to the selection rules [25]. The real part $\epsilon_1(\omega)$ can be calculated from the imaginary part $\epsilon_2(\omega)$ via the Kramer-Kronig relationship [26]. Knowledge of the imaginary ($\epsilon_2(\omega)$) and real ($\epsilon_1(\omega)$) parts of the dielectric function allows one to calculate all the important optical characteristics of materials, such as the refractive index $n(\omega)$, optical reflectivity $R(\omega)$, extinction coefficient $k(\omega)$, absorption coefficient $\alpha(\omega)$ and energy-loss function $L(\omega)$, using the well-known relationships [27, 28]. Calculations of the optical properties require more k -points than ordinary self-consistent field calculations; a $20 \times 20 \times 20$ k -points grid is used in the present work. The LiSrP and LiBaP compounds have a hexagonal structure and are thus optically biaxial systems. For this reason, the optical functions of the considered crystals are calculated for polarized incident radiation with electric field vector \vec{E} parallel to the principal crystallographic axes, i.e., \vec{E}/a ($\vec{E}/[100]$) and \vec{E}/c ($\vec{E}/[001]$). Because some of the synthesized samples are polycrystalline, the optical spectra are also predicted for the polycrystalline phase.

The absorptive $\epsilon_2(\omega)$ and dispersive $\epsilon_1(\omega)$ parts of the dielectric function for both LiSrP and LiBaP are shown in Fig. 5. The figure displays noticeable differences between the magnitudes, shapes and locations of the main features and peaks in the $\epsilon_2(\omega)/\epsilon_1(\omega)$ spectra corresponding to \vec{E}/a and \vec{E}/c , demonstrating a strong anisotropy of the dielectric response of these materials to the incident radiation. The absorption edge is slightly shifted toward lower energies for the \vec{E}/c polarization in both compounds; the absorption edge starts at 1.003 eV (0.510 eV) for \vec{E}/a and at 0.960 eV (0.4680 eV) for \vec{E}/c in LiSrP (LiBaP). Now,

Table 2 Calculated electron and hole effective masses (m_e^* and m_h^* , respectively; in units of free electron mass) for the LiSrP and LiBaP compounds

System	$m_e^*(M-\Gamma)$	$m_e^*(M-A)$	$m_h^*(\Gamma-K)$	$m_h^*(\Gamma-M)$
LiSrP	0.0668	0.0492	0.0437	0.0438
LiBaP	0.0579	0.0390	0.0337	0.0337

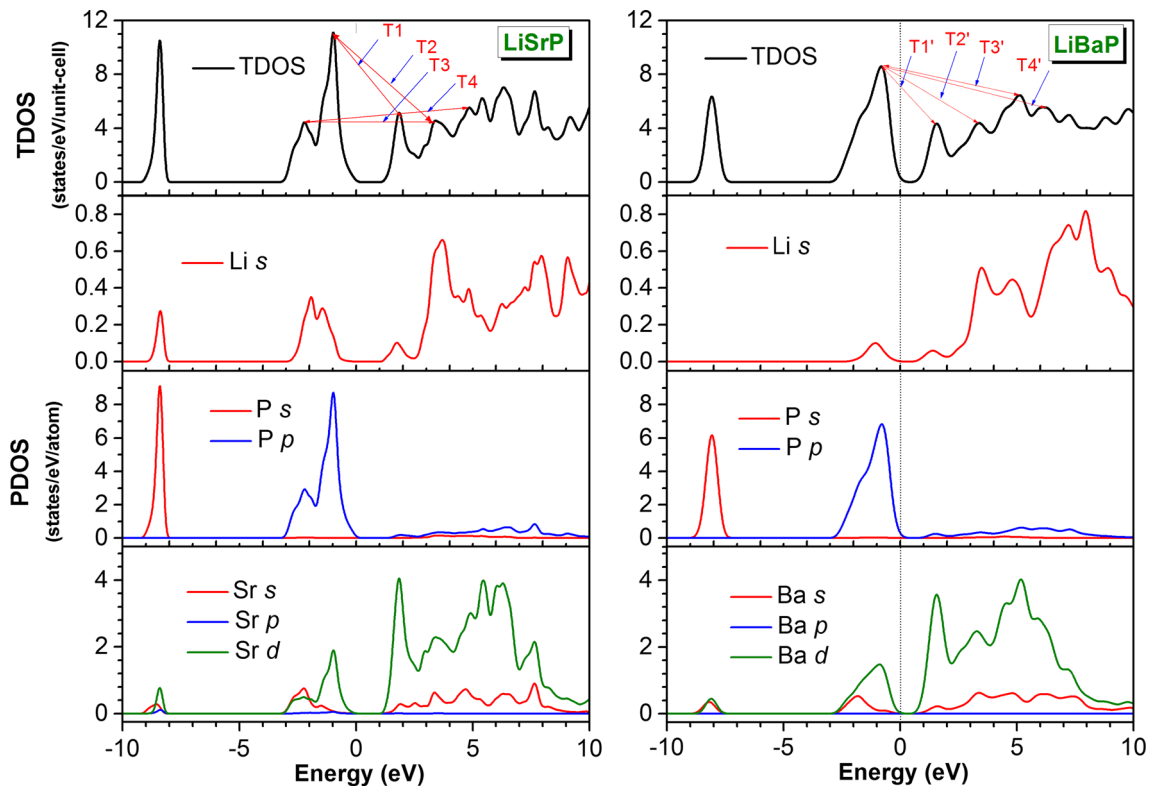


Fig. 3 Total (TDOS) and partial (PDOS) densities of states diagrams for the LiAeP ($\text{Ae} = \text{Sr}, \text{Ba}$) compounds. T1 (T1'), T2 (T2'), T3 (T3') and T4 (T4') represent the electronic transitions from the valence bands to the conduction bands

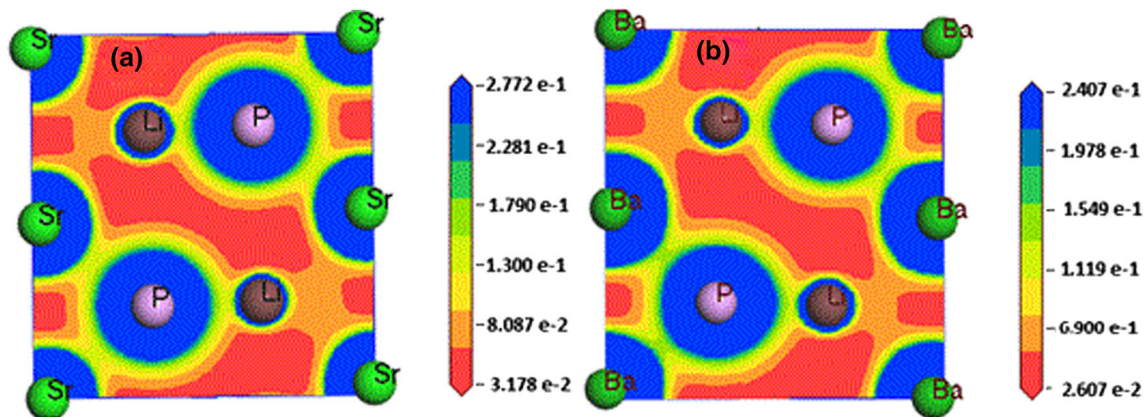
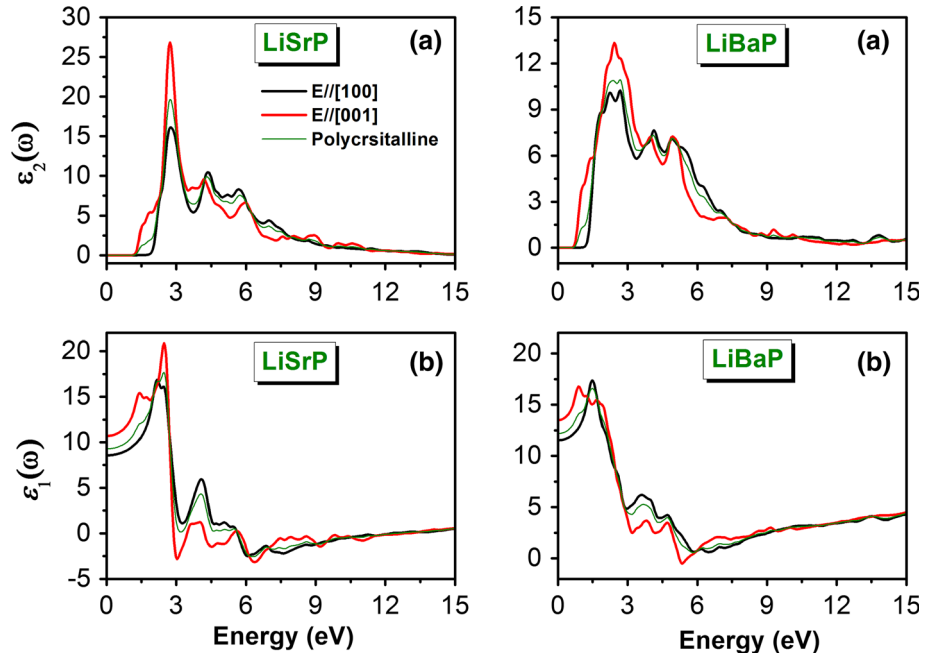


Fig. 4 Charge density distribution maps in the (110) plane for the LiSrP (a) and LiBaP (b) systems

we try to determine the origin of the occupied and unoccupied states involved in the direct interband transitions that caused the main peaks in the $\epsilon_2(\omega)$ spectra based on the calculated electronic structure discussed in Sect. 3.2. The absorptive part $\epsilon_2(\omega)$ of the dielectric function $\epsilon(\omega)$ of LiSrP exhibits four structures labeled A, B, C and D. The lowest energy peak, A, centered at approximately 2.77 eV for \vec{E}/a and 2.72 eV for \vec{E}/c , is caused by the interband transition T1 (see Fig. 3), which is due mostly to the electronic transitions from the $\text{Sr-}3d$ and $\text{P-}3p$ valence

states to the $\text{Sr-}3d$ conduction states. Structure B, centered at approximately 4.37 eV for \vec{E}/a and 4.19 eV for \vec{E}/c , is due to the direct interband transition T2. Peak C, centered at approximately 5.23 eV for \vec{E}/a and 6.68 eV for \vec{E}/c , is attributable to the direct interband transition T3, which is due mostly to the electronic transitions from the $\text{Sr-}3d$, $\text{P-}3p$ and $\text{Li-}2s$ valence states to the $\text{Sr-}3d$ and $\text{Li-}2s$ conduction states. The fourth peak, D, centered at approximately 5.66 eV for \vec{E}/a and absent for \vec{E}/c , is caused by the direct interband transition T4. The $\epsilon_2(\omega)$

Fig. 5 Calculated (a) imaginary ($\varepsilon_2(\omega)$) and (b) real ($\varepsilon_1(\omega)$) parts of the dielectric function for incident radiation polarized along the two principal crystallographic directions, i.e., \vec{E}/a and \vec{E}/c , for the LiAeP ($Ae = \text{Sr, Ba}$) crystals. The obtained spectra for the LiAeP ($Ae = \text{Sr, Ba}$) polycrystals are also shown



spectrum of LiBaP also exhibits four structures labeled A', B', C' and D'. Peak A', centered at approximately 2.23 eV for \vec{E}/a and 2.67 eV for \vec{E}/c , is caused by the direct interband transition T1' (see Fig. 3) (mostly Ba-4d and P-3p \rightarrow Ba-4d). Peak B', centered at approximately 4.13 eV for \vec{E}/a and 3.97 eV for \vec{E}/c , is due to the direct interband transition T2'. Peak C', centered at approximately 4.92 eV for \vec{E}/a and 4.93 eV for \vec{E}/c , is attributable to the direct interband transition T3' (mostly Ba-4d, P-3p and Li-2s \rightarrow Ba-4d and Li-2s). The fourth peak, D', centered at approximately 9.28 eV for \vec{E}/a and absent for \vec{E}/c , is caused by the direct interband transition T4'. The zero frequency limit $\varepsilon_1(0) = \varepsilon_1(\omega \rightarrow 0)$ —the electronic part of the static dielectric constant—is the most important quantity in the $\varepsilon_1(\omega)$ spectrum. The calculated value of $\varepsilon_1(0)$ for LiSrP (LiBaP) is equal to 8.569 (11.530) for \vec{E}/a and 10.694 (13.498) for \vec{E}/c . The values of $\varepsilon_1(0)$ for both considered light polarizations in LiSrP are larger than their corresponding ones in LiBaP; i.e., $\varepsilon_1(0)$ increases with decreasing band gap. This trend can be explained on the basis of the Penn model [29]: $\varepsilon(0) \approx 1 + (h\omega_p/E_g)^2$.

The absorption coefficient $\alpha(\omega)$ is a basic way to measure how far light with a specific energy can penetrate a material before being absorbed. The calculated absorption coefficients for LiSrP and LiBaP for both considered light polarizations, i.e., \vec{E}/a and \vec{E}/c , are displayed in Fig. 6(a), in which the fundamental absorption edge starts approximately at 1.003 eV (0.510 eV) for \vec{E}/a and 0.960 eV (0.468 eV) for \vec{E}/c in LiSrP (LiBaP). The absorption coefficient increases with increasing photon energy, reaching a maximum and then decreasing to reach

its minimum. The absorption spectrum shows some peaks that can be explained by the interband transitions using the band structure results. LiSrP has an absorptive energy region larger than that of LiBaP. The LiSrP compound can be used as an absorptive layer in the energy range from 1.37 to 12 eV, whereas LiBaP can be used in the energy range from 0.84 to 9 eV.

The frequency-dependent reflectivity $R(\omega)$ spectra of the considered systems for both polarizations of the incident radiation are depicted in Fig. 6(b). The zero frequency limit $R(0)$ is equal to 24 % (30 %) for \vec{E}/a and 28 % (32 %) for \vec{E}/c in LiSrP (LiBaP). The reflectivity $R(\omega)$ increases from $R(0)$ with increasing photon energy to attain a maximum, and then a rapid decrease of $R(\omega)$ occurs at approximately 13.85 eV (5.88 eV) for \vec{E}/a and 13.34 eV (5.41 eV) for \vec{E}/c . Fig. 6(b) shows that the maximum reflectivity in LiSrP (LiBaP) occurs at approximately 7.7 eV (1.62 eV) for \vec{E}/a and at approximately 2.85 eV (2.44 eV) for \vec{E}/c . The maximum reflectivity is approximately 47 % (39 %) for \vec{E}/a and 56 % (41 %) for \vec{E}/c in LiSrP (LiBaP).

The energy-loss spectrum $L(\omega)$ describes the energy loss of a fast electron passing through a material [30]. The main peak in the $L(\omega)$ spectrum represents the characteristic associated with the plasma resonance; the corresponding frequency is called plasma frequency ω_p , which occurs when $\varepsilon_2(\omega) < 1$ and $\varepsilon_1(\omega)$ reaches a zero value [31]. From the energy-loss spectrum [Fig. 6(c)], the plasma frequency ω_p for LiSrP (LiBaP) is equal to approximately 13.85 eV (7.43 eV) for \vec{E}/a and approximately 13.34 eV (6.05 eV) for \vec{E}/c . When the frequency of the incident

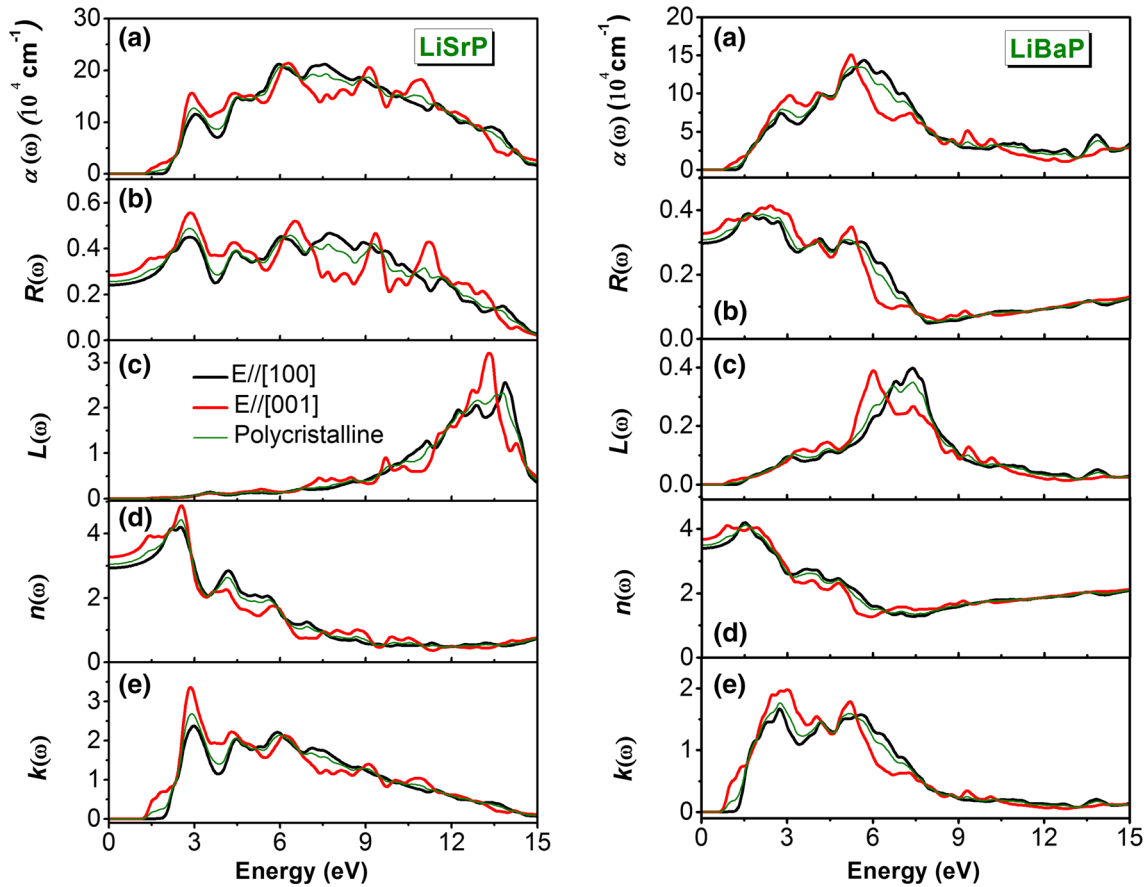


Fig. 6 Calculated optical function spectra: (a) absorption $\alpha(\omega)$, (b) reflectivity $R(\omega)$, (c) energy loss function $L(\omega)$, (d) refractive index $n(\omega)$ and (e) extinction coefficient $k(\omega)$ for incident radiation

light is higher than the plasma frequency, the material becomes transparent and hence an abrupt reduction of the reflectivity $R(\omega)$ occurs at the plasma frequency.

The refractive index $n(\omega)$ of a substance is the ratio of the speed of an electromagnetic wave in a vacuum to its speed in the substance. Knowledge of the refractive index of an optical material is important because its use in optical devices, such as photonic crystals and waveguides. The calculated refractive index spectra of LiSrP and LiBaP are shown in Fig. 6(d). The static refractive index $n(0)$ (the refractive index at zero energy) of LiSrP (LiBaP) is equal to 2.94 (3.39) for \vec{E}/a and 3.27 (3.67) for \vec{E}/c . In both considered compounds, the refractive index increases with increasing energy, shows some peaks for the two polarization directions of the incident radiation and then decreases at high energy. Moreover, the refractive index for LiSrP goes below unity in certain energy ranges. When the refractive index is lower than unity, it indicates that the group velocity $V_g = c/n$ of the incident radiation is greater than the speed of light c , which means that the group velocity shifts to the negative domain and the nature of the medium changes from linear to non-linear. It is known that

polarized along the two principal crystallographic directions, i.e., \vec{E}/a and \vec{E}/c , for the LiAeP ($Ae = \text{Sr, Ba}$) crystals. Obtained spectra for the LiAeP ($Ae = \text{Sr, Ba}$) polycrystals are also shown

the refractive index has the same trend of variation with photon energy as the real part of the dielectric function, which means that all peaks appearing in the spectrum of the refractive index are related to the ones appearing in the real part of the dielectric function, whereas the extinction coefficient $k(\omega)$ [Fig. 6(e)] follows the imaginary part of the dielectric function. The polycrystalline sample optical behavior for both materials closely mimics the optical behavior observed for the [100] polarized incident light.

3.4. Thermodynamic properties

We have investigated the thermodynamic properties of the LiAeP ($Ae = \text{Sr, Ba}$) systems in the temperature range from 0 to 800 K and the pressure range from 0 to 15 GPa using the quasi-harmonic Debye model as implemented in the Gibbs program [32]. A detailed description of the quasi-harmonic Debye model can be found elsewhere [32–36]. The relationship between the normalized unit-cell volume and temperature at some fixed pressures for LiSrP and LiBaP is shown in Fig. 7(a), which shows that the normalized volume V/V_0 is nearly constant at low

temperature and that an abrupt change occurs with increasing temperature. The normalized volume increases more rapidly at a high temperature for both compounds; however, the rate becomes a little slower with increasing pressure; these materials become less expandable at 15 GPa than at 0 GPa. The variation of the bulk modulus versus temperature at four fixed pressures (0, 5, 10 and 15 GPa) is depicted in Fig. 7(b). It can be seen that the bulk modulus remains nearly constant at a low temperature for both compounds and then decreases rapidly with increasing temperature; the increasing temperature causes a decrease in the hardness of materials due to the increase of the unit-cell volume. The bulk modulus values of LiSrP (LiBaP) at 0, 5, 10 and 15 GPa decrease by 29.43 % (32.70 %), 16.37 % (17.19 %), 10.75 % (10.86 %) and 7.92 % (7.62 %), respectively, when the temperature increases from 0 to 800 K. At zero pressure and temperature, our calculated bulk moduli for LiSrP and LiBaP are 45.12 GPa and 41.09 GPa, respectively. LiSrP is slightly more resistant to the compression of volume.

Figure 8(a) illustrates the variation in the Debye temperature θ_D as a function of temperature at some fixed pressures for LiSrP and LiBaP. It can be seen that θ_D decreases slightly with increasing temperature in both considered compounds. When the temperature increases from 0 to 800 K, the Debye temperature θ_D is reduced by 12.04 % (13.82 %) at 0 GPa, 6.11 % (6.24 %) at 5 GPa, 3.85 % (3.80 %) at 10 GPa and 2.82 % (2.65 %) at 15 GPa in LiSrP (LiBaP). This indicates that the reduction rate of θ_D with temperature becomes small at higher pressure; the high pressure suppresses the temperature effect on the Debye temperature. The calculated

Debye temperatures θ_D at zero pressure and zero temperature are 398.27 K for LiSrP and 320.47 K for LiBaP.

The Grüneisen parameter describes the change in the vibrational properties of a crystal lattice due to the increase or decrease of its volume as a result of temperature change. The variation of the Grüneisen parameter as a function of temperature is shown in Fig. 8(b). At a given pressure, the Grüneisen parameter γ increases slowly with temperature. Moreover, the Grüneisen parameter γ increases more slowly at high pressure than at low pressure. At 300 K and zero pressure, our calculations yield a γ equal to 1.94 (2.073) for LiSrP (LiBaP).

Figures 9(a) and 9(b) show the temperature dependencies of the constant pressure heat capacity C_P and constant volume heat capacity C_V , respectively, at some fixed pressures. One can see that the constant volume heat capacity C_V and the constant pressure capacity C_P are very similar for the temperature range from 0 to approximately 300 K; C_V and C_P increase rapidly with temperature at a fixed pressure. When the temperature is higher than 300 K, the anharmonic effect on the heat capacity C_V is suppressed and increases slowly with increasing temperature to approach a constant value—the so-called Dulong–Petit limit [37] which is common for all solids at high temperatures—whereas C_P still increases monotonously with increasing temperature. At high temperature, C_V approaches approximately $147.71 \text{ J mol}^{-1} \text{ K}^{-1}$ ($148.77 \text{ J mol}^{-1} \text{ K}^{-1}$) in LiSrP (LiBaP). At zero pressure and ambient temperature, C_V and C_P of LiSrP (LiBaP) are $137.88 \text{ J mol}^{-1} \text{ K}^{-1}$ ($141.94 \text{ J mol}^{-1} \text{ K}^{-1}$) and $144.37 \text{ J mol}^{-1} \text{ K}^{-1}$ ($149.47 \text{ J mol}^{-1} \text{ K}^{-1}$), respectively.

Fig. 7 (a) The normalized primitive-cell volume V/V_0 as a function of temperature for the LiSrP and LiBaP compounds at some fixed pressures; V is the primitive-cell volume at the considered temperature; V_0 is the primitive-cell volume at zero temperature. (b) The normalized bulk modulus B/B_0 as a function of temperature for the LiSrP and LiBaP compounds at some fixed pressures; B is the bulk modulus at the considered temperature and B_0 is the bulk modulus at the zero temperature

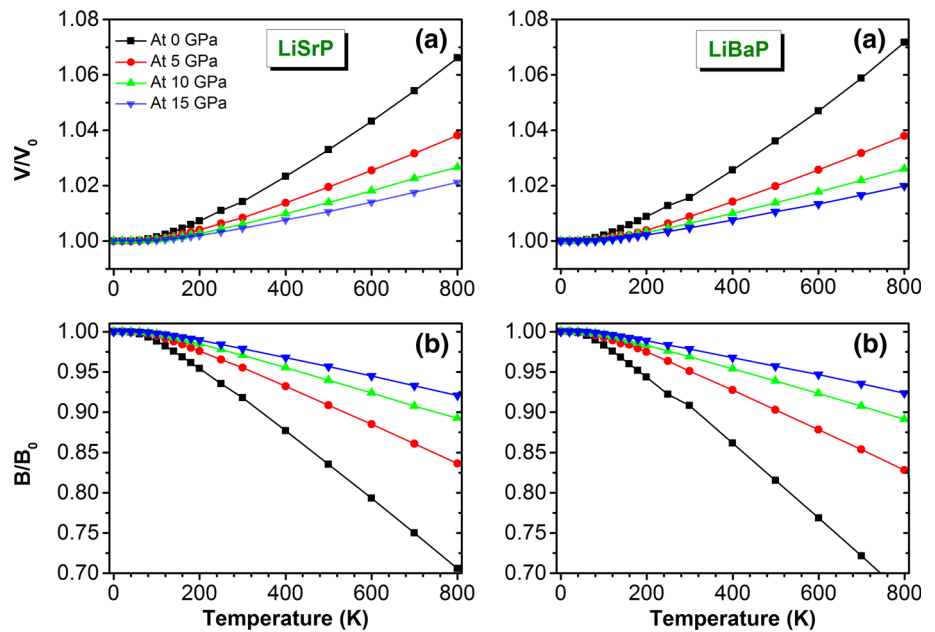


Fig. 8 (a) Variations of the Debye temperature and (b) Grüneisen parameter versus temperature at some fixed pressures for the LiSrP and LiBaP compounds

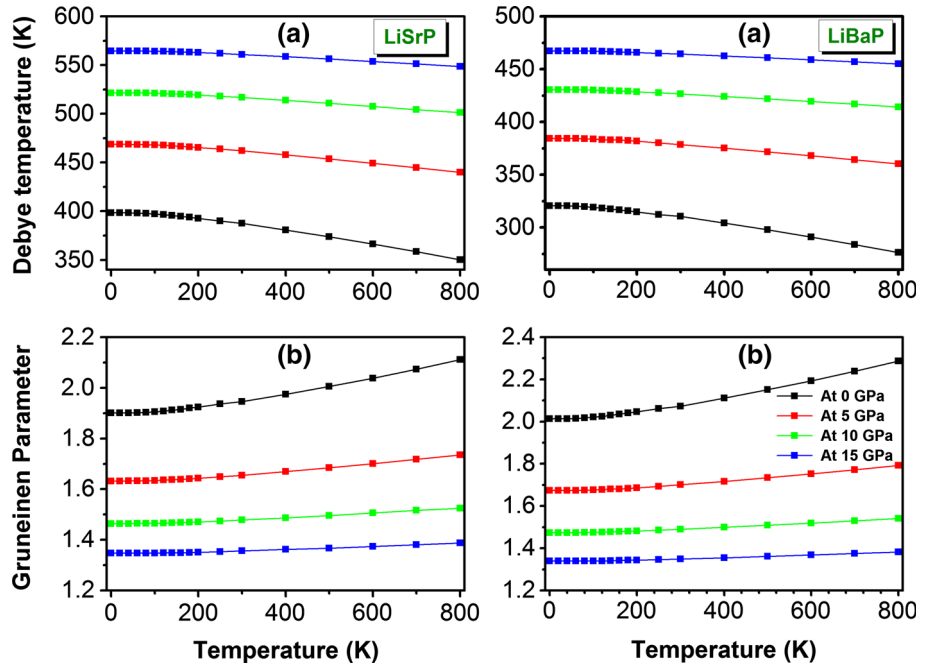
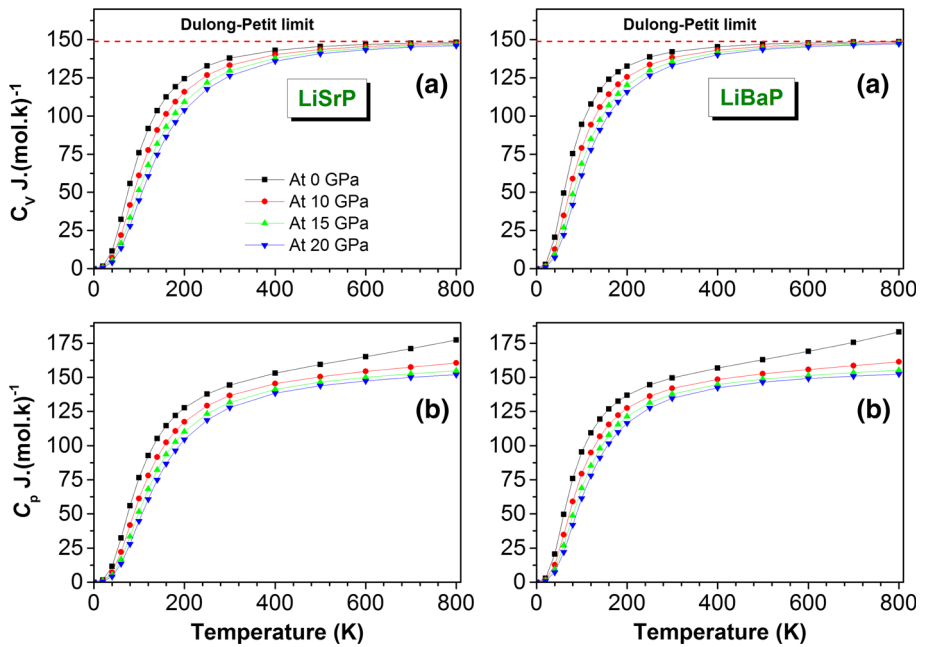


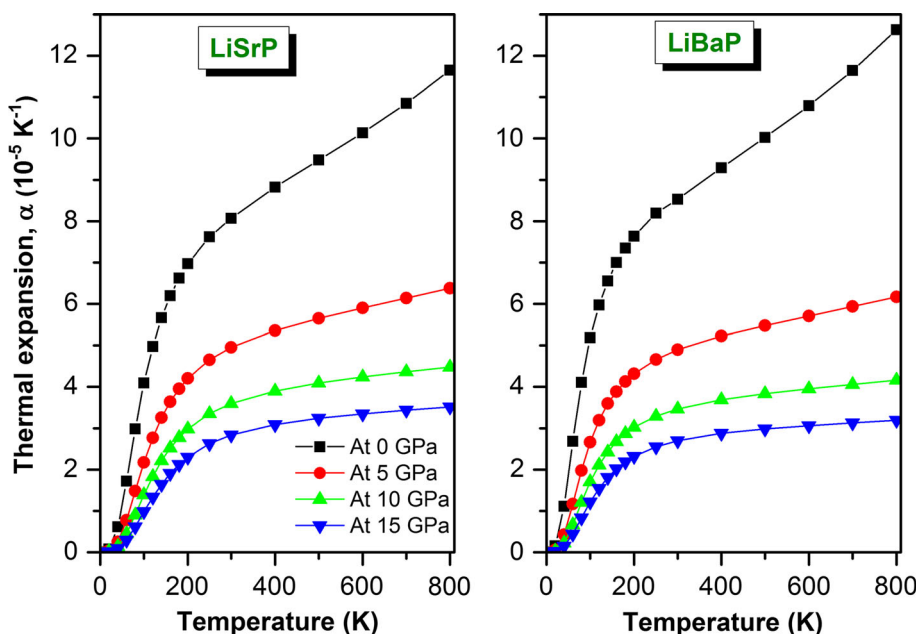
Fig. 9 (a) Variations of the heat capacity at constant volume C_V and (b) the heat capacity at constant pressure C_p versus temperature at some fixed pressures for the LiSrP and LiBaP compounds



Variations in the volume thermal expansion coefficient α of LiSrP and LiBaP as a function of temperature T at certain fixed pressures are shown in Fig. 10. For $T \leq 250$ K, the thermal expansion coefficient α increases rapidly with increasing temperature at fixed pressure in both considered compounds. For $T > 250$ K, the increase of α with increasing temperature becomes more gradual and approaches a linear behavior. The rate of increase of α with increasing temperature decreases with

increasing pressure. Figure 10 shows that the pressure effect on α is small at low temperature and becomes substantial at high temperature. This means that there is a large volume thermal expansion coefficient at low pressure, which is in accordance with the variation of the unit-cell volume with pressure and temperature. At zero pressure and room temperature, α is approximately equal to 8.0672 K^{-1} for LiSrP and 8.5318 K^{-1} for LiBaP.

Fig. 10 Variation of the volume thermal expansion coefficient as a function of temperature at some fixed pressures for LiSrP and LiBaP



4. Conclusions

Ab initio calculations based on the DFT within the GGA-PBEsol are performed to investigate the systematic trends for the structural, electronic, optical and thermodynamic properties of the LiAeP family, depending on the type of the alkaline earth (Ae) elements (Ae are Sr and Ba). First, the optimized structural parameters are obtained and compared with the available data in the scientific literature. The good agreement between our calculated structural parameters and their corresponding measured ones confirms the reliability of the used calculation approaches. The examined materials have an indirect band gap. The value of the fundamental energy gap decreases when the Ae atom in the isostructural LiAeP series is substituted in the sequence: $\text{Sr} \rightarrow \text{Ba}$. Analysis of the bonding properties via the density of states and charge density maps reveals that the considered materials are rather covalent. Optical functions are predicted for two different polarizations of the incident radiations for an energy range up to 20 eV. The obtained optical spectra exhibit a strong optical anisotropy. LiSrP is more absorptive than LiBaP. The static dielectric function of LiBaP is larger than that of LiSrP, which can be explained on the basis of the Penn model. The obtained results through the quasi-harmonic Debye model show that at a fixed pressure the increase of temperature leads to an increase in the unit-cell volume, heat capacity and volume thermal expansion coefficient, but it leads to a decrease in the bulk modulus and Debye temperature. At a fixed temperature, the increase of pressure leads to the increase of the bulk modulus and Debye temperature whereas it leads to the decrease of the unit-cell volume, volume

thermal expansion coefficient and heat capacity. There are no available experimental data for the electronic, optical and thermodynamic properties of the examined materials; our results are therefore purely theoretical predictions and must be tested experimentally in the future.

Acknowledgments The authors extend their appreciation to the International Scientific Partnership Program ISPP at King Saud University for funding this research work through JSPPP# 0025.

References

- [1] M L Fornasini and F Merlo *J. Alloys Compd.* **219** 63 (1995)
- [2] T Graf, C Felser and S S P Parkin *Prog. Solid State Chem.* **39** 1 (2011)
- [3] F Casper, R Seshadri and C Felser *Phys. Status Solidi A* **206** 1090 (2009)
- [4] B Balke, J Barth, M Schwall, G H Fecher and C Felser *J. Electron. Mater.* **40** 702 (2011)
- [5] S Chadov, X Qi, J Kübler, G H Fecher, C Felser and S C Zhang *Nature Mater.* **9** 541 (2010)
- [6] H Lin, L A Wray, Y Xia, S Xu, S Jia, R J Cava, A Bansil and M Z Hasan *Nature Mater.* **9** 546 (2010)
- [7] J W Bennett, K F Garrity, K M Rabe and D Vanderbilt *Phys. Rev. Lett.* **109** 167602 (2012)
- [8] Q D Gibson, L M Schoop, L MÜchler, L S Xie, M Hirschberger, N P Ong, C Car and R J Cava *arXiv preprint arXiv: 1411.0005*, 2014
- [9] X Wan, A M Turner, A Viswanathan and S Y Savrasov *Phys. Rev. B* **83** 205101 (2011)
- [10] A A Burkov and L Balents *Phys. Rev. Lett.* **107** 127205 (2011)
- [11] S M Young, S Zaheer, J C Y Teo, C L Kane, E J Mele and A M Rappe *Phys. Rev. Lett.* **108** 140405
- [12] Z Wang, Y Sun, X Q Chen, C Franchini, G Xu, H Weng, X Dai and Z Fang *Phys. Rev. B* **85** 195320 (2012)
- [13] Z K Liu *et al. Science* **343** 864 (2014)

- [14] Z Wang, H Weng, Q Wu, X Dai and Z Fang *Phys. Rev. B* **88** 125427 (2013)
- [15] M Reffas, A Bouhemadou, R Khenata, T Ouahrani and S Bin-Omran, *Phys. B Condensed Matter* **405** 4079 (2010)
- [16] Y Dong and F J DiSalvo *J Solid State Chem.* **180** 432 (2007)
- [17] G Brauer and E Zintl *Z Phys Chem B* **37** 323 (1937)
- [18] S J Clark, M D Segall, C J Pickard, P J Hasnip, M J Probert, K Refson and M C Payne *Zeitschrift fuer Kristallographie* **220** 567 (2005)
- [19] J P Perdew *et al. Phys. Rev. Lett.* **10** 136406 (2008)
- [20] D Vanderbilt *Phys. Rev. B* **41** 7892 (1990)
- [21] H J Monkhorst and J D Pack *Phys. Rev. B* **13** 5188 (1976)
- [22] T H Fischer and J Almlof *J. Phys. Chem.* **96** 9768 (1992)
- [23] S Zh Karazhanov, P Ravindran, H Fjellvag and B G Svensson *J. Appl. Phys.* **106** 123701 (2009)
- [24] P W Tasker *J. Phys. C: Solid State Phys.* **12** 4977 (1979)
- [25] L Makinistian and E A Albanesi *Phys. Rev. B* **74** 045206 (2006)
- [26] M Alouani and J M Wills *Phys. Rev. B* **54** 2487 (1996)
- [27] M Fox *Optical Properties of Solids* (New York: Oxford University Press) (2001)
- [28] M Dressel and G Gruner *Electrodynamics of Solids: Optical Properties of Electrons in Matter* (United Kingdom: Cambridge University Press) (2002)
- [29] D R Penn *Phys. Rev.* **128** 2093 (1962)
- [30] A Bouhemadou and R Khenata *Comput. Mater. Sci.* **39** 803 (2007)
- [31] R Saniz, L H Ye, T Shishidou and A J Freeman *Phys. Rev. B* **74** 014209 (2006)
- [32] M A Blanco, E Francisco and V Luaña *Comput. Phys. Commun.* **158** 57 (2004)
- [33] A Bouhemadou, R Khenata and B Amrani *Physica B: Condensed Matter* **404** 3534 (2009)
- [34] M Flórez, J M Recio, E Francisco, M A Blanco and A M Pendás *Phys. Rev. B* **66** 144112 (2002)
- [35] E Francisco, J M Recio, M A Blanco and A M Pendás *J. Phys. Chem. A* **102** 1595 (1998)
- [36] E Francisco, M A Blanco and G Sanjurjo *Phys. Rev. B* **63** 049107 (2001)
- [37] A T Petit and P L Dulong *Ann. Chim. Phys.* **10** 395 (1819)



Structural, elastic, electronic, optical and thermoelectric properties of the Zintl-phase Ae_3AlAs_3 (Ae = Sr, Ba)

A. Benahmed, A. Bouhemadou, B. Alqarni, N. Guechi, Y. Al-Douri, R. Khenata & S. Bin-Omran

To cite this article: A. Benahmed, A. Bouhemadou, B. Alqarni, N. Guechi, Y. Al-Douri, R. Khenata & S. Bin-Omran (2018): Structural, elastic, electronic, optical and thermoelectric properties of the Zintl-phase Ae_3AlAs_3 (Ae = Sr, Ba), Philosophical Magazine, DOI: [10.1080/14786435.2018.1425013](https://doi.org/10.1080/14786435.2018.1425013)

To link to this article: <https://doi.org/10.1080/14786435.2018.1425013>



Published online: 19 Jan 2018.



Submit your article to this journal [↗](#)



Article views: 5




View related articles [↗](#)



View Crossmark data [↗](#)



Structural, elastic, electronic, optical and thermoelectric properties of the Zintl-phase Ae_3AlAs_3 ($Ae = Sr, Ba$)

A. Benahmed^a, A. Bouhemadou^a, B. Alqarni^b, N. Guechi^c, Y. Al-Douri^{d,e} ,
R. Khenata^f and S. Bin-Omran^b

^aLaboratory for Developing New Materials and their Characterization, University of Setif 1, Setif, Algeria; ^bDepartment of Physics and Astronomy, College of Science, King Saud University, Riyadh, Saudi Arabia; ^cFaculty of Science, Department of Science of Matter, University of Medea, Medea, Algeria; ^dNanotechnology and Catalysis Research Center (NANOCAT), University of Malaya, Kuala Lumpur, Malaysia; ^eFaculty of Science, Physics Department, University of Sidi-Bel-Abbes, Algeria; ^fLaboratoire de Physique Quantique de la Matière et de Modélisation Mathématique (LPQ3 M), Université de Mascara, Mascara, Algeria

ABSTRACT

First-principles calculations were performed to investigate the structural, elastic, electronic, optical and thermoelectric properties of the Zintl-phase Ae_3AlAs_3 ($Ae = Sr, Ba$) using two complementary approaches based on density functional theory. The pseudopotential plane-wave method was used to explore the structural and elastic properties whereas the full-potential linearised augmented plane wave approach was used to study the structural, electronic, optical and thermoelectric properties. The calculated structural parameters are in good consistency with the corresponding measured ones. The single-crystal and polycrystalline elastic constants and related properties were examined in details. The electronic properties, including energy band dispersions, density of states and charge-carrier effective masses, were computed using Tran-Blaha modified Becke-Johnson functional for the exchange-correlation potential. It is found that both studied compounds are direct band gap semiconductors. Frequency-dependence of the linear optical functions were predicted for a wide photon energy range up to 15 eV. Charge carrier concentration and temperature dependences of the basic parameters of the thermoelectric properties were explored using the semi-classical Boltzmann transport model. Our calculations unveil that the studied compounds are characterised by a high thermopower for both carriers, especially the p -type conduction is more favourable.

ARTICLE HISTORY

Received 15 September 2017
Accepted 20 December 2017

KEYWORDS

Zintl-phase; first-principles calculations; elastic constants; optoelectronic properties; thermoelectric properties

1. Introduction

Thermoelectric (TE) materials play an important role in global sustainable energy solution. These materials are investigated not only owing to their high potential

of converting directly waste thermal energy to useful electrical energy but also to their capability to reduce effectively the environmental pollution. The ability of a TE material to convert heat directly into electricity is controlled by the dimensionless parameter ZT [1,2], the so-called figure of merit, which is given by $ZT = \frac{S^2\sigma}{\kappa}T$, where S is the Seebeck coefficient (thermopower), σ is the electrical conductivity, κ is the thermal conductivity and T is the absolute temperature. A promising TE material should have a large ZT value. From its expression, it is very clear that a high ZT , requires a large thermopower S , high electrical conductivity σ and a low thermal conductivity κ , i.e. an ideal thermoelectric material must strike a balance between these conflicting requirements. However, due to the strongly coupled nature between S , σ and the electronic component of the thermal conductivity κ , it is difficult for a material to have simultaneously high S , high σ and low κ . A high Seebeck coefficient is attained in a low charge-carrier concentration, while a large electrical conductivity is attained in a high charge-carrier concentration; S and σ have an opposite dependence on charge-carrier concentration, so a balance between S and σ must be achieved through a chemical doping [1,3]. Therefore, obtaining a TE material with a high ZT value is a challenging task.

Currently, many kinds of thermoelectric materials have been widely studied, such as Zintl-phases, nanostructured compounds, zinc antimonides, oxides, half-Heusler compounds, clathrates and skutterudites [4–12]. Zintl-phases, a broad class of intermetallic compounds characterised by cations that donate their electrons to support the formation of covalency bonded anionic substrates, have emerged as a promising class of materials for thermoelectric applications due to their complex crystal structures, interesting electronic, chemical and physical properties [13,14]. The structural requirements of Zintl-phases are explained by assuming the presence of both anionic networks and electropositive cations [13]. The anionic networks are covalent and the cationic part is ionic in nature. The resulting mix of ionic and covalent bonds frequently leads to complex crystal structures with large unit cells; such a complex crystal can enable them to have low thermal conductivity [15–17]. Additionally, the Zintl-phase chemistry suggests that the fundamental transport parameters can be modified by doping to achieve a good balance between S and σ , consequently thus can lead to a high power factor [18,19]. Therefore, Zintl-phases provide desired characteristics for high ZT and improved thermoelectric performance since their thermal conductivities are intrinsically low. This has been demonstrated in several previous studies, including Ca_3AlSb_3 [20], $\text{Ca}_5\text{Al}_2\text{Sb}_6$ [21] and $\text{Ca}_5\text{Ga}_2\text{As}_6$ [22]. This further actuates us to search for other possible new Zintl-phase materials for suitable TE candidates. In the current study, we are interested in investigating the Ae_3AlAs_3 ($\text{Ae} = \text{Sr}, \text{Ba}$) compounds that were recently synthesised [23]. These compounds crystallise in the Ba_3AlSb_3 structure type with the space group $Cmce$. The structural properties of the title compounds, including the lattice parameters and atomic position coordinates, have been investigated using single-crystal *X-ray* diffraction. The

band structure and density of states of Ba_3AlAs_3 have been carried out using the tight-binding linear muffin-tin orbital (TB-LMTO) method [23]. To the best of our knowledge, some basic physical properties, such as elastic, optical and thermoelectric properties of these newly synthesised compounds are not studied. Therefore, the main object of the present study is the investigation of the structural, elastic, electronic, optical and thermoelectric properties of the Ae_3AlAs_3 ($\text{Ae} = \text{Sr}, \text{Ba}$) compounds. The structure of the present paper is as follows: Section 2 describes briefly the computation setting. Section 3 reports and discusses the obtained results, with subsections dedicated to structural, elastic, electronic, optical and thermoelectric properties. The paper is finished with a general conclusion.

2. Computational details

First-principles calculations were performed by employing two complementary methods based on density functional theory. The elastic properties were evaluated using the pseudopotential plane wave (PP-PW) method as implemented in the CASTEP code [24], while the electronic and optical properties were carried out using the full potential linearised augmented plane wave method (FP-LAPW) as incorporated in the WIEN2k suite of programs [25]. The structural properties were evaluated using both the aforementioned methods. The structural data from Ref. [23] were taken as initial input for our calculations.

For the pseudopotential plane wave approach, Vanderbilt ultra-soft pseudopotentials [26] were used to describe the interactions between core and valence electrons of each atom. The Ba: $5s^25p^66s^2$, Sr: $4s^24p^65s^2$, Al: $3s^23p^1$ and As: $4s^24p^3$ states were treated as valence electrons. The electronic exchange and correlation effects were treated through the generalised gradient approximation functional in the version of Perdew et al. [27], the so-called GGA-PBESol. The plane-wave basis set energy cut-off was set at 350 eV. The Brillouin zone integration was replaced by a summation over a $6 \times 6 \times 3$ k -point mesh generated according to Monkhorst-Pack scheme [28]. This set of parameters assures a total energy tolerance of 1×10^{-5} eV/atom, a maximum force tolerance of 0.01 eV/Å, a maximum stress of 0.02 GPa and a maximum displacement of 5.0×10^{-4} Å.

It is well known that the first-principles methods with the common generalised gradient approximation (GGA) yield good values for the ground state structures but they underestimate the band gaps of semiconductors and insulators typically by 30–50% [29–31] when compared to experiments. The underestimation of the band gaps of semiconductors and insulators when using GGA is because this approximation cannot describe exactly the exchange–correlation potential. Some sophisticated approaches, such as the weighted density approximation (WDA) [32], the GW approximation [33] and the Tran-Blaha modified Becke-Johnson (TB-mBJ) potential [34], have been developed in order to overcome this insufficiency and to obtain reliable band gap values for semiconductors and insulators

compared to the measured ones. The TB-mBJ is computationally cheaper than the other aforementioned methods and produces energy band gaps almost comparable with the corresponding measured ones with a reasonable computation time. Therefore, in addition to the GGA-PBEsol, the electronic, optical and thermoelectric properties of the investigated compounds were calculated using the TB-mBJ functional as implemented in the WIEN2k package [25]. The WIEN2k code is an implementation of the full-potential linearised augmented plane wave (FP-LAPW). In the FP-LAPW method, the unit cell is divided into non-overlapping spheres centred at the atomic sites (labelled muffin-tin spheres (MTS)) and the space between the MTS (labelled interstitial region (IR)). A linear combination of radial atomic functions time spherical harmonics is used inside the MTS to expand the wave functions, whereas a plane wave basis set is used in the IR. In order to achieve the energy convergence of the eigenvalues, the wave functions in the interstitial regions were expanded in plane waves with a cut-off parameter $K_{\text{Max}} = 4 (a.u.)^{-1}$. The Brillouin zone integration was replaced by a $6 \times 6 \times 3$ k -point mesh. The iteration process was repeated until the calculated total energy of the crystal converged to less than 10^{-5} Ry. The muffin-tin radii were selected as 2.35 $a.u.$ for Sr, 2.40 $a.u.$ for Ba, 2.18 $a.u.$ for Al and 2.44 $a.u.$ for As.

3. Results and discussion

3.1. Structural parameters

Single-crystal *X-ray* diffraction technique reveals that the Ae_3AlAs_3 ($Ae = \text{Sr, Ba}$) compounds crystallise in the orthorhombic Ba_3AlSb_3 -type structure, space group $Cmce$, with eight formula units in one unit cell [23] (Figure 1). There are two kinds of Ae ($Ae1$ and $Ae2$) and As ($As1$ and $As2$) atoms. The Wyckoff atomic positions in the Ae_3AlAs_3 unit cell are $Ae1$: $8f(0, y_{Ae1}, z_{Ae1})$; $Ae2$: $16g(x_{Ae2}, y_{Ae2}, z_{Ae2})$; Al: $8d(x_{Al}, 0, 0)$; $As1$: $8f(0, y_{As1}, z_{As1})$ and $As2$: $16g(x_{As2}, y_{As2}, z_{As2})$. The fully optimised crystal structure, including lattice parameters and atomic positions, for the orthorhombic Sr_3AlAs_3 and Ba_3AlAs_3 crystals, using both the PP-PW and FP-LAPW methods, are collected in Tables 1 and 2 in comparison with experimental findings. The inspection of Table 1 data indicates a good agreement between the calculated values for the lattice parameters (a , b and c) and the corresponding measured ones. Using the PP-PW (FP-LAPW) method, the deviations between the theoretical values of a , b and c and the corresponding experimental ones do not exceed +2.03% (−0.51%), −0.72% (−3.27) and +0.67% (−0.01%), respectively, in Sr_3AlAs_3 , and −0.03% (−1.38%), −0.34% (−7.48%) and −0.107% (−0.51%), respectively, in Ba_3AlAs_3 . Table 2 data show also a very good agreement between the calculated atomic position coordinates (x , y , z) and the corresponding measured ones, indicating the reliability of the performed calculations.

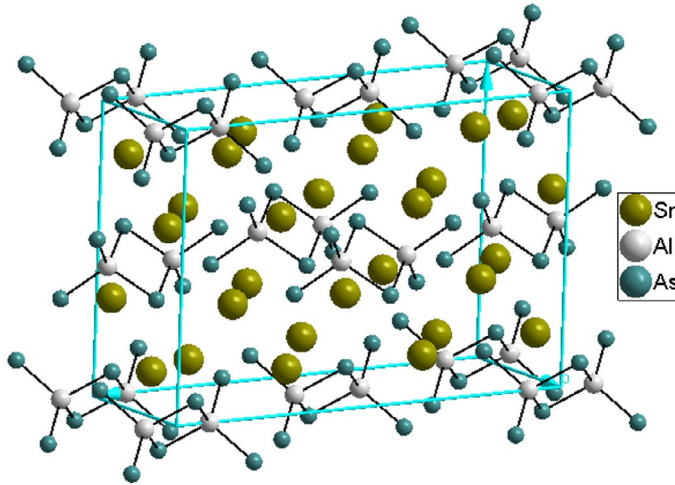


Figure 1. (colour online) One unit cell of Sr_3AlAs_3 .

Table 1. Calculated lattice parameters (a , b and c , in Å) and unit-cell volume (V , in Å³) for the Sr_3AlAs_3 and Ba_3AlAs_3 compounds, compared with the available experimental data.

	a	b	c	V
Sr_3AlAs_3				
Present work ^a	19.0503	6.3501	12.7002	1587.22
Present work ^b	19.5368	6.5174	12.7729	1626.39
Expt. [23]	19.149	6.5652	12.6871	1595.0
Ba_3AlAs_3				
Present work ^a	19.5795	6.3501	13.2294	1737.92
Present work ^b	19.8475	6.8406	13.2741	1802.22
Expt. [23]	19.854	6.8636	13.3589	1810.3

^aUsing FP-LAPW method within GGA-PBEsol.

^bUsing PP-PW method within GGA-PBEsol.

Table 2. Atomic position coordinates for the Sr_3AlAs_3 and Ba_3AlAs_3 compounds, compared with the available experimental data.

Atom	x			y			z		
	Present ^a	Present ^b	Expt. ^c	Present ^a	Present ^b	Expt. ^c	Present ^a	Present ^b	Expt. ^c
Sr_3AlAs_3									
Sr1	0	0	0	0.17601	0.17924	0.17463	0.34919	0.34707	0.34891
Sr2	0.17701	0.17755	0.17691	0.31155	0.30838	0.31222	0.13114	0.13009	0.13126
Al	0.08477	0.08377	0.08500	0	0	0	0	0	0
As1	0	0	0	0.21042	0.21277	0.20879	0.10330	0.10079	0.10250
As2	0.34107	0.34207	0.34135	0.29518	0.29326	0.29606	0.12081	0.11794	0.12022
Ba_3AlAs_3									
Ba1	0	0	0	0.17027	0.17109	0.17015	0.34671	0.34766	0.34685
Ba2	0.17572	0.17535	0.17563	0.31309	0.31201	0.31318	0.13024	0.12975	0.13014
Al	0	0.08316	0.08294	0	0	0	0	0	0
As1	0	0	0	0.20320	0.20566	0.20319	0.09628	0.09791	0.09613
As2	0.34335	0.34294	0.34345	0.30899	0.30728	0.30905	0.11818	0.11954	0.11805

^aUsing the FP-LAPW method within the GGA-PBEsol.

^bUsing the PP-PW method within the GGA-PBEsol.

^cRef. [23].

Table 3. Calculated elastic constants (C_{ij} in GPa) for the Ae_3AlAs_3 ($Ae = Sr, Ba$) compounds.

System	C_{11}	C_{22}	C_{33}	C_{44}	C_{55}	C_{66}	C_{12}	C_{13}	C_{23}
Sr_3AlAs_3	61.7	74.6	76.6	32.4	28.6	30.3	27.1	22.6	31.3
Ba_3AlAs_3	80.2	71.1	81.5	17.1	4.7	14.1	21.6	15.3	24.0

3.2. Elastic constants and related properties

Accurate calculations of the elastic constants C_{ij} are very helpful to understand many physical properties of solids. The elastic constants C_{ij} provide valuable information on the stability and stiffness of crystals against externally applied strain, bonding characteristics, specific heat, thermal expansion, Debye temperature, Grüneisen parameter and so on [35–37]. In general, the elastic behaviour of a completely asymmetric material is specified by 21 independent elastic constants C_{ij} but due to the presence of some symmetries, this number can be reduced. Only nine independent elastic constants, namely C_{11} , C_{22} , C_{33} , C_{44} , C_{55} , C_{66} , C_{12} , C_{13} and C_{23} , are required to characterise the elastic properties of an orthorhombic crystal. The elastic constants C_{ij} were evaluated via the calculation of three stress tensors corresponding to three different deformation patterns applied to the equilibrium lattice. The calculated elastic constants C_{ij} using the strain–stress method [24] for the title compounds are reported in Table 3. There are no theoretical or experimental results for the elastic constants C_{ij} in the scientific literature to be compared with the present results. Then, our results can serve as a prediction for future investigations.

The elastic constants C_{11} , C_{22} and C_{33} reflect the resistance to the linear compression along the [100], [010] and [001] crystallographic directions, respectively. From Table 3, one can note that the values of the three aforementioned elastic constants are not remarkably different, suggesting that the resistance to the compression deformation along the [100], [010] and [001] directions are approximately equal. The values of C_{11} , C_{22} and C_{33} are higher than those of the other elastic constants C_{ij} , demonstrating that the resistance of the two studied compounds to the shear distortion is lower than their resistance against the compressional deformation.

The mechanical stability of crystals leads to some restrictions on their elastic constants. For orthorhombic crystals, these mechanical stability criteria are [38]:

$$C_{11} + C_{22} - 2C_{12} > 0, \quad C_{11} + C_{33} - 2C_{13} > 0, \quad C_{22} + C_{33} - 2C_{23} > 0, \quad C_{11} > 0, \quad C_{22} > 0, \\ C_{33} > 0, \quad C_{44} > 0, \quad C_{55} > 0, \quad C_{66} > 0, \quad C_{11} + C_{22} + C_{33} + 2C_{12} + 2C_{13} + 2C_{23} > 0$$

The calculated elastic constants of the two studied compounds (Table 3) satisfy the aforementioned criteria. This indicates that these compounds are mechanically stable.

It is not possible to measure the individual elastic constants C_{ij} when single-crystal samples cannot be obtained. In this case, polycrystalline elastic moduli, such as the bulk modulus B and the shear modulus G , can be measured. Theoretically,

we can deduce the polycrystalline (aggregates of single-crystals with random orientations) elastic moduli, which are more desirable for technological characterisation of materials, from the calculated single-crystal elastic constants C_{ij} . The isotropic shear and bulk moduli (G and B) can be calculated from the anisotropic single-crystal elastic constants C_{ij} using the Hill approximation [39], which takes the arithmetic average of the Voigt [40] and Reuss [41] approximations. The Voigt approach determines the upper limit of the actual effective moduli, while the Reuss approach determines the lower limit of these parameters. The expression of the Voigt bulk and shear moduli (B_V and G_V) and the Reuss bulk and shear moduli (B_R and G_R) can be found in Ref. [42]. The Young's modulus E and Poisson's ratio σ can be obtained from B and G using the well-known relationships [43,44]. The calculated values of the aforementioned elastic moduli are given in Table 4. The obtained results allow us to make the following conclusions:

- (i) Due to the low value of the bulk modulus, which represents the resistance to volume change by external applied pressure, one can conclude that the considered materials are characterised by a weak resistance to the volume change; i.e. by a high compressibility. The lower value of the shear modulus, which characterises the resistance to shear deformation, demonstrates that Ba_3AlAs_3 and Sr_3AlAs_3 have also a weak resistance to shape change. Besides, the bulk modulus B is larger than the shear modulus G in both considered compounds, indicating a better capability of resistance to volume change than to shape change.
- (ii) The Young's modulus E , defined as the ratio of linear stress to linear strain, can be used to provide a measure of the stiffness of a material. It is found that E of the two studied compounds is weak, indicating that these compounds will show a rather small stiffness. The results also demonstrate that Sr_3AlAs_3 is stiffer than Ba_3AlAs_3 in terms of B , G and E moduli.
- (iii) The most widely used criterion to distinguish between ductile and brittle materials is the Pugh's one (B/G ratio) [45]. According to this criterion, a material can be classified as ductile if the B/G ratio is greater than 1.75; otherwise, it demonstrates brittleness. The obtained data foretell that Sr_3AlAs_3 ($B/G = 1.55$) should behaves as brittle material, while Ba_3AlAs_3 should demonstrates ductility. The classical criteria of Cauchy pressure can also be used to examine the brittle/ductile

Table 4. Calculated Reuss, Voigt and Hill bulk (B_R , B_V and B_H in GPa) and shear (G_R , G_V and G_H in GPa) moduli, Young's modulus (E , in GPa) and Poisson's ratio (σ , dimensionless) for isotropic polycrystalline Ae_3AlAs_3 ($\text{Ae} = \text{Sr}, \text{Ba}$) aggregates.

System	B_V	G_V	B_R	G_R	B_H	G_H	E_j			E	σ
							E_x	E_y	E_z		
Sr_3AlAs_3	41.65	39.60	40.92	26.15	41.29	26.60	72.80	60.30	72.52	65.70	0.23
Ba_3AlAs_3	39.41	32.73	39.39	12.02	39.40	15.32	72.80	60.30	72.52	40.69	0.32

character of materials [46]. Pettifor [47] indicated that Cauchy pressure can be adopted to capture the nature of the bonding. Materials with a positive Cauchy pressure possess metallic like bonds, thereby holding ductile characteristics. On the other hand, brittle materials would hold a negative Cauchy pressure. In orthorhombic materials, the Cauchy pressure in the three lattice directions can be expressed as follows [48]: $P_a^{Cauchy} = C_{22} - C_{44}$, $P_b^{Cauchy} = C_{13} - C_{55}$ and $P_c^{Cauchy} = C_{12} - C_{66}$. Based on the calculated single-crystal C_{ij} (Table 3), $P_a^{Cauchy} = -1.10 \text{ GPa}$ (6.90 GPa), $P_b^{Cauchy} = -6.0 \text{ GPa}$ (10.60 GPa) and $P_c^{Cauchy} = -3.0 \text{ GPa}$ (7.50 GPa) for Sr_3AlAs_3 (Ba_3AlAs_3). These results confirm the brittleness of Sr_3AlAs_3 and ductility of Ba_3AlAs_3 .

From the computed bulk and shear moduli, we can evaluate the longitudinal (V_l), transverse (V_t) and average (V_m) sound wave velocities in a polycrystalline material through the following relationships [49]:

$$V_l = \sqrt{(B_H + 4G_H/3)/\rho}; \quad V_t = \sqrt{G_H/\rho}; \quad V_m = [(2/V_t^3 + 1/V_l^3)/3]^{-1/3}$$

Debye temperature θ_D , which is associated with the lattice vibration, elastic constants, specific heat and melting point, can be predicated via the following common relation [49]:

$$\theta_D = \frac{h}{k_B} \left[\frac{3n}{4\pi} \left(\frac{N_A \rho}{M} \right) \right]^{\frac{1}{3}} V_m$$

Here, h and k_B are the constants of Planck and Boltzmann, respectively, n is the number of atoms per one formula unit, N_A is Avogadro's number, ρ denotes the mass density, M is the molecular mass. The calculated values of ρ , V_l , V_t , V_m and θ_D for the Ae_3AlAs_3 ($\text{Ae} = \text{Sr}, \text{Ba}$) compounds are collected in Table 5. Sr_3AlAs_3 has a larger Debye temperature than Ba_3AlAs_3 ; this is a predicted result because the bulk modulus of Sr_3AlAs_3 is somewhat larger than that of Ba_3AlAs_3 . Up to now, there are no available data for these parameters in the scientific literature to be compared with our present findings.

An isotropic material displays the same physical properties irrespective of the direction in which those properties are measured. In general, the elastic response of a single-crystal is seldom isotropic; almost all the known crystals are elastically anisotropic, so their elastic moduli depend on the orientation of the applied force

Table 5. Calculated mass density (ρ), longitudinal, transverse and average sound velocities (V_l , V_t and V_m , in m/s unit) and Debye temperatures (θ_D , in K unit) for the Ae_3AlAs_3 ($\text{Ae} = \text{Sr}, \text{Ba}$) polycrystals.

System	ρ	V_l	V_t	V_m	θ_D
Sr_3AlAs_3	4.2033	4273.50	2331.94	2600.81	251.95
Ba_3AlAs_3	4.8925	3961.10	1769.79	1996.65	186.91

in respect of the crystallographic axes. The description of elastic anisotropy in materials is important because it influences various physical properties, such as unusual phonon modes, phase transformations, precipitation, dislocation dynamics, anisotropic plastic deformation, anomalous bcc slip, mechanical yield points, crack behaviour, elastic instability and internal friction [50]. The anisotropy in mechanical properties might be estimated using various anisotropy indexes and factors [51–56]. An even detailed picture of the elastic anisotropy can be emerged by plotting a three-dimensional surface representation showing the variation of the Young's modulus with the crystallographic directions. This directional dependence of the Young's modulus E for an orthorhombic crystal in an arbitrary direction is defined as [57]:

$$E = [S_{11}l_1^4 + 2S_{12}l_1^2l_2^2 + S_{22}l_2^4 + 2S_{23}l_2^2l_3^2 + S_{33}l_3^4 + 2S_{13}l_1^2l_3^2 + S_{44}l_2^2l_3^2 + S_{55}l_1^2l_3^2 + S_{66}l_1^2l_2^2]^{-1}$$

Here, l_1 , l_2 and l_3 are the direction cosines, which determine the angles between the axes a , b and c , respectively, and a given direction, and S_{ij} is the elastic compliance constants, which can be acquired from the inverse of the matrix of elastic constants. The distance from the origin of the coordinate system to this surface is equal to the Young's modulus in a given direction. For a perfectly isotropic medium, this surface would be a sphere, while the deviation of this surface from the spherical shape indicates the presence of a certain degree of elastic anisotropy. Figure 2 illustrates the directional dependence of the Young's modulus of the Sr_3AlAs_3 and Ba_3AlAs_3 compounds. Figure 1 shows that the degree of elastic anisotropy of Ba_3AlAs_3 is much more appreciable than that of Sr_3AlAs_3 . A deeper look into the peculiar features of elastic anisotropy can be gauged by plotting the cross-section of the closed surface of E in the principal planes. For isotropic crystal, the plane projection curves are circular. From the cross sections plotted separately in Figure 1, we can see that there is a clear deviation from circular shape.

3.3. Electronic properties

3.3.1. Band structure

The electronic energy band dispersions along the high-symmetry directions in the Brillouin zone (BZ) for the Sr_3AlAs_3 and Ba_3AlAs_3 compounds, performed at the optimised structural parameters, using the FP-LAPW method with both the GGA-PBEsol and TP-mBJ approaches, are depicted in Figure 3. The Γ , Z, T, Y, S and R letters indicate the high symmetry points in the BZ of the Ae_3AlAs_3 ($\text{Ae} = \text{Sr}, \text{Ba}$) compounds and their coordinates are respectively (0,0,0), (0,0,0.5), (−0.5,0.5,0.5), (−0.5, 0.5, 0), (0,0.5,0) and (0,0.5,0.5) in the unit vectors of the reciprocal lattice. From Figure 2, one can note that Sr_3AlAs_3 has a direct band gap; the top of the valence band (VB) and the bottom of the conduction band (CB) are located at the Γ -point, while Ba_3AlAs_3 has an indirect band gap; the top

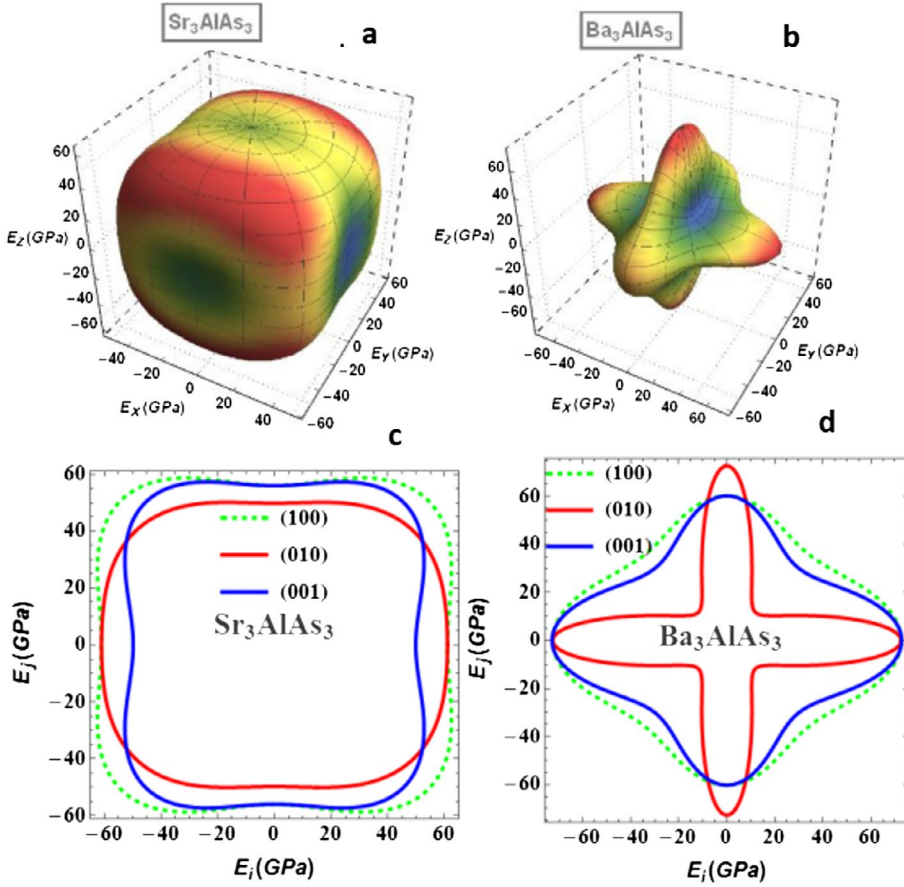


Figure 2. (colour online) 3D-directional dependence of the Young's modulus (E , in GPa) and its projection on the ab - $\{(001)\}$, ac - $\{(010)\}$ and ab - $\{(100)\}$ planes for the Sr_3AlAs_3 and Ba_3AlAs_3 compounds.

of the VB is located at the Y -point and the bottom of the CB is at the Γ -point. The calculated band structures using the TB-mBJ and GGA-PBESol functionals have practically same features except the band gap values that are disparate. The calculated Sr_3AlAs_3 (Ba_3AlAs_3) energy band gap is 1.51 eV (1.28 eV) when using the TB-mBJ formalism, and is 0.90 eV (0.61 eV) when using the GGA-PBESol. We note that the GGA and LDA functionals usually underestimate the energy band gap by 30–50% [30–32]. Therefore, one can appreciate that the TB-mBJ considerably improves the band gap values. There are no experimental values for the gaps of the studied compounds. The GGA-PBESol band gap value for Ba_3AlAs_3 is in good agreement with the one predicted by Stanislav et al. [24] using the tight-binding linear muffin tin orbital (TB-LMTO) method within the LDA.

3.3.2. Density of states

Assignment of the electronic states composing the electronic energy bands of the considered systems can be made with the help of the total and atomic decomposed

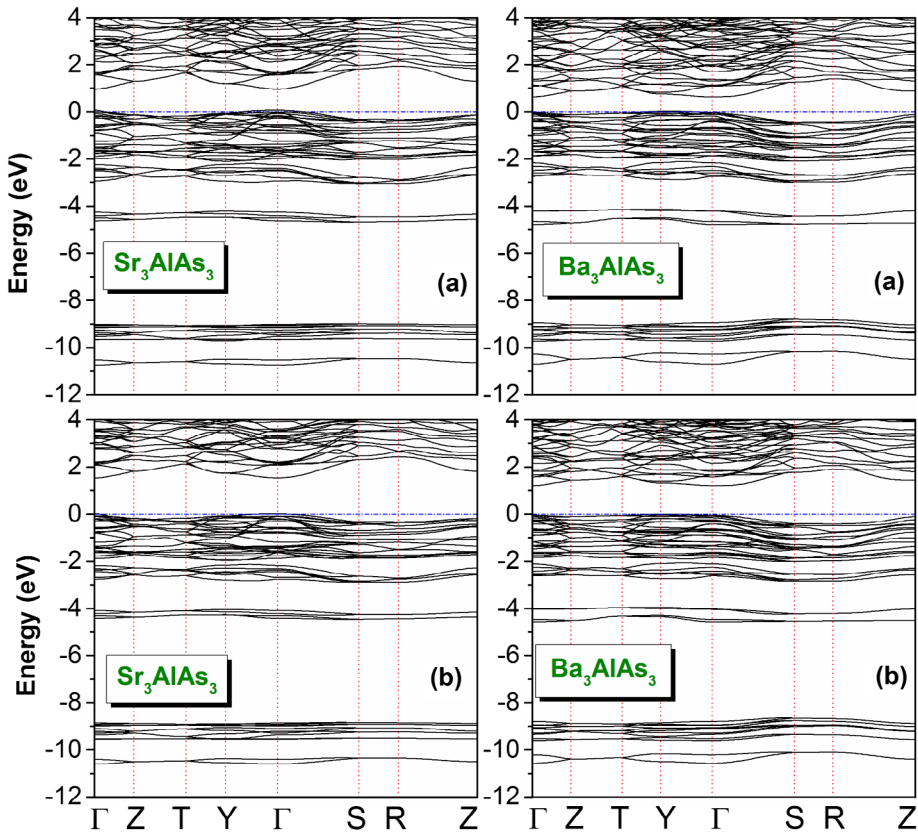


Figure 3. (colour online) Electronic band dispersion curves along some high symmetry directions in the Brillouin zone for the Ae_3AlAs_3 ($Ae = Sr, Ba$) compounds using the GGA-PBEsol (a) and the TB-mBJ (b) functionals.

partial densities of states (TDOS and PDOS) diagrams, which are shown in Figure 4. The Sr_3AlAs_3 and Ba_3AlAs_3 valence bands located in the energy range from -12 eV up to Fermi level (E_F) can be separated into four groups that are labelled V1, V2, V3 and V4 in the figure. For Sr_3AlAs_3 , the lowest energy group V1, which is stretched from approximately -10.6 to -9.9 eV, is mainly formed of the As1-4s and As2-4s states. The second group V2, which spreads approximately from -9.7 to -8.5 eV, is mainly due to the As1-4p and Al-3s states with a very small contribution from an admixture of the Al-3s, Al-3p, Sr1-4p and Sr2-4p orbitals. The third group V3, located in the energy range from -4.6 to -3.97 eV, is mainly due to the As1-4p and Al-3s states. The fourth valence band group V4, which lays approximately from -3.0 eV up to Fermi level (E_F), is completely dominated by the As1-4p and As2-4p states with a small contribution from the Al-3p, Sr1-4s, Sr2-4s, Sr1-4p, Sr2-4p, Sr1-3d and Sr2-3d states. The bottom of the conduction band (C1) comes from the Sr1-3d and Sr2-3d states with a small contribution from the Al-3p and Al-3s states. For the Ba_3AlAs_3 compound, the V1 valence band group, from -10.7 to -9.97 eV, is mainly occupied by the As1-4s states with a small

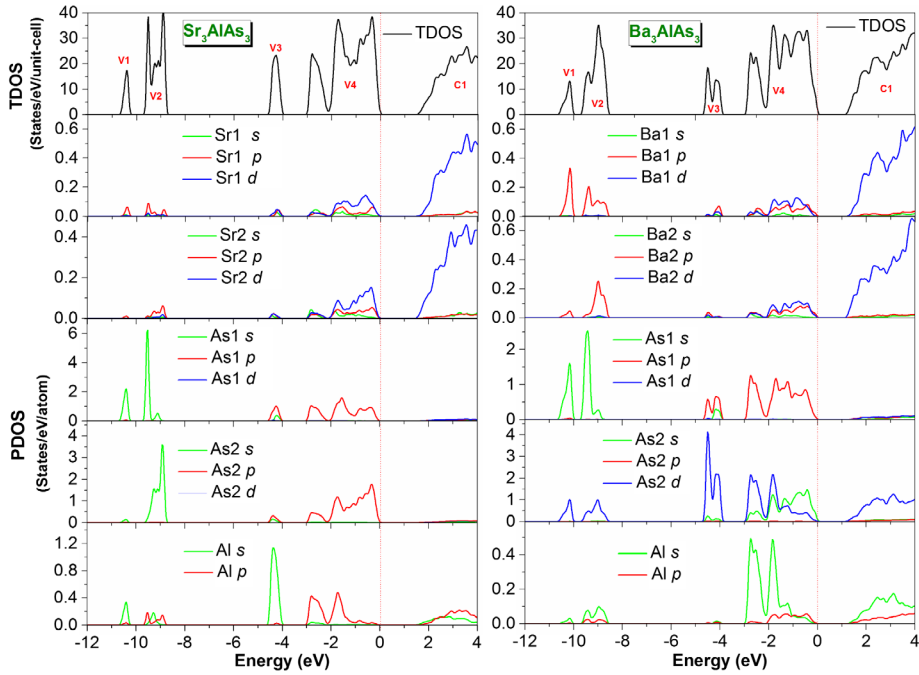


Figure 4. (colour online) Total and partial densities of states (TDOS and PDOS) diagrams for the Ae_3AlAs_3 ($Ae = Sr, Ba$) compounds.

contribution from an admixture of the Ba1-5*p*, Ba2-5*p*, As2-4*d* and Al-3*s* states. The second group V2, from -9.7 to -8.5 eV, is mainly formed of the As1-4*s* states with a small contribution from an admixture of the Ba1-5*p*, Ba2-5*p*, As2-4*d* and Al-3*sp* states. The third group V3, from -4.7 to -3.82 eV, is mainly composed of the As2-4*d* and As1-4*p* states with a small contribution from the Ba1-4*p*, Ba1-4*d*, Ba2-4*p* and Ba2-4*d*. The upper valence band group V4, from -3.05 eV up to Fermi level, is mainly due to the As1-4*p* and As2-4*sd* states with a small contribution from the Al-3*p* and Ba1-4*pd* orbitals. The bottom of the conduction band C1 is made up basically of the As2-4*d*, Ba1-4*d* and Ba2-4*d* states with a small contribution from the Al-3*s* and Al-3*p* states.

3.3.3. Effective mass

The effective mass of charge-carrier provides an opposite contribution to the Seebeck coefficient and electrical conductivity. A large effective mass of charge-carrier is favourable to improve the Seebeck coefficient; however, the high charge-carrier mobility requires a lighter effective mass. To further understand the electrical behaviour of the Ae_3AlAs_3 ($Ae = Sr, Ba$) compounds, it is necessary to estimate their effective masses of the charge-carriers in various electron and hole pockets at the band edges. The effective mass of electrons (m_e^*) at the conduction band minimum (CBMi) and holes (m_h^*) at the valence band maximum (VBMa) can be evaluated through a simple parabolic fitting of the dispersion energy $E(k)$

Table 6. Calculated electron and hole effective masses (m_e^* and m_h^* in units of free electron mass m_0) for the Sr_3AlAs_3 and Ba_3AlAs_3 compounds.

System	$m_e^*(\Gamma \rightarrow S)$	$m_e^*(\Gamma \rightarrow Y)$	$m_h^*(\Gamma \rightarrow S)$	$m_h^*(\Gamma \rightarrow Y)$
Sr_3AlAs_3	0.2007	0.2202	0.3225	4.0226
	$m_e^*(\Gamma \rightarrow S)$	$m_e^*(\Gamma \rightarrow Y)$	$m_h^*(Y \rightarrow T)$	$m_h^*(Y \rightarrow \Gamma)$
Ba_3AlAs_3	0.2158	0.3738	0.6161	0.5514

diagram: $E = \frac{\hbar k^2}{2m^*}$, where \hbar is the Planck's constant, E is the band-edge energy as a function of the wave vector k and m^* is the effective mass. For Ba_3AlAs_3 , the effective masses of the holes at the VBma were calculated along the $Y \rightarrow T$ and $Y \rightarrow \Gamma$ directions and those of the electrons at the CBmi were evaluated along the $\Gamma \rightarrow S$ and $\Gamma \rightarrow Y$ directions. For Sr_3AlAs_3 , the effective masses of holes and electrons are calculated along the $\Gamma \rightarrow S$ and $\Gamma \rightarrow Y$ directions. The obtained results are listed in Table 6. From Table 6, it is clear that the electrons and holes effective masses show a relevant dependence on the k -direction in the two considered compounds, implying the anisotropy of this physical property. It is found also that the effective mass of electron at the conduction band minimum is small than that of the hole at the valence band maximum. Consequently, the p -type Ae_3AlAs_3 ($\text{Ae} = \text{Sr}, \text{Ba}$) compounds would have the highest Seebeck coefficient, while the n -type Ae_3AlAs_3 ($\text{Ae} = \text{Sr}, \text{Ba}$) compounds would have the largest electrical conductivity. In addition, we can predict that the charge-carrier mobility of the p -type Sr_3AlAs_3 (Ba_3AlAs_3) compound along the $\Gamma \rightarrow S$ ($\Gamma \rightarrow Y$) direction should be larger than that in the $\Gamma \rightarrow Y$ ($Y \rightarrow T$) direction.

3.4. Optical properties

The fundamental features of the linear response of a medium to the effect of an incoming electromagnetic radiation can be accessed from the knowledge of its complex dielectric function $\epsilon(\omega)$, which is directly related to the interaction of photons with electrons. The imaginary part of the dielectric function $\epsilon_2(\omega)$ ($\epsilon_2(\omega) = \text{Im } \epsilon(\omega)$; $\epsilon(\omega) = \epsilon_1(\omega) + j\epsilon_2(\omega)$) is directly proportional to the intensity of optical absorption. In the framework of the linear-response theory, $\epsilon_2(\omega)$ is calculated from the matrix elements of the electric dipole operator between the occupied states in the valence band and unoccupied states in the conduction band within the respect of the selection rules [58]. The real part of the dielectric function $\epsilon_1(\omega)$ ($\epsilon_1(\omega) = \text{Re } \epsilon(\omega)$) can be assessed from the imaginary part $\epsilon_2(\omega)$ via the Kramer–Kronig relationship [59]. All frequency dependent macroscopic optical functions, such as refractive index $n(\omega)$, absorption coefficient $\alpha(\omega)$, reflectivity $R(\omega)$ and electron energy-loss function $L(\omega)$, can be deduced from $\epsilon_2(\omega)$ and $\epsilon_1(\omega)$ using the well-known relationships [60,61]. Since the investigated compounds belong to the orthorhombic system, space group $Cmce$, it is necessary to calculate the three non-zero components of the dielectric tensor that correspond to the three polarisations of the electric field \vec{E} of the incident electromagnetic

radiation along the three principal crystallographic directions: a ([100]), b ([010]) and c ([001]).

The calculated imaginary parts of the Sr_3AlAs_3 and Ba_3AlAs_3 dielectric functions for the three different polarisations, i.e. $\vec{E} // [100]$, $\vec{E} // [010]$ and $\vec{E} // [001]$, are presented in Figure 5(a). It is clear from Figure 5(a) that the optical properties of the considered compounds exhibit a noticeable anisotropy. To account for the features observed in the optical spectra, it is customary to consider transitions from occupied to unoccupied states in the electronic energy band structure, especially at the high symmetry points in the Brillouin zone. Our scrutiny of the $\epsilon_2(\omega)$ curve of Sr_3AlAs_3 indicates that it rises speedily with practically the same rate for the three different polarisations of the incident radiation. The $\epsilon_2(\omega)$ spectrum exhibits two peaks centred at approximately 3.99 and 4.56 eV when the incident radiation is polarised parallel to the [100] crystallographic direction, at 4.01 and 4.91 eV for $\vec{E} // [010]$ and at 4.53 and 4.97 eV when $\vec{E} // [001]$. Based on the calculated band structure and density of states diagrams, one can conclude that these peaks are mainly originated from the direct transitions between the $\text{Sr}1-4p$ and $\text{Sr}2-4p$ or $\text{As}1-4p$ and $\text{As}2-4p$ states in the valence band and the $\text{Sr}-3d$ states in the conduction band. The absorptive part of the dielectric function of the single-crystal Ba_3AlAs_3 exhibits one peak centred at approximately 4.20 eV for $\vec{E} // [100]$, at 4.97 eV for $\vec{E} // [010]$ direction and at approximately 4.23 eV for $\vec{E} // [001]$. This peak is mainly due to the electronic direct transitions from the occupied state $\text{As}1-4p$ or $\text{As}2-4s$ to the unoccupied states $\text{Ba}1-3d$ or $\text{Ba}2-3d$.

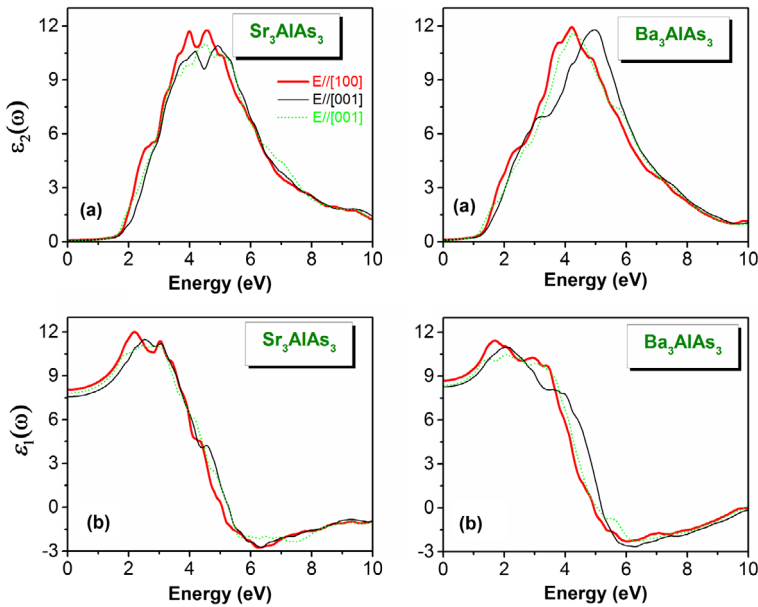


Figure 5. (colour online) Calculated imaginary ($\epsilon_2(\omega)$) and real ($\epsilon_1(\omega)$) parts of the dielectric function ($\epsilon(\omega)$) as functions of photon energy for the Ae_3AlAs_3 ($\text{Ae} = \text{Sr}, \text{Ba}$) single-crystals for three different polarisations: $\vec{E} // [100]$, $\vec{E} // [010]$ and $\vec{E} // [001]$.

The dispersive parts ($\epsilon_1(\omega)$) of the Sr_3AlAs_3 and Ba_3AlAs_3 dielectric functions are shown in Figure 5(b). The most important quantity in $\epsilon_1(\omega)$ spectrum is the static dielectric constant, which is defined as the zero-energy value of the real part of the complex dielectric function: $\epsilon_1(0) = \epsilon_1(\omega \rightarrow 0)$. The $\epsilon_1(0)$ is a parameter of fundamental importance in many aspects of material properties. Calculated $\epsilon_1(0)$ value for Sr_3AlAs_3 (Ba_3AlAs_3) is found to be equal 8.048 (8.683) when $\vec{E} // [100]$, 7.566 (8.255) when $\vec{E} // [010]$ and 7.810 (8.361) when $\vec{E} // [001]$. One can note that the $\epsilon_1(0)$ values corresponding to the three different polarisation directions are larger than the corresponding ones for Ba_3AlAs_3 . This demonstrates that $\epsilon_1(0)$ value is inversely proportional with the band gap; a smaller energy gap yields a larger $\epsilon_1(0)$ value. This is consistent with the Penn's model [59] based on the expression $\epsilon(0) \approx 1 + (\hbar\omega_p/E_g)^2$.

The absorption coefficient $\alpha(\omega)$ describes the relative decrease in the incident radiation intensity when it passes through a medium. The calculated Sr_3AlAs_3 and Ba_3AlAs_3 absorption coefficients in a wider spectral region up to 15 eV for three different polarisations of the incident radiation: $\vec{E} // [100]$, $\vec{E} // [010]$ and $\vec{E} // [001]$ are displayed in Figure 6(a). The absorption edge in the Sr_3AlAs_3 compound starts at approximately 1.51 eV for the three different polarisations of the incident radiation. For the Ba_3AlAs_3 compound, the absorption edge begins approximately at 1.28 eV for the three different polarisations of the incident

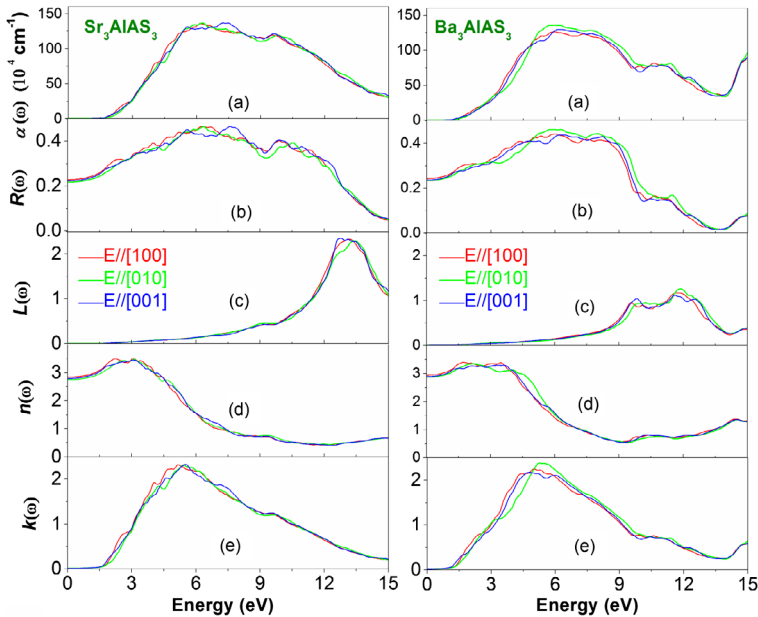


Figure 6. (colour online) Calculated optical function spectra: Absorption coefficient $\alpha(\omega)$, reflectivity $R(\omega)$, energy loss function $L(\omega)$, refractive index $n(\omega)$ and extinction coefficient $k(\omega)$ for the Sr_3AlAs_3 and Ba_3AlAs_3 single-crystals for three different polarisations: $\vec{E} // [100]$, $\vec{E} // [010]$ and $\vec{E} // [001]$.

radiation. A wide absorption band, located between 2 and 12 eV, characterises the considered compounds.

Figure 6(b) displays the calculated dependence of the reflectivity on the incident photon energy for three different polarisations for the Sr_3AlAs_3 and Ba_3AlAs_3 single-crystals. The zero frequency limit $R(0)$ of the Sr_3AlAs_3 (Ba_3AlAs_3) compound is equal to 23% (24%) for $\vec{E}/[100]$, 21% (23%) for $\vec{E}/[010]$ and 22% (23%) for $\vec{E}/[001]$. The reflectivity $R(\omega)$ enhances from $R(0)$ with increasing photon energy to acquire a maximum and then it decreases rapidly. From Figure 5(b), one can note that the maximum reflectivity in Sr_3AlAs_3 (Ba_3AlAs_3) arises approximately at 6.27 eV (6.00 eV) for $\vec{E}/[100]$, 6.35 eV (5.75 eV) for $\vec{E}/[010]$ and 7.60 eV (6.35 eV) for $\vec{E}/[001]$. This maximum attains 46% (44%) for $\vec{E}/[100]$, 46% (46%) for $\vec{E}/[010]$ and 43% (42%) for $\vec{E}/[001]$ in Sr_3AlAs_3 (Ba_3AlAs_3).

The energy-loss function $L(\omega)$ describes the energy-loss of a fast electron passing through a material [62]. The main peak of the $L(\omega)$ spectrum is generally defined as the bulk plasma frequency $(\omega)_p$, which occurs when $\epsilon_2(\omega) < 1$ and $\epsilon_1(\omega)$ reaches the zero point [63]. The plasma frequency for Sr_3AlAs_3 (Ba_3AlAs_3) is approximately equal to 13.15 eV (11.68 eV) for $\vec{E}/[100]$, 13.34 eV (11.87 eV) for $\vec{E}/[010]$ and 12.77 eV (11.60 eV) for $\vec{E}/[001]$ (Figure 6(c)). When the frequency of incident light is higher than the plasma frequency, the material becomes transparent, and hence an abrupt reduction of the reflectivity occurs at the corresponding energy.

The refractive index $n(\omega)$ of a material describes the difference between the propagation of an electromagnetic wave through vacuum and in a material. The extinction coefficient directly describes the attenuation of the electromagnetic waves in a material, and it is also known as a damping constant attenuation coefficient. The knowledge of the refractive index of an optical compound is important for its use in optical devices, such as photonic crystals and waveguides. Figure 6(d) shows the refractive index of Sr_3AlAs_3 and Ba_3AlAs_3 in relation with the energy of incident radiation. It is found that the static refractive index $n(0)$ (the value of refraction index at zero energy) for Sr_3AlAs_3 (Ba_3AlAs_3) compound is 2.83 (2.94) for $\vec{E}/[100]$, 2.75 (2.87) for $\vec{E}/[010]$ and 2.79 (2.89) for $\vec{E}/[100]$.

Static optical anisotropy for the title compounds can be quantified by an anisotropy rate, which can be expressed as follows [64,65]:

$$A_{OPT} = \left[\frac{\epsilon_1(0)^{[direction]}}{\epsilon_1(0)^{[polycrystalline]}}, \frac{n(0)^{[direction]}}{n(0)^{[polycrystalline]}} \right]$$

Here, $\epsilon_1(0)^{[direction]}$ ($n(0)^{[direction]}$) is the value of $\epsilon_1(0)$ ($n(0)$) along principal optical axes and $\epsilon_1(0)^{[polycrystalline]}$ ($n(0)^{[polycrystalline]}$) is its value in polycrystalline. A material is optically isotropic if $A_{OPT} = 1$; otherwise, it is optically anisotropic. The degree of deviation of A_{OPT} from unity reveal the extent of the optical anisotropy. The calculated values of A_{OPT} are shown in Table 7. The calculated A_{OPT} values

Table 7. Calculated static dielectric constants $\epsilon_1(0)$, static refractive indexes $n(0)$ and optical anisotropy A_{OPT} for the Sr_3AlAs_3 and Ba_3AlAs_3 compounds in polycrystalline and along the principal optical axes: [100], [010] and [001].

System		$\epsilon_1(0)$	$n(0)$	A_{OPT}
Sr_3AlAs_3	Polycrystalline	7.808	2.79	
	[100]	8.048	2.82	[1.031, 1.011]
	[010]	7.566	2.75	[0.969, 0.986]
	[001]	7.810	2.79	[1.0, 1.0]
Ba_3AlAs_3	Polycrystalline	8.433	2.90	
	[100]	8.683	2.94	[1.030, 1.014]
	[010]	8.255	2.87	[0.979, 0.990]
	[001]	8.361	2.89	[0.991, 0.997]

reveal that the two studied compounds exhibit a certain optical anisotropy. The maximum optical anisotropy occurs along the [010] crystallographic direction.

3.5. Thermoelectric properties

When two dissimilar points of a thermoelectric material are held at different temperatures, a voltage of several microvolts per Kelvin between these two points arises. An efficient thermoelectric material should possess high Seebeck coefficient (S) (in order to convert maximum heat to electrical power) and high electrical conductivity σ while keeping the thermal conductivity κ low as much as possible. So, in order to study the thermoelectric properties of the orthorhombic Ae_3AlAs_3 ($\text{Ae} = \text{Sr}, \text{Ba}$) compounds, we have calculated the basic transport parameters, e.g. Seebeck coefficient (S , in μVK^{-1}), electrical conductivity scaled by relaxation time (σ/τ , in $\Omega^{-1}\text{m}^{-1}\text{s}^{-1}$), thermal conductivity scaled by relaxation time (κ/τ , in $\text{WK}^{-1}\text{m}^{-1}\text{s}^{-1}$), power-factor ($PF = S^2 s/\tau$, in $\text{WK}^{-2}\text{m}^{-1}\text{s}^{-1}$) and factor of merit ($ZT = \sigma S^2 T/\kappa$, dimensionless), as function of both charge-carrier concentration and temperature. The thermoelectric properties of the examined compounds were calculated for temperature between 300 and 900 K and for charge-carrier concentration between 1×10^{18} and $1 \times 10^{21}\text{cm}^{-3}$, which is an optimum charge-carrier concentration range for better thermoelectric performance, using the semi classical Boltzmann theory as implanted in the BoltzTraP computer package [66] with a dense k -mesh of $50 \times 50 \times 50$. As the investigated compounds crystallise in an orthorhombic system, we have first investigated the directional dependence of the thermoelectrical parameters. We find that the two considered compounds exhibit almost isotropic behaviour in the TE parameters along the three principal crystallographic directions. Since there is no significant anisotropy observed in the TE parameters, we have presented only their average values.

Figure 7 shows the variation of the Seebeck coefficient S (thermopower), electrical conductivity scaled by relaxation time σ/τ , electronic thermal conductivity scaled by relaxation time κ/τ and power-factor PF with charge-carrier concentration for both n -type and p -type Sr_3AlAs_3 and Ba_3AlAs_3 compounds at 300, 600 and 900 K. Panel (a) of Figure 6 demonstrates that the absolute value (magnitude)

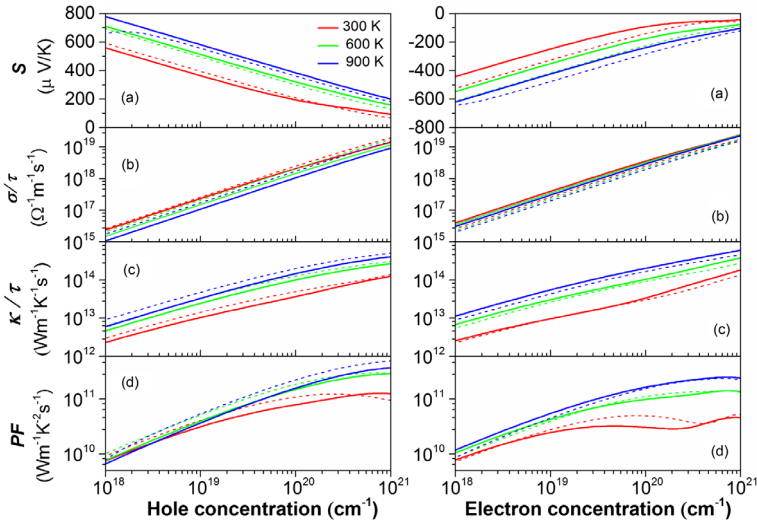


Figure 7. (colour online) Calculated average Seebeck coefficient (S ; panel a), electrical conductivity scaled by relaxation time (σ/τ ; panel b), thermal conductivity scaled by relaxation time (κ/τ ; panel c) and power-factor ($PF = S^2\sigma/\tau$ panel d) as functions of both electron and hole concentrations at 300, 600 and 900 K for the Sr_3AlAs_3 (solid lines) and Ba_3AlAs_3 (dotted lines) compounds.

of S decreases with an increasing charge-carrier concentration for both n -type and p -type doping at a fixed temperature. The magnitude of S increases with an increasing temperature due to the increase of charge-carrier concentration for both charge-carrier types; this is a common trend in thermoelectric materials. One can note that the considered compounds possess larger thermopower for the holes compared with the electrons throughout the considered temperature range. For the same carrier concentration, the difference in Seebeck coefficient between electrons and holes is of the order of 200 $\mu\text{V}/\text{K}$. This result is consistent with the calculated charge-carrier masses; large Seebeck coefficient translates to large effective masses of charge-carriers. The thermopower shows practically the same behaviour regarding the variation of charge-carrier concentration and temperature for the two title compounds. This comportment is might be due to the similarity of their band dispersions around the Fermi level and their effective masses, which are close to each other. For the same concentration and same type of charge-carrier, the two studied compounds have almost equal value for the thermopower at the same fixed temperature. To have an idea about the thermopower efficiency of the title compounds, we have compared their Seebeck coefficient S with a traditional thermoelectric material, Bi_2Te_3 . It was reported that at 300 K and charge-carrier concentration of $4 \times 10^{18} \text{ cm}^{-3}$, Bi_2Te_3 has a thermopower of 313 μVK^{-1} for p -doping and of 196 μVK^{-1} for n -doping [67,68], while our investigated compound Sr_3AlAs_3 (Ba_3AlAs_3), at the same conditions, has a Seebeck coefficient S equal to approximately 442 (472) μVK^{-1} for p -doping and -327 (-404) μVK^{-1} for n -doping. From this, one can appreciate that the thermopower value of the examined materials is larger than that of the traditional thermoelectric compound. This allows

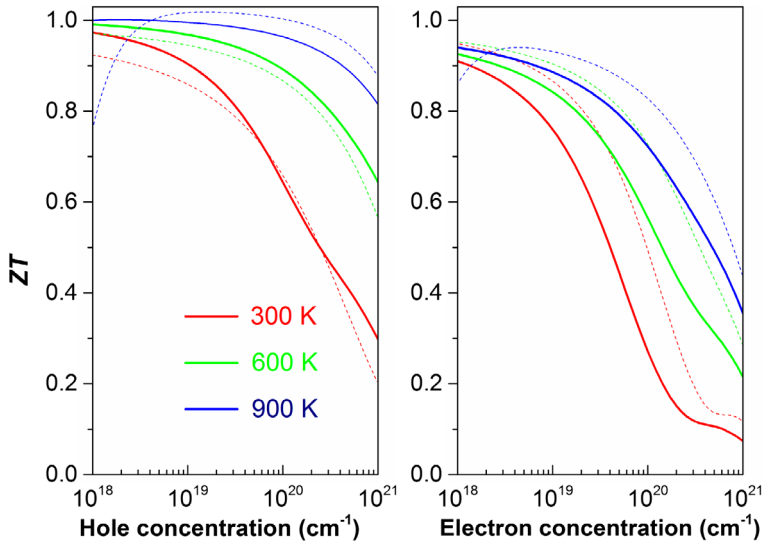


Figure 8. (colour online) Calculated figure of merit ZT as a function of charge-carrier concentration of both electron and hole concentrations at 300, 600 and 900 K for the Sr_3AlAs_3 (solid lines) and Ba_3AlAs_3 (dotted lines) compounds.

us to claim that the Sr_3AlAs_3 and Ba_3AlAs_3 systems are potential candidates for thermoelectric applications if one can more reduce their thermal conductivity by some techniques, such as alloying, nano-structuring or superlattice growth.

Panels (b) and (c) of Figure 7 demonstrate that the electrical and thermal conductivities scaled by relaxation time (σ/τ and κ/τ) increase with an increasing charge-carrier concentration in the two considered compounds for both n -type and p -type doping at a fixed temperature. It is found that the σ/τ value of the electrons is larger than that of the holes.

Figure 8 depicts the variation of the figure of merit (ZT) as function of hole and electron concentrations at 300, 600 and 900 K for Sr_3AlAs_3 and Ba_3AlAs_3 . One can note that at the same temperature and same charge-carrier concentration, the maximum figure of merit (ZT) is found in the hole-doped systems. At 900 K, the ZT is equal 1.02 (1.00) in the p -doped Sr_3AlAs_3 (Ba_3AlAs_3) and 0.93 (0.89) in the n -doped Sr_3AlAs_3 (Ba_3AlAs_3).

4. Conclusion

In summary, we have investigated in detail the structural, electronic, optical and thermoelectric properties of the new ternary arsenides Ae_3AlAs_3 ($\text{Ae} = \text{Sr}, \text{Ba}$) using first principles calculations.

Our main findings are as follows:

- (i) The calculated structural parameters agree very well with the available experimental findings.

- (ii) The two examined compounds are mechanically stable and exhibit a noticeable elastic anisotropy. Sr_3AlAs_3 (Ba_3AlAs_3) will behave as brittle (ductile) with rather moderate stiffness.
- (iii) The calculated band structures using the TB-mBJ potential reveal that Sr_3AlAs_3 and Ba_3AlAs_3 are semiconductors with band gaps equal to 1.51 and 1.28 eV, respectively.
- (iv) The calculated dielectric function, extinction coefficient, reflective index, reflectivity and electron energy-loss function for polarised incident radiation along the principal crystallographic directions show noticeable anisotropy. The origin of the features that appear in the optical spectra has discussed. The static dielectric constants $\epsilon(0)$, refractive index $n(0)$ and plasmon energy were estimated.
- (v) We found that Sr_3AlAs_3 and Ba_3AlAs_3 are promising TE materials with a high Seebeck coefficient and electrical conductivity, but their figures of merit are limited by their large thermal conductivity.

Acknowledgement

The authors (A. Bouhemadou and S. Bin-Omran) extend their appreciation to the International Scientific Partnership Program ISPP at King Saud University for funding this research work through JSPP# 0025.

Disclosure statement

No potential conflict of interest was reported by the authors.

Funding

This work was supported by the International Scientific Partnership Program ISPP at King Saud University [grant number JSPP# 0025].

ORCID

Y. Al-Douri  <http://orcid.org/0000-0002-5175-6372>

References

- [1] G.J. Snyder and E.S. Toberer, *Complex thermoelectric materials*, Nat. Mater. 7 (2008), pp. 105–114.
- [2] A.I. Hochbaum, R. Chen, R.D. Delgado, W. Liang, E.C. Garnett, M. Najarian, A. Majumdar, and P. Yang, *Enhanced thermoelectric performance of rough silicon nanowires*, Nature 451 (2008), pp. 163–167.
- [3] Y. Pei, A.D. LaLonde, N.A. Heinz, X. Shi, S. Iwanaga, H. Wang, L. Chen, and G.J. Snyder, *Stabilizing the optimal carrier concentration for high thermoelectric efficiency*, Adv. Mater. 23 (2011), pp. 5674–5678.

- [4] S.M. Kauzlarich, S.R. Brown, and G.J. Snyder, *Zintl phases for thermoelectric devices*, Dalton Trans. 133 (2007), pp. 2099–2107.
- [5] G. Chen, M.S. Dresselhaus, G.J.P. Fleurial, and T. Caillat, *Recent developments in thermoelectric materials*, Int. Mater. Rev. 48 (2003), pp. 45–66.
- [6] M.S. Dresselhaus, G. Chen, M.Y. Tang, R.G. Yang, H. Lee, D.Z. Wang, Z.F. Ren, J.P. Fleurial, and P. Gogna, *New directions for low-dimensional thermoelectric materials*, Adv. Mater. 19 (2007), pp. 1043–1053.
- [7] C. Uher, *Skutterudites: Prospective Novel Thermoelectrics*, in *Recent Trends in Thermoelectric Materials Research I, Semimetals and Semimetals Series*, Terry M. Tritt, eds., Vol. 69, Elsevier, Amsterdam, 2001, pp. 139–253.
- [8] G.S. Nolas, J. Poon, and M. Kanatzidis, Recent developments in bulk thermoelectric materials, MRS Bull. 31 (2006), pp. 199–205.
- [9] G.J. Snyder, M. Christensen, E. Nishibori, T. Caillat, and B.B. Iversen, *Disordered zinc in Zn₄Sb₃ with phonon-glass and electron-crystal thermoelectric properties*, Nat. Mater. 3 (2004), pp. 458–463.
- [10] F. Casper, T. Graf, S. Chadov, B. Balke, and C. Felser, Half-Heusler compounds: Novel materials for energy and spintronic applications, Semicond. Sci. Technol. 27 (2012), p. 063001.
- [11] K. Koumoto, Y. Wang, R. Zhang, A. Kosuga, and R. Funahashi, Oxide thermoelectric materials: A nanostructuring approach, Annu. Rev. Mater. Res. 40 (2010), pp. 363–394.
- [12] K. Koumoto, I. Terasaki, and R. Funahashi, *Complex oxide materials for potential thermoelectric applications*, MRS Bull. 31 (2006), pp. 206–210.
- [13] S.M. Kauzlarich (ed.), *Chemistry, Structure and Bonding of Zintl Phases and Ions, Selected Topics and Recent Advances*, John Wiley-VCH, Weinheim, 1996.
- [14] E.S. Toberer, A.F. May, and G.J. Snyder, *Zintl chemistry for designing high efficiency thermoelectric materials*, Chem. Mater. 22 (2010), pp. 624–634.
- [15] E.S. Toberer, A. Zevalkink, N. Crisosto, and G.J. Snyder, The Zintl compound Ca₅Al₂Sb₆ for low-cost thermoelectric power generation, Adv. Funct. Mater. 20 (2010), pp. 4375–4380.
- [16] E.S. Toberer, C.A. Cox, S.R. Brown, T. Ikeda, A.F. May, S.M. Kauzlarich, and G.J. Snyder, *Traversing the metal-insulator transition in a Zintl phase: Rational enhancement of thermoelectric efficiency in Yb₁₄Mn_{1-x}Al_xSb₁₁*, Adv. Funct. Mater. 18 (2008), pp. 2795–2800.
- [17] A. Zevalkink, G. Pomrehn, Y. Takagiwa, J. Swallow, and G.J. Snyder, *Thermoelectric properties and electronic structure of the Zintl-phase Sr₃AlSb₃*, ChemSusChem. 6 (2013), pp. 2316–2321.
- [18] G.J. Snyder and E.S. Toberer, *Complex thermoelectric materials*, Nat. Mater. 7 (2008), pp. 105–114.
- [19] Y. Pei, A.D. LaLonde, N.A. Heinz, X. Shi, S. Iwanaga, H. Wang, L. Chen, and G.J. Snyder, Stabilizing the optimal carrier concentration for high thermoelectric efficiency, Adv. Mater. 23 (2011), pp. 5674–5678.
- [20] A. Zevalkink, E.S. Toberer, W.G. Zeier, E. Flage-Larsen, and G.J. Snyder, *Ca₃AlSb₃: An inexpensive, non-toxic thermoelectric material for waste heat recovery*, Energy Environ. Sci. 4 (2011), pp. 510–518.
- [21] Y.L. Yan and Y.X. Wang, *Crystal structure, electronic structure, and thermoelectric properties of Ca₅Al₂Sb₆*, J. Mater. Chem. 21 (2011), pp. 12497–12502.
- [22] J.P. Perdew and A. Zunger, *Self-interaction correction to density-functional approximations for many-electron systems*, Phys. Rev. B 23 (1981), pp. 5048–5079.

- [23] S.S. Stoyko, L.H. Voss, H. He, and S. Bobev, Synthesis, crystal and electronic structures of the pnictides $AE_3\text{TrPn}_3$ ($AE = \text{Sr, Ba}$; $\text{Tr} = \text{Al, Ga}$; $\text{Pn} = \text{P, As}$), *Crystals* 5 (2015), pp. 433–446.
- [24] S.J. Clark, M.D. Segall, C.J. Pickard, P.J. Hasnip, M.J. Probert, K. Refson, and M.C. Payne, *First principles methods using CASTEP*, *Z. Kristallogr.* 220 (2005), pp. 567–570.
- [25] P. Blaha, K. Schwarz, G.K.H. Madsen, D. Kvasnicka, and J. Luitz, *WIEN2k: An Augmented plane wave plus local orbitals program for calculating crystal properties*, Vienna University of Technology, Vienna, 2001.
- [26] D. Vanderbilt, *Soft self-consistent pseudopotentials in a generalized eigenvalue formalism*, *Phys. Rev. B.* 41 (1990), pp. 7892–7895.
- [27] J.P. Perdew, A. Ruzsinszky, G.I. Csonka, O.A. Vydrov, G.E. Scuseria, L.A. Constantin, X.L. Zhou, and K. Burke, Restoring the density-gradient expansion for exchange in solids and surfaces, *Phys. Rev. Lett.* 100 (2008), p. 136406.
- [28] H.J. Monkhorst and J.D. Pack, Special points for Brillouin-zone integrations, *Phys. Rev. B.* 13 (1976), pp. 5188–5192.
- [29] P. Dufek, P. Blaha, and K. Schwarz, *Applications of Engel and Vosko's generalized gradient approximation in solids*, *Phys. Rev. B* 50 (1994), pp. 7279–7283.
- [30] E. Engel and S.H. Vosko, *Exact exchange-only potentials and the virial relation as microscopic criteria for generalized gradient approximations*, *Phys. Rev. B* 47 (1993), pp. 13164–13174.
- [31] X. Zhu, S. Fahy, K.J. Chang, and S.G. Louie, *Ab initio calculation of pressure coefficients of band gaps of silicon: Comparison of the local-density approximation and quasiparticle results*, *Phys. Rev. B* 39 (1989), pp. 7840–7847.
- [32] P.P. Rushton, D.J. Tozer, and S.J. Clark, *Nonlocal density-functional description of exchange and correlation in silicon*, *Phys. Rev. B.* 65 (2002), p. B864.
- [33] B. Králik, E.K. Chang, and S.G. Louie, *Structural properties and quasiparticle band structure of zirconia*, *Phys. Rev. B* 57 (1998), pp. 7027–7036.
- [34] F. Tran and P. Blaha, *Accurate band gaps of semiconductors and insulators with a semilocal exchange-correlation potential*, *Phys. Rev. Lett.* 102 (2009), p. 226401.
- [35] P.E. Blöchl, O. Jepsen, and O. K. Andersen, *Improved tetrahedron method for Brillouin-zone integrations*, *Phys. Rev. B* 49 (1994), pp. 16223–16233.
- [36] C.A. Ponce, R.A. Casali, M.A. Caravaca, *Ab initio study of mechanical and thermo-acoustic properties of tough ceramics: Applications to HfO_2 in its cubic and orthorhombic phase*. *J. Phys.: Condens. Mater.* 20 (2008), p. 045213.
- [37] A. Bouhemadou, R. Khenata, M. Chegaar, and S. Maabed, *First-principles calculations of structural, elastic, electronic and optical properties of the antiperovskite AsNMg_3* , *Phys. Lett. A* 371 (2007), pp. 337–343.
- [38] D.C. Wallace, *Thermodynamics of Crystals*, John Wiley, New York, NY, 1972.
- [39] R. Hill, *The elastic behaviour of a crystalline aggregate*, *Proc. Phys. Soc. Lond. A.* 65 (1952), pp. 349–354.
- [40] W. Voigt, *Lehrbuch der Kristallphysik*, Taubner, Leipzig, 1928.
- [41] A. Reuss, *Berechnung der fließgrenze von mischkristallen aufgrund der plastizitätsbedingung für Einkristalle*, *Zeitschrift Angew. Math. Mech.* 9 (1929), pp. 49–58.
- [42] A. Bedjaoui, A. Bouhemadou, S. Aloumi, R. Khenata, S. Bin-Omran, Y. Al-Douri, F. Saad Saoud, and S. Bensalem, *Structural, elastic, electronic and optical properties of the novel quaternary diamond-like semiconductors Cu_2MgSi_4 and Cu_2MgGe_4* , *Solid State Sci.* 70 (2017), pp. 21–35.
- [43] E. Schreiber, O.L. Anderson, and N. Soga, *Elastic Constants and Their Measurements*, McGraw-Hill, New York, NY, 1973.

- [44] J.W. Soh, H.M. Lee, and H.-S. Kwon, Relation between Poisson's ratio and ionicity in simple binary cubic compounds, *J. Alloys Compd.* 194 (1993), pp. 119–125.
- [45] S.F. Pugh, *Relations between the Elastic Moduli and the plastic properties of polycrystalline pure metals*, *Phil. Mag.* 45 (1954), pp. 823–843.
- [46] S. Chen, Y. Sun, Y.-H. Duan, B. Huang, and M.-J. Peng, Phase stability, structural and elastic properties of C15-type Laves transition-metal compounds MCo₂ from first-principles calculations, *J. Alloys Compd.* 630 (2015), pp. 202–208.
- [47] D.G. Pettifor, *Theoretical predictions of structure and related properties of intermetallics*, *Mater. Sci. Technol.* 8 (1992), pp. 345–349.
- [48] P. Jund, R. Viennois, X. Tao, K. Niedziolka, and J.C. Tédénac, *Physical properties of thermoelectric zinc antimonide using first-principles calculations*, *Phys. Rev. B* 85 (2012), p. 423.
- [49] A.L. Anderson, A simplified method for calculating the debye temperature from elastic constants, *J. Phys. Chem. Solids* 24 (1963), pp. 909–917.
- [50] V. Tvergaard and J.W. Hutchinson, *Microcracking in ceramics induced by thermal expansion anisotropy*, *J. Am. Ceram. Soc.* 71 (1988), pp. 157–166.
- [51] B. Xiao, J. Feng, C.T. Zhou, Y.H. Jiang, and R. Zhou, *Mechanical properties and chemical bonding characteristics of Cr₇C₃ type multicomponent carbides*, *J. Appl. Phys.* 109 (2011), p. 023507.
- [52] K. Lau and A.K. McCurdy, *Elastic anisotropy factors in orthorhombic, tetragonal, and hexagonal Crystals*, *Phys. Rev. B* 58 (1998), pp. 8980–8984.
- [53] P. Ravindran, L. Fast, P.A. Korzhavyi, and B. Johansson, *Density functional theory for calculation of elastic properties of orthorhombic crystals: Application to TiSi₂*, *J. Appl. Phys.* 84 (1998), pp. 4891–4904.
- [54] D.H. Chung and W.R. Buessem, *The Elastic Anisotropy of Crystals*, in *Proceeding of International Symposium 2*, F.W. Vahldiek and S.A. Mersol, eds., Plenum Press, New York, NY, 1968, pp. 217–245.
- [55] K.B. Panda and K.S.R. Chandran, *Determination of elastic constants of titanium diboride (TiB₂) from first principles using FLAPW implementation of the density functional theory*, *Comput. Mater. Sci.* 35 (2006), pp. 134–150.
- [56] S. Ranganathan and M. Ostoja-Starzewski, *Universal elastic anisotropy index*, *Phys. Rev. Lett.* 101 (2008), p. 055504.
- [57] J.F. Nye, *Physical Properties of Crystals: Their Representation by Tensors and Matrices*, Oxford University Press, Great Britain, 1957.
- [58] F. Wooten, *Optical Properties of Solid*, Academic, New York, NY, 1972.
- [59] M. Alouani and J.M. Wills, *Calculated optical properties of Si, Ge, and GaAs under hydrostatic pressure*, *Phys. Rev. B* 54 (1996), pp. 2480–2490.
- [60] M. Fox, *Optical Properties of Solids*, Oxford University Press, New York, NY, 2001.
- [61] M. Dressel and G. Gruner, *Electrodynamics of solids: Optical properties of electrons in matter*, Cambridge University Press, Cambridge, 2002.
- [62] A. Bouhemadou and R. Khenata, *Ab initio study of the structural, elastic, electronic and optical properties of the antiperovskite SbNMg₃*, *Comput. Mater. Sci.* 39 (2007), pp. 803–807.
- [63] R. Saniz, L.H. Ye, T. Shishidou, and A.J. Freeman, *Structural, electronic, and optical properties of NiAl₃: first-principles calculations*, *Phys. Rev. B* 74 (2006), pp. 014209.
- [64] D. Yonghua, M. Lishi, L. Ping, and C. Yong, *First-principles calculations of electronic structures and optical, phononic, and thermodynamic properties of monoclinic α -spodumene*, *Ceram. Internat.* 43 (2017), pp. 6312–6321.
- [65] D. Cherrad, D. Maouche, M. Boudissa, M. Reffas, L. Louail, M. Maamache, K. Haddadi, and Y. Medkour, *Ultra soft pseudo potential investigation of fundamental physical properties*

- of CaXO₃ (X=Sn and Hf) distorted perovskites: A reference study to the perfect perovskites*, Physica B 429 (2013), pp. 95–105.
- [66] G.K.H. Madsen and D.J.S. Singh, BoltzTraP. A code for calculating band-structure dependent quantities, Comput. Phys. Commun. 175 (2006), pp. 67–71.
- [67] P.C. Sreeparvathy, V. Kanchana, and G. Vaitheeswaran, *Thermoelectric properties of zinc based pnictide semiconductors*, J. App. Phys. 119 (2016), p. 085701.
- [68] T.J. Scheidemantel, C. Ambrosch-Draxl, T. Thonhauser, J.V. Badding, and J.O. Sofo, *Transport coefficients from first-principles calculations*, Phys. Rev. B 68 (2003), p. 331.